2014 | Faculty of Sciences

DOCTORAL DISSERTATION

How to master vanadium oxide stoichiometry and phase formation? Insights in the aqueous precursor chemistry

Doctoral dissertation submitted to obtain the degree of doctor
of Science: Chemistry, to be defended by:

Nick Peys

Promoter: Prof. Dr Marlies K. Van Bael | UHasselt
Co-promoters: Prof. Dr An Hardy | UHasselt
Prof. Dr Stefan De Gendt | KULeuven / IMEC

D/2014/2451/31

Supported by:

imec

Chairman

Prof. Dr Karen Coninx
Dean Faculty of Sciences, UHasselt

Promoter

Prof. Dr Marlies K. Van Bael, UHasselt

Co-promoter

Prof. Dr An Hardy, UHasselt
Prof. Dr Stefan De Gendt, KULeuven / IMEC

Members of the jury

Prof. Dr Sabine Van Doorslaer, University of Antwerp
Prof. Dr Peter Adriaensens, UHasselt
Prof. Dr Theodor Schneller, RWTH Aachen University

Acknowledgments

Doctoral research and the preparation of a Ph.D. thesis are like a roller coaster. Full of confidence you hop on board, pretending that you are well prepared. The project is there, you just need to keep track of the milestones and occasionally present the results to either the research team, the Ph.D. commission or an international audience. In fact, just like on a roller coaster ride, you just see the first meters. After these few meters, the tracks deflect and an adventure awaits. Sometimes an ascent, which is obviously rather tedious, emerges. Thorough literature elaborations or writing that first paper are a few of those ascents passed by the cart. Fortunately, each ascent comes to an end and is often followed by a steep descent on which the cart gains speed and excellent results come pouring in. At this point, you can hardly wait for new data or for opportunities to present your work at an international conference. When the cart is at full speed, the long awaited conference or the paper acceptance mail from an editor emerges like a looping or screw, pushing your happiness to an elevated level. Suddenly a sharp turn looms, pushing the cart and the research into a new, unexpected direction. Magnetic resonance spectroscopy enters the research and collaboration opportunities present themselves. Anyway, the point is clear: a Ph.D. is indeed like a roller coaster.

Not only the Ph.D. path is similar to a roller coaster, also the setting compares. You're not alone in the cart, colleagues accompany and encourage you. Some are in the same cart and look to the path ahead full of curiosity and astonishment. Others are in front of you, see a little bit more of the path and are able to guide you past all kinds of obstacles. Still, others are behind you and rely on you as their guide. Together with all the colleagues - in front, behind or next to you - the path becomes pleasant, highlights become kicks and obstacles become passable. Besides the direct colleagues, also the professors (who act as promoter, commission member and/or as walking library) and the university staff are of great importance. You can compare them with the safety belt in the cart or the brakes/accelerators on the roller coaster path which are indispensable for the cart and its participant to reach the finish line. This section intends to thank and acknowledge everyone who helped me during my doctoral research and in the preparation of my Ph.D. thesis.

Firstly, I'd like to thank Marlies and An for giving me the opportunity to work on a Ph.D. project. Marlies, you are in particular gifted with a positive mind and the ability to convert complex research output into a more agreeable, clear and readable story. An, I appreciate your critical point of view and your skills to bring experiments and data to higher scientific level. Thank you for your support and motivation!

A special word of gratitude goes to Stefan. Already during my master studies, you introduced me to the IMEC machinery. The high level and quality of the research, the nearly inexhaustible fleet of synthesis and/or characterization tools and the application driven spirit still amaze me. You learned me to look at my research data from a different perspective (which is rarely the original perspective or the chronological order), how to present for a scientific audience and how to bring the figures in a clear, understandable and readable fashion. In addition, your door was always open for good advice, a motivational speech or *off the record* conversations. Moreover, you are also just a pleasant guy to talk to and drink a beer with. Thank you so much for everything!

Next, I'd like to thank the NMR tandem, Peter and Gunter, for the many ^{51}V-NMR experiments, their support during the subsequent data interpretation and their smile when I (again!) lost paper printed spectra. Peter, I still remember our first discussion concerning ^{51}V-NMR. Even though there was no experience with ^{51}V-NMR, you accepted this challenge without hesitation! But look what fortune this challenge brought: one paper published, two more in the pipeline and an excellent talk during a dedicated MR conference! The same goes for the EPR team (Sabine, Ling and Sara) in Antwerp. I had never heard about EPR spectroscopy before my Ph.D. and yet in the aforementioned output, EPR analyses proved to be most important. Sabine, thank you for the EPR opportunities, for teaching me about EPR (at your office or during the regular courses), for sharing your enthusiasm and for all the effort concerning the papers and this Ph.D. thesis. I also like to thank Sara for performing the analyses and for the nice company during the MR conference in Spa. Furthermore, I apologize for the *crazy* analyses that have not found their way into this thesis. I must admit that the NMR/EPR analyses have lifted this work to a higher, fundamental scientific level for which I'm very grateful.

Let's turn back to the IMEC setting . . . Sven and Philippe, thank you for all the ideas and input during the three-monthly Ph.D. meetings. Despite our different synthesis approaches you were always able to find and correct flaws or inconsistencies in the experimental design or presented results. In this context, your broad experience as senior researchers was more than helpful. I'd like to acknowledge Koen and Iuliana for their guidance through the wonderful world of Amsimec. Furthermore, I'd like to thank Johnny for his support on the Heat Pulse (especially when I managed to melt a silicon sample on the carrier wafer . . .) and the pleasant conversations.

I think it's about time to thank all the colleagues from Inorganic and Physical Chemistry who were (and still are) burdened with my presence, my incessant nagging about lab safety/cleanliness and my ramblings on the complicated vanadium chemistry. Thus, a well appreciated thank you is more than in place! Let's start with Kevin, who of all was mostly *blessed* . . . Kevin, already during the lab practices of our bachelor studies we were a winning team. Despite your adventure in Antwerp, our friendship and mutual support remained. Thank you for everything and I wish you all the luck you deserve as an inspiring teacher! Since you're settling nearby, I'm sure we can keep exchanging stories! Besides Kevin, also Bertie and Anke followed the same track. I wish both of you a bright future with a motivating job and a lovely family at home! Daan, do you remember the first times(s) we met? At that time, you just started your Ph.D. and I was still a master student at the KUL. Together we managed to survive a Keithley training session by Sven and personal high-k lecture by Marc Heyns, which was quite the challenge! Thank you for dumping your CV/XRD samples, for leaving your desk to me, for all the GATR measurements, for the Vampire Diaries, for teaching the Congo method concerning grapefruit. But most of all thank you for being a friend! Equally important for me is Christopher. Thank you for the scientific help (our many, successful discussions and your efforts to improve papers). Furthermore, I enjoy your company during the daily coffee/water breaks, during our Balkan trip and all the activities outside the working hours! I'm sure you will find a new, challenging job after your post-doc career! And don't forget: running only works if you do it more than once a week. Sven, thank you for all the (X-)SEM measurements and the small conversations in the early working hours. Without you, we would have never met the Croatian hunter Branco from Plitvice who indulged us with fresh trout, stew of shot venison and a nightly campfire! On to the ladies: Hanne and Lize! Always enthusiastic, motivated, smiling, straightforward, targeted, . . . much appreciation from a proud Chambers Trophy coach and handsome groom ;). Ellen, you deserve a special applause, since you managed to survive your internship under the supervision of that tyrant who overburdened you with lots of work. Yet, you have found your way back to Hasselt and you are even sharing a lab table with the same tyrant. I wish you all the best and hope you can reveal the aqueous manganese chemistry in collaboration with Sabine. Thomas, we teamed up to design and build the new *gas panel*. I enjoyed working with you, apart from those days when you entered the office with the phrase *Ik heb eens zitten denken* . . . Thank you for your agreeable company and clean up that mess on your desk! Ken, our offline wikipage, thank you for your agreeable company during the many social activities! Alexander, our projects had nothing to do with each other. So their was little scientific overlap which gave you the perfect opportunity to catch up on sleep during my presentations . . . Yet, as a seasoned entertainer you brought life in the lab and office! Nikolina, thank you for your guidance through Croatia and Serbia. The lakes of Plitvice are really a miracle of nature! Giedrius, I left you an ill functioning Raman tool for which I apologize. Yet, you succeeded to get the damn tool operational, well done!

Maarten, you were always up for a critical talk on the battery project, on politics or whatever was in the news that day. I am sure your godfather is proud seeing you as our new lab harlequin! At this very moment, a new flock of motivated Ph.D. students invades the lab and makes things unsafe and messy. Jonathan, Giulia, Gilles, Wouter and Boaz, good luck with your projects (of course I'm confident that one project might go better than another ;))!

Obviously, I could count on the support of many people outside our research group. I'd like to express my gratitude to them. Robert, Elsy, Martine, Huguette, Guy, Jenny (the morning coffees!) and Yvo from applied chemistry; Jan and Bart from IMO for powder XRD measurements; Koen and Johan for technical support on various tools and projects and Gene from didactics for all the small things (such as borrowing glassware and small talks in the corridor).

This brings me to the people at home . . . I'd like to thank my parents for giving me the opportunity to start my studies on Chemistry and for their continuous support! This leaves just one more person to thank: Liesbeth. Thank you for all the great moments we have spent so far (and will be spending). Also, thank you for your unconditional support during difficult times (whether related to my Ph.D. or not). I know I don't say this as often as you would have me say it: *Ik zie je graag!*

Nick

Almost forgotten $\cdots$ thank you to all the ladies: Amelie, Anouk, Axelle, Lana, Adele, Emmylou, Sinead, Skin, Geike, Noemie and many others ;)

Contents

Statement and objectives

In our modern world, technology has - indispensably - penetrated all facets of life: households, mobility, healthcare and leisure are just a few of these facets. Moreover, it seems obvious that with each new generation a device becomes smaller, works faster, has more functionalities and has a longer battery lifetime. Since the *Happy days of CMOS scaling* came to an end about a decade ago, further technological evolution had to be found elsewhere. So in the last decade, new materials and new architectures have been introduced into e.g. integrated circuits, batteries, intelligent windows and solar cells.

Prior to the integration of these new materials - which is often neglected or forgotten by society - is the exploratory research, necessary to answer the many technological questions. Possibly the first questions that emerge are *How can we synthesize this material?* and *What are the major synthetic parameters controlling the final properties of the obtained material?* Even though this work focuses just on one material, i.e. vanadium oxides, the last question is the guideline throughout this work: *How can we master the vanadium oxide stoichiometry and phase formation?* To answer that question, a water-based process is selected and the aqueous vanadium species present in the aqueous solution are studied. Moreover, differences between these vanadium species are related to the final vanadium oxide stoichiometry and phase formation.

Statement

Vanadium exists in different oxidation states, ranging from +II to +V, forming a variety of vanadium oxides, as given in the vanadium-oxygen phase diagram (Figure 1) established by Wriedt.[1, 2] This variety includes single valence oxides (such as VO, V_2O_3, VO_2 and V_2O_5) and mixed valence oxides either belonging to the Magnéli phases, V_nO_{2n-1}, or the Wadsley phases, $V_{2n}O_{5n-2}$.[1–4] Some of these vanadium oxides with a specific structure and crystallinity are intensively investigated as candidate active materials in future technological devices. (i) Monoclinic VO_2 M1 exhibits a temperature induced semiconductor-to-metal transition at a temperature of 68 °C. This transition is accompanied by a structural – monoclinic to tetragonal – phase transition, characterized by a lattice distortion along the c-axis, and abruptly changes its electrical resistivity and infrared optical properties.[5–7] The change in electrical resistivity and infrared transmittance is associated with a hysteresis loop around 68 °C.

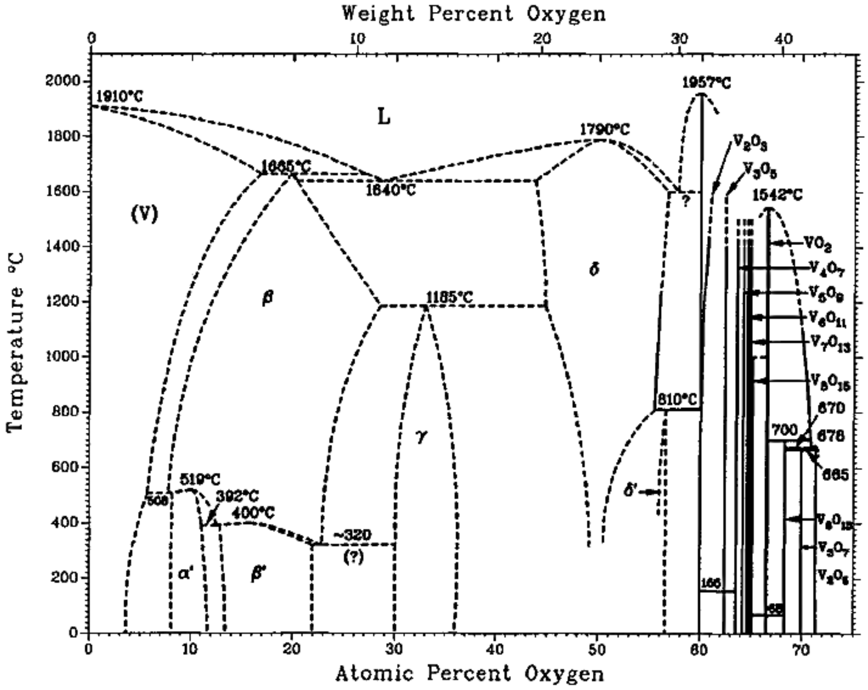

Figure 1: The vanadium-oxygen phase diagram established by Wriedt.[1] The phases below 60 at.% oxygen in the phase diagram correspond to a solid phase – i.e. body-centered cubic (V), body-centered tetragonal (α', β, β' and δ'), monoclinic (γ) and face-centered cubic (δ) – or a liquid phase (L).[1]

In bulk materials and thin films, this hysteresis width is about 1 °C and 10-15 °C, respectively.[7] However, in VO_2 particles a larger hysteresis width in the order of 30 °C has been observed.[8, 9] This makes them more applicable as a switching material in memory and optical devices.[7] For its synthesis, caution is required, because up to six polymorphs have been reported for VO_2. These polymorphs include VO_2 B and VO_2 M1 which belong to the monoclinic space groups C2/m and $P2_1/c$, respectively.[7] (ii) Layered vanadium oxides such as V_6O_{13} and V_2O_5 are proposed as alternatives for the reasonably thermally unstable and expensive $LiCoO_2$ cathode in rechargeable Li-ion micro-batteries.[10, 11] V_6O_{13} single crystals exhibit a lithium intercalation/extraction plateau around 2.7 V vs. a Li^+/Li reference electrode and reversibly host up to 6 Li atoms per formula unit, leading to a maximal theoretical gravimetric charge capacity of 310 $mAhg^{-1}$.[12] If V_2O_5 is electrochemically cycled, the first lithium intercalation/extraction plateaus are observed at 3.2 V and 3.4 V vs. a Li^+/Li reference electrode. In this region, V_2O_5 can reversibly host up to 0.8 Li atoms per formula unit, which results in a maximum theoretical gravimetric charge capacity of 118 $mAhg^{-1}$.[10, 13]

As evidenced by the large variety of vanadium oxides and the complex vanadium-oxygen phase diagram[1], the synthesis of VO_2 and V_6O_{13} is not straightforward. In addition, the occurrence of multiple VO_2 polymorphs further emphasises the challenge to synthesize stoichiometric and phase pure monoclinic or tetragonal VO_2, mutually associated by the structural phase transition. Various methods for their synthesis have been reported including chemical vapour deposition[7, 14], atomic layer deposition[15, 16], pulsed laser deposition[7, 17, 18] and sputtering[7, 19, 20]. Wet chemical synthesis routes are widely considered as valuable alternatives for the vacuum based techniques.[21] In these routes, VO_2 and V_6O_{13} are commonly prepared starting from vanadium alkoxides.[7, 22, 23] However, such alkoxides are scarcely available, expensive and very reactive to ambient humidity, which implies the use of inconvenient experimental circumstances.[21] Alternatively, aqueous synthesis routes are proposed by Livage et al. and Dachaun et al. who prepared VO_2 or V_6O_{13} films starting from a V_2O_5 gel or sol, respectively.[24, 25] However, the aforementioned wet chemical routes intermediately form V_2O_5 films and require an additional, reductive anneal to obtain VO_2 or V_6O_{13} films.[24, 25] This emphasizes the large challenge in the direct formation of VO_2 M1 or V_6O_{13} from an aqueous solution.

Objectives

The main objective of this work is to obtain fundamental insights in the aqueous vanadium precursor chemistry and in their relation to the vanadium oxide stoichiometry/phase formation, obtained via a solution deposition route. To achieve this objective, three milestones are defined.

Acquiring insights in the aqueous citrato/oxalato-VO^{2+} solution chemistry: synthesis, structure and stability

The complexation of citric acid and its pH-dependent derivatives with the VO^{2+} ion is previously studied both in the solid state[26–29] and in solution[26, 30, 31]. The formation of dimeric structures with composition $[(VO)_2(C_6H_4O_7)_2]^{4-}$ is generally accepted in or from solutions with, approximately, an equimolar ligand:VO^{2+} ratio and a neutral pH value.[26–31] Note that in this dimeric structure, all chelating groups interact with the coupled VO^{2+} centers leading to a sixfold chelation of each V center in a secluded dimeric structure without free available carboxylate groups. Only for very high citrate excesses (citrate:VO^{2+} ~ 100:1), pH-dependent mononuclear citrato-VO^{2+} complexes were observed by Lodyga-Chruscinska et al.[32]. Our work aims to synthesize mononuclear citrate-VO^{2+} complexes without inserting a high amount of citrate or thermally non-decomposable species. Alternatively, the prevention of the secluded, dimeric structure – by the formation of ammonium carboxylate interactions, bridging two or more citrato-VO^{2+} complexes into a network – is targeted. This network allows the formation of an amorphous gel by its cross-linking nature upon evaporation of water during a chemical solution deposition process.[21, 33] A low amount of citrate is preferred since this decreases the amount of carbon which must be thermally removed during the film processing and the vanadium oxide phase formation.[21, 33]

Prior to the synthesis of an aqueous solution containing citrato-VO^{2+} complexes, a detailed literature study on the behavior of vanadium ions and their coordination with citrato ligands in water is required. This survey includes the work of bio-inorganic chemists who investigate the medical applications of vanadium coordination compounds. Next, the actual synthesis of such an aqueous solution is intended. From a fundamental scientific perspective, it is interesting to study and understand each step, and the associated chemical transformations, during this synthesis. For this understanding, various characterization techniques will be required to probe and identify each vanadium-based species during the entire synthesis sequence. The structure and stability of the final citrato-VO^{2+} complexes, present in the aqueous solution, and their relation to the synthesis parameters will be explored in particular.

Understanding the thermal decomposition pathway of the ammonium-citrato/oxalato-VO^{2+} gel

The formation of a vanadium oxide, starting from an aqueous vanadium precursor solution, via the chemical solution deposition route, requires the, thermally-induced, transformation of the precursor gel into the oxide. Hence, it is important to understand these transformations or, alternatively, the chemical decomposition pathway of the precursor gel. In addition, this understanding will aid in determining the initial processing conditions and in establishing the relation between the precursor composition and the vanadium oxide stoichiometry/phase formation. Here, the thermal decomposition pathway of the ammonium-citrato/oxalato-VO^{2+} gel, obtained by evaporation of the precursor solution, will be studied via (i) simultaneous Thermogravimetric - Differential Scanning Calorimetry (TG-DSC), (ii) hyphenated Thermogravimetric - Mass Spectrometry (TG-MS) and (iii) ex-situ analysis of the remaining product by Fourier Transform Infrared (FTIR) spectroscopy.

Relating the aqueous precursor chemistry to the vanadium oxide stoichiometry and phase formation

Once the composition and structure of the VO^{2+} complexes, present in the aqueous solution, and their thermal decomposition pathway are understood, the actual vanadium oxide formation – via chemical solution deposition and subsequent processing – can be explored. Prior to this study, a brief literature elaboration on the technological importance of vanadium oxide nanomaterials and a description of the chemical solution deposition route will be given.

For the achievement of this milestone, each step and parameter of the chemical solution deposition route is investigated with the formation of VO_2 M1, VO_2 B, V_6O_{13} and V_2O_5 intended. The temperatures of the hot plate steps, the intermediate anneal conditions and the multiple deposition cycle will be key parameters. Finally, the vanadium oxide stoichiometry and phase formation will be investigated and related to the composition and thermal decomposition pathway of the VO^{2+} complexes present in the aqueous, precursor solution (as is previously elaborated on). In addition, insights on the influence of the application-dependent substrate (SiO_2, Al_2O_3, TiO_2, Pt and TiN) and the total thermal budget on the vanadium stoichiometry and phase formation will introduced.

Part I

ACQUIRING INSIGHTS IN THE AQUEOUS CITRATO/OXALATO-VO^{2+} SOLUTION CHEMISTRY: SYNTHESIS, STRUCTURE AND STABILITY

Chapter 1

Review on aqueous vanadium chemistry and its citrate complexation

1.1 Vanadium discovery and occurrence

The element vanadium has a remarkable discovery.[34–36] In 1801, a Spanish mineralogist Andrés Manuel del Río examined a specimen of a brown lead ore, mined in Zimapán, central Mexico. He concluded that the ore contained a new metal, similar to chromium and uranium and named it *Erythronium*. After further study and with confirmation of the French chemist Hippolyte-Victor Collet-Descotils, he recognized his mistake and classified the brown lead ore as 80.72 % lead oxide and 14.80 % chromium oxide. For several years, the so-called new element *Erythronium* was not spoken of, until the German chemist Friedrich Wöhler began to investigate the same brown lead ore in 1828. In contrast to the findings of Collet-Descotils, its properties did not match those of chromium. Due to illness, Wöhler ceased his research on the ore from Zimapán.[34]

In 1831, the Swedish chemist Nils Gabriel Sefström discovered a new element in a black powder obtained by treating an iron ore, from the Taberg mine in South Sweden, with hydrochloric acid. Even though the new element showed similarities with chromium and uranium, Sefström found that the new element was neither chromium, nor uranium. His experiments were continued in the laboratory of Jöns Jacob Berzelius where the discovery of the new element was confirmed. Sefström named the new element *Vanadium*[1] after Vanadis, a synonym for the Nordic goddess Freya who symbolizes beauty, one of the features of the vanadium chemistry.[34]

---

[1] During its discovery period, in the first part of the 19th century, besides *Erythronium*, *Vanadium* was also named *Panchromium*, *Odinium*, *Erian* or *Sefströmium*.[34]

Immediately after the vanadium discovery, Berzelius sent a letter with a charming anecdote to Wöhler to describe his misfortune:

In the far North there lived in olden times the goddess Vanadis, beautiful and lovably. One day someone knocked at her door. The goddess remained comfortably seated and thought: let the person knock again; but there was no more knocking, and the one who knocked went down the steps. The goddess was curious to see who it might be that was so indifferent to being admitted, sprang the window, and looked at the one who was going away. 'Alas!' she said to herself, that's that fellow Wöhler. Well, he surely deserved it; if he had been a little more concerned about it, he would have been admitted. The fellow does not look up the window once in passing by . . . After a few days someone knocked again at the door; but this time the knocking continued. The goddess finally came herself and opened the door. Sefström entered, and from this union vanadium was born.[34, 35]

Eventually Wöhler was able to show that the sample from the Zimapán ore was identical with Sefström's new element, vanadium, from the Taberg mine. Sir Henry Enfield Roscoe successfully isolated the metallic vanadium, in 1869, by the reduction of VCl_2 with H_2. However, its first large-scale synthesis (purity > 99) was not carried out until 1927, through heating of a mixture of V_2O_5, Ca and $CaCl_2$ at 720 °C. Nowadays, this reduction process is still used for the production of pure metallic vanadium, but also the *van Arkel-de Boer*[2] process is often followed.[36]

Vanadium (atomic number 23 and [Ar] $3d^3$ $4s^2$ electron configuration) has two natural isotopes: ^{51}V and ^{50}V, with an abundance of respectively 99.75 % and 0.25.[37] The estimated vanadium concentration in the Earth's crust is 0.013 w/w % and it is considered the 22th in abundance.[36] Vanadium is widely distributed[38]: (i) in more than 60 minerals, mainly mined in Russia, China and South-Africa and (ii) in crude oil, especially from Venezuela and Canada. In addition, large quantities of vanadium, mainly as $H_2VO_4^-$, are found in seawater with a concentration of 20–35 nM[3].[36]

1.2 Metal cations in an aqueous solution

Before describing the behavior of vanadium ions in an aqueous solution, some general principles and reaction types must be discussed. In this paragraph, the focus will be on the hydrolysis and condensation, via olation and oxolation, of metal ions in an aqueous solution.

Due to its high polarity (μ = 1.84 debye) and high dielectric constant (ϵ = 78.5), water is most suitable for the dissolution of ionic compounds such as NH_4VO_3. This high

---

[2] In the *Arkel-de Boer* process, impure vanadium reacts with iodine at ~ 500 °C to form the volatile VI_3. This volatile VI_3 decomposes at a tungsten filament (~ 1400 °C) and the metallic vanadium deposits on the tungsten filament.

[3] Molybdenum is the most abundant transition metal in seawater with a concentration of about 100 nM.

polarity and high dielectric constant of water are, respectively, responsible for its good solvation power and its ability to decrease the electric forces between solvated metal ions. Thus, the properties of water allow the formation of a stable solution. The solvation of a metal cation with charge z, M^{z+}, to an aqua complex with coordination number n is given in Equation 1.1.

$$M^{z+} + nH_2O \longrightarrow [M(OH_2)_n]^{z+} \tag{1.1}$$

The number of water molecules, involved in the solvation of a metal cation with radius r is linearly dependent on its polarizing strength (z/r^2). Small ions or ions with a large charge have a higher polarizing strength and are, therefore, solvated by more water molecules. The attraction and organization of water molecules around an ion occur over several spheres. The first solvation sphere contains the water molecules, in direct contact with the ion, which are involved in further reactions (i.e. hydrolysis and condensation, see next sections). The water molecules of the higher solvation spheres are of minor importance due to their continuous exchange with bulk water molecules and their indifference in further reactions.[39, 40] Despite the favorable physical/chemical properties of water and the solvation of the metal cations in solution, these solvated metal cations are subject to hydrolysis and condensation. In the next sections, the aforementioned reactions will be discussed briefly. A detailed and more fundamental description is given by Livage et al.[39] and Jolivet et al.[40].

1.2.1 Hydrolysis of metal ions in water

General considerations

The $M^{z+} \longleftarrow OH_2$ transfer decreases the electron density around the oxygen and weakens the O–H bond. The ionic character of the O–H bond and the positive charge on the hydrogen increase. The positive charge on the metal cation decreases. Consequently, coordinated water molecules are more acidic than bulk water molecules and tend to deprotonate according to Equations 1.2 and 1.3.[40]

$$[M{-}OH_2]^{z+} + H_2O \rightleftharpoons [M{-}OH]^{z-1} + H_3O^+ \tag{1.2}$$

$$[M{-}OH]^{z-1} + H_2O \rightleftharpoons [M{-}O]^{z-2} + H_3O^+ \tag{1.3}$$

The acidity of the aqua metal ion complex depends directly on the magnitude of the $M^{z+} \longleftarrow OH_2$ transfer and thus on the charge of the metal cation. The hydrolysis can result in three ligand types: aqua (H_2O), hydroxo (OH^-) or oxo (O^{2-}) ligands. The hydrolysis of a solvated metal cation, $[M(OH_2)_n]^{z+}$, can be expressed using the hydrolysis ratio h ($0 < h < 2n$) in Equation 1.4.[40] Depending on the hydrolysis ratio, a variety of complexes can be obtained (Table 1.1).

$$[M(OH_2)_n]^{z+} + hH_2O \rightleftharpoons [M(OH)_h(OH_2)_{n-h}]^{z-h} + hH_3O^+ \tag{1.4}$$

Hydrolysis ratio	Complex	Chemical formula
$h = 0$	aqua complex	$[M(OH_2)_n]^z$
$0 < h < n$	aqua-hydroxo complex	$[M(OH)_h(OH_2)_{n\text{-}h}]^{z-h}$
$h = n$	hydroxo complex	$[M(OH)_n]^{z-n}$
$n < h < 2n$	oxo-hydroxo complex	$[M(O)_{h\text{-}n}(OH)_{2n\text{-}h}]^{z-h}$
$h = 2n$	oxo-complex	$[MO_n]^{z-2n}$

Table 1.1: Overview of the possible aqua, hydroxo, oxo or hybrid metal ion complexes in an aqueous solution after hydrolysis of the solvated metal ion. The symbols h, n and z represent the hydrolysis ratio, the coordination number and the metal's charge.[40]

Since the solvated metal cation, $[M(OH_2)_n]^{z+}$, exhibits acid-base properties (Equation 1.4), its hydrolysis ratio depends on the acidity (i.e. pH) of the solution. The relationship between this hydrolysis ratio and the pH of the aqueous solution is derived by Jolivet et al.[40]. In their derivation, Jolivet et al. assume that proton exchange takes place until the average electronegativity of the formed hydrolyzed metal cation, $\chi_{[M(OH)_h(OH_2)_{n-h}]^{z-h}}$, equals that of the solvent, χ_s. Thus, the equilibrium condition will be obtained at the value of h for which $\chi_{[M(OH)_h(OH_2)_{n-h}]^{z-h}}$ equals χ_s. The pH-dependence is embedded in the expression for the solvent's electronegativity, as given in Equation 1.5[4].[40] The average electronegativity for the hydrolyzed metal cation, $[M(OH)_h(OH_2)_{n\text{-}h}]^{z-h}$, is expressed in Equation 1.6.[40]

$$\chi_s = 2.621 - 0.02\,\mathrm{pH} \tag{1.5}$$

$$\chi_{[M(OH)_h(OH_2)_{n-h}]^{z-h}} = \frac{\sum_i \sqrt{\chi_i} + 1.36z}{\sum_i \frac{1}{\sqrt{\chi_i}}} = \frac{\sqrt{\chi_M} + n\sqrt{\chi_O} + (2n-h)\sqrt{\chi_H} + 1.36(z-h)}{\frac{1}{\sqrt{\chi_M}} + \frac{n}{\sqrt{\chi_O + \frac{(2n-1)}{\sqrt{\chi_H}}}}} \tag{1.6}$$

In accordance with the equalization of the electronegativity, using Equations 1.5 and 1.6, the hydrolysis ratio can be expressed as function of the solution's pH value (Equation 1.7).[40] The value of h indicates the number of protons theoretically released by $[M(OH_2)_n]^{z+}$ in an aqueous solution. In general, a negative value of h indicates that the $[M(OH_2)_n]^{z+}$ does not exhibit any acidic properties in the aqueous solution. On the other hand, an h value higher than 2n suggest that the $[M(OH_2)_n]^{z+}$ does not exhibit any alkaline properties. The calculated value for h can be non-integer. In this case, two species coexist in an equilibrium in which at least one should be an hydroxo based species.[40] The model only considers α-type interactions between the metal cation and possible aqua, hydroxo or oxo ligands. If π-type interactions occur, as is often the case for a vanadium cation, the observed hydrolysis ratio deviates from the calculated one.[40]

---

[4] This χ_s is determined using the electronegativity of the solvated solvent species at a certain pH value: $\chi_{[H_9O_4]^+} = 2.621$ at pH 0, $\chi_{H_2O} = 2.491$ at pH 7 and $\chi_{[H_7O_4]^-} = 2.334$ at pH 14.

$$h = \frac{1}{1+0.41pH}\left((1.36z{-}n)(0.236{-}0.08pH){-}\frac{2.62-0.02pH-\chi_M}{\sqrt{\chi_M}}\right) \qquad (1.7)$$

As indicated by equation 1.7, the acidic nature of $[M(OH_2)_n]^{z+}$ is governed by three parameters: its charge (z), its coordination number (n) and its electronegativity (χ). The most important factor, however, is the charge (z).[40] Generally, cations with a charge lower or equal to 4 ($z \leq 4$) form aqua-hydroxo complexes, $[M(OH)_h(OH_2)_{n\text{-}h}]^{z-h}$, in an acidic or neutral medium. In an alkaline medium, they exist as hydroxo complexes, $[M(OH)_x]^{z-x}$.[40] Cations with a higher charge ($z > 4$) typically form oxo-hydroxo complexes, $[MO_{h\text{-}n}(OH)_{2n\text{-}h}]^{z-h}$.[40]

Structural peculiarity of hydrolyzed vanadium complexes

According to the aforementioned model, proposed by Jolivet et al., one should expect an aqua vanadium complex, $[V(OH_2)_6]^{5+}$, or an aqua-hydroxo vanadium complex, $[V(OH_2)_5(OH)]^{4+}$, in an acidic medium. At a pH value of 0, the calculated hydrolysis ratio amounts 0.9 (assuming $z_V = 5$, $\chi_V = 1.56$ and $n = 6$).[40]. Yet, the experimental hydrolysis ratio for V^{5+} is 4 and the main species in an acid medium is the aqua-cis-dioxo-vanadium(V) complex: $[VO_2(OH_2)_4]^{+}$. This peculiarity is explained by the formation of V-O bonds with a strong π character, allowing a decrease in its charge. This results in a shortening of the V-O bonds and a distortion of the geometry of the vanadium(V) complex. This effect is not so strong in the case of vanadium(IV) due to its lower oxidation state. Vanadium(IV) also forms an aqua-oxo complex, but contains only one shortened V-O bond with a strong π character: $[VO(OH_2)_5]^{2+}$. Besides the shortened V-O bond(s) in both V(V) and V(IV), the water ligand in trans of such a V-O bond is bonded very weakly. This explains their lability and the multiple coordination of V(V) and V(IV) ions.[40] More details on the exact structure of vanadium complexes will be given in paragraph 1.3.

1.2.2 Condensation of hydrolyzed metal cations

In an aqueous environment, hydrolyzed metal cations can condensate to form more complex structures, such as oligomers, polymers and solids. Analogue to organic polymerization processes, the following steps are identified in the condensation reactions of hydrolyzed metal cations: initiation, propagation and termination.

Initiation

The condensation of hydrolyzed metal ion cations follows the pathway of the nucleophilic substitution. This requires the presence of a nucleophilic species in the direct environment of the hydrolyzed metal cation. From the three possible ligand types after hydrolysis (i.e. aqua, hydroxo or oxo), only the hydroxo ligand can act as a nucleophilic species. The initiation can therefore be considered as the introduction of the hydroxo ligand on the monomer (Equation 1.8).[40]

$$[\mathrm{M{-}O}]^- + \mathrm{H_3O^+} \longrightarrow \mathrm{M{-}OH} + \mathrm{H_2O} \longleftarrow [\mathrm{M{-}OH_2}] + \mathrm{OH^-} \tag{1.8}$$

However, the presence of this nucleophilic species on its own is not sufficient to ensure condensation. The nucleophilic attack by the hydroxo ligand can only occur if the cation can be subjected to it. Thus, the electrophilic nature of the cation must be high enough. Empirical studies have shown that condensation only occurs if the partial charge on the cation is higher than 0.3. This partial charge is dependent on the ligands of the hydrolyzed species. The replacement of (i) an oxo ligand by an hydroxo ligand and (ii) an hydroxo ligand by an aqua ligand increases the partial charge on the cation in the hydrolyzed species. The ligands are determined by the hydrolysis ratio. Thus, the hydrolysis ratio a.o. determines the partial charge on the cation in the hydrolyzed species.[40]

Propagation

Once the requirements for condensation are fulfilled, two reaction types may take place: olation with the formation of an hydroxo-bridge (M-OH-M) and oxolation with the formation of an oxo-bridge (M-O-M).

Olation

Olation (Equation 1.9) is a two-step, dissociative nucleophilic substitution (S_N1). In the first step an aqua ligand is eliminated and an intermediate species with an unsaturated coordination appears. Obviously, this step is controlled by the lability of the $\mathrm{M{-}OH_2}$ bond. This increases if the charge of the metal cation decreases or if its size increases. In the second step, the intermediate species reacts with the nucleophilic hydroxo ligand. This results in the coupling of two (hydrolyzed) metal cations by an -OH bridge. In the absence of other complexing ligands or steric effects, the olation reaction is very fast and is essentially diffusion-controlled. Aqua-hydroxo complexes, $[\mathrm{M(OH)_h(OH_2)_{n\text{-}h}}]^{z-h}$, with an hydrolysis ratio below the coordination number (i.e. $0 < h < n$) are typical subjects of this olation reaction.[40]

$$\mathrm{M{-}OH} + \mathrm{M{-}OH_2} \longrightarrow \mathrm{M{-}OH{-}M} + \mathrm{H_2O} \tag{1.9}$$

Oxolation

Oxolation (Equation 1.10) is an associative nucleophilic substitution (S_N2). First a nucleophilic hydroxo ligand is added to the electrophilic metal cation. This results in the formation of a temporary -OH bridge in which the proton is much more acidic than in the terminal -OH group of the attacked metal cation. This acidic proton leaves the -OH bridge and reacts with the terminal -OH group to form an aqua ligand. Finally, this aqua ligand leaves the metal cation and an oxo bridge is formed between both metal cations. Oxolation reactions typically occur between metal cations that do not have aqua ligands in their coordination sphere. Thus, only hydroxo-oxo or oxo complexes, $[MO_{h\text{-}n}(OH)_{2n\text{-}h}]^{z-h}$ ($n \leq h \leq 2n$), are involved in such an oxolation process. Oxolation reactions are typically much slower than olation reactions.[40]

$$M{-}OH + M{-}OH \longrightarrow M{-}OH{-}M{-}OH \longrightarrow M{-}O{-}M{-}OH_2 \longrightarrow M{-}O{-}M + H_2O \quad (1.10)$$

Chemical formula of hydroxo or oxo bridges

Due to the olation and oxolation reactions, hydroxo and oxo bridges can be formed between two or more metal cations. The formula for hydroxo or oxo bridged metal cations is built as follows: $x\mu_i$- OH or $x\mu_i$- O. The index i corresponds to the number of metal cations bonded by the considered hydroxo or oxo bridge. The x corresponds to the number of bridging -OH- or -O- groups between the considered metal cations. A few examples are given in Figure 1.1.[40]

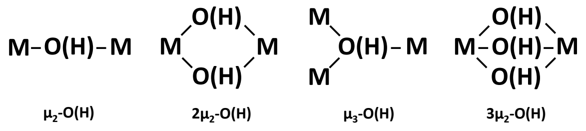

Figure 1.1: Examples of typical hydroxo or oxo bridges between two or more metal cations and their naming.

Termination

Under given acid-base conditions, spontaneous interruption of the growth of a condensed species can occur. Condensation can be limited to the formation of oligomers or continue until a solid precipitates. Termination will occur if the requirements for nucleophilic substitution are no longer fulfilled. Condensation results in a new structure with a specific composition. This causes a charge redistribution within the formed structure and therefore a change in its reactivity. As a consequence, the hydroxo ligand can lose its nucleophilic character and the metal cation can lose its electrophilic character.

1.3 Aqueous vanadium chemistry

The aqueous vanadium chemistry is very versatile and colorful, and at the same time very complicated: many cationic vanadium species occur in the aqueous solution. Their occurrence strongly depends on the pH value of the solution and the presence/absence of electrochemically active components. In a reducing sequence, the following vanadium species are often referred to: the yellow VO_2^+, the blue VO^{2+}, the green V^{3+} and the violet V^{2+}.[36, 41, 42] This beautiful color change has fascinated chemists dealing with vanadium and certainly justifies the naming of vanadium after Vanadis. A detailed study on the thermodynamics of the vanadium redox chemistry in an aqueous solution is performed by Pourbaix et al. The resulting Potential-pH equilibrium diagram is given in Figure 1.2 for the vanadium-water system at 25 °C[5].

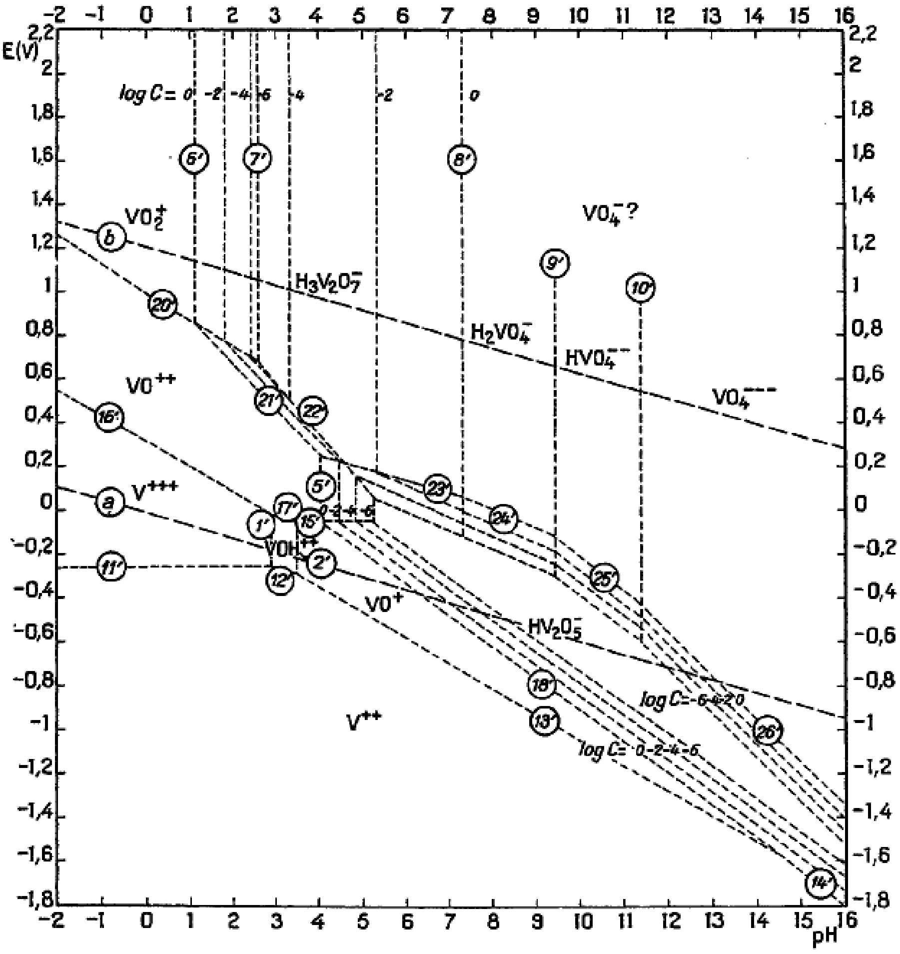

Figure 1.2: Potential-pH equilibrium diagram for the dissolved forms of vanadium in the vanadium-water system at 25 °C.[43]

Metallic vanadium and V(II) species will not be discussed, since they occur in an area with an E and pH value beyond the thermodynamic stability domain of water.[43].

---

[5] For simplicity, only dissolved forms of vanadium are considered in this Potential-pH equilibrium diagram. A full Potential-pH equilibrium diagram for the vanadium-water system, which includes solid vanadium species, is discussed by Pourbaix et al.[43]

The stability domain of water is bordered by the H_2 and O_2 evolution, as given in Equations 1.11 and 1.12[6].[43]

$$H_2(g) \rightleftharpoons 2\,H^+ + 2\,e^- \qquad E^0{=}0.000{-}0.00591pH \tag{1.11}$$

$$2\,H_2O \rightleftharpoons O_2(g) + 4\,H^+ + 4\,e^- \qquad E^0{=}1.228{-}0.00591pH \tag{1.12}$$

1.3.1 Vanadium(III)

V(III) species persist in an acidic, aqueous solution under reducing conditions near the H_2 evolution (Equation 1.11), as the V^{3+} cation. Depending on the concentration of the V(III) species, the aforementioned acidic condition ends at a pH value between 7 ($c_{V(III)}$ = 0.1 M) and 8 ($c_{V(III)}$ = 10^{-6} M).[43] In such an acidic solution, octahedral, $[V(OH)_n(H_2O)_{6\text{-}n}]^{3-n}$ (n = 0 – 2), complexes are observed. These complexes are associated to the acid-base equilibria, given by Equation 1.13.[44] In addition, oxolation reactions may occur, which result in the presence of di- ($[V_2(\mu_2\text{-}O)(H_2O)_{10}]^{4+}$), tri- ($[V_3(\mu_3\text{-}O)(\mu_2\text{-}O)_3(H_2O)_9]^+$) and tetranuclear ($[V_4(\mu_3\text{-}O)_2(\mu_2\text{-}O)_4(H_2O)_{10}]$) complexes at a pH value above 3.5.[44]

$$[V(H_2O)_6]^{3+} \xrightleftharpoons{pK_{a1} = 2.7} [V(OH)(H_2O)_5]^{2+} + H^+ \xrightleftharpoons{pK_{a2} = 4.0} [V(OH)_2(H_2O)_4]^+ + 2\,H^+ \tag{1.13}$$

Certain Ascidians accumulate V(III) in their blood cells. Concentrations up to 0.35 M, which is a factor 10^7 higher than in their seawater environment, have been reported for the *Ascidia Gemmata*.[45] This high V(III) concentration is accompanied by a large amount of sulfates, coexisting in the blood cells, which results in an acidic environment (pH ~ 1). The fan worm, *Pseudopotamilla Occelata*, is found to be the second V(III) accumulating, marine organism with a V(III) concentration in the order of $1\ mg \cdot g^{-1}_{\text{dry weight of the whole body}}$.[36, 45]

1.3.2 Vanadium(IV)

In contrast to the limited stability and occurrence of V(III) species, V(IV) species are more frequently reported in the aqueous vanadium chemistry. In an acidic solution (i.e. pH value below 7), the V(IV) stability domain is bordered by its equilibrium with V(V) and V(III). In an alkaline solution (i.e. pH value above 7), V(III) species are no longer stable in water and the stability domain of V(IV) is bordered by the H_2 evolution (Equation 1.11).[43]

The aqueous and coordination chemistry of V(IV) is dominated by oxovanadium(IV) complexes which contain the very stable vanadyl, $[V{=}O]^{2+}$, unit. The geometrical structure of these VO^{2+} containing complexes usually approaches one of the three

---

[6] These equations assume a H_2 and O_2 partial pressure of 1 atmosphere and a temperature of 25 °C.

idealized geometries shown in Figure 1.3: square bipyramidal, square pyramidal or trigonal bipyramidal.[46, 47] This last geometrical configuration, trigonal bipyramidal, is only reported in protein complexes and requires a specific, steric arrangement of the ligands.[46, 47]

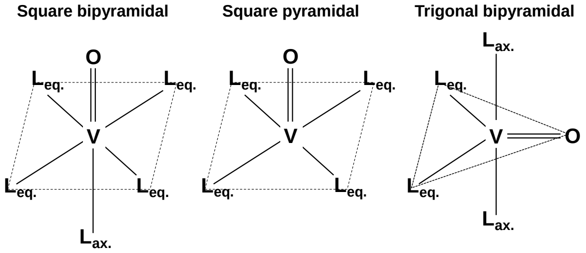

Figure 1.3: Common coordination geometries of complexes containing the VO^{2+} cation with equatorial ($L_{eq.}$) and axial ($L_{ax.}$) ligands. [46]

The $[VO(H_2O)_5]^{2+}$ complex, pH < 4

The VO^{2+} ion is stable in an aqueous solution with a pH value below 4 – 5 (respectively for a $c_{VO^{2+}}$ of 0.1 M or 10^{-6} M) and without the presence of chelating compounds. The VO^{2+} ion occurs as a mononuclear aqua complex, $[VO(H_2O)_5]^{2+}$, with a square bipyramidal geometrical structure.[43, 46]. In this $[VO(H_2O)_5]^{2+}$ complex, the first axial position is occupied by the oxide ion and the other positions are taken by water ligands. The V(IV) ion is located 10 – 30 pm above the plane formed by the equatorial water ligands. The vanadyl, V=O, bond is the strongest bond and is characterized by a bond length of about 159 pm. The interaction distance of an equatorial water ligand with the V(IV) center is about 200 pm. The interaction of the V(IV) center with the axial water ligand is the weakest and is featured with an interaction distance of about 223 pm. The kinetic, ligand exchange rates follow the same trend as the bond or interaction distances: $k_{O,axial} \sim 3.10^{-5}\ s^{-1}$, $k_{L,equatorial} \sim 10^3\ s^{-1}$ and $k_{L,axial} \sim 10^8\ s^{-1}$.[46]

Electronic structure of the $[VO(H_2O)_5]^{2+}$ complex

In this section, the electronic structure of the $[VO(H_2O)_5]^{2+}$ complex, in a square bipyramidal geometry, will be described using two models: the *Crystal Field Theory* and the *Ligand Field Theory*. Both models have their strengths and their weaknesses. The *Crystal Field Theory* is a rather straightforward theory which only considers electrostatic interactions and can be employed for spectral studies of transition metal ion complexes. The *Ligand Field Theory* is a more complicated theory which considers covalent bonding (σ and π) interactions using the *Molecular Orbital Theory*. The latter one is more suitable for the description of bond related properties such as the bond length.

Crystal Field Theory

The *Crystal Field Theory* is an ionic approach to describe the electronic structure of a transition metal ion complex. In this theory, the electron cloud of each ligand is considered a point charge and each metal-to-ligand interaction is described as an electrostatic interaction between the central metal cation and the point charge representing the electron cloud of the ligand: i.e. an ion-ion interaction if the ligand is negatively charged or an ion-dipole interaction if the ligand is neutral. This theory focuses on the repulsion between the d electrons of the central metal ion and the point charge of each ligand, and positions these electrons in d-orbital(s) which are geometrically the furthest away from the approach direction of the ligands.[48] Originally, this *Crystal Field Theory* was intended to describe the spectral properties of crystalline solids. Later on, this theory became more popular to describe the (electronic) structure of transition metal ion complexes. Currently, the *Crystal Field Theory* is still successfully employed in spectral studies of transition metal ion complexes.

The *Crystal Field Theory* for the $[VO(H_2O)_5]^{2+}$ complex is proposed by Ballhausen and Gray.[49] Figure 1.4 shows the Crystal Field energy level diagram in the case of an ideal O_h symmetry and a distorted O_h symmetry (i.e. a C_{4v} symmetry) with the further splitting of the two sets of degenerate orbitals (e_g and t_{2g}) into non-degenerate orbitals. In an O_h symmetry, the ligands are directly positioned on the axes of the Cartesian coordinate system. As a consequence, the d_{z^2} and $d_{x^2-y^2}$ orbitals of the central V^{4+} ion are destabilized and their relative energy increases. The inter-axis d orbitals (i.e. d_{xy}, d_{xz} and d_{yz}), on the other hand, are stabilized by the positioning of the ligands on the axes. Thus, in an O_h symmetry, 2 sets of degenerate energy levels are obtained: the doubly degenerated e_g (d_{z^2} and $d_{x^2-y^2}$) and the triple degenerate t_{2g} (d_{xy}, d_{xz} and d_{yz}). In the case of the $[VO(H_2O)_5]^{2+}$ complex, one ligand is replaced by another, non-equivalent (i.e. O_2^-), one which perturbs the O_h symmetry, leading to a C_{4v} symmetry. This perturbation results in further splitting of the two sets of degenerate energy levels: the d_{z^2} orbital is more destabilized than the $d_{x^2-y^2}$ orbital and the d_{xy} orbital is more stabilized than the d_{xz} or the d_{yz} orbitals. This results in four new energy levels: the non-degenerate b_2 (d_{xy}), the doubly degenerate e (d_{xz} and d_{yz}), the non-degenerate b_1 ($d_{x^2-y^2}$) and the non-degenerate a_1 (d_{z^2}).

Each energy level in the Crystal Field diagram is defined in terms of Dq, Ds and Dt. D and q correspond to the polarizability of the V^{4+} ion and the charge of the ligands and are treated as one empirical parameter, Dq. In a complex with an O_h symmetry, the energy difference is usually defined as 10 Dq. Ds and Dt are two, additional energy terms expressing the degree of perturbation in the O_h symmetry towards C_{4v} symmetry. Using Absorption Spectroscopy, Ballhausen and Gray, determined numerical values for these terms: $Dq = 1600\,cm^{-1}$, $Ds = -4570cm^{-1}$ and $Dt = -143cm^{-1}$.[49] Since the V^{4+} ion has just 1 electron left in a 3d orbital, only this single, unpaired electron must be placed in one of the orbitals defined by the

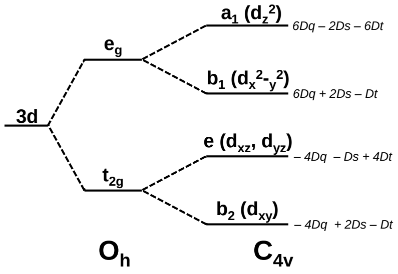

Figure 1.4: Crystal Field energy level diagram for the d orbitals of a transition metal ion in a octahedral (O_h) or square bipyramidal (C_{4V}) geometry.[49]

Crystal Field Theory (i.e. b_2, e, b_1 or a_1). In the ground state, this single d electron will occupy the b_2 orbital. As a consequence, three d-d transitions are possible with following energy differences[49]:

- $\Delta E(b_2 \longrightarrow \mathrm{e}) = 13000\,\mathrm{cm}^{-1}$ or 770 nm,
- $\Delta E(b_2 \longrightarrow \mathrm{b}_1) = 16000\,\mathrm{cm}^{-1}$ or 625 nm,
- $\Delta E(b_2 \longrightarrow \mathrm{a}_1) = 35000\,\mathrm{cm}^{-1}$ or 286 nm.

Despite the potential and strength of the *Crystal Field Theory* to explain the spectral features of the $[VO(H_2O)_5]^{2+}$ complex, this theory does not consider the covalent bonding interactions (e.g. the π bond in the VO^{2+} unit). A more accurate description of the electronic structure of $[VO(H_2O)_5]^{2+}$ complex should include these bonding interactions. For this purpose the *Ligand Field Theory* will be elaborated on in the next section.

Ligand Field Theory

The *Ligand Field Theory* can be considered as a specific case of the *Molecular Orbital Theory* and focuses on the d orbitals of the central metal atom. The atomic orbitals, originating from the metal and the ligand group orbitals, are used to construct molecular orbitals. The relative energy of the molecular orbitals; including bonding, non-bonding and anti-bonding; is estimated using orbital overlap considerations and experimental data. Here, molecular orbitals will be derived for the $[VO(H_2O)_5]^{2+}$ complex, assuming a molecular, C_{4v} symmetry. The Character table of the C_{4v} symmetry group is given in Table 1.2

This Character table can be used to determine to symmetry of the orbitals of the central vanadium atom and the ligand group orbitals. Before doing so, some notes on the non-equivalent ligands in the $[VO(H_2O)_5]^{2+}$ complex: (i) The oxide oxygen is the nearest ligand and will participate by its $\sigma(O)$ and its $\pi(O)$ ($2\,p_x$ and $2\,p_y$) ligand

C_{4v}, 4mm	E	C_2	2 C_4	2 σ_v	2 σ_d	h = 8
A_1	1	1	1	1	1	z, z^2, x^2+y^2
A_2	1	1	1	-1	1	
B_1	1	1	-1	1	-1	x^2-y^2
B_2	1	1	-1	-1	1	xy
E	2	-2	0	0	0	x, y, xy, yz

Table 1.2: Character table of the C_{4v} symmetry group.[50]

orbital. (ii) The four, equatorial water ligands are equivalent and will participate by four $\sigma_i(H_2O)$ ligand orbitals. (iii) The fifth, axial water ligand is the furthest from the central vanadium and will participate by its $\sigma(H_2O')$ ligand orbital. A possible, additional π-bonding of the water ligands is considered unlikely and ignored. Using the Character table of the C_{4v} symmetry group, the symmetry of each orbital can be deduced (Table 1.3).[49]

Representation	Vanadium orbitals	Ligand orbitals
a_1	$3\,d_{z^2}$	$\sigma(O)$
	$4\,s$	$\sigma(H_2O')$
	$4\,p_z$	$\frac{1}{2}\,[\sigma_1(H_2O) + \sigma_2(H_2O) + \sigma_3(H_2O) + \sigma_4(H_2O)]$
e	$3\,d_{xz}$	2 x $\pi(O)$ ($2p_x$ and $2p_y$)
	$3\,d_{yz}$	$\frac{1}{\sqrt{2}}\,[\sigma_1(H_2O) - \sigma_3(H_2O)]$
	$4\,p_x$	$\frac{1}{\sqrt{2}}\,[\sigma_2(H_2O) - \sigma_4(H_2O)]$
	$4\,p_y$	
b_1	$3\,d_{x^2-y^2}$	$\frac{1}{2}\,[\sigma_1(H_2O) - \sigma_2(H_2O) + \sigma_3(H_2O) - \sigma_4(H_2O)]$
b_2	$3\,d_{xy}$	

Table 1.3: Symmetry assignment of the vanadium orbitals and ligand orbitals considered in the *Molecular Orbital Theory* for the $[VO(H_2O)_5]^{2+}$ complex.[49] Note that the b_2 vanadium orbital is non-bonding (see Figure 1.5).

In the next step - the construction of the molecular orbital diagram - an overlap is considered between vanadium orbitals and ligand group orbitals of the same symmetry. Figure 1.5 shows the molecular orbital diagram for the $[VO(H_2O)_5]^{2+}$ complex, proposed by Ballhausen and Gray.[49, 51] Since the ligands are more electronegative than the vanadium atom, the relative energies of the group orbitals are lower than the orbitals of the vanadium atom. The relative energies of the molecular orbitals are determined by considering orbital overlap and experimental data. By comparing the Crystal Field diagram from Figure 1.4 with the molecular orbital diagram from Figure 1.5, the same increase in the energy levels of b_2, e_π^*, b_1^* and Ia_1^* can be noticed. The bonding and anti-bonding molecular orbitals are expressed by Equations 1.14 and 1.15 in which Φ refers to the proper combination of vanadium orbitals or ligand group orbitals. The o_i correspond to orbital coefficients and are listed for each molecular orbital in Table 1.4. From this Table and graphically from Figure 1.5, it is clear that the bonding orbitals are mainly situated on the ligands and that the anti-bonding orbitals are situated on the vanadium atom.

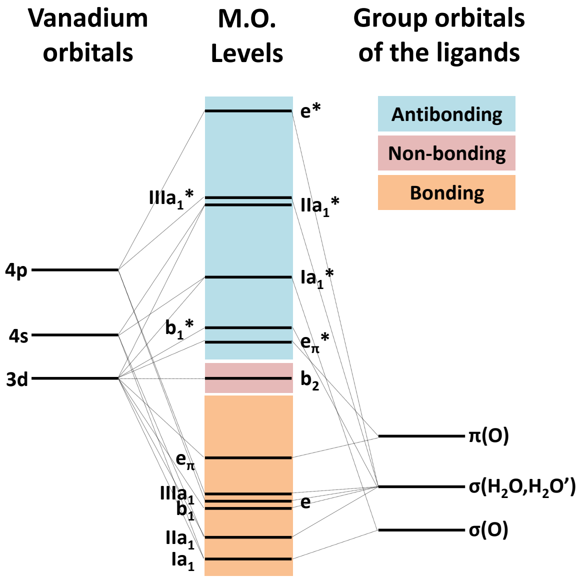

Figure 1.5: Molecular orbital diagram for the $[VO(H_2O)_5]^{2+}$ complex, assuming a molecular, C_{4v} symmetry.[49]

$$\psi = o_1\Phi(vanadium) + o_2\Phi(ligand) \tag{1.14}$$

$$\psi^* = o_1^*\Phi(vanadium) + o_2^*\Phi(ligand) \tag{1.15}$$

Molecular orbital	o_1	o_2	o_1^*	$-o_2^*$
e_π	0.446	0.834	0.907	0.567
b_1	0.381	0.853	0.946	0.555
Ia_1	0.345	0.883	0.996	0.620
IIa_1	0.409	0.765	1.006	0.770
$IIIa_1$	0.154	0.941	1.042	0.474
e	0.201	0.888	1.113	0.689

Table 1.4: Orbital coefficients for the formation of bonding and anti-bonding molecular orbitals in the $[VO(H_2O)_5]^{2+}$ complex.[49, 51]

By placing 17 electrons in the molecular orbitals, given in Figure 1.5, the ground state can be determined: $(Ia_1)^2$ $(IIa_1)^2$ $(b_1)^2$ $(e)^4$ $(IIIa_1)^2$ $(e_\pi)^4$ $(b_2)^1$. Note that this ground state can be represented by ^2D. This ground state will be used for further evaluation of the electronic spectrum of the $[VO(H_2O)_5]^{2+}$ complex. Electrons of the σ-bonding molecular orbitals do not participate in electronic transitions. These orbitals are denoted as invariant inner core (IC) orbitals. Thus, the ground state is simplified as: $(\mathrm{IC})^{12}\ (e_\pi)^4\ (b_2)^1$. The following transitions correspond to the d-d transitions discussed in the *Crystal Field Theory* and are associated with a transition energy of 770 nm, 625 nm and 286 nm, respectively.[49]

- $(\mathrm{IC})^{12}\ (e_\pi)^4\ (b_2)^1 \longrightarrow (\mathrm{IC})^{12}\ (e_\pi)^4\ (b_2)^0\ (e_\pi^*)^1$,
- $(\mathrm{IC})^{12}\ (e_\pi)^4\ (b_2)^1 \longrightarrow (\mathrm{IC})^{12}\ (e_\pi)^4\ (b_2)^0\ (b_1^*)^1$,
- $(\mathrm{IC})^{12}\ (e_\pi)^4\ (b_2)^1 \longrightarrow (\mathrm{IC})^{12}\ (e_\pi)^4\ (b_2)^0\ (Ia_1^*)^1$.

In addition, the promotion of an electron from the e_π orbital to a b_2 or e_π^* orbital occurs. The following transition energies are determined by Ballhausen and Gray.[49]:

- $\Delta E\left((IC)^{12}\ (e_\pi)^4\ (b_2)^1 \longrightarrow (\mathrm{IC})^{12}\ (e_\pi)^3\ (b_2)^2\right) = 41700\,\mathrm{cm}^{-1}$ or 240 nm,
- $\Delta E\left((IC)^{12}\ (e_\pi)^4\ (b_2)^1 \longrightarrow (\mathrm{IC})^{12}\ (e_\pi)^3\ (b_2)^1\ (e_\pi^*)^1\right) = 44000\,\mathrm{cm}^{-1}$ or 227 nm.

Note that both transitions transfer the electron from an orbital localized on the ligand group to an orbital localized on the vanadium atom (Figure 1.5). Each transition results in a charge transfer and is called a *Ligand-to-Metal Charge Transfer* (LMCT). Both transitions are characterized by a broad absorption band in the high energy region of an UV-Vis spectrum. As a consequence, the third, d-d transition (at ~ 333 nm) is not resolved.[49]

Finally, the *Molecular Orbital Theory* aids in the understanding of the paramagnetic properties of the $[VO(H_2O)_5]^{2+}$ complex. The formulas for the g values are expressed as function of the orbital coefficients and the spin-orbit coupling constant, ξ, in Equations 1.16 and 1.17.[49, 52] The free electron g value, g_e, equals 2.0023 and a spin-orbit coupling constant of 135 cm^{-1} is suggested by Dunn.[52–54].

$$\mathrm{g}_{\parallel} = \mathrm{g}_{\mathrm{e}} - \frac{8\xi(o_{1,b_2}.o_{1,b_1^*})^2}{\Delta E(b_2 \rightarrow b_1^*)} = 1.942 \qquad (1.16)$$

$$\mathrm{g}_{\perp} = \mathrm{g}_{\mathrm{e}} - \frac{2\xi(o_{1,b_2}.o_{1,e_\pi^*})^2}{\Delta E(b_2 \rightarrow e_\pi^*)} = 1.985 \qquad (1.17)$$

$$<\mathrm{g}> = \frac{2g_\perp + g_\parallel}{3} = 1.971 \qquad (1.18)$$

Other aqueous VO^{2+} species, pH > 4

The previous considerations assume a mononuclear $[VO(H_2O)_5]^{2+}$ complex. However, according to the Potential-pH diagram, shown in Figure 1.2, the VO^{2+} cation is only stable in solutions with pH value below 4 – 5.[43] Indeed, as the pH increases, the $[VO(H_2O)_5]^{2+}$ complex reacts, according to Equations 1.19, 1.20 and 1.21. A dinuclear $[\{VO(H_2O)\}_2(2\mu_2\text{-}OH)]$ complex or an insoluble $VO(OH)_2$ is formed at a pH value below 6.5.[36, 46] As the pH further increases (up to 11 – 12), the precipitated hydroxide ($VO(OH)_2\downarrow$) redissolves, according to Equation 1.22, and forms a brownish solution.[36, 46, 52]

$$2\,[VO(H_2O)_5]^{2+} \rightleftharpoons [\{VO(H_2O)_3\}_2(2\mu_2\text{-}OH)] + 2\,H_2O + 2\,H^+ \tag{1.19}$$

$$[VO(H_2O)_5]^{2+} \rightleftharpoons [VO(OH)(H_2O)_4]^+ + H^+ \rightleftharpoons [VO(OH)_2(H_2O)_3] + 2\,H^+ \tag{1.20}$$

$$[VO(OH)_2(H_2O)_3] \rightleftharpoons [VO(OH)_2]\downarrow + 3\,H_2O \tag{1.21}$$

$$[VO(OH)_2(H_2O)_3] + OH^- \rightleftharpoons [VO(OH)_3(H_2O)_2]^- + H_2O \tag{1.22}$$

Iannuzzi et al. compared the geometrical and electronic structure of the $[VO(H_2O)_5]^{2+}$ complex with the $[VO(OH)_3(H_2O)_2]^-$ complex, using UV-Vis and EPR Spectroscopy (Table 1.5).[52] Both solutions exhibit three absorption bands. The complementary color associated with these absorption bands corresponds to the observed blue or brown color. The position of the first band (i.e. $b_2 \longrightarrow e_\pi^*$) is almost unperturbed. The energy of the second, $\Delta E(b_2 \longrightarrow b_1^*)$, and third, $\Delta E(b_2 \longrightarrow a_1^*)$, transition have changed, respectively, to higher and lower values. This indicates a destabilization of the $d_{x^2-y^2}$ orbital and a stabilization of the d_{z^2} orbital of the V(IV) center. This suggests a change in one or more of the equatorial ligands by a stronger interacting ligand featured by a shorter interaction distance. A subtle difference between the anisotropic $g_\parallel$ value of the solution containing the $[VO(H_2O)_5]^{2+}$ complexes and that of the solution containing the $[VO(OH)_3(H_2O)_2]^-$ complexes can be seen. According to the Equation 1.16 this anisotropic $g_\parallel$ value is related to $\Delta E(b_2 \longrightarrow b_1^*)$ for a V(IV) species in a C_{4v} symmetry environment. Thus, an increase in this anisotropic $g_\parallel$ value corresponds to an increase in $\Delta E(b_2 \longrightarrow b_1^*)$. This supports the UV-Vis results and suggests that the equatorial V(IV)-to-ligand bonds are somewhat more covalent in the $[VO(OH)_3(H_2O)_2]^-$ complex. On the other hand, the anisotropic $g_\perp$ value is identical for both complexes. According Equation 1.17 this $g_\perp$ value is related to $\Delta E(b_2 \longrightarrow e_\pi^*)$. Thus no change in the axial water ligand can be assumed. In conclusion, Iannuzzi et al. show that, in a basic aqueous solution, the $[VO(H_2O)_5]^{2+}$ complex is replaced by the $[VO(OH)_3(H_2O)_2]^-$ complex. Based on UV-Vis and EPR spectroscopic studies, both complexes have a similar square bipyramidal structure, with a weakly interacting water ligand at the axial position (w.r.t. to VO^{2+} unit). In an acidic solution, the equatorial positions are occupied by water ligands. In a basic solution, three out of four equatorial water ligands are replaced by OH^- ligands. The V(IV)-to-OH^- bond has a more covalent nature than the V(IV)-to-H_2O bond.[52]

Complex	pH	Color	UV-Vis spectroscopy			EPR spectroscopy		
			$b_2 \longrightarrow e^*_\pi$	$b_2 \longrightarrow b^*_1$	$b_2 \longrightarrow a^*_1$	<g>	$g_{\|}$	$g_\perp$
$[VO(H_2O)_5]^{2+}$	2	Blue	763	625	223	1.964	1.935	1.978
$[VO(OH)_3(H_2O)_2]^-$	14	Brown	781	521	410	1.970	1.957	1.977

Table 1.5: Comparison between an aqueous solution containing $[VO(H_2O)_5]^{2+}$ complexes at pH 2 and $[VO(OH)_3(H_2O)_2]^-$ complexes at pH 14. The electronic transitions, observed by UV-Vis spectroscopy, are given in nm. From X-band EPR spectra, respectively recorded on the solution at T_{Room} and the frozen solution, the isotropic g value (<g>) and anisotropic g values ($g_{\|}$ and $g_\perp$) are obtained.[52]

1.3.3 Vanadium(V)

V(V) species occur in more oxidative conditions and their thermodynamic stability domain is bordered by the O_2 evolution (Equation 1.12) and their equilibrium with V(IV) species.[43] A large variety of vanadium(V) species, including mono- and polynuclear species, is found in the aqueous solution within the stability domain. Figure 1.6 shows the pH and concentration dependent regions in which a specific vanadium(V) species dominates (at 25 °C). Generally, three concentration dependent regions are discussed:

- Low vanadium concentration ($\leq 10^{-4}$ M): predominance of mononuclear vanadium(V) species,
- Intermediate vanadium concentration (10^{-4} M – 1 M): predominance of polynuclear vanadium(V) species,
- High vanadium concentration ($\geq$ 1 M): formation of a $V_2O_5 \cdot nH_2O$ gel.

Mononuclear vanadium(V) species: $c_{V(V)} \leq 10^{-4}$ M

In an acidic environment, the mononuclear VO_2^+ is the major species. This VO_2^+ species typically occurs in an octahedral geometry in which four positions are occupied by H_2O ligands. As the pH increases to a value of 3.2, the $[VO_2(H_2O)_4]^+$ transforms to the neutral vanadic acid, H_3VO_4. Just as the the VO_2^+ ion, the vanadic acid typically occurs in an octahedral geometry with two additional H_2O ligands forming the neutral $VO(OH)_3(H_2O)_2$ complex. In this complex, the first water ligand is positioned along the axis opposite to the short V=O double bond and the second water ligand occupies a position in the plane perpendicular to the axis of the V=O

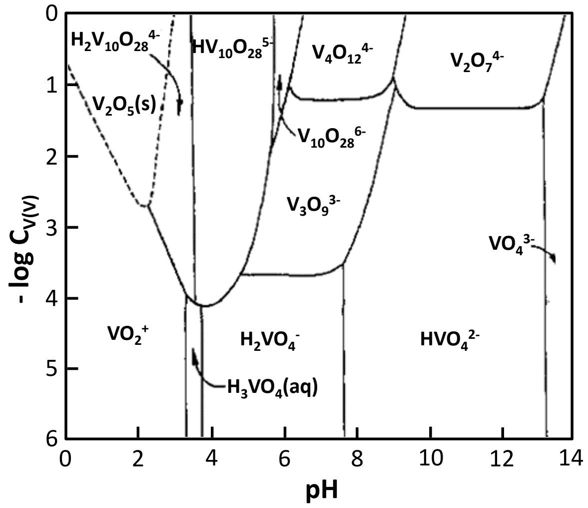

Figure 1.6: Predominance diagram, showing the pH and concentration dependent region in which the indicated vanadium(V) species is dominant in an aqueous solution at 25 °C.[55]

bond. Although the H_3VO_4 or $VO(OH)_3(H_2O)_2$ complex only appears in a very narrow pH area (between 3.2 and 3.8), the $VO(OH)_3(H_2O)_2$ complex is crucial for the formation of polynuclear species and the $V_2O_5 \cdot nH_2O$ gel.[24] The deprotonation reaction of the vanadic acid is given in Equation 1.23.[36, 56] Between a pH value of 5 and 7, the $H_2VO_4^-$ species has an abundance of almost 100 %. At a pH value of 7.5, the onset of a further deprotonation is observed and the first HVO_4^{2-} ions are formed. Between a pH value of 7.5 and 9.5 both species appear in the aqueous solution. The latter one has an abundance of almost 100 % at a pH value of 10. If the pH is further increased to 13, a final deprotonation is observed and VO_4^{3-} ions are formed. These mononuclear species only appear in very diluted solutions (i.e. $c_{V(V)} \leq 10^{-4}$ M). If the vanadium(V) concentration exceeds 10^{-4} M, condensation into polynuclear species takes place.[24, 37, 56]

$$H_3VO_4 \xrightleftharpoons{pK_{a1} = 3.5} H_2VO_4^- + H^+ \xrightleftharpoons{pK_{a2} = 7.8} HVO_4^{2-} + 2\,H^+ \xrightleftharpoons{pK_{a3} = 12.7} VO_4^{3-} + 3\,H^+ \tag{1.23}$$

Polynuclear vanadium(V) species: 10^{-4} M $\leq c_{V(V)} \leq$ 1 M

At intermediate vanadium concentrations, a comprehensive series of pH-dependent, polynuclear vanadium species exist (Figure 1.6). In acidic conditions (i.e. pH < 2.5), the yellow and cationic, $[VO_2(H_2O)_4]^+$, species is the only one that exists. As the pH value rises, condensation via olation, oxolation and acid-base reactions of the $VO(OH)_3(H_2O)_2$ complex emerges (Equation 1.24). These condensations result in the formation of pH-dependent decavanadate species (Equation 1.25) which consist of octahedral units. Figure 1.7 shows the structure of such polynuclear vanadium(V) species. In these decavanadate species, three different vanadium sites can be observed: V_c , V_a and V_b in a ratio of 1:2:2. The V_c sites correspond to a central, regular VO_6 octahedra. The V_a and V_b sites are peripheral, tetragonal-pyramidal $O{=}VO_4$ units, additionally linked to a bridging oxo group. Besides the vanadium sites, also seven non-equivalent oxygen sites are present. The peripheral oxygen sites are available for protonation and are, hence, involved in the acid-base behavior of decavanadate species (Equation 1.25). Obviously, only the peripheral vanadium sites are affected by the acid-base behavior. Since each vanadium site corresponds to a specific chemical shift in ^{51}V-NMR, only those associated with the peripheral sites are pH-dependent.[36, 40, 56, 57]

$$10\,[VO(OH)_3(H_2O)_2] \rightleftharpoons [H_2V_{10}O_{28}]^{4-} + 28\,H_2O + 4\,H_3O^+ \tag{1.24}$$

$$[H_2V_{10}O_{28}]^{4-} + 2\,H_2O \rightleftharpoons [HV_{10}O_{28}]^{5-} + H_3O^+ + H_2O \rightleftharpoons [V_{10}O_{28}]^{6-} + 2\,H_3O^+ \tag{1.25}$$

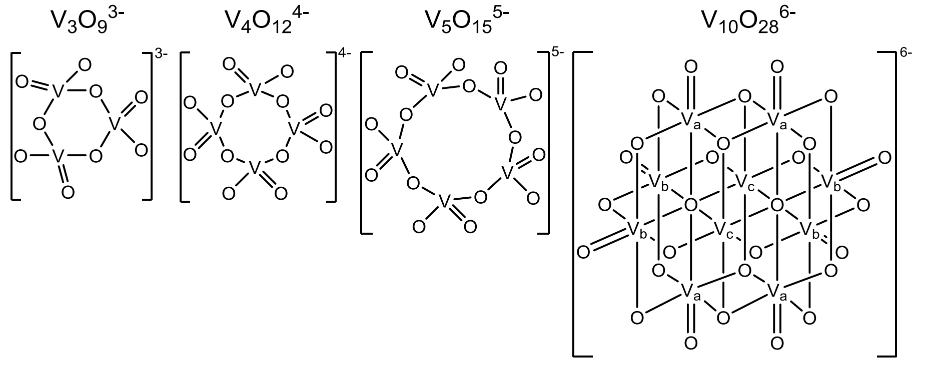

Figure 1.7: Schematic structure of the main polynuclear vanadium(V) species occurring in an aqueous solution if 10^{-4} M $\leq c_{V(V)} \leq$ 1 M. Note that the bonds are not drawn to scale and do not relate to the corresponding bond lengths.[36, 56]

In neutral and alkaline solutions, the decavanadates are unstable. Depending on the vanadium concentration, the cyclic tetravandate ($V_4O_{12}^{4-}$) or the cyclic trivanadate ($V_3O_9^{3-}$) becomes dominating. Traces of a cyclic pentavanadate ($V_5O_{15}^{5-}$) are observed as well. In the formation of these cyclic oligomers, (i) the deprotonated decavanadate decondensates (Equation 1.26), (ii) the orthovanadate ($[VO_4]^{3-}$) forms and (iii) this orthovanadate re-condenses (Equation 1.27). The cyclic oligomers have a very similar structure: (i) each vanadium center is tetrahedrally surrounded by oxygen atoms, (ii) two oxygen atoms are double bonded to the vanadium center and (iii) the other two oxygen atoms form a dioxo bridge, 2 μ_2- O, connected to the neighboring vanadium centra.[24, 36, 56–58]

$$[V_{10}O_{28}]^{6-} + 36\,H_2O \rightleftharpoons 10\,[VO_4]^{3-} + 24\,H_3O^+ \tag{1.26}$$

$$n[VO_4]^{3-} + 2\,nH_3O^+ \rightleftharpoons [V_nO_{3n}]^{n-} + 3\,nH_2O \text{ with } n = 3, 4 \text{ or } 5 \tag{1.27}$$

Continuing on the pH series, the cyclic vanadates are no longer dominant at a pH value above 9. At this point divanadate species, $HV_2O_7^{3-}$ and $V_2O_7^{4-}$, dominate (Equations 1.28 and 1.29). The latter is replaced by the mononuclear orthovanadate at a pH value above 13.[36, 40, 57]

$$2\,[VO_4]^{3-} + 3\,H_3O^+ \rightleftharpoons [HV_2O_7]^{3-} + 4\,H_2O \tag{1.28}$$

$$[HV_2O_7]^{3-} + H_2O \rightleftharpoons [V_2O_7]^{4-} + H_3O^+ \tag{1.29}$$

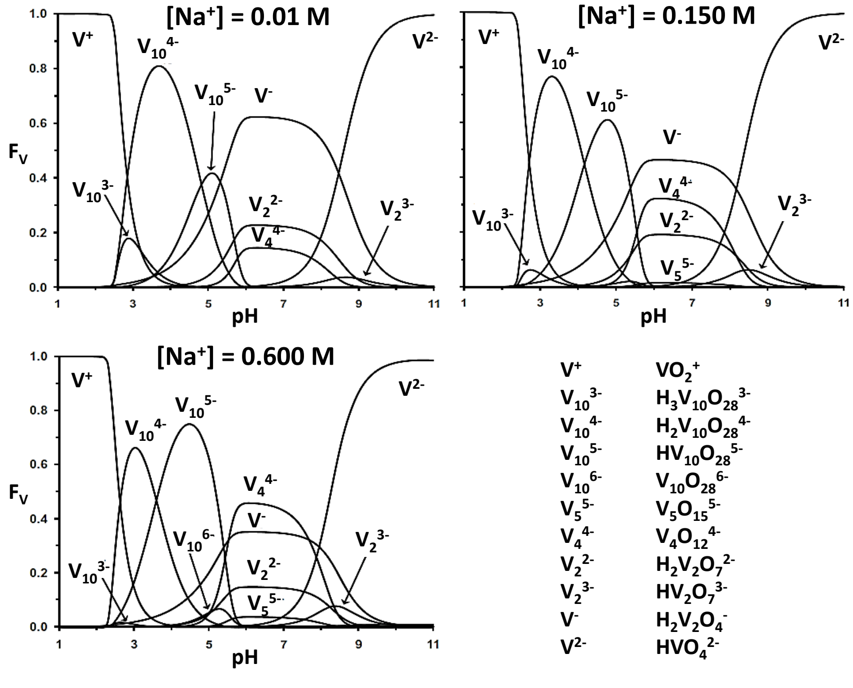

Figure 1.8: Speciation curves, showing the distribution of vanadium, F_V, as function of the pH in an aqueous solution with different Na^+ concentrations. The total vanadium concentration amounts 1 mM.[59]

Besides the pH, the ionic medium (i.e. the concentration of a counter cation) plays an important role in the dominance of certain polynuclear vanadium(V) species. This effect is studied by the Pettersson group. The results of their speciation study with various Na^+ concentrations are given in Figure 1.8.[59] The differences are mainly situated between a pH value of 2.5 and 8. As the ionicity of the solution increases, the more negatively charged polynuclear species become increasingly present.

Formation of $V_2O_5 \cdot nH_2O$ gel: $c_{V(V)} \geq 1$ M

If the concentration of vanadium(V) species exceeds 1 M, the solution gels in a few hours. The red and viscous gel contains fibers of vanadium pentoxide, $V_2O_5 \cdot nH_2O$: length of ~ 100 nm, width of ~ 10 nm and thickness of ~ 1 nm. As shown in Figure 1.9, the structure of such a $V_2O_5 \cdot nH_2O$ fiber differs significantly from the polynuclear vanadium(V) species discussed in the previous section. Moreover, this $V_2O_5 \cdot nH_2O$ is the result of decondensation of polynuclear vanadium(V) species into the hydroxo $VO(OH)_3(H_2O)_2$ complex. This complex is systemically removed from the solution via unlimited condensation reactions, shifting the aforementioned equilibrium in favor of the $VO(OH)_3(H_2O)_2$ complex.[24, 40]

Figure 1.9: Condensation pathway, suggested by Livage et al., leading to the formation of $V_2O_5 \cdot nH_2O$ gels.[24]

The condensation mechanism of the $V_2O_5 \cdot nH_2O$ gel, proposed by Livage et al., is schematically shown in Figure 1.9 and consists of olation and oxolation reactions, starting from the hydroxo $VO(OH)_3(H_2O)_2$ complex.[24] In this complex, the V-O bonds are not equivalent in the equatorial plane: $H_2O{-}V{-}OH$ or $HO{-}V{-}OH$. Condensation, preferentially, occurs via olation along the $H_2O{-}V{-}OH$ direction where a good nucleophilic group, OH, and a good leaving group, H_2O, are present. This results in the formation of olated chain polymers (Figure 1.9) with $\mu_2 - OH$ bridges and terminal H_2O and OH groups. Slower oxolation reactions convert these $\mu_2 - OH$ bridges into $\mu_3 - O$ bridges, forming edge sharing double chains.[24]

1.4 Citrato VO^{2+} and VO_2^+ complexes

From the study on the aqueous vanadium chemistry (section 1.3), it is clear that the vanadium ion (either V(IV) or V(V)) is easily hydrolyzed and involved in complex condensation reactions leading to (insoluble) hydroxides, oligomers or polymers. In the description of the hydrolysis (section 1.2.1), only the presence of aqua (H_2O), hydroxo (OH^-) and oxo (O^{2-}) ligands in the coordination sphere is considered. However, this hydrolysis (drastically) alters if another – electron donating – chelating compound is introduced in the aqueous solution. This additional ligand will compete with the already present ligands in the complexation of the vanadium ion. The exchange of a coordinated water molecule in an aqua complex by a ligand X^{m-} is given in Equation 1.30. In this equation, n corresponds to the original number of water ligands. The number of coordinating bonds between the metal cation M^{z+} and the ligand X^{m-} is represented by α. Ligands in which α equals 1, 2 or 3 are named as monodentate, bidentate or tridentate ligands.

$$[M(OH_2)_n]^{z+} + aX^{m-} \longrightarrow [MX_a(OH_2)_{n-\alpha a}]^{(z-\alpha a)+} + \alpha a H_2O \qquad (1.30)$$

The formation of a new complex, involving ligand X^{m-}, will reduce the hydrolysis probability because: (i) Water ligands are expelled from the coordination sphere of the metal cation. (ii) The ligand, sterically, hinders the water ligand to reach the metal cation. (iii) The coordination of the metal cation with ligand X^{m-} lowers the partial positive charge on the metal cation.

1.4.1 Citric acid as coordinating ligand

Citric acid (2-hydroxy-1,2,3-propanetricarboxylic acid, Figure 1.10) has the ability to form a stable and water soluble complex with a large variety of metal cations, such as Ti^{4+}, Zr^{4+}, Nb^{5+}, Ta^{5+}, Gd^{3+} and Ln^{3+}.[60–62]

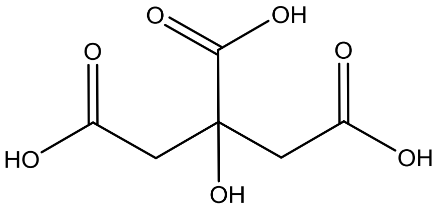

Figure 1.10: Structure of citric acid (2-hydroxy-1,2,3-propanetricarboxylic acid).

Citric acid is a polyprotic acid with three acidic groups: $pK_{a1} = 3.13$, $pK_{a2} = 4.76$ and $pK_{a3} = 6.40$.[63] If the pH value exceeds pK_{a1}, at least one free carboxylate group is available for the coordination of the metal cation. Generally, a pH value higher than pK_{a3} is chosen to ensure the formation of a citrate complex. In addition, the α-hydroxyl group is often involved in the complexation of the metal ion complex. In these complexes, a tetravalent citrate ion is present at a pH value ~ 7.

1.4.2 Citrato VO_2^+ complexes

Citrato-VO_2^+ complexes from or in an aqueous solution are almost exclusively studied by two groups: the Salifoglou group from the University of Thessaloniki and the Pettersson group from the University of Umeå. Both groups study these citrato-VO_2^+ complexes from a biochemical and medical point of view. It seems that the

Salifoglou group is specialized in the aqueous synthesis of such complexes, their interconversion and their structural analysis performed on isolated crystals. The Pettersson group, on the other hand, focuses on the speciation of the citrato-VO_2^+ complexes as function of the pH and ionicity of the aqueous solution. Such a speciation curve is theoretically determined starting from chemical equilibria and mass balances. Multinuclear NMR (^1H, ^{13}C, ^{14}N, ^{17}O, ^{31}P and ^{51}V) and potentiometric techniques are employed either to verify the obtained speciation curves or to generate input for the theoretical model. Another important difference between the work of both groups is the considered vanadium concentration. The Salifoglou groups considers VO_2^+ complexes in an aqueous solution with a vanadium concentration of ~ 0.2 M. The Pettersson group works at much lower concentrations (~ 1 μM). The structure of the citrato-VO_2^+ complexes, reported by both groups, differs significantly: (i) At a vanadium concentration of ~ 0.2 M and a similar citric acid concentration, the citrato-VO_2^+ complexes are dinuclear with a very stable, $(VO_2)_2\,(\mu_2 - O)$ unit.[64–69] (ii) At a vanadium concentration of ~ 1 μM and a similar citric acid concentration, the citrato-VO_2^+ complexes are, essentially, mononuclear.[59, 70, 71]. In this doctoral research, a vanadium concentration of ~ 0.1 M is aimed for and, hence, only the dinuclear citrato-VO_2^+ complexes will be considered.

In the last decade, the Salifoglou group is using a fixed procedure to synthesize various citrato-VO_2^+ complexes.[64–69] In this procedure, there are three parameters:

- The vanadium source: V_2O_5 or VCl_3. Obviously, the vanadium oxidation state in VCl_3 equals +III, which suggests that an oxidation occurs during the synthesis of the citrato-VO_2^+ complex.
- The base: KOH, NH_3, NaOH or NH_4OH. In all cases, the base is used to create an aqueous solution with a required pH value and the cation from the base acts as the counter ion for the negatively charged citrato-VO_2^+ complexes.
- The addition of H_2O_2 during the synthesis, which results in the formation of a citrato-peroxo-VO_2^+ complex.

If V_2O_5 is used as vanadium source, the first synthesis step is the dissolution of V_2O_5 in water with a targeted vanadium concentration of ~ 0.2 M. However, its solubility is limited (i.e. $0.8\ g \cdot L^{-1}$[72]) and therefore a small amount of base (~ 1/1 m.r.[7]) is added to the aqueous solution. This mixture is stirred for a few hours at an elevated temperature (~ 50 °C). After cooling to T_{Room}, citric acid (1/1 to 4/1 m.r.) is added to the clear solution. Finally, the pH is adjusted to the required value by the same base. The overall reaction is given in Equation 1.31.[64–69] Depending on the pH value of the solution, the free carboxylic acid groups of the resulting complex can be protonated or deprotonated.

---

[7] In this work, *molar ratio* is systematically abbreviated as *m.r.* and is always, unless otherwise specified, relative to the metal cation.

$$\begin{aligned} &V_2O_5 + 2\,C_6H_8O_7 + (6-2x)OH^- \longrightarrow \\ &\left[V_2O_4\left(C_6H_{(4+x)}O_7\right)_2\right]^{(2x-6)} + (7-2x)H_2O \\ &\text{with x = 0, 1 or 2} \end{aligned} \tag{1.31}$$

This procedure is also used for the formation of citrato-peroxo-VO_2^+ complexes. In the last synthesis step, though, an excess of H_2O_2 (m.r. ~ 16/1) is added to the solution. The overall reaction slightly differs and is given in Equation 1.32

$$\begin{aligned} &V_2O_5 + 2\,C_6H_8O_7 + 2\,H_2O_2 + (6-2y)OH^- \longrightarrow \\ &\left[V_2O_2(O_2)_2\left(C_6H_{(4+y)}O_7\right)_2\right]^{(2y-6)} + (9-2y)H_2O \\ &\text{with y = 0, 1 or 2} \end{aligned} \tag{1.32}$$

If the other vanadium source (i.e. VCl_3) is chosen, the synthetic procedure and the overall reaction change. In the first synthesis step VCl_3, citric acid and the base are dissolved in water. The aimed vanadium concentration and pH value are, respectively, ~ 0.2 M and ~ 9. The solution is stirred for ~ 24h. To this clear solution, H_2O_2 is added very slowly and under continuous stirring. The pH drops and an orange colored solution is obtained. Depending on the amount of added H_2O_2, either a citrato-VO_2^+ (Equation 1.33) or a citrato-peroxo-VO_2^+ (Equation 1.34) complex is obtained. 1.33.[64–69]

$$\begin{aligned} &4\,VCl_3 + 4\,C_6H_8O_7 + 2\,H_2O_2 + (24-4x)OH^- + O_2 \longrightarrow \\ &2\left[V_2O_4\left(C_6H_{(4+x)}O_7\right)_2\right]^{(2x-6)} + 12\,Cl^- + (22-4x)H_2O \\ &\text{with x = 0, 1 or 2} \end{aligned} \tag{1.33}$$

$$\begin{aligned} &4\,VCl_3 + 4\,C_6H_8O_7 + 4\,H_2O_2 + (28-4y)OH^- + O_2 \longrightarrow \\ &2\left[V_2O_2(O_2)_2\left(C_6H_{(4+y)}O_7\right)_2\right]^{(2y-6)} + 12\,Cl^- + (26-4y)H_2O \\ &\text{with y = 0, 1 or 2} \end{aligned} \tag{1.34}$$

After each synthesis, the Salifoglou group crystallizes the citrato-(peroxo-)VO_2^+ complex by cooling the aqueous solution at 4 °C and by adding ethanol to the solution. After a few days colored crystals appear: yellow-green, citrato-VO_2^+ crystals and red, citrato-peroxo-VO_2^+ crystals.[64–69] The crystals are isolated from the solution and analyzed to elucidate the structure of the complex.

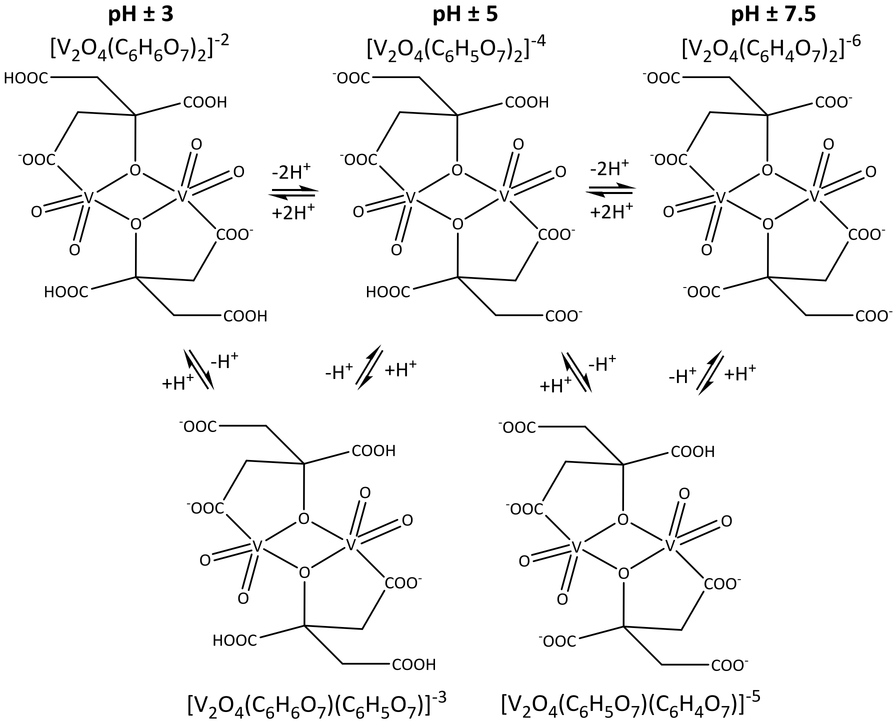

Figure 1.11: Scheme of the pH-dependent conversions of dinuclear citrato-VO$_2^+$ species in an aqueous solution.[65]

Figure 1.11 shows the possible crystalline citrato-VO$_2^+$ complexes. From this Figure, it is clear that dinuclear VO$_2^+$ species are formed systematically with a strong dioxo bridge resulting in the very stable, $(VO_2)_2\,(\mu_2 - O)$ unit. This dioxo bridge is due to the α-hydroxyl functionality of the citric acid, which is already deprotonated at a low pH value. Furthermore, each VO$_2^+$ center is directly coordinated by one carboxylate group. As a result, each citrate ligand has two free carboxylic acid or carboxylate groups. Depending on the pH of the solution from which the considered complex is crystallized, the free carboxylic acid groups can be protonated or deprotonated. This results in three main species: $\left[V_2O_4(C_6H_6O_7)\right]^{2-}$, $\left[V_2O_4(C_6H_5O_7)\right]^{4-}$ and $\left[V_2O_4(C_6H_4O_7)\right]^{6-}$. Under specific synthetic conditions, *non-symmetrical* deprotonation is possible, resulting in the less common $\left[V_2O_4(C_6H_6O_7)(C_6H_5O_7)\right]^{3-}$ and $\left[V_2O_4(C_6H_5O_7)(C_6H_4O_7)\right]^{5-}$ complexes. In each of these complexes, the coordination number of each vanadium(V) ion equals 5. Therefore, these complexes are typically observed in a square pyramidal geometry.[64–69]

In the presence of H_2O_2, one V=O bond per vanadium ion in the $(VO_2)_2\,(\mu_2 - O)$ unit is sacrificed and replaced by the O_2^{2-} entity, resulting in a $(VO(O_2))_2\,(\mu_2-O)$ unit. This reaction is schematically shown in Figure 1.12.[66–69]. After the transformation, a $\left[V_2O_2(O_2)_2(C_6H_5O_7)_2\right]^{4-}$ complex is formed. Obviously, the free carboxylic acid or carboxylate groups are subject to protonation and deprotonation. Similar to the citrato-VO_2^+ complex, the $\left[V_2O_2(O_2)_2(C_6H_5O_7)_2\right]^{4-}$ complex is a dinuclear species with a strong dioxo bridge. Again the deprotonated α-hydroxyl functionality of the citric acid is responsible for the formation of this dioxo bridge. In this complex, the coordination number of each vanadium ion equals 6. The associated geometry is a pentagonal pyramid with the free V=O bond in the axial position and the peroxo-group in the equatorial position. Often, an additional (weak) interaction with a free carboxylate group is observed at the position opposite the V=O bond. In this case, the geometry changes to a pentagonal bipyramid, as shown in Figure 1.12.[66, 68, 69, 73] Interestingly, the peroxo-group in the citrato-peroxo-VO_2^+ complexes can easily be removed by a mild heating (~ 60 °C), which results in the five coordinated citrato-VO_2^+ complex.[66, 69]

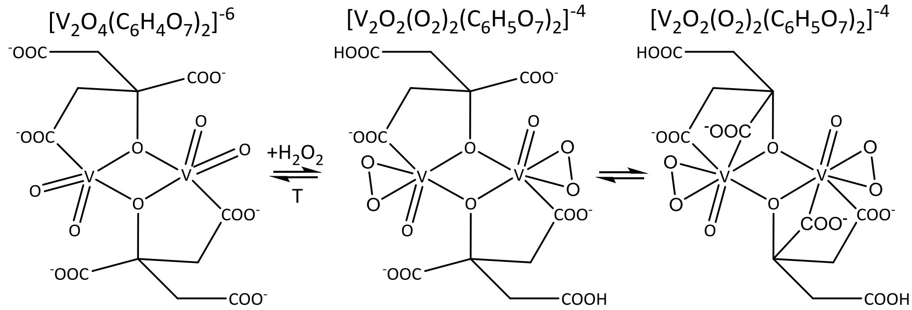

Figure 1.12: Scheme of the H_2O_2-induced or thermal transformation between $[V_2O_4(C_6H_4O_7)_2]^{5-}$ and $[V_2O_2(O_2)_2(C_6H_5O_7)_2]^{4-}$ complexes.[66, 68]

1.4.3 Citrato VO^{2+} complexes

Similar to the VO_2^+ complexes, also two approaches for the formation and structural analysis of citrato-VO^{2+} complexes are reported. In the first approach, these citrato-VO^{2+} complexes are synthesized in an aqueous solution and isolated as crystalline solids.[26, 28, 29] In the second approach, these citrato-VO^{2+} complexes are directly characterized in their aqueous environment using Spectroscopic techniques, such as UV-Vis Spectroscopy and EPR Spectroscopy. In EPR Spectroscopy, the aqueous solution can be characterized at T_{Room} in which isotropic or average spin Hamiltonian parameters (i.e. <g> and <A>) are obtained. Alternatively, the aqueous solution can be frozen which allows the determination of the anisotropic spin Hamiltonian parameters.[30–32] Interestingly, no reports have been found on the synthesis of citrato-peroxo-VO^{2+} complexes. A possible explanation is the H_2O_2-induced oxidation of the VO^{2+} ion.

The synthetic procedure for the formation of citrato-VO^{2+} complexes typically consists of three steps[26, 28, 29]:

- The formation of a V^{4+} species by (i) the oxidation of V^{3+}, originating from VCl_3, in an aqueous solution, (ii) the direct dissolution of $VOSO_4$ in water or (iii) the reduction of V^{5+}, originating from V_2O_5 or NH_4VO_3, in an aqueous solution using an excess of citric acid.
- The addition of citric acid and the adjustment of the pH using KOH, NaOH or NH_3.
- The isolation of blue crystals by (i) the addition of ethanol or 2−propanol to the aqueous solution at 4 °C or (ii) the slow evaporation of water from the aqueous solution.

An example of this procedure is given by Tsaramyrsi et al. who dissolve $VOSO_4$ and citric acid in water, and add a base (e.g. KOH, NaOH or NH_3) to obtain a blue solution (Equation 1.35).[29]

$$\begin{aligned} &2\,\mathrm{VOSO_4} + 2\,\mathrm{C_6H_8O_7} + (8-2x)\mathrm{H_2O} \longrightarrow \\ &\left[\mathrm{V_2O_2}\left(\mathrm{C_6H_{(4+x)}O_7}\right)_2\right]^{(2x-4)} + (8-2x)\mathrm{H_2O} \\ &\qquad\qquad\qquad \text{with x = 0 or 1} \end{aligned} \tag{1.35}$$

Note that in these procedures, the aimed vanadium concentration and the amount of citric acid are, respectively, ~ 0.1 M and ~ 1/1 or 2/1 m.r.. The pH-dependent and crystalline citrato-VO^{2+} complexes are shown in Figure 1.13. Each complex consists of the very stable $(VO)_2(\mu_2\text{-}O)$ unit in which the dioxo bridge is formed by the deprotonated α-hydroxyl functionality of the citric acid. The dinuclear complex is directly coordinated by 2 citric acid/citrate molecules. Of each ligand, one carboxylate group coordinates to the first vanadium ion of the $(VO)_2(\mu_2\text{-}O)$ unit and a second carboxylate group coordinates to the other vanadium ion of the same $(VO)_2(\mu_2\text{-}O)$ unit. This means that each ligand has one carboxylic acid or carboxylate group left. At a low pH value (i.e. ~ 5), this group is protonated and is, hence, not involved in the coordination of a vanadium ion. The $\left[V_2O_2(C_6H_5O_7)_2\right]^{2-}$ complex is formed. As the pH increases (i.e. ~ 8), this group deprotonates and the resulting carboxylate directly coordinates to one of the vanadium ions of the $(VO)_2(\mu_2\text{-}O)$ unit, resulting in the $\left[V_2O_2(C_6H_4O_7)_2\right]^{4-}$ complex. In rare cases, a mixed form occurs in which one citric acid ligand is fully deprotonated and the other citric acid ligand still retains one free carboxylic acid group (i.e. $\left[V_2O_2(C_6H_5O_7)(C_6H_4O_7)\right]^{3-}$). If an additional

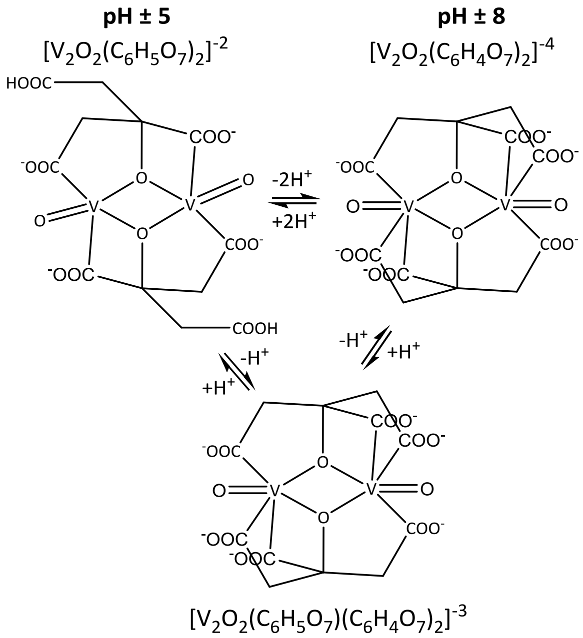

Figure 1.13: Conversion of $[V_2O_2(C_6H_5O_7)_2]^{2-}$, $[V_2O_2(C_6H_5O_7)(C_6H_4O_7)]^{3-}$ and $[V_2O_2(C_6H_4O_7)_2]^{4-}$ as function of the pH.[26, 28, 29]

carboxylate group is involved in the coordination, the coordination number and the geometrical arrangement change: (i) In the $\left[V_2O_2(C_6H_5O_7)_2\right]^{2-}$ complex, each vanadium ion has a coordination number of 5. The associated geometry is a distorted square pyramid with the V=O bond in the axial position. (ii) Each vanadium in the $\left[V_2O_2(C_6H_4O_7)_2\right]^{4-}$ complex has a coordination number of 6. This corresponds to a distorted octahedral geometry with the V=O bond in one of the axial positions. The other axial position is occupied by a (very weakly) coordinating carboxylate group. Thus, a dynamic conversion between the distorted square pyramidal and the distorted octahedral geometry is often observed.[26, 28, 29]

Previous citrato-VO^{2+} complexes are systematically formed in a solution with a similar vanadium and citric acid concentration (i.e. m.r. ~ 1/1). Lodyga–Chruscinska et al. studied the complexation when a large excess of citric acid is available. In these conditions, the formation of the $(VO)_2(\mu_2\text{-}O)$ unit is suppressed and at a neutral pH, mononuclear citrato-VO^{2+} complexes can be synthesized. Figure 1.14 shows the speciation diagram for an aqueous vanadium solution with a large excess of citric acid (i.e. m.r. ~ 100/1). Indeed at a pH value of 6, the $\left[V_2O_2(C_6H_4O_7)_2\right]^{4-}$ complex is no longer dominant. Instead, the mononuclear $\left[VO(C_6H_4O_7)\right]^{2-}$ complex dominates.

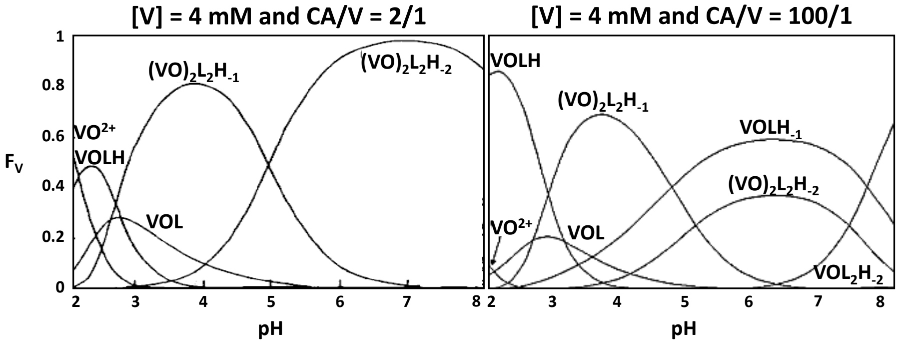

	Citrate		Citrato-VO^{2+}
LH_3	$C_6H_8O_7$	VOLH	$[VO(C_6H_6O_7)]$
LH_2	$C_6H_7O_7^{1-}$	VOL	$[VO(C_6H_5O_7)]^-$
LH	$C_6H_6O_7^{2-}$	$VOLH_{-1}$	$[VO(C_6H_4O_7)]^{2-}$
L	$C_6H_5O_7^{3-}$	VOL_2H_{-2}	$[VO(C_6H_4O_7)_2]^{6-}$
LH_{-1}	$C_6H_4O_7^{4-}$	$(VO)_2L_2H_{-1}$	$[(VO)_2(C_6H_5O_7)(C_6H_4O_7)]^{3-}$
		$(VO)_2L_2H_{-2}$	$[(VO)_2(C_6H_4O_7)_2]^{4-}$

Figure 1.14: Speciation curves, showing the distribution of citrato-VO^{2+} species as function of the pH in an aqueous solution with a different amount of citric acid (m.r. of 1/1 and m.r. of 100/1).[30–32]

The high relative abundance of the mononuclear $\left[VO(C_6H_4O_7)_2\right]^{6-}$ complex at a higher pH further stresses the suppression of the $(VO)_2(\mu_2\text{-} O)$ unit.[32]

1.5 Importance for this work

The review of the aqueous vanadium chemistry, discussed in this chapter, indicates that the aqueous vanadium chemistry is indeed rather complicated. Several aspects of this aqueous vanadium chemistry must be taken into account when synthesizing an aqueous vanadium precursor solution. First of all, vanadium can occur with three different oxidation states in the aqueous solution (i.e. +III, +IV and +V). The conversion from one to another oxidation state must be anticipated, especially when other components (such as citric acid or H_2O_2) are introduced in the aqueous solution. E.g. a V(V)-based species can reduce in the presence of citric acid to a V(IV)-based species. Alternatively, a V(IV)-based species can oxidize to a V(V)-based species in the presence of H_2O_2. Secondly, in the absence of an additional chelating compound (such as citric acid), the vanadium(V) ion easily hydrolyzes. This hydrolyzed species is subsequently subjected to condensation reactions leading to pH-dependent polynuclear species such as tri-, tetra-, penta- or decavanadates.

Condensation can be prevented by forming citrato complexes in the aqueous solution. Citrato-VO_2^+ complexes are typically observed as dinuclear complexes with a very stable $(VO_2)_2\,(\mu_2 - O)$ unit, formed by the deprotonated α-hydroxyl functionality of the citric acid/citrate. The associated geometry is a square pyramidal with the free V=O bond in the axial position. Citrato-VO^{2+} complexes are also observed as dinuclear complexes with a very stable $(VO)_2(\mu_2-O)$ unit. Here, the associated geometry is pH-dependent and can be a square pyramidal with the V=O bond at the axial position (pH $\sim$ 5) or a distorted octahedral with the V=O bond at the first axial position and a carboxylate group at the second axial position (pH $\sim$ 8). Mononuclear complexes are only observed if a high amount of citrate is added to the solution (i.e. m.r. 100:1).

The discussed characterization techniques to analyze the aqueous vanadium species (i.e. ^{51}V-NMR, UV-Vis and EPR spectroscopy[8]) will be used in the next chapters to identify the vanadium species obtained by our synthesis routes. The elaboration on the $[VO(H_2O)_5]^{2+}$ complex, as a fundamental species, will aid us in the analyses of our VO^{2+} species. In this context its Crystal field and Ligand field description will prove most worthy.

---

[8] A fundamental description of NMR and EPR theory is given in Appendix A.

Chapter 2

Synthesis of the aqueous citrato(-oxalato)-VO^{2+} solution

Figure 2.1: Picture of aqueous vanadium(V/IV) solutions with a vanadium oxidation state ranging between +V (left, orange) and +IV (right, blue), illustrating the colorful vanadium chemistry in an aqueous solution.

The solution-based synthesis of VO_2 M1, VO_2 B and V_6O_{13} is mostly reported as a two step route, in which first V_2O_5 is formed and subsequently reduced in an H_2, CO/CO_2 or NH_3 ambient. This work aims to avoid such an additional (hazardous) reduction step by (i) achieving a vanadium +IV oxidation state already in the solution phase and (ii) a careful control of this vanadium oxidation state during the deposition and film processing.

In this chapter, the synthesis of an aqueous citrato-oxovanadate precursor solution is intended. This synthesis involves two key steps: (i) the achievement of the vanadium +IV oxidation state and (ii) the stabilization of the formed vanadium species in a network of citrato complexes to allow chemical solution deposition (see Objectives). The content of this chapter, with exception of the study concerning the vanadium source (section2.2.1), is either published [74] or accepted for publication (Dalton Transactions).

2.1 Experimental

The synthesis of the aqueous citrato-oxalato-VO^{2+} and citrato-VO^{2+} solutions is schematically given in Figure 2.2. In the first step of this synthesis, ammonium metavanadate (NH_4VO_3) was dissolved in water under reflux conditions (90 °C, 10 minutes). In a next step, oxalic acid dihydrate ($C_2O_4H_2 \cdot 2\,H_2O$) was added, under reflux conditions (90 °C, 10 minutes), in a molar ratio to VO_2^+ ranging from 0.25:1 to 5:1. An optimal oxalic acid excess (3:1 against VO_2^+) was determined and maintained in the following steps. The obtained VO^{2+} solution was then systematically used for the synthesis of both the citrato-oxalato-oxovanadate(IV) and citrato-oxovanadate(IV) solutions. For the synthesis of an aqueous citrato-oxalato-VO^{2+} solution, citric acid ($C_6H_8O_7$) was added to the VO^{2+} solution in a 2:1 molar ratio to VO^{2+}. Next, ammonia (NH_3, 32 %) was added, dropwise, to the solution until a pH value of 7 was reached. A nominal vanadium concentration of 0.1 M was finally obtained. For the synthesis of an aqueous citrato-VO^{2+} solution, a separate solution of ammonium citrate was prepared by dissolving di-ammonium hydrogen citrate ($C_6H_8O_7 \cdot 2\,NH_4$) in water and by adding ammonia to this solution. A nominal citrate concentration of 3 M and a pH value of 7 were experimentally set. Before mixing the VO^{2+} solution with the ammonium citrate solution, the pH of the VO^{2+} solution was increased to a value of 7 by adding ammonia and the volume was adjusted by adding Milli-Q water to achieve a nominal VO^{2+} concentration of 1.5 M. Next, both solutions (the 1.5 M VO^{2+} solution with a pH value of 7 and the 3 M citrate solution with a pH value of 7) were mixed in a volume ratio of 1:1. This mixed solution was aged for 7 days at 4 °C to induce precipitation, which was subsequently removed by filtration (Pall Life Sciences Supor^{TM} 100 filters with 0.1 μm pore sizes). The precipitate was further washed with Milli-Q water and dried at 60 °C in an air flow furnace to allow further powder analysis. Finally, the pH of the filtrate was adjusted using NH_3 to a value of 7 to obtain an aqueous citrato-VO^{2+} solution with a nominal vanadium con-

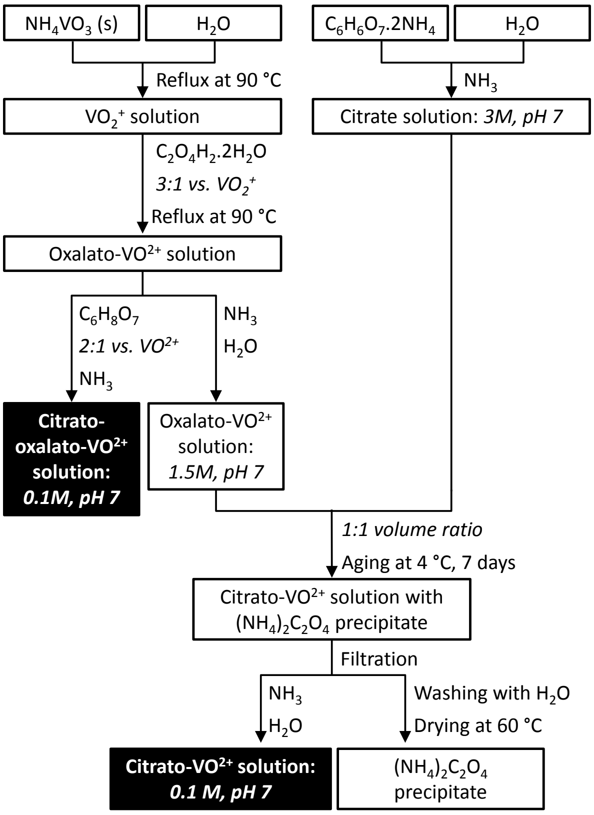

Figure 2.2: Schematic representation for the synthesis of the aqueous citrato-oxalato-VO^{2+} and citrato-VO^{2+} precursor solutions. All ratios are molar ratios, unless specified otherwise.

centration of 0.6 M. Vanadium free solutions of ammonium oxalate and ammonium citrate were also prepared by the dissolution of ammonium oxalate monohydrate ($(COONH_4)_2 \cdot H_2O$) or di-ammonium hydrogen citrate in water, respectively. For both vanadium free solution solutions, ammonia and Milli-Q water were added to obtain a solution with a pH value of 7 and a nominal oxalate or citrate concentration of 0.3 M.

2.2 Aqueous citrato-oxalato-VO^{2+} solution

2.2.1 NH_4VO_3 vanadium source

A first step in the synthesis of a stable, aqueous VO^{2+} solution is choosing and dissolving an appropriate vanadium source. During the deposition and subsequent processing steps, the precursor solution must convert into a crystalline vanadium oxide. This imposes two major requirements for the vanadium source: (i) The amount of vanadium deposited per process cycle depends, amongst others, on the vanadium concentration in the aqueous solution. It is experimentally convenient that an aqueous solution can be synthesized with an acceptable vanadium concentration (~ 0.1 M). Thus a vanadium source with an acceptable solubility in water is required. The amount of vanadium deposited per process cycle can be decreased by dilution of the aqueous VO^{2+} solution, while an increase is not always feasible due to e.g. the limited solubility of the vanadium source in water. Thus, a highly soluble vanadium source, experimentally, facilitates the preparation of nanostructured vanadium oxide materials. (ii) During the processing steps, the aqueous VO^{2+} is converted, via thermal steps, into the nanostructured vanadium oxide material. To prevent the persistence of undesired components in the final vanadium oxide, its precursor species must be decomposable during one of the thermal steps applied to obtain the final oxide material. Thus, during the synthesis of the aqueous VO^{2+} solution only vanadium atoms and thermally decomposable species can be introduced. Suppose only vanadium sources with a non-decomposable component should be commercially available, then an additional synthesis step is required to remove, quantitatively, these non-decomposable components. This surely impedes the synthesis of the aqueous VO^{2+} solution.

The majority of the vanadium compounds listed in the *CRC Handbook of Chemistry and Physics* can be grouped either as a vanadium salt or as a vanadium oxide.[72] The vanadium salts are based on the following vanadium containing ions: VO_4^{3-}, VO_3^-, VO_2^+, VO^{2+}, V^{3+} or V^{2+}. Since all these ions contain components that are allowed in the aqueous solution (i.e. vanadium and oxygen), its counter ion will determine if a certain salt is a candidate vanadium source. From the listed counter ions (i.e. F^-, Cl^-, Br^-, I^-, NH_4^+, Li^+, Na^+, K^+ and $C_5H_7O_2^-$), only the NH_4^+ and the $C_5H_7O_2^-$ ions are decomposable. This narrows the vanadium source candidates based on a vanadium salt to NH_4VO_3 and $VO(C_5H_7O_2)_2$. In the oxide group, on the other hand, all the oxides (i.e. V_2O_5, VO_2, V_2O_3 and VO) are candidate. Next, the solubility (in g per 100 g H_2O at T_{Room}) of each candidate vanadium source is compared in Table 2.1[72]:

NH_4VO_3	$VO(C_5H_7O_2)_2$	V_2O_5	VO_2	V_2O_3	VO
0.52 g	insoluble in H_2O	0.8 g	insoluble in H_2O	insoluble in H_2O	insoluble in H_2O

Table 2.1: Solubility, expressed in g per 100 g H_2O, of candidate vanadium source satisfying the counter ion combustion condition.[72].

Obviously, only two vanadium sources remain. NH_4VO_3 is preferred over V_2O_5 due to its higher solubility in H_2O. In conclusion, the synthesis of an aqueous VO^{2+} precursor will start using NH_4VO_3 as vanadium source.

The FTIR spectrum of the NH_4VO_3 vanadium source and its thermal decomposition profile in air is given in Figure 2.3. The FTIR spectrum shows the vibrations originating from the NH_4^+ and VO_3^- ion. A full assignment of the observed vibrations is listed in Table 2.2.

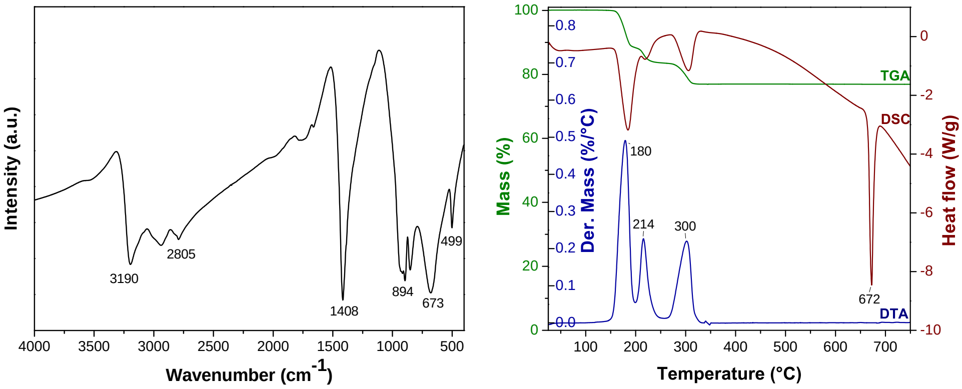

Figure 2.3: NH_4VO_3 vanadium source: FTIR spectrum (left) and TGA-DTA profile performed in 100 mL.min^{-1} dry air at a heating rate of 10 °C.min^{-1} (right). The TGA, DTA and DSC curves correspond to the mass, derivative of the mass and the heat flow, respectively.

Wavenumber (cm^{-1})		Assignment(s)
3200–3100	ν_{N-H}	N-H stretch in NH_4^+
2820–2800	-	First overtone of the NH_4^+ deformation in NH_4^+
1408	$\delta_{NH_4^+}$	NH_4^+ deformation in NH_4^+
950–850	$\nu_{V=O}$	Stretch of the unshared V=O bond in the tetrahedral VO_3^- unit
700–600	ν_{V-O-V}	Stretch of the V-O-V chain
500	ν_{VO_3}	Stretch and deformation of the VO_3^- unit

Table 2.2: Band assignments of the FTIR spectrum of NH_4VO_3. The assignments are based on references [75–78].

According to the thermal decomposition profile, shown in Figure 2.3, the thermal decomposition of NH_4VO_3 in air takes places in three successive steps with a final weight loss of 22 %, already at 320 °C. Legrouri et al. have studied the thermal decomposition pathway of NH_4VO_3 and suggest the reactions given in Equations 2.1, 2.2 and 2.3.[78] In each step gaseous NH_3 and H_2O are released and already at 300 °C V_2O_5 is formed. The release of gaseous NH_3 and H_2O is an endothermic process, which is reflected in the negative heat flow peaks. Over the three successive decomposition steps, a total weight loss of 22 % is observed. The overall decomposition reaction is given in Equation 2.4. Assuming molar masses of 116.98 $^{g}/_{mol}$ and 181.88 $^{g}/_{mol}$ for NH_4VO_3 and V_2O_5 respectively, 6 moles of NH_4VO_3 and 3 moles of V_2O_5 correspond to 701.88 g and 545.64 g respectively. This result in a theoretical

V_2O_5 % of 77.74 and thus a weight loss of 22.26 %. This theoretical value equals the experimental value. An additional strong endothermic peak, without weight loss, is observed at 672 °C. This peak results from a V_2O_5 melting process.[37, 72] In conclusion, NH_4VO_3 successively decomposes into NH_3(g), H_2O(g) and V_2O_5. V_2O_5 is already formed at 300 °C and can be experimentally confirmed by a strong endothermic step due to its melting at 672 °C.

$$180\,^{\circ}C: \quad 4\,NH_4VO_3 \longrightarrow (NH_4)_2V_4O_{11} + 2\,NH_3(g) + H_2O(g) \tag{2.1}$$

$$214\,^{\circ}C: \quad 3\,(NH_4)_2V_4O_{11} \longrightarrow 2\,(NH_4)_2V_6O_{16} + 2\,NH_3(g) + H_2O(g) \tag{2.2}$$

$$300\,^{\circ}C: \quad (NH_4)_2V_6O_{16} \longrightarrow 3\,V_2O_5 + 2\,NH_3(g) + H_2O(g) \tag{2.3}$$

$$\mathit{Overall}: \quad 6\,NH_4VO_3 \longrightarrow 3\,V_2O_5 + 6\,NH_3(g) + 3\,H_2O(g) \tag{2.4}$$

2.2.2 Dissolution of NH_4VO_3 in H_2O

NH_4VO_3 is dissolved in water under reflux conditions at 90 °C. After cooling down to T_{Room} , a yellow solution with a pH value of 7 is obtained.

Solution characterization

As discussed in Chapter 1 and indicated by the Pourbiax diagram in Figure 1.2, vanadium species in an aqueous solution with pH 7 can have an +V or +IV oxidation state. Thus, the first objective is the determination of the vanadium oxidation state. In this context, ^{51}V-NMR and UV-Vis spectroscopy can be applied to selectively identify vanadium(V) or vanadium(IV) species, respectively. The UV-Vis and ^{51}V-NMR spectra are shown in Figure 2.4. Due to the absence of peaks in the UV-Vis spectrum, associated with the d-d transitions discussed in Chapter 1, and the presence of signals in the ^{51}V-NMR spectrum, it is concluded that all vanadium species present in the aqueous solution have a +V oxidation state.

Immediately after the dissolution of ammonium metavanadate, a solution with a pH value of 7 is obtained. According to ^{51}V-NMR spectrum, given in Figure 2.4, the solution is dominated by the presence of cyclic tetravanadate, $[V_4O_{12}]^{4-}$, species. This cyclic tetravanadate species results from the condensation of orthovanadate ions, $H_2VO_4^-$, formed by hydration of the metavanadate ion at a pH value of 7 (Equations 2.5 and 2.6, n = 4).[24, 79] In addition, cyclic pentavanadate (Equation 2.6, n = 5) and linear divanadate (Equation 2.7) are observed in the ^{51}V-NMR analysis.[24, 79] After a peak integration and correction for the vanadium accumulation per peak, the relative abundance of each species is determined: $[V_4O_{12}]^{4-}$ (~ 67 %), $[V_5O_{15}]^{5-}$ (~ 9 %), $[H_2V_2O_7]^{2-}$ (~ 13 %) and $H_2VO_4^-$ (~ 11 %). A similar speciation is reported by

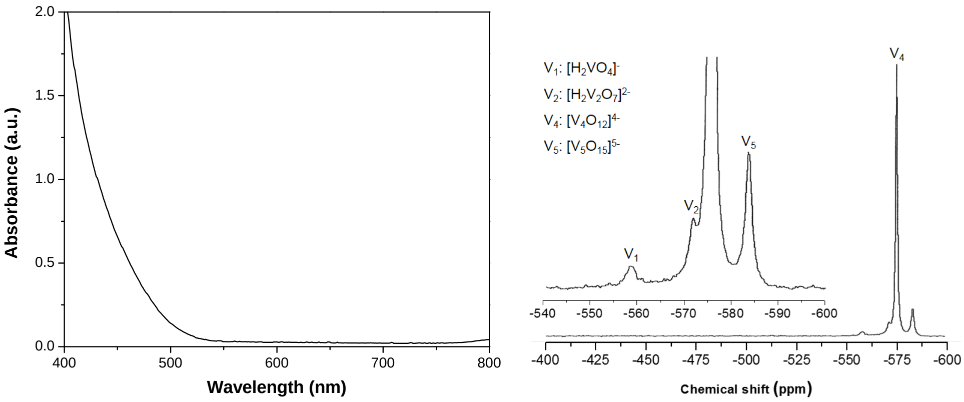

Figure 2.4: UV-Vis (left) and ^{51}V-NMR (right) spectra of the vanadium(V) species present in an aqueous solution immediately after the dissolution of NH_4VO_3 in water. The pH of this solution and the vanadium concentration amount 7 and 50 mM, respectively. The assignments in the ^{51}V-NMR spectrum are based on references [24, 36].

McCann et al. for an aqueous solution a vanadium concentration of 50 mM and a pH value of 7.31.[79]

$$NH_4VO_3 + H_2O \rightleftharpoons NH_4^+ + H_2VO_4^- \tag{2.5}$$

$$nH_2VO_4^- \rightleftharpoons [V_nO_{3n}]^{n-} + nH_2O \text{ with } n = 4 \text{ or } 5 \tag{2.6}$$

$$2\,H_2VO_4^- \rightleftharpoons [H_2V_2O_7]^{2-} + 2\,H_2O \tag{2.7}$$

Powder characterization

Besides the solution characterization by UV-Vis and ^{51}V-NMR spectroscopy, the associated powder obtained by evaporation of the solvent at 60 °C is analyzed by FTIR and TGA-DTA. Obviously, by evaporation of the solvent and in the absence of complexing agents, it is expected that the condensed vanadate(V) species will disappear in favor of the NH_4^+ and VO_3^- ions which will precipitate as the NH_4VO_3 salt, if no other chemical transformations have occurred during the reflux step. The FTIR spectrum and thermal decomposition profile are given in Figure 2.5. Both are identical to the FTIR spectrum and the TGA-DTA profile of the NH_4VO_3 source, given in Figure 2.3. The FTIR spectrum shows vibrations originating from the NH_4^+ and VO_3^- ion. A full assignment of the observed vibrations is listed in Table 2.2. Just as the NH_4VO_3 source, the thermal decomposition profile of the powder takes places in three successive steps (Equations 2.1, 2.2 and 2.3) with a final weight loss of 22 % at 320 °C. In each step, gaseous NH_3 and H_2O are released in an endothermic process, as suggested by the negative heat flow peaks. At 300 °C V_2O_5 is formed, which is proven by the endothermic peak at 670 °C, ascribed to the melting of V_2O_5. Thus, after the reflux step at 90 °C, besides condensation reactions in water, no significant chemical transformations have occurred and thus the reflux step only aids in the dissolution of the NH_4VO_3 source.

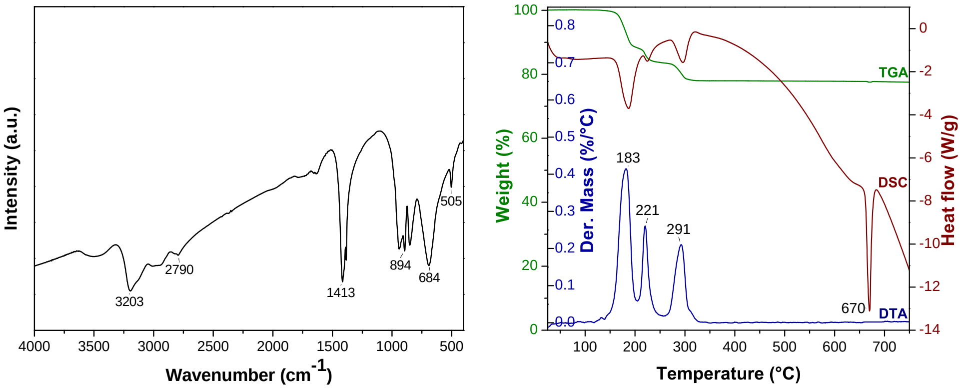

Figure 2.5: Powder obtained, from the aqueous solution with the dissolved NH_4VO_3, by water evaporation of the at 60 °C in air: FTIR spectrum (left) and TGA-DTA profile performed in 100 mL.min^{-1} dry air at a heating rate of 10 °C.min^{-1} (right). The TGA, DTA and DSC curves correspond to the mass, derivative of the mass and the heat flow, respectively.

2.2.3 VO_2^+/VO^{2+} reduction with oxalic acid

In this stage of the synthesis, the vanadium oxidation state equals +V. However, an aqueous solution with vanadium in its +IV oxidation state is aimed for in this chapter and required for the preparation of VO_2 M1,VO_2 B and V_6O_{13} without an additional post-deposition reduction step. Hence, the vanadium(V) species (i.e. $[V_4O_{12}]^{4-}$, $[V_5O_{15}]^{5-}$, $H_2V_2O_7^{2-}$ and H_2VO^-) must be reduced to vanadium(IV) species first. For this reason, oxalic acid is added to the aqueous solution as a reducing agent.

Thus, in the second synthesis step, oxalic acid is added to the aqueous solution, under reflux conditions (90 °C, 10 minutes). Immediately a color change from orange-yellow to blue, a pH drop and a strong gas evolution are observed.

In order to monitor the VO_2^+/VO^{2+} reduction as function of the amount of oxalic acid, ^{51}V-NMR and UV-Vis spectroscopy are employed. ^{51}V-NMR spectroscopy[1] is successfully applied to selectively identify vanadium(V) species over the paramagnetic, NMR silent vanadium(IV) species in an aqueous environment. Total peak integration is used as a quantitative determination of the amount of the vanadium(V), as

---

[1] The basic principles of ^{51}V-NMR and EPR spectroscopy are described in Appendix A.

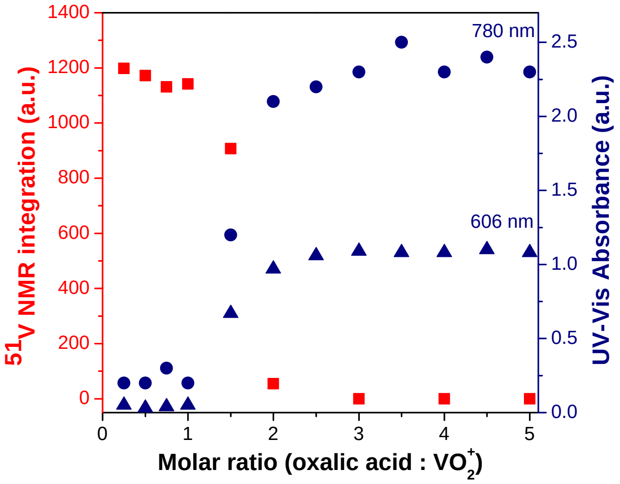

Figure 2.6: Evolution of the VO_2^+/VO^{2+} reduction as function of the molar ratio of oxalic acid to VO_2^+: total ^{51}V-NMR integration (■) and UV-Vis absorbance at 606 nm (▲) and 780 nm (●).

given in Figure 2.6. Clearly, the amount of dioxovanadate(V) species starts to diminish at a 1.5 molar ratio of oxalic acid to dioxovanadate(V) and falls to zero at a ratio of 3. This indicates that, by adding oxalic acid, dioxovanadate(V) species are systematically reduced to oxovanadate(IV) species. Complementary, the appearance of oxovanadate(IV) species - for which three electronic d-d transitions are reported (see section 1.3.2): $\Delta E(b_2 \longrightarrow e^*)$, $\Delta E(b_2 \longrightarrow b_1^*)$ and $\Delta E(b_2 \longrightarrow a_1^*)$ at respectively ~ 780, 606 and 333 nm - is confirmed by UV-Vis spectroscopy (Figure 2.6). The latter transition overlaps with the low energy tail of a high-intensity charge-transfer band (see section 1.3.2) and is therefore not examined. Based on the increased absorbance at 606 and 780 nm, the VO_2^+/VO^{2+} reduction by oxalic acid is further confirmed. For the synthesis of oxovanadate(IV) complexes, it is preferred that all dioxovanadate(V) species are reduced using the lowest possible amount of oxalic acid. Any oxalic acid excess is undesirable, since it must be removed thermally during the deposition process afterwards. In this synthesis a molar oxalic acid to vanadium ratio of 3 is chosen as the optimal condition, as this is the lowest excess that results in a complete VO_2^+/VO^{2+} reduction.

Supplementary to the qualitative analysis of the VO_2^+/VO^{2+} reduction by oxalic acid, ^{51}V-NMR is employed to identify the intermediate vanadium species during this reduction and to propose a reduction mechanism (Figure 2.7). Besides monitoring the vanadium(V) species using ^{51}V-NMR, also the pH is systematically studied as function of the oxalic acid to vanadium(V) molar ratio (Figure 2.7).

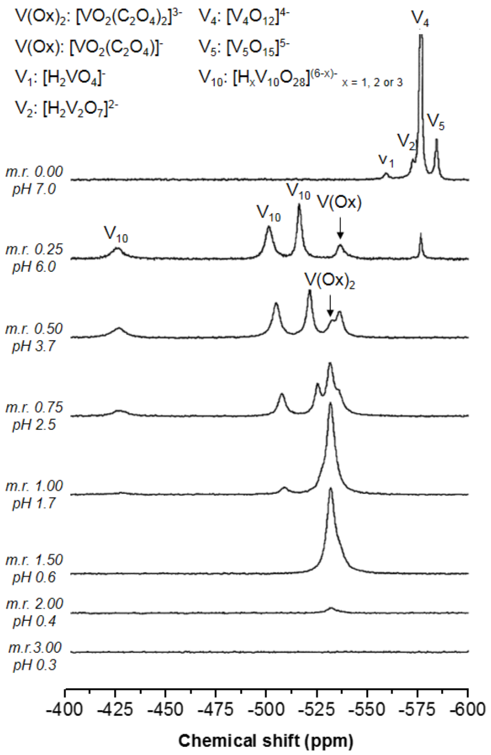

Figure 2.7: ^{51}V-NMR of the vanadium(V) species present in the aqueous solution after the addition of oxalic acid with an increasing molar ratio (m.r.) to V(V). Besides the NMR spectra, the pH value of the considered solution is indicated. The peak assignments are based on reference [36].

Firstly, the pH of the aqueous solution drops from 7 to 0.3. Secondly, the chemical shifts in the ^{51}V-NMR change drastically upon the addition of oxalic acid, as observed in Figure 2.7. Already at an oxalic acid to vanadium molar ratio of 0.25, signals for the tetravanadate species start to diminish and the penta-, di- and monovanadate species completely disappear. However, new peaks in the ^{51}V-NMR spectra appear at chemical shift values of -422.9, -499.8 and -514.9 ppm, corresponding to the appearance of decavanadate species (Equation 2.8).[79] In such a decavanadate entity, vanadium occupies three different sites, as represented by three different ^{51}V-NMR signals. The first vanadium site consists of a central and regular VO$_6$ octahedron, corresponding to a chemical shift at -422.9 ppm. The two other vanadium sites correspond to peripheral tetragonal-pyramidal O=VO$_4$ units additionally linked to a sixth, bridging oxo group (Figure 1.7).[36] Note that a decavanadate species is subjected to acid-base equilibria (Equation 2.9) with pK$_{a1}$, pK$_{a2}$ and pK$_{a3}$ equal to 1.9, 4.2 and 6.6, respectively.[80] Thus the decavanadate species, present in considered solution with a pH value of 6.0, are dominated by the presence of HV$_{10}$O$_{28}^{5-}$ (molar ratio of 4.2:1 w.r.t. $V_{10}O_{28}^{6-}$).

$$10\,H_2VO_4^- + 4\,H^+ \rightleftharpoons [V_{10}O_{28}]^{6-} + 12\,H_2O \tag{2.8}$$

$$[H_3V_{10}O_{28}]^{3-} \rightleftharpoons [H_{3-x}V_{10}O_{28}]^{(3+x)-} + xH^+ \quad (\text{with } x = 1\,2 \text{ or } 3) \tag{2.9}$$

Besides the three decavanadate signals, a signal at -535.7 ppm is observed in the ^{51}V-NMR spectrum. This one originates from a first oxalato, $[VO_2(C_2O_4)(OH_2)_2]^-$, complex which is formed by the oxalate complexation of the VO^{2+} hydrate, originated from the orthovanadate in an acidic media (Equations 2.10 and 2.11).[71, 81]

$$[H_2VO_4]^- + 2\,H^+ + 2\,H_2O \rightleftharpoons [VO_2(OH_2)_4]^+ \tag{2.10}$$

$$[VO_2(OH_2)_4]^+ + C_2O_4^{2-} \rightleftharpoons [VO_2(C_2O_4)(OH_2)_2]^- + 2\,H_2O \tag{2.11}$$

$$[VO_2(OH_2)_4]^+ + 2\,C_2O_4^{2-} \rightleftharpoons [VO_2(C_2O_4)_2]^{3-} + 4\,H_2O \tag{2.12}$$

As the oxalic acid to vanadium molar ratio further increases up to 0.75, the peaks corresponding to the peripheral vanadium sites in a decavanadate species shift towards higher field. Such a high field shift is typical for the protonation of decavanadate species in the direct environment of the peripheral sites.[70] At a pH value of 2.5, the $H_3V_{10}O_{28}^{3-}$ is the dominating decavanadate species (molar ratio of 4.0:1 w.r.t. $H_2V_{10}O_{28}^{4-}$). Simultaneously, the peak height of the signal originating from the $[VO_2(C_2O_4)(OH_2)_2]^-$ complex slightly increases. However, an additional peak is observed at -530.8 ppm, corresponding to a second oxalato complex, $[VO_2(C_2O_4)_2]^{3-}$ (Equation 2.12), which is typically present at a lower pH value.[71] Voronova et al. report the stability constant of both oxalato complexes, log β_1 and log β_2, in an acidic media and at 20 °C as 6.6 and 10.2 respectively.[82] Next, at a molar ratio of 1 and 1.5, the peaks associated with the decavanadate species disappear again and only the peak of the $[VO_2(C_2O_4)_2]^{3-}$ complex at a chemical shift of -530.8 ppm remains. This last signal diminishes as well upon further increasing the vanadium to oxalic acid ratio (1.5 to 2). Finally, at a molar ratio of 3 to 1, no ^{51}V-NMR signals remain and all vanadium(V) species are assumed to be reduced. Since the pH of the solution decreases from 7 to 0.3 during the addition of oxalic acid, all the vanadate transformations are associated with the acidification of the aqueous solution and the concurrent oxalate complexation of vanadium species.[24, 70] Since both oxalate complexes precede the disappearance of all ^{51}V-NMR signals stemming from vanadium(V) species, these complexes are considered as the oxidative agents (Equation 2.13).[83]

$$\begin{gathered} 2\,[VO_2(C_2O_4)_y(OH_2)_{4-2y}]^{1-2y} + 4\,H^+ + (1 + 2\,z-2\,y)C_2O_4^{2-} \longrightarrow \\ 2\,[VO(C_2O_4)_z(OH_2)_{5-2z}]^{2-2z} + 4\,(z-y)H_2O + 2\,CO_2(g) \quad (y, z = 1 \text{ or } 2) \end{gathered} \tag{2.13}$$

The electrochemical potentials of the oxalate complexes and the oxalate-free VO^{2+} species are determined by Bruyere et al. or can be estimated using the equilibria listed by Pourbaix et al., respectively (Equations 2.14, 2.15 and 2.16)[43, 83]:

$$E^0_{[VO_2(C_2O_4)]^-/[VO(C_2O_4)]} = 1.13\,\mathrm{V} \tag{2.14}$$

$$E^0_{[VO_2(C_2O_4)_2]^{3-}/[VO(C_2O_4)_2]^{2-}} = 1.22\,\mathrm{V} \tag{2.15}$$

$$E^0_{VO_2^+/VO^{2+}} = 0.77\,\mathrm{V} \tag{2.16}$$

The electrochemical potentials associated with the oxalate complexes are higher than the one from the oxalate-free VO^{2+} species. Thus, the VO^{2+}/VO_2^+ reduction is thermodynamically more favored if the VO^{2+} cation is surrounded by one or two bidentate oxalate ligands, and preferably by two. This explains the necessity of an oxalic acid to vanadium molar ratio of 3:1 to ensure a complete reduction of all vanadium(V) species in the aqueous solution. If pure, uncoordinated VO^{2+} would reduce to VO_2^+ and oxalate would only act as a reducing agent, a much lower oxalic acid to vanadium molar ratio would suffice.[43]

In conclusion, the following reduction mechanism is proposed based on UV-Vis spectroscopy, the ^{51}V-NMR analysis and on the aforementioned thermodynamic considerations. The addition of oxalic acid initially results in an acidification of the aqueous solution in which tetravanadate species - present at a pH value of 7 - convert to dioxovanadate species at a pH value of 2, via the protonation of decavanadate species. Simultaneously, the dioxovanadate species present form oxalato-VO_2^+ complexes which are, in turn, reduced towards oxalato-VO^{2+} complexes by free oxalate ions. After the complete reduction process, ^{51}V-NMR silent oxalato-VO^{2+} complexes remain in the aqueous solution.

2.2.4 VO^{2+} citrate complexation

At this stage, all aqueous vanadium species are successfully converted into VO^{2+} species in which the oxidation state of vanadium equals +IV, as aimed for. To prevent the undesired formation of an insoluble hydroxide, i.e. $VO(OH)_2$[80], the VO^{2+} ion must be stabilized in an α-hydroxy-carboxylato-VO^{2+} complex (see objectives). These complexes allow the formation of a cross-linked, amorphous gel. This cross-linked gel emerges by intermolecular H-bridge formation upon the evaporation of water during the chemical solution deposition process.[21, 33, 84] However, the bidentate oxalate ligands lack this cross-linking nature. Thus, oxalate ligands are not adequate for this purpose. A cross-linkable α-hydroxy-carboxylato complexing agent must be added to the solution. Since citrate is successfully used for the formation of stable α-hydroxy-carboxylato complexes with other metal ions such as Ti^{4+}, Zr^{4+}, Nb^{5+}, Ta^{5+}, Gd^{3+}, Ln^{3+} and Zn^{2+}[61, 62, 85–87], citrate is chosen for this purpose.

In the third step of the synthesis of the aqueous citrato-oxalato-VO^{2+} solution, citric acid is added in a 2:1 molar ratio (citric acid : vanadium) and the pH is subsequently increased using NH_3 to a value of 7, which is sufficient for the deprotonation of the carboxylic acid groups of citric acid (pK_{a3} = 6.4 [72]), thus ensuring the formation of an ammonium bridged network of citrato-oxalato-oxovanadate(IV) complexes. The evolution of these complexes as function of the pH value of the solution is studied by UV-Vis, EPR and FTIR spectroscopy on the solution at T_{Room} , on the frozen solution and on the powder, obtained by evaporation of the solvent at 60 °C.

UV-Vis study on solutions at T_{Room}

Figure 2.8 shows the UV-Vis spectra of the aqueous citrato-oxalato solution at various pH values. At all pH values, the following electronic transitions can be observed: $b_2 \longrightarrow e^*$, $b_2 \longrightarrow b_1^*$ and $b_2 \longrightarrow a_1^*$ (see section 1.3.2). The latter one coincides with a high intensity charge-transfer band, is not resolved and will not be considered in the following discussion. As function of the pH three situations can be distinguished: (i) At a more acidic pH value (i.e. below 4.8), two transitions are observed at ~ 780 (high absorbance peak) and at ~ 602 nm (less intense peak). (ii) As the pH increases (from 4.8 to 6.5), both peaks shift towards higher energy (or lower wavelength). This blueshift is almost negligible at ~ 780 nm, but strongly pronounced at ~ 602 nm. In addition to the blueshift, the intensity of the low energy peak lowers, while the intensity of the high energy peak grows. (iii) If the pH further increases (to ~ 7 or 8), only a shoulder corresponding to the low energy peak remains at ~ 755 nm, while the absorbance at the high energy peak continues to increase. The peak position of this high energy peak at a pH value of 7 to 8 amounts ~ 560 nm.

Similar, pH-dependent changes in a UV-Vis spectrum are reported by Iannuzzi et al. They compared the geometrical and electronic structure of the $[VO(H_2O)_5]^{2+}$ complex, formed at pH 2, with those of the $[VO(OH)_3(H_2O)_2]^-$ complex, formed at pH 14 (see section 1.3.2). The blueshift of the $b_2 \longrightarrow b_1^*$ band is explained by a destabilization of the $d_{x^2-y^2}$ orbital. This destabilization is caused by a stronger interaction of the ligands at the equatorial positions with respect to the V=O bond in VO^{2+} unit. The orientation of the $d_{x^2-y^2}$ orbital coincides with the axis of approach of the ligands at the equatorial positions. In the situation of Iannuzzi et al., the H_2O ligands at the equatorial positions are exchanged with charged OH^- ligands.[52] Here, the ligands at a low pH value are either H_2O or protonated carboxylic acid groups $R{-}CO_2H$, associated with oxalic acid or citric acid. As the pH increases, each acidic group is systematically deprotonated (the pK_a values of citric acid amount 3.1, 4.8 and 6.4) and the destabilization of the $d_{x^2-y^2}$ orbital commences. As the pH value exceeds pK_{a3} (e.g. at a pH value of 7), all the acidic groups are deprotonated. The ligands at the equatorial positions consist of $R{-}CO_2^-$ groups which interact more strongly with the VO^{2+}, in comparison with $R{-}CO_2H$ or H_2O. Thus, the blueshift in the UV-Vis spectra as function of the pH value is associated with the deprotonation

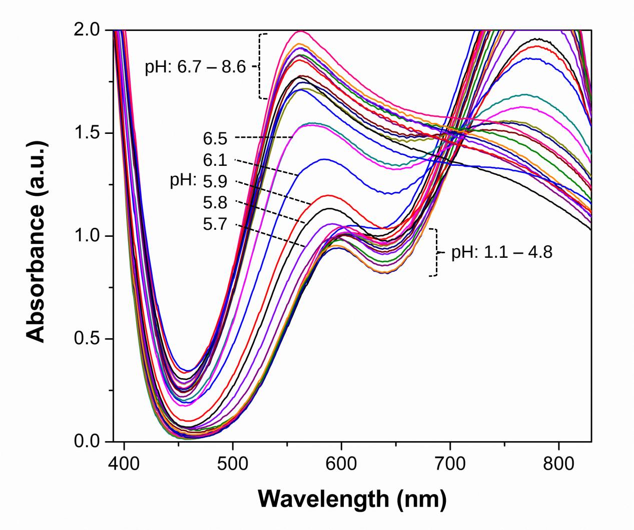

Figure 2.8: UV-Vis spectra of the aqueous citrato-oxalato-VO^{2+} solution at various pH values, ranging from 1.1 to 8.6.

of the carboxylic acid groups at the equatorial positions.

EPR study on frozen solutions and solutions at T$_{Room}$

CW-EPR

Figure 2.9 (left) shows the X-band CW-EPR spectra recorded at 100 K for different stages during the synthesis of the aqueous citrato-oxalato-oxovanadate(IV) precursor: without citric acid, with citric acid at a pH value of 1.4 (no NH_3), with citric acid at a pH value of 5.0 (increased by NH_3) and with citric acid at a pH value of 7.0 (increased by NH_3).[2] The CW-EPR spectrum of the sample without citric acid reveals one broad feature, characteristic for dipolarly interacting oxovanadate(IV) centers (clusters). Upon addition of citric acid, a clear multi-line spectrum becomes visible, which is typical for mononuclear oxovanadate(IV) complexes.[46, 88] The spectrum is superimposed on a broad feature stemming from dipolarly coupled oxovanadate(IV) centers. Room-temperature CW-EPR (Figure 2.9, right) indicates that the cluster formation in the sample without citric acid and the sample with citric acid at a pH value of 1.4 could be induced by freezing: at room temperature both samples exhibit the same isotropic spectrum due to fast tumbling of the mononuclear oxovanadate(IV) complexes. The spectral features of the room- and low-temperature

---

[2] All CW- and Pulsed-EPR results are listed in Appendix B: sample without citric acid (EPR A), with citric acid at a pH value of 1.4 (EPR B), with citric acid at a pH value of 5.0 (EPR F) and with citric acid at a pH value of 7.0 (EPR I)

EPR spectra further change upon addition of NH_3 and depend on the pH value of the solution (samples with citric acid at a pH value of 5.0 and 7.0 in Figure 2.9).

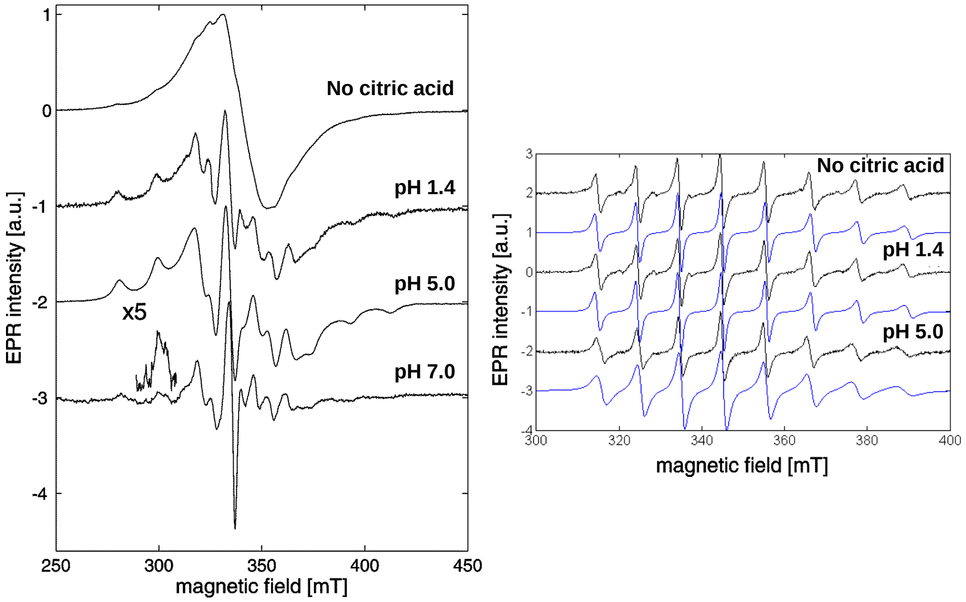

Figure 2.9: X-band CW-EPR spectra taken at 10 K of frozen solutions (left) and at T_{Room} (right): experimental (black) and simulated (blue) spectra. The presented CW-EPR spectra were either measured at 100 K using a modulation amplitude of 0.5 mT, a microwave power of 1 mW and a modulation frequency of 100 kHz or at room temperature using a modulation amplitude of 0.2 mT, a microwave power of 0.46 mW and a modulation frequency of 9.725 GHz.

The room-temperature CW-EPR spectra of samples with citric acid at a pH value of 1.4 and 5.0 could be simulated, assuming a fast motion of the molecule with correlation times of $4 \cdot 10^{-11}$ s (sample with citric acid at pH 1.4) and $9 \cdot 10^{11}$ s (sample with citric acid at pH 5.0), confirming that the isolated vanadyl species observed at low temperature persist at room temperature. No broad signal of vanadyl clusters was observed for these samples at room temperature, strongly suggesting that the broad feature found at low temperature is due to freezing-induced clustering. This is corroborated by the fact that the room-temperature CW-EPR spectrum of the sample without citric acid is identical to that of the sample with citric acid at pH 1.4. This not only indicates that the same vanadyl ligation modes are present in both samples, it also shows that the dominant broad signal found for the sample without citric acid at low temperature is most likely due to freezing-induced clusters. Apparently, the presence of carboxylate groups in citrate prevents freezing-induced clustering of the vanadyl species.

Table 2.3 gives the principal g and ^{51}V hyperfine values for the different mononuclear

Sample	g_x	g_y	g_z	A_x (MHz, ± 5)	A_y (MHz, ± 5)	A_z (MHz, ± 5)
Citric acid, pH 1.4	1.978	1.978	1.940	192	192	524
Citric acid, pH 5.0	1.978	1.979	1.941	184	174	510
Citric acid, pH 7.0	1.976	1.976	1.944	179	179	500
Citric acid, pH 7.0	1.978	1.978	1.950	174	174	455

Table 2.3: Principal g and ^{51}V hyperfine values of the oxovanadate(IV) complexes observed in samples with citric acid at a pH of 1.4, 5.0 and 7.0.

oxovanadate(IV) complexes determined by simulation. These values are sensitive to the direct environment of the oxovanadate(IV) ion.[46, 88] An increase in the value of g_z is observed as the pH increases from 1.4 to 7.0, while the g_x and g_y values are invariant. In section 1.3.2 (Equations 1.16 and 1.17), the values for $g_{||}$ (here g_z) and $g_\perp$ (here g_x and g_y) are related to the following electronic transitions respectively: $b_2 \longrightarrow b_1^*$ and $b_2 \longrightarrow e^*$. An increase in g_z is associated with an increase in the transition energy of $b_2 \longrightarrow b_1^*$ as function of the pH. However, the transition energy of $b_2 \longrightarrow e^*$ stays the same. This is consistent with the results from the UV-Vis analysis studied above and further supports the hypothesis that the $d_{x^2-y^2}$ orbital is destabilized as the pH increases and the carboxylic acid ($R{-}CO_2H$) groups deprotonate.

The additivity relationship, proposed by Chasteen et al.[46] and given in Equation A.51, allows a prediction of the equatorial ligation types to the oxovanadate(IV) ion (see Appendix A). Table A.6 lists some partial parallel hyperfine coupling constants, $A_{||,i}$, for various ligand types.[36, 46]. The principal g and ^{51}V hyperfine values of $[VO(H_2O)_5]^{2+}$, 1.933 (g_z) and 547 MHz (A_z)[46], differ from those observed in the samples with citric acid at pH values 1.4, 5.0 and 7.0. Theoretically, the consecutive replacement of H_2O molecules present in an equatorial position by $R{-}CO_2^-$ ligands decreases the A_z value[46, 88]: (i) 539 MHz for three H_2O molecules and one $R{-}CO_2^-$ ligand, (ii) 530 MHz for two H_2O molecules and two $R{-}CO_2^-$ ligands, (iii) 521 MHz for one H_2O molecule and three $R{-}CO_2^-$ ligands and (iv) 512 MHz for an all $R{-}CO_2^-$ ligation. In addition, a full equatorial ligation by $R{-}NH_2$ groups gives a theoretical A_z value of 480 MHz and a ligation by two RO^- and two $R{-}CO_2^-$ leads to 466 MHz. Inspection of Table 2.3 shows that the mononuclear oxovanadate(IV) complex in the sample with citric acid at a pH of 1.4 most likely involves an equatorial interaction with one or two water molecules and three or four carboxylate groups. The CW-EPR spectrum of the sample with citric acid at a pH of 5.0 stems from oxovanadate(IV) ions, equatorially ligated to four $R{-}CO_2^-$ groups. Since two sets of principal g and ^{51}V hyperfine values are simulated from the CW-EPR spectrum of the sample with citric acid at a pH of 7.0, this solution contains two oxovanadate(IV) components. The first component corresponds to oxovanadate(IV) ions, equatorially ligated to four $R{-}CO_2^-$ groups. The small differences between the EPR parameters of this form and the sample with citric acid at a pH of 5.0 are presumably due to differences in the axial (sixth) coordination to V(IV).

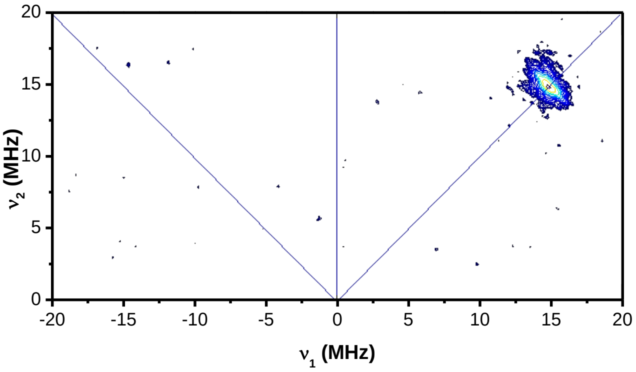

Figure 2.10: Experimental HYSCORE spectrum of the sample with citric acid at a pH value of 7.0, taken at observer position $B_0 = 348\,mT$. More experimental details are given in Appendix B, sample EPR I

HYSCORE

To elucidate on this, pulsed EPR experiments are performed on the aforementioned samples. For the first three samples (i.e. without citric acid, with citric acid at pH 1.4 and with citric acid at pH 5.0) no electron spin echo could be detected, indicating a very fast spin-spin relaxation. This very fast spin-spin relaxation is in line with the observed broad features and large line-widths in the CW-EPR spectra. The sample with citric acid at pH 7.0 gives an appreciable spin echo (see Appendix B) and HYSCORE experiments could be performed (Figure 2.10). The HYSCORE data reveals proton hyperfine couplings of maximum 2.5 MHz in magnitude. Furthermore, no echo modulations stemming from interactions with ^{14}N nuclei could be detected. This indicates that neither $-OH$, H_2O nor ammonia are equatorially ligating to the oxovanadate(IV) ion. Indeed, the protons of equatorially bound water or $-OH$ groups have hyperfine values that are far larger than 2.5 MHz.[89, 90] In fact, the maximum hyperfine values of axially ligated water are expected to be higher[89] as well, ruling out that water is axially ligating V(IV) in the sample with citric acid at pH 7.0. The lack of clear cross peaks due to interactions with ^{14}N nuclei also excludes ammonia ligation.[89, 91] The small proton hyperfine value is consistent with proton nuclei further away from the oxovanadate(IV) center, as is expected in the case of $R{-}CO_2^-$ ligation.

FTIR study on powders obtained after water evaporation at 60 °C

In a further investigation of the structure of the citrato(-oxalato)-oxovanadate(IV) complexes, FTIR spectra (recorded on powders obtained after water evaporation at

60 °C) are investigated as a function of the pH value of the solution. Figure 2.11 shows these spectra for the pH of the solution equal to 1.1, 3.7, 5.3 and 6.9. An assignment of the main vibrations is listed in Table 2.4. All assignments in the following discussion are based on references [75, 92–95].

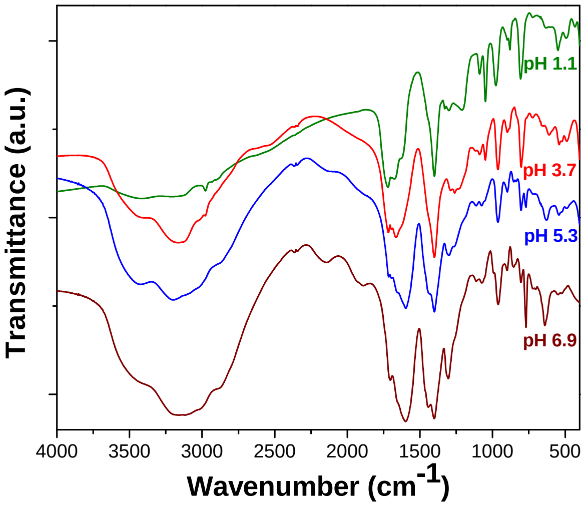

Figure 2.11: FTIR spectra of powders obtained by evaporation of water at 60 °C of the solutions with citric acid at a pH value of 1.1, 3.7, 5.3 and 6.9.

At all pH values, a strong absorbance in the area covering 3200 cm^{-1} to 2800 cm^{-1} is visible. In this area, the typically O−H, N−H and C−H stretch vibrations; originating from remaining H_2O molecules, from the NH_4^+ group and from the citric acid's or citrate's CH_2 group; are positioned. The width of the absorbance band is largely broadened by intermolecular hydrogen bridge formation between the hydroxyl groups, the ammonium ions and the carboxylic acid or carboxylate groups. Secondly, at all pH values, an intense absorbance peak is observed at 1400 cm^{-1}. At acidic pH values, this absorbance peak can be assigned to the ammonium deformation. At higher pH values (i.e. 5.3 and 6.9), this absorbance peak could also be assigned to a symmetric CO_2^- stretch vibration. Since the pKa value of ammonium equals 9.25[72], it is plausible to assign this absorbance peak to the ammonium deformation, possibly complemented by a symmetric CO_2^- stretch vibration at higher pH values. Thirdly, at all pH values, the vanadyl stretch vibration $\nu(V^{4+} = O)$ is observed at ~ 965 cm^{-1} originating from the VO^{2+} ion.

Besides a few fixed vibrations, differences in the pH dependent FTIR spectra can be observed. The differences can be ascribed to the appearance of ammonium oxalate $(NH_4)_2C_2O_4$ at a pH value of 5.3 and the deprotonation of the citric acid's COOH groups with increasing pH.

1. The onset of ammonium oxalate is seen by the rise of absorbance peaks starting from a pH value of 5.3, associated with a N−H stretching vibration in a $(NH_4)_2C_2O_4$ molecule at ~ 2150 and ~ 1900 cm^{-1}. A second indication for the presence of $(NH_4)_2C_2O_4$ starting at a pH value of 5.3 is its symmetric COO$^-$ stretching vibration at ~ 1465 cm^{-1} and ~ 1440 cm^{-1}.

2. At a low pH value (i.e. 1.1 and 3.7), the C=O stretching vibration in a COOH group is found by the absorbance peak at ~ 1725 cm^{-1}. This suggests that at least one of the citric acid's carboxylic acid groups is still protonated. As the pH exceeds 5.3, the majority of the acid groups is deprotonated (COO$^-$) and interacts with either VO^{2+} or NH_4^+ as observed by the absorbance peak at ~ 1600 cm^{-1}, associated with the asymmetric $\nu(COO^-)$ in NH_4^+/COO$^-$ or VO^{2+}/COO$^-$. In the region between 1110 cm^{-1} and 1040 cm^{-1} absorbance peaks assigned to the C−O stretch vibration are present. Starting from pH 1.1 towards pH 6.9, the two absorbance peaks shift from ~ 1110 cm^{-1} and ~ 1075 cm^{-1} to ~ 1085 cm^{-1} and ~ 1045 cm^{-1}. This might indicate the deprotonation of the citric acid's α-hydroxyl functionality. At a pH value of 1.1 these vibrations are clearly visible in the spectrum. However, as the pH value increases, they seem to disappear in the background of the spectrum. Thus, some caution concerning the α-hydroxyl functionality and its stretching vibrations is required.

pH 1.1	pH 3.7	pH 5.3	pH 6.9	Assignment	
3200–2800 (br)	3200–2800 (br)	3200–2800 (br)	3200–2800 (br)	$\nu(O-H)$	O–H stretching in hydrated H_2O
3200–2800 (br)	3200–2800 (br)	3200–2800 (br)	3200–2800 (br)	$\nu(N-H)$	N–H stretching in NH_4^+
3200–2800 (br)	3200–2800 (br)	3200–2800 (br)	3200–2800 (br)	$\nu(C-H)$	C–H stretching in CH_2
-	-	-	2150	$\nu(N-H)$	N–H stretching in $(NH_4)_2C_2O_4$
-	-	-	1900	$\nu(N-H)$	N–H stretching in $(NH_4)_2C_2O_4$
1724	1722	-	-	$\nu(C=O)$	C=O stretching in COOH
1710–1640	1710–1640	1710–1640	1710–1640	$\nu_{as}(COO^-)$	Oxalate's asymmetric COO^- stretching interacting with NH_4^+ or VO^{2+}
-	-	1601	1600	$\nu_{as}(COO^-)$	Citrate's asymmetric COO^- stretching interacting with NH_4^+ or VO^{2+}
-	-	1465–1440	1465–1440	$\nu_s(COO^-)$	Oxalate's symmetric COO^- stretching interacting with NH_4^+ or VO^{2+}
1401	1400	1398	1402	$\nu_s(COO^-)$	Citrate's symmetric COO^- stretching interacting with NH_4^+ or VO^{2+}
1401	1400	1398	1402	$\delta(NH_4^+)$	NH_4^+ deformation
1305	1307	1304	1303	$\delta(O-C=O)$	O–C=O deformation
-	-	1105 and 1072	1110 and 1077	$\nu(C-O)$	C–O stretching in the deprotonated α-hydroxyl group
1089 and 1045	1083 and 1042	-	-	$\nu(C-O)$	C–O stretching in the α-hydroxyl group
972	968	964	962	$\nu(V^{4+}=O)$	V^{4+}=O stretching
< 900	< 900	< 900	< 900	$\pi(C-O)$	C–O out of plane deformation
< 900	< 900	< 900	< 900	$\gamma(CH_2)$	CH_2 skeleton vibration
< 900	< 900	< 900	< 900	$\delta(O-C=O)$	O–C=O in plane deformation

Table 2.4: Band assignments of the main vibrations (expressed in cm^{-1}) of the FTIR spectra of the powders obtained by evaporation of water at 60 °C of solution with citric acid at a pH value of 1.1, 3.7, 5.3 and 6.9. The presence of multiple bands associated with the oxalate ion in $(NH_4)_2C_2O_4$) is possibly due the presence of multiple oxalate structures such as monodentate oxalate, bidentate oxalate and free oxalate, in varying degrees of concentration.[92] The assignments are based on [75, 92–95].

Conclusion on the structure of the citrato-oxalato-VO^{2+} complexes

Despite the state differences for the sample analyzed by UV-Vis spectroscopy (solution at T$_{Room}$), EPR spectroscopy (frozen solution) and FTIR spectroscopy (dried solution), structural similarities are clearly present as a function of the solution's pH value. At a low pH value (i.e. below 5), the VO^{2+} ion is surrounded by weakly interacting H_2O or R–CO$_2$H ligands. At this point, no traces of $(NH_4)_2C_2O_4$ are observable, probably due to the protonated state of the oxalic acid's second carboxylic acid group ($C_2O_4H^-$). As the pH increases (i.e. above 5), the carboxylic acid groups of both oxalic acid and citrate deprotonate and form carboxylate groups (R–CO$_2^-$). These carboxylate groups interact either with NH_4^+ or with VO^{2+}, forming an ammonium bridged network of carboxylato-VO^{2+} complexes. The VO^{2+} species are identified as mononuclear citrato-oxovanadate(IV) complexes in a square bipyramidal geometry with a four R–CO$_2^-$ ligation at the equatorial positions and likely a fifth, more weakly interacting, R–CO$_2^-$ ligation at the axial position. Similar to the deprotonation of the citric acid, oxalic acid completely deprotonates at a pH value above 5. The resulting oxalate interacts either with ammonium to form the ammonium oxalate ($(NH_4)_2C_2O_4$) or, possibly, with the VO^{2+} ion as one of the R–CO$_2^-$ ligands.

2.3 Aqueous citrato-VO^{2+} solution

From the previous section it is clear that ammonium oxalate residues remain in the final citrato-oxalato-oxovanadate(IV) solution. These oxalate residues originate from the VO$_2^+$/VO^{2+} reduction. Hence, oxalate residues are inevitable in the synthesis of an aqueous VO^{2+} solution. However, this ammonium oxalate will, probably, influence the thermal decomposition pathway of the precursor gel and the VO$_x$ phase formation. E.g. during the thermal treatment all organic fragments of the solution, including oxalate residues and citrate ligands, must be decomposed. Thus, in a solution with fewer oxalate residues, fewer organics must be, thermally, removed. Therefore, in this section a procedure is proposed for the removal of ammonium oxalate, without corrupting the ammonium bridged network of citrato-VO^{2+} complexes or their square bipyramidal structure with a four R–CO$_2^-$ ligation at the equatorial positions and likely a fifth R–CO$_2^-$ ligation at the axial position.

In the synthesis of the aqueous citrato-oxalato-VO^{2+} solution (see Figure 2.2), citric acid is directly added to the aqueous oxalato-VO^{2+} solution in a 2:1 molar ratio of citric acid to VO^{2+}. Next, the pH is increased by adding NH_3 until a value of 7 is obtained. In the synthesis of the aqueous citrato-oxalato-VO^{2+} precursor solution, the superfluous oxalate is thus retained. Alternatively, the removal of superfluous oxalate ions is aimed for in the synthesis of the aqueous, oxalate-free citrato-VO^{2+} solution (see Figure 2.2). For this purpose, the pH of the oxalate solution is adjusted to 7 by adding NH_3 and the vanadium concentration is set to 1.5 M by dilution with water. This solution is then mixed with a 3 M citrate solution having a pH of 7, in a 1:1 volume ratio to maintain the 2:1 molar ratio of citrate ions to the VO^{2+} species. Precipitation occurs immediately after mixing and the solution is aged for 7 days at 4 °C to settle the precipitate. Next, the precipitate is filtrated from the solution and the synthesis of the citrato-VO^{2+} solution is finalized by adding NH_3 to re-adjust the pH to a value of 7. This pH is sufficient to guarantee the deprotonation of citric acid's carboxylic acid groups and thus the formation of citrato-oxovanadate(IV) complexes.

2.3.1 Removal of $(NH_4)_2CO_4$

During precipitation from the mixed oxalato-VO^{2+} and citrate solution, large needle-like crystals are formed. This precipitate is analyzed by XRD and FTIR spectroscopy and compared to either reference data or a powder obtained from the vanadium free ammonium oxalate solution. According to the X-Ray diffractogram in Figure 2.12, the precipitate consists of orthorhombic ammonium oxalate, $(NH_4)_2C_2O_4$, and orthorhombic ammonium oxalate hydrate, $(NH_4)_2C_2O_4 \cdot H_2O$, as indicated by the JCPDS 44-0724 and JCPDS 14-0801 reference patterns, respectively.[96]

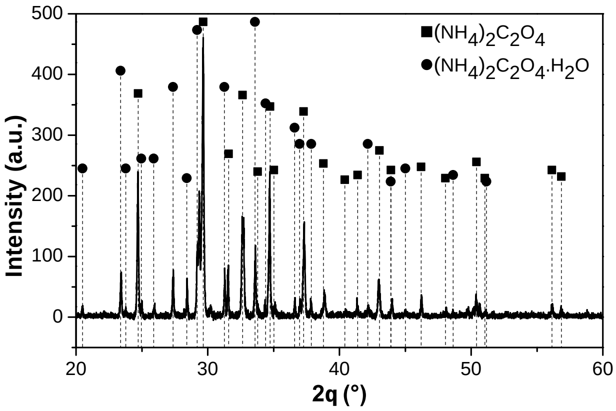

Figure 2.12: XRD pattern of the precipitate originating from the synthesis of the citrato-VO^{2+} solution. The assignments are based on JCPDS 44-0724 for $(NH_4)_2C_2O_4$ and JCPDS 14-0801 for $(NH_4)_2C_2O_4 \cdot H_2O$.[96]

The FTIR spectra of the precipitate and the powder, obtained from the vanadium free ammonium oxalate solution, and the assignment of their main vibrations are given in Figure 2.13 and Table 2.5. Both infrared spectra show a strong absorption band between 3200 and 2800 cm^{-1} due to the O−H stretching mode of the hydrate molecules and the N−H stretching mode of the ammonium ion, broadened by H-bridge formation. Additional N−H stretching modes of the ammonium ion can be observed in both spectra at about 2150 and 1900 cm^{-1}. Typical carboxylate stretch vibrations in $(NH_4)_2C_2O_4$ appear at 1710, 1655 and 1605 cm^{-1} for $\nu_{as}(COO^-)$ and at 1450 and 1410 cm^{-1} for $\nu_s(COO^-)$.[75, 92–94] Frost et al. explain the multiplicity of

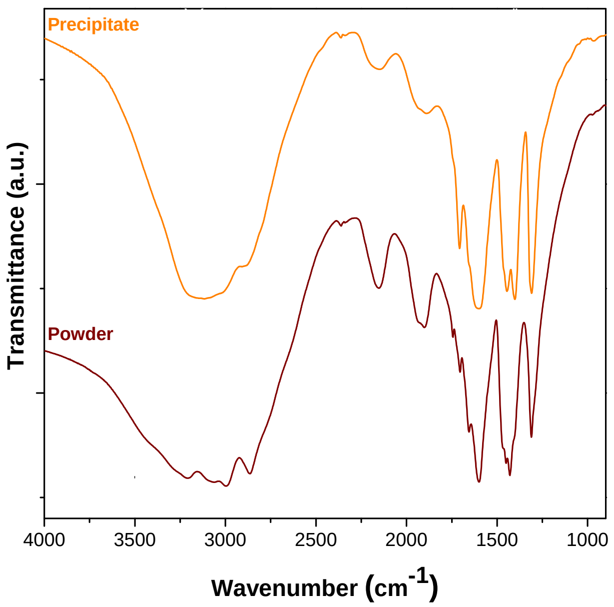

Figure 2.13: FTIR spectra of the precipitate, originating from the synthesis of the aqueous citrato-VO^{2+} solution, and the powder obtained from the vanadium free, ammonium oxalate solution.

bands by the structural variety of oxalate species in ammonium oxalate (i.e. mono-, di- and poly-oxalates).[92] Furthermore, the band at 1410 cm^{-1} coincides with the ammonium deformation. The intense absorption peak observed at 1315 cm^{-1} corresponds to the O−C=O deformation.[75, 92–94] No vanadyl stretching mode, corresponding to $\nu(V^{4+} = O)$ or $\nu(V^{5+} = O)$, is observed between 900 cm^{-1} and 1100 cm^{-1}.[95] Based on both the XRD and FTIR data, the precipitate is unambiguously identified as vanadium free, crystalline ammonium oxalate (possibly present as a monohydrate).

In conclusion, the precipitation of vanadium free ammonium oxalate indicates that oxalate residues, originating from the VO_2^+/VO^{2+} reduction, can be isolated from the citrato-VO^{2+} solution. Additionally, the incorporation of ammonium into the oxalate crystals explains the pH drop of the filtrate and hence the necessity to add ammonia to the citrato-VO^{2+} solution in order to re-obtain a solution with a pH value of 7.

2.3.2 Structural investigation of the citrato-VO^{2+} complexes

The complexation of citric acid and its pH-dependent derivatives with the VO_2^+ ion is previously studied both in the solid state[26–29] and in the solution[26, 30, 31]. The formation of dimeric structures with composition $[(VO)_2(C_6H_4O_7)_2]^{4-}$ is generally

Precipitate	Powder	Assignment	
3200–2800 (br)	3200–2800 (br)	$\nu(O-H)$	O–H stretching in hydrated H_2O
3200–2800 (br)	3200–2800 (br)	$\nu(N-H)$	N–H stretching in NH_4^+
2151	2160	$\nu(N-H)$	N–H stretching in $(NH_4)_2C_2O_4$
1904	1900	$\nu(N-H)$	N–H stretching in $(NH_4)_2C_2O_4$
1710	1702	$\nu_{as}(COO^-)$	Asymmetric COO^- stretching in $(NH_4)_2C_2O_4$
1655	1660	$\nu_{as}(COO^-)$	Asymmetric COO^- stretching in $(NH_4)_2C_2O_4$
1607	1605	$\nu_{as}(COO^-)$	Asymmetric COO^- stretching in $(NH_4)_2C_2O_4$
1450	1460	$\nu_s(COO^-)$	Symmetric COO^- stretching in $(NH_4)_2C_2O_4$
1400	1410	$\nu_s(COO^-)$	Symmetric COO^- stretching in $(NH_4)_2C_2O_4$
1400	1410	$\delta(NH_4^+)$	NH_4^+ deformation
1315	1313	$\delta(O-C=O)$	O–C=O deformation

Table 2.5: Band assignments of the main vibrations (expressed in cm^{-1}) of the FTIR spectra of the precipitate, originated from the synthesis of the aqueous citrato-VO^{2+} solution, and the powder obtained from the vanadium free, ammonium oxalate solution. The assignments are based on references [75, 92–94].

accepted in or from solutions with, approximately, an equimolar ligand:VO^{2+} ratio and a neutral pH value.[26–31] Note that (i) the VO^{2+} coupling into a dimeric structure is realized by two deprotonated α-hydroxyl groups each originating from one citrate ligand in the dimeric composition and (ii) each citrate ligand chelates a first VO^{2+} ion by two carboxylate groups and a second VO^{2+} ion with one carboxylate group which leads to a hexagonal chelating of each V center in a secluded dimeric structure without free available carboxylate groups. In aforementioned solution studies, the formation of this secluded, dimeric structure is intended by limiting the vanadium and ligand concentration ($\sim 10^{-3}$ M)[30, 31] and by aversion or active removal of ammonium[26, 30, 31] which is well known as bridging ion between two or more citrato complexes[61, 85–87, 97, 98]. In this work, the annihilation of the secluded structure and the formation of ammonium carboxylate interactions, bridging two or more citrato-VO^{2+} complexes into a network is aimed for. For this purpose, a higher vanadium concentration (two orders in magnitude) is set and ammonium is, deliberately, added to the solution. This network of citrato-VO^{2+} complexes will allow the formation of an amorphous gel by its cross-linking nature upon evaporation of water during a chemical solution deposition process.[21]

Gels of both solutions, obtained by drying at 60 °C, are analyzed by FTIR spectroscopy and compared with spectra of the VO^{2+}-free ammonium citrate[3] in Figure 2.14. A full assignment of the measured absorption bands is reported in Table 2.6. The infrared spectra of the citrato-oxalato-VO^{2+}, citrato-VO^{2+} and the VO^{2+}-free ammonium citrate gel all show a strong absorption band between 3400 and 2800 cm^{-1} due to[75, 94, 95]:

---

[3] This ammonium citrate gel is obtained from a solution with a pH of 7 and is assumed to have the following chemical formula $(NH_4)_3C_6H_5O_7$.

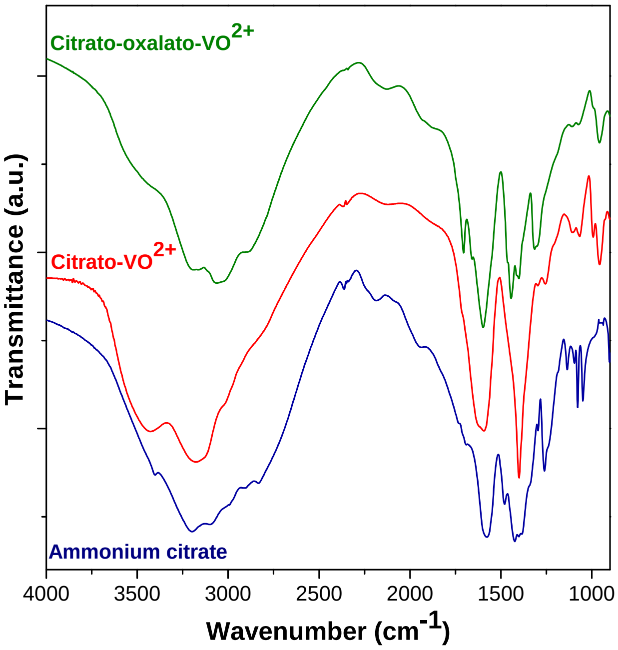

Figure 2.14: FTIR spectra of gels of the aqueous citrato-oxalato-VO^{2+}, citrato-VO^{2+} and ammonium citrate solutions obtained by drying at 60 °C.

- the O-H stretching mode of hydroxyl groups and absorbed H_2O molecules,
- the N-H stretching mode of the ammonium ions and
- the C-H stretching mode of the citrate's methylene bridges.

These absorption bands are broadened by H-bridge formation. For the typical asymmetric and symmetric carboxylate stretch vibrations, differences in the citrato-oxalato-VO^{2+} and the citrato-VO^{2+} precursor gels are observed. In the presence of oxalate, a first $\nu_{as}(CO_2^-)$ appears at 1710 cm^{-1} and is associated with the ammonium oxalate present in the citrato-oxalato-VO^{2+} precursor.[92] Both the citrato-VO^{2+} precursor gel and the gel of the VO^{2+}-free ammonium citrate solution have no clear vibration peak at this position. However, in all spectra a similar $\nu_{as}(CO_2^-)$ arises around 1590 cm^{-1} and is assigned to asymmetric stretch vibrations in the carboxylate groups interacting with (i) VO^{2+} in the citrato-oxalato-VO^{2+} and the citrato-VO^{2+} precursor gel and (ii) the ammonium ion in all the studied gels.[75, 94, 95] Again in the presence of oxalate, a first $\nu_s(CO_2^-)$ appears at 1441 cm^{-1} and is associated with the ammonium oxalate present in the citrato-oxalato-VO^{2+} precursor solution.[92] In the spectra a clear $\nu_s(CO_2^-)$ appears around 1400 cm^{-1} and is assigned to a symmetric stretch vibration of the carboxylate groups interacting with VO^{2+} in the citrato-oxalato-VO^{2+} and the citrato-VO^{2+} precursor gel. [75, 94, 95] The peak at 1400 cm^{-1} coincides with that of the ammonium deformation, which explains its presence in the spectrum of the VO^{2+}-free ammonium citrate gel. In all spectra, a doublet assigned to the C-O stretching mode is observed between 1120 and 1070 cm^{-1}.[75, 94, 95]

Citrato-oxalato-VO^{2+}	Citrato-VO^{2+}	Ammonium citrate		Assignment
3200–2800 (br)	3200–2800 (br)	3200–2800 (br)	$\nu(O-H)$	O–H stretching in hydrated H_2O
3200–2800 (br)	3200–2800 (br)	3200–2800 (br)	$\nu(N-H)$	N–H stretching in NH_4^+
3200–2800 (br)	3200–2800 (br)	3200–2800 (br)	$\nu(C-H)$	C–H stretching in hydrated CH_2
1708	-	-	$\nu_{as}(COO^-)$	Asymmetric COO^- stretching in $(NH_4)_2C_2O_4$
1595	1587	1594	$\nu_{as}(COO^-)$	Asymmetric COO^- stretching interaction with VO^{2+} or NH_4^+
1441	-	-	$\nu_s(COO^-)$	Symmetric COO^- stretching in $(NH_4)_2C_2O_4$
1400	1402	1402	$\nu_s(COO^-)$	Symmetric COO^-stretching interaction with VO^{2+} or NH_4^+
1400	1402	1402	$\delta(NH_4^+)$	NH_4^+ deformation
1119 and 1076	1115 and 1067	1138 and 1078	$\nu(C-O)$	C–O stretching in the deprotonated α-hydroxyl group
960	960	-	$\nu(V^{4+}=O)$	V^{4+}=O stretching

Table 2.6: Band assignments of the main vibrations (expressed in cm^{-1}) of the FTIR spectra of gels (obtained by drying at 60 °C) of the aqueous citrato-oxalato-VO^{2+}, citrato-VO^{2+} and vanadium-free ammonium citrate solutions. The assignments are based on references [75, 92, 94, 95]

The vanadyl stretching mode, $\nu(V^{4+}=O)$, is observed in the gels associated with the citrato-oxalato-VO^{2+} and the citrato-VO^{2+} precursor solution at 960 cm^{-1}, indicating the presence of the oxovanadate species in each precursor solution.[97] Moreover, the absence of VO$_2^+$ species is supported by the absence of the $\nu(V^{5+}=O)$ stretching mode around 1020 cm^{-1}.[95] In conclusion, the presence of the citrato-VO^{2+} complexes and the ammonium groups linking the excess citrate, is suggested by the FTIR spectra of the citrato-oxalato-VO^{2+} and citrato-VO^{2+} precursor gels. Vibrations owing to the ammonium oxalate are observed in the spectra of the citrato-oxalato-VO^{2+} precursor gel, but not in the citrato-VO^{2+} precursor gel, which indicates the removal of $(NH_4)_2C_2O_4$ in the precipitation step during the synthesis of the citrato-VO^{2+} precursor solution. To elucidate the direct environment of the VO^{2+} cation, EPR studies are analyzed in the next section.

Figure 2.15 shows the experimental and simulated X-band CW-EPR spectra recorded at 100 K for the oxalate-free citrato-VO^{2+} precursor solution.

1. The anistropic spectrum exhibits a multiline pattern, corresponding to a chelated VO^{2+} system with an axial symmetry[46], with a well resolved hyperfine structure and without a superimposed broad feature. However, Kiss et al. and Velayutham et al. report X-band EPR spectra recorded on frozen solutions with such a broad feature and ascribe this broad feature to the presence of paramagnetic dimeric structures.[27, 30] According to Chasteen et al. and Smith et al., a broad feature, superimposed on a multiline spectrum, is characteristic for dipolarly interacting VO^{2+} centers (clusters).[46, 88] The absence of this broad feature in the X-band EPR spectrum, shown in Figure 2.15, indicates the presence of mononuclear VO^{2+} entities in the frozen citrato-VO^{2+} solution similar to the observations of Garriba et al. and Buglyo et al. in the case of mononuclear VO^{2+} complexes with alternative carboxylate based ligands[99, 100]. Note that dimeric citrato-VO^{2+} complexes could be present without exhibiting a feature in the EPR spectrum if they would be antiferromagnetically coupled. This contradicts the observations of Kiss et al.[30] and Velayutham et al.[27], and is considered unlikely. Thus, the X-band spectrum, shown in Figure 2.15, stems from mononuclear VO^{2+} complexes present in the citrato-VO^{2+} solution.

2. The principal g and ^{51}V hyperfine values are determined for this mononuclear VO^{2+} complex by simulation of the experimental CW-EPR spectrum: $g_{x,y} = 1.976$, $g_z = 1.944$ and $A_{x,y} = 179 \pm 5$ MHz and $A_z = 500 \pm 5$ MHz. The g_z and A_z values are sensitive to the direct environment of the oxovanadate(IV) ion and allow, in combination with the additivity relationship, a prediction of the equatorial ligation types to the oxovanadate(IV) ion.[46, 88] The principal g and ^{51}V hyperfine values of $[VO(H_2O)_5]^{2+}$, 1.933 (g_z) and 547 MHz (A_z)[46], differ from those observed for the citrato-VO^{2+} solution. Theoretically, the consecutive replacement of H_2O molecules present in an equatorial position by R-CO$_2^-$ ligands decreases the A_z value[46, 88]:

- 539 MHz for three H_2O molecules and one R-CO_2^- ligand,
- 530 MHz for two H_2O molecules and two R-CO_2^- ligands,
- 521 MHz for one H_2O molecule and three R-CO_2^- ligands and
- 512 MHz for an all R-CO_2^- ligation.

A full equatorial ligation by R-NH_2 groups gives a theoretical A_z value of 480 MHz and a ligation by two RO^- and two R-CO_2^- leads to 466 MHz. The theoretical value for an all R-CO_2^- ligation best fits the simulated ^{51}V hyperfine value. Additionally, the simulated principal g and ^{51}V hyperfine values differ significantly from those obtained by Kiss et al. in the case of dimeric citrato-VO^{2+} complexes (i.e. g_z = 1.953 and A_z = 231 MHz)[30] which stresses the different structure of the citrato-VO^{2+} complexes in this work. Contrarily, the simulated values correspond well to those of mononuclear carboxylato-VO^{2+} complexes with an axial symmetry such as the glycolato-VO^{2+} reported by Garribba et al. ($g_{x,y}$ = 1.980, g_z = 1.941, $A_{x,y}$ = 180 MHz and A_z = 505 MHz).[100]

Summarizing, the observed X-band EPR spectrum and its simulated principal g and ^{51}V hyperfine values are ascribed to the presence of mononuclear VO^{2+} complexes, with an axial symmetry and a four R–CO_2^- ligation at the equatorial positions, present in the citrato-VO^{2+} solution. Note that the presence of oxalato-VO^{2+} complexes would result in $g_{x,y}$ = 1.966, g_z = 1.939, $A_{x,y}$ = 295 MHz and A_z = 515 MHz[99], and is therefore excluded.

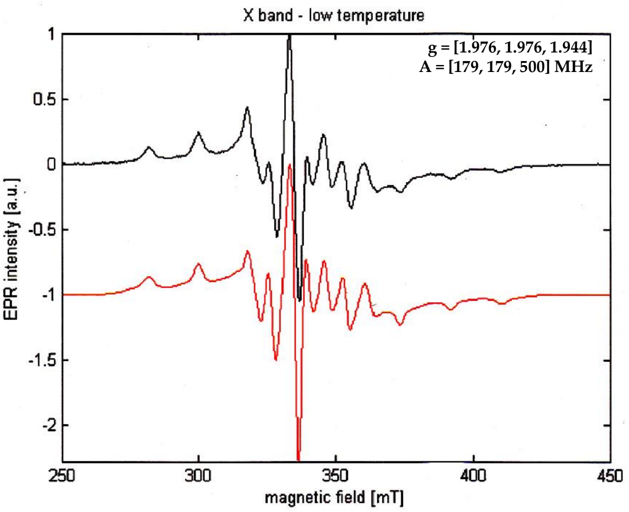

Figure 2.15: Experimental (black) and simulated (red) CW-EPR spectrum of the frozen citrato-VO^{2+} solution. The CW-EPR spectrum is measured at 100 K using a modulation amplitude of 0.5 mT, a microwave power of 1 mW and a modulation frequency of 100 kHz.

To elucidate the structure of these mononuclear VO^{2+} complexes in more detail, pulsed EPR experiments are performed on the citrato-VO^{2+} solution. HYSCORE experiments are performed at a magnetic-field setting known to excite all molecular orientations. The HYSCORE spectrum, depicted in Figure 2.16, reveals only a weak hyperfine coupling with protons (maximum coupling 2.5 MHz in magnitude). The hyperfine coupling of protons present in equatorially or axially ligated water or hydroxyl groups is expected to be much larger.[90] The small proton hyperfine value is consistent with proton nuclei further away from the oxovanadate(IV) center, as is expected in the case of R-CO_2^- ligation. In addition, the lack of clear cross peaks due to interactions with ^{14}N nuclei excludes ammonia ligation. Thus, the HYSCORE data indicates that neither water, nor hydroxyl groups or ammonia are involved in the ligation of the oxovanadate(IV) ion and thus this data supports the all equatorial, R-CO_2^- ligation.

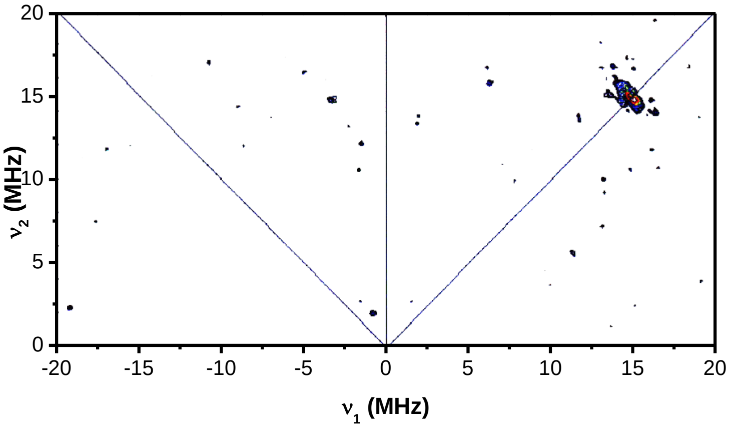

Figure 2.16: HYSCORE spectrum of the frozen citrato-VO^{2+} solution, recorded at 10 K and taken at observer position B_0 = 348 mT. More experimental details are given in Appendix B, sample EPR K

In conclusion, the EPR and HYSCORE results of the citrato-VO^{2+} precursor solution are in agreement with the FTIR characteristics of the dried precursor. The present VO^{2+} species are structurally identified as mononuclear citrato-VO^{2+} complexes with a four R-CO_2^- ligation at the equatorial positions, each originating from citrate species present in the solution. In contrast to the reported dimeric and secluded structures, the citrato-VO^{2+} complexes, studied in this work, are cross-linked by ammonium carboxylate interactions.

2.4 Conclusion

A new synthesis for an aqueous citrato-oxovanadate(IV) solution is proposed and each step in it is studied in detail by various spectroscopic techniques. During synthesis, cyclic tetravanadate(V) is converted into VO^{2+} using oxalic acid as an acidifier and reducing agent. The subsequent complexation of the VO^{2+} ion with citrato complexing agents and the differentiation between a citrato-oxalato-VO^{2+} and a citrato-VO^{2+} solution is studied by Electron Paramagnetic Resonance and Fourier Transform Infra-Red Spectroscopy:

- A successful procedure based on the limited solubility of $(NH_4)_2C_2O_4$ in water, is developed for the removal of the oxalate excess (which was necessary for a complete VO_2^+/VO^{2+} reduction).
- In both solutions, the VO^{2+} ion is anchored in a mononuclear complex with a square bipyramidal geometry and a four $R{-}CO_2^-$ ligation at the equatorial positions and likely a fifth $R{-}CO_2^-$ ligation at the axial position.

Chapter 3

Oxalato- and citrato-VO^{2+} complexes: structure and reactivity

In the previous chapter, a procedure for the synthesis of an aqueous solution - containing mononuclear, citrato-VO^{2+} complexes with a distorted octahedral geometry - is proposed. In this procedure, a fixed molar ratio of citrate versus VO^{2+} is chosen and maintained (i.e. citrato:VO^{2+} = 2:1). This chapter focuses on the complexation of the oxovanadate(IV) ion by oxalate and/or citrate ligands into mononuclear complexes and on their ligand exchange reaction. The content of this chapter is submitted for publication.

The complexation of citric acid and its pH-dependent derivatives with the VO^{2+} ion is previously studied both in the solid state[26–29] and in the aqueous solution[26, 30, 31]. The formation of dimeric structures with composition $[(VO)_2(C_6H_4O_7)_2]^{4-}$ is generally accepted in or from solutions with, approximately, an equimolar ligand:VO^{2+} ratio and a neutral pH value.[26–31] Note that in this dimeric structure, all chelating groups interact with the coupled VO^{2+} centers leading to a hexagonal chelation of each V center in a secluded dimeric structure without free available carboxylate groups. Only for very high citrate excesses (citrate:VO^{2+} ± 100:1), pH-dependent mononuclear citrato-VO^{2+} complexes are observed by Lodyga-Chruscinska et al.[32] Our work aims to synthesize mononuclear citrate-VO^{2+} complexes without inserting a high amount of citrate. Alternatively, the prevention of the secluded, dimeric structure – by the formation of ammonium carboxylate interactions, bridging two or more citrato-VO^{2+} complexes into a network – is targeted. This network of citrato-VO^{2+} complexes allows the formation of an amorphous gel by its cross-linking nature upon evaporation of water during a chemical solution deposition process.[21, 33] A low amount of citrate is preferred since this limits the amount of carbon atoms that must be, thermally, removed during the film processing and the vanadium oxide phase formation.[21, 33] Additionally, the time-dependent reactivity of the VO^{2+} complexes present in the aqueous solution, towards the dissolved O_2 is analyzed. This reactivity could change the structure and oxidation state of the complexes and hence drastically alter the vanadium oxide phase formation.

3.1 Solution synthesis

Firstly, an aqueous VO^{2+} solution was synthesized by the consecutive dissolution of ammonium metavanadate and oxalic acid dihydrate in water under reflux conditions (90 °C, 10 min.) in a molar ratio of 3:1 (oxalic acid : ammonium metavanadate). Secondly, a separate solution of ammonium citrate was prepared by dissolving di-ammonium hydrogen citrate in water and by adding ammonia to this solution. A nominal citrate concentration of 3 M and a pH value of 7 were experimentally set. Before mixing the VO^{2+} solution with the ammonium citrate solution, the pH of the VO^{2+} solution was increased to a value of 7 by adding ammonia and the volume was adjusted by adding Milli-Q water to achieve a nominal VO^{2+} concentration of 1.5 M. Next, both solutions (1.5 M VO^{2+} solution with a pH value of 7 and 3 M citrate solution with a pH value of 7) were mixed in a volume ratio ranging between 2.67:1 and 0.44:1. All solutions were aged for 7 days at 4 °C to induce $(NH_4)_2C_2O_4$ precipitation, which was subsequently removed by filtration. Finally, the pH and volume of each filtrate was adjusted by NH_3 and H_2O to obtain aqueous VO^{2+} solutions with a pH value of 7 and a vanadium concentration of 0.1 M. In this study, the molar ratio of citrate to VO^{2+} is varied between 0.75:1 and 4.5:1 by varying the aforementioned volume. All nominal vanadium concentrations were experimentally confirmed by Inductively Coupled Plasma-Atomic Emission Spectrometry.

3.2 Structural investigation

3.2.1 X-band CW-EPR and HYSCORE

The experimental X-band CW-EPR spectra, recorded at 10 K, of the solutions with a molar ratio (citrate:VO^{2+}) ranging between 0.75:1 and 4.5:1 are shown in Figure 3.1. Firstly, all solutions exhibit an anistropic, multiline spectrum – corresponding to a chelated VO^{2+} system with an axial symmetry[46] – with a well resolved hyperfine structure. However, not only are the lines of the multiline pattern in the spectrum of the solution with a molar ratio of 0.75:1 broader, the pattern is also superimposed onto a broad feature. Such a line-broadening and broad background feature is characteristic of oxovanadate(IV) clusters or dipolarly interacting oxovanadate(IV) centers.[46, 88]

Room-temperature CW EPR does not show this broad feature and indicates that

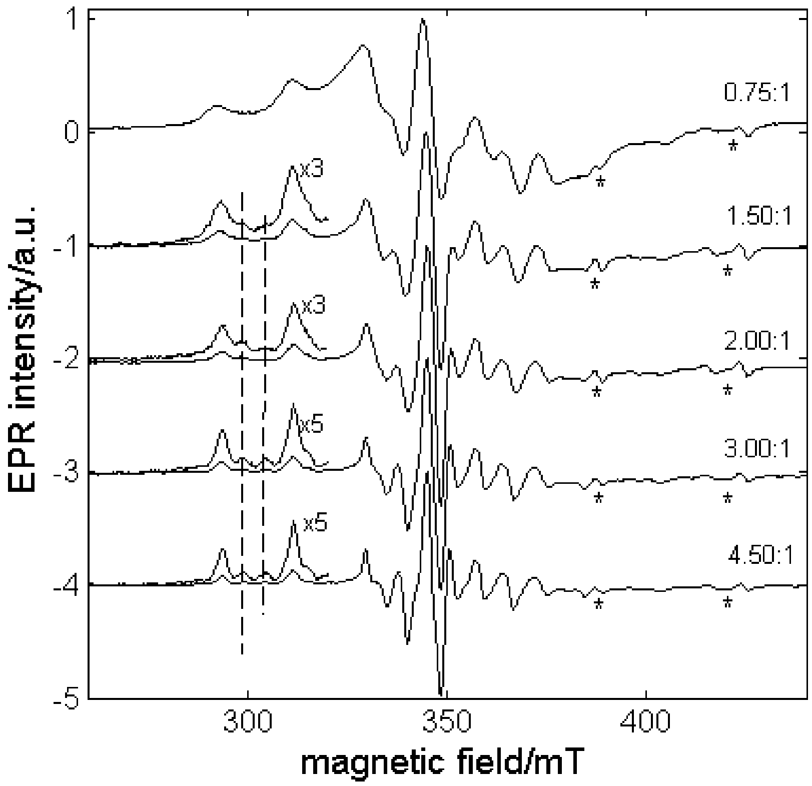

Figure 3.1: X-band CW-EPR spectra recorded at 10 K of frozen solutions with a molar ratio (citrate:VO^{2+}) of 0.75:1, 1.50:1, 2.00:1, 3.00:1 and 4.50:1. The spectra are recorded with a microwave power of 0.15 mW. Each solution has a vanadium concentration of 5 mM and a pH value of 7. The asterisk indicates a cavity background signal. The simulations are shown in Appendix B.

the cluster formation is induced by freezing, as is corroborated by the temperature-dependent EPR measurements (Figure 3.2). As more citrate is added to the solution, the broad feature disappears in the low-temperature EPR spectra and the freezing-induced clustering does no longer occur. The lack of freezing-induced clustering as the amount of citrate increases, suggests that citrate aids in the glass formation during freezing as corroborated earlier (Chapter 2). Although the EPR spectra of the solutions with higher citrate concentration are all dominated by the characteristic features of mononuclear VO^{2+} complexes, low-intensity lines can be found in between these features as indicated by the dashed lines in Figure 3.1. These lines are part of a multi-line pattern (Figure 3.3), characteristic of ferromagnetically coupled dinuclear citrate-VO^{2+} complexes.[27] Thus, under the conditions used here, all solutions contain predominantly mononuclear oxovanadate(IV) species, similar to the observations of Garribba et al. and Buglyo et al. in the case of mononuclear VO^{2+}

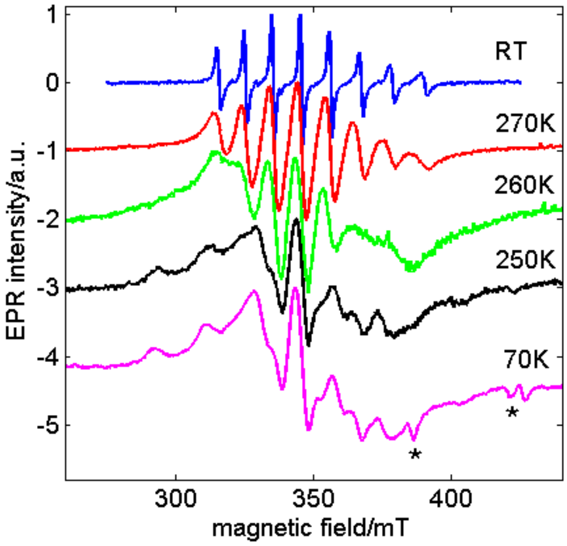

Figure 3.2: Experimental CW-EPR spectra of the solution with a molar ratio (citrate:VO^{2+}) of 0.75:1 recorded at different temperatures. The asterisks indicate cavity background signals.

complexes with alternative carboxylate-based ligands[99, 100]. Dimeric citrate-VO^{2+} complexes are also present in a smaller amount ($\leq$ 20 %).

The principal g and ^{51}V hyperfine values (Table 3.1) are determined for the mononuclear VO^{2+} complexes by simulation of the experimental CW-EPR spectra in Figure 3.1 (see also Figures B.14, B.15 and B.16). The g_z and A_z value are known to vary strongly depending on the type of equatorial coordination to the VO^{2+} ion.[46, 88]

Complex	Molar ratio	$g_{x,y}$	g_z	A_x (MHz)	A_y (MHz)	A_z (MHz)
1	0.75:1	1.975	1.938	180	180	514
2	1.50:1	1.975	1.940	175	180	500
3	2.00:1 to 4.50:1	1.975	1.943	165	170	496

Table 3.1: Principal g and ^{51}V hyperfine values of the dominating mononuclear oxovanadate(IV) species observed in the samples with a molar ratio (citrate:VO^{2+}) of 0.75:1, 1.50:1, 2.00:1, 3.50:1 and 4.50:1. The g and A values are determined with an error of ± 0.003 and ± 5. The simulations are shown in Appendix B (samples L, M and N).

The spectral features of the EPR spectrum at a molar ratio of 2.00:1 and upwards (Figure 3.1) are very similar and stem essentially from two contributions: a dimeric species and the monomeric complex 3. The EPR spectrum of oxovanadium(IV) complexes formed at pH 7.1 by citrate in aqueous solution at high ligand to metal

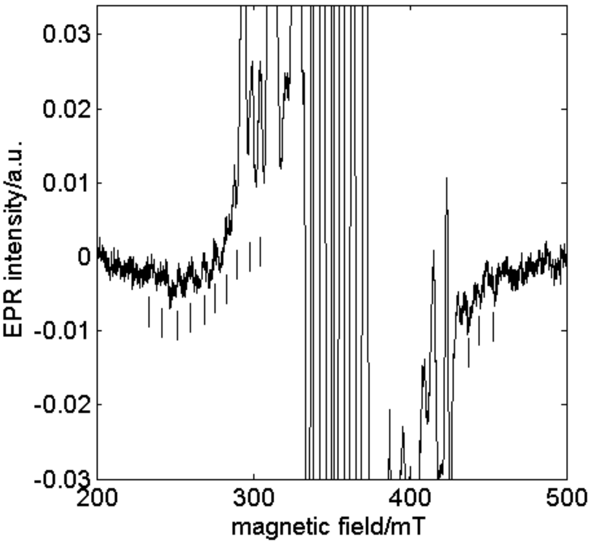

Figure 3.3: Enlargement of the experimental CW-EPR spectrum of the solution with a molar ratio (citrate:VO^{2+}) of 4.5:1 recorded at 10 K. The lines indicate part of the multi-line spectrum stemming from dimeric vanadyl species.

molar ratios show a similar heterogeneity, albeit with a significantly larger relative contribution from the dimeric species.[32] The spin Hamiltonian values of complex 3 (Table 3.1) are assigned by Lodyga-Chruscinska et al.[32] to a $VOLH_{-1}$-type complex in which the VO^{2+} ion is coordinated to two water molecules and one citrate via a (RCO_2^-, RO^-) coordination mode. In order to verify this assignment, HYSCORE spectra were recorded for the sample with the 3:1 ratio (citrate:VO^{2+}) (Figure 3.4). The electron-spin-echo-detected EPR spectrum was first recorded to ascertain that the observed electron spin echo stemmed from the monomeric oxovanadate species. The HYSCORE experiments in Figure 3.4 were recorded at the magnetic field position at which almost all spatial orientations are selected. The low-frequency part of the spectrum (Figure 3.4a) shows different peaks. One peak is centered around the ^{14}N Larmor frequency ν_N and indicates the presence of nitrogen nuclei at non-coordinating distances from the vanadium center. Furthermore, a ridge with maximal width of 2.8 MHz is centered around (ν_C, ν_C) and (ν_V, ν_V) with ν_C and ν_V the Larmor frequencies of ^{13}C and ^{51}V, respectively. Although both types of nuclei may contribute to the signal, the ridge seems somewhat better centered around (ν_V, ν_V), indicating the presence of diamagnetic vanadium ions (i.e. V(V)) in the vicinity of the VO^{2+} center. Similar signals have been found in vanadyl-containing systems and been ascribed to oxidation of the V(IV) ions.[101] Note that these signals do not stem from the dimeric $(VO^{2+})_2$ species, where the ^{51}V nuclei have hyperfine couplings in the order of those of the mononuclear complexes. Figure 3.4b shows the HYSCORE spectrum in the area where weak proton hyperfine couplings are expected. A ridge around the (ν_H, ν_H) (ν_H = proton Larmor frequency) can be observed. The maximum extent of this ridge is 6.5 MHz, which agrees with the maximum ^{1}H hyperfine coupling. No stronger hyperfine couplings could be detected. Furthermore, a slight shift of the proton ridge with respect to the anti-diagonal through (ν_H, ν_H) can be seen (Figure 3.4b). This shift can be interpreted in terms of the dipolar hyperfine coupling.[102] The observed shift (0.15 MHz) relates to a dipolar part of the hyperfine tensor of the form [-2.85 -2.85 5.7] MHz. Since the maximum hyperfine component is (in absolute value) 6.5 MHz, the isotropic (Fermi contact) hyperfine coupling is then either 0.7 MHz or -3.65 MHz. The ^{1}H HYSCORE experiment was repeated in deuterated water (Figure 3.4c). The ^{1}H ridge has now significantly reduced in size showing that the largest hyperfine coupling stems from exchangeable protons. The maximum spread of the ^{1}H feature in Figure 3.4c agrees with a maximum coupling of 2.45 MHz for the non-exchangeable CH protons. The ^{1}H hyperfine tensors for the protons of equatorially and axially coordinating water molecules of $[VO(H_2O)_5]^{2+}$ have been reported[89, 90, 103]. The dipolar part of the equatorial water protons is in the order of [-5 -4 9] MHz, while that of the axial protons is [-3 -3 6] MHz. The hyperfine contribution observed here for the closest exchangeable protons resembles more the latter condition. Moreover, the maximum couplings of the equatorial water protons range from 8 to 16 MHz depending on the orientation of the protons with respect to the V=O part. This strongly argues against the assignment of Lodyga-Chruscinska et al.[32], who interpreted the g and ^{51}V hyperfine values of complex 3 in terms of a (RCO_2^-, RO^-) + 2 H_2O equatorial coordination mode. Using the additivity relationship proposed by Chasteen[46], a coordination mode involving three RCO_2^- and one RO^- would lead to ^{51}V A_z value of 489 MHz, while an all R-CO_2^- ligation would give 512 MHz. The observed A_z value of 496 MHz of complex 3 could point to the former coordination mode with an additional water or ROH axial ligation explaining the HYSCORE observed contribution of exchangeable protons.

For the low molar ratio (0.75:1), the EPR features (Figure 3.1) and the spin Hamiltonian parameters of the contributing monomeric complex 1 (Table 3.1) are similar to what we observed previously for a solution of NH_4VO_3 with oxalic acid (3:1) and citric acid (2:1) at pH 5 (Chapter 2).[74] In that chapter, we also showed that the EPR spectrum of a solution of NH_4VO_3 with oxalic acid (3:1) alone is essentially a broad line due to dipolarly interacting vanadyl centers, explaining also the broad background when only a small molar ratio of citric acid is added. According to the additivity relationship proposed by Chasteen[46], the ^{51}V hyperfine values of complex 1 can be interpreted in terms of ligation of VO^{2+} to four R-CO_2^-. According to Buglyo et al. the cis-oxalato-VO^{2+}, $[VO(C_2O_4)_2(H_2O)]^{2-}$, complex with an axial symmetry dominates in an aqueous solution with pH 7. Its anisotropy CW-EPR spectrum and the associated principle g and ^{51}V hyperfine values are determined[99]: $g_x = g_y$ = 1.979, g_z = 1.939, $A_x = A_y$ =184 MHz and A_z = 515 MHz. The g_z and A_z values are identical to those observed for the solution with a molar ratio of 0.75:1, suggesting that

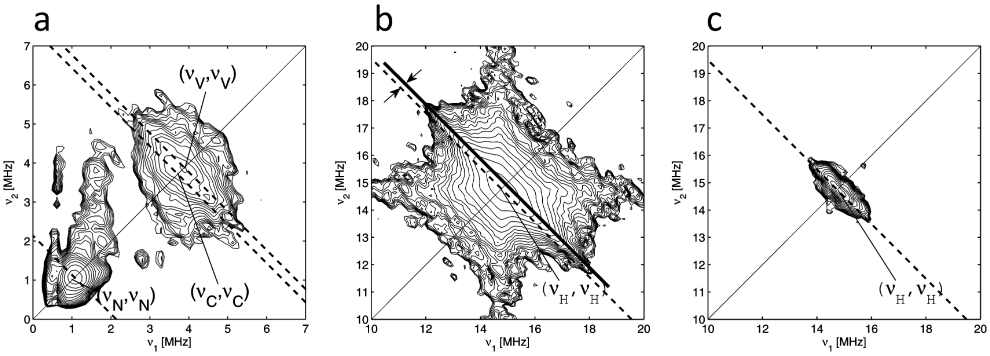

Figure 3.4: Experimental HYSCORE spectra of the frozen solutions with a molar ratio (citrate:VO^{2+}) of 3.00:1 in H_2O (a,b) and ^2H_2O (c) recorded at 4 K at observer position B_0 = 346 mT. (a) Low-frequency area. The anti-diagonals through the Larmor frequency positions of ^{14}N, ^{13}C and ^{51}V are indicated with dashed lines. (b,c) ^1H HYSCORE spectra. The anti-diagonal through the proton Larmor frequency is indicated with a dashed line. In (b) the shift of the proton ridge versus this diagonal is indicated. The HYSCORE spectra are the sum of experiments recorded for interpulse distances τ = 104, 136 and 152 ns.

oxalate is indeed chelating the VO^{2+} unit at the equatorial positions. Thus, complex 1 is probably a cis-oxalato-VO^{2+}, $[VO(C_2O_4)_2]^{2-}$, complex. In order to determine whether axial water ligation is occurring or whether the complex has a distorted square pyramidal geometry, pulsed EPR experiments were performed. However, no electron spin echo could be detected, indicating a very fast spin-spin relaxation. This very fast spin-spin relaxation is in line with the observed broad feature and corroborates the close proximity of VO^{2+} centers. The spin Hamiltonian parameters of monomeric complex 2 found in the solution with the 1.5:1 citrate:VO^{2+} ratio lie between those of complex 1 and complex 3 and may indicate a mixed oxalate/citrate ligation.

To explain the occurrence of mononuclear oxalato-VO^{2+} and mononuclear citrato-VO^{2+} complexes at a molar ratio of 0.75:1 – 1.50:1 and 2.00:1 – 4.50:1, respectively, their ligand exchange equilibrium is examined (Equation 3.1). The formation of citrato-VO^{2+} complexes is favored if (i) oxalate is actively removed from the solution, which is pursued in this work by its precipitation as $(NH_4)_2C_2O_4$ with an estimated solubility product of 1.85 10^{-4} (Equation 3.2) and (ii) a significant amount of citrate is present in the solution ($\geq$ 2:1).

$$[VO(C_2O_4)_2]^{2-} + 3\,R_iCO_2^- + R_jOH \rightleftharpoons [VO(R_iCO_2)_3(R_jOH)]^- + 2\,C_2O_4^{2-} \tag{3.1}$$

$$(NH_4)_2C_2O_4(s) \rightleftharpoons C_2O_4^{2-} + 2\,NH_4^+ \tag{3.2}$$

3.2.2 FTIR

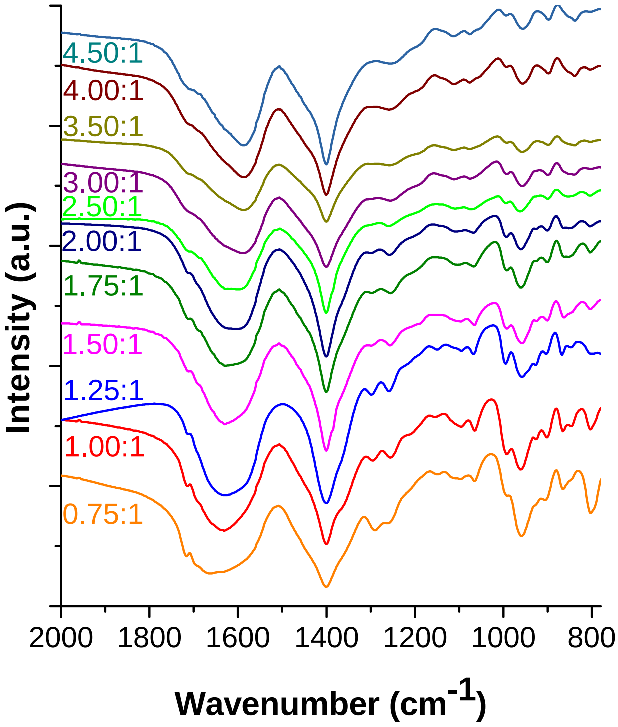

Figure 3.5: FTIR spectra of gels, obtained after drying at 60 °C, from the aqueous solutions with a molar ratio (citrate:VO^{2+}) ranging between 0.75:1 and 4.50:1.

To support the structure of the observed oxalato-VO^{2+} and citrato-VO^{2+} complexes, gels of the solution with a molar ratio ranging between 0.75:1 and 4.50:1 were prepared by drying at 60 °C and analyzed by FTIR spectroscopy (Figure 3.5). All spectra exhibit the typical vibrations associated with an ammonium bridged network of carboxylato-VO^{2+} complexes.[75, 92, 94, 95] Firstly, all spectra show a strong absorption band between 3400 and 2800 cm^{-1} (not shown) due to (i) the O-H stretching mode of H-bonded hydroxyl groups and absorbed H_2O molecules, (ii) the N-H stretching mode of the ammonium ions and (iii) the C-H stretching mode of the citrate's methylene groups. The absorption bands, corresponding to the O-H and N-H stretching modes, are broadened by H-bridge formation and the individual stretching modes are not resolved. At 1715 cm^{-1}, the C=O stretching mode, $\nu(C = O)$, associated with carboxylic acid groups (-COOH) is present, indicating that in all gels a minor fraction of the acidic groups is still protonated. Between 1670 and 1585 cm^{-1} the asymmetric carboxylate stretch vibrations $\nu_{as}(COO^{-})$, for metal-carboxylates and ammonium-carboxylates, is detected. In this region, the only variation in the FTIR spectra of the different gels occurs. The gels originating from the solutions with a molar ratio ≤

1.75:1 demonstrate a local absorbance maximum at 1670 cm^{-1}, while those with a molar ratio $\geq$ 3.00:1 exhibit this local maximum at 1585 cm^{-1}. The FTIR spectra of gels obtained from the solutions with a molar ratio between 1.75:1 and 3.00:1 rather show a plateau with an equal absorbance at 1670 and 1585 cm^{-1}. Thus as the molar ratio increases, and the oxalato-VO^{2+} complexes are exchanged for citrato-VO^{2+} complexes, the position of the $\nu_{as}(COO^{-})$ for VO^{2+}-carboxylates shifts. In the case of oxalate, Baruah et al. and Mohamed et al. report the $\nu_{as}(COO^{-})$ around 1670 cm^{-1}.[104, 105] In the case of citrate, though, Kaliva et al. and Djordjevic et al. report the $\nu_{as}(COO^{-})$ around 1585 cm^{-1}.[65, 95] Around 1400 cm^{-1}, all gels show a strong absorbance peak which is assigned to the symmetric carboxylate stretch vibrations, $\nu_{s}(COO^{-})$, for metal-carboxylates and to the ammonium deformation, $\delta(NH_4^{+})$. Note that no significant shift in the position of this $\nu_{s}(COO^{-})$ is observed as a function of the molar ratio or depending on the dominating VO^{2+} chelating ligand. At 960 cm^{-1}, the vanadyl stretching mode, $\nu(V^{4+} = O)$, is observed in all the gels.

In conclusion, CW-EPR, pulsed EPR and FTIR spectra indicate three situations, depending on the molar ratio (citrate:VO^{2+}). (i) At a low molar ratio (i.e. 0.75:1), monomeric cis-oxalato-VO^{2+} complexes occur with a distorted square pyramidal geometry. (ii) At high molar ratio (i.e. 2:1 and up), mono- and dimeric citrato complexes are observed. The monomeric citrato complex dominates (abundance $\geq$ 80 %) and is characterized by sixfold chelation of the vanadium(IV) ion by a RCO$_2^-$ ligation at the equatorial positions and a H$_2$O/R-OH ligation at the axial position. (iii) At a molar ratio of 1.5:1, the spin Hamiltonian parameters lie between those of monomeric complex 1 and monomeric complex 3 and indicate a mixed oxalate/citrate ligation.

3.3 Reactivity

For all solutions, no ^{51}V-NMR signals could be detected immediately after the synthesis, suggesting that the vanadium species are paramagnetic with a +IV oxidation state for the vanadium ion.[58] However, as a function of time (in days), peaks in the ^{51}V-NMR spectra appear, indicating that the vanadium ion oxidizes from a +IV to a +V oxidation state. Note that the HYSCORE spectrum (Figure 3.4a) already indicated the presence of diamagnetic vanadium ions (i.e. V(V)) in the vicinity of a VO^{2+} center. In this section, the reactivity of the oxalato-VO^{2+} and citrato-VO^{2+} complexes is studied as a function of time (age) for the aqueous solutions with a molar ratio of 0.75:1, 2.00:1 and 3.00:1. The ^{51}V-NMR spectra of the considered solutions are presented in Figure 3.6. The solution with a molar ratio of 0.75:1 already shows the onset of a peak at -535 ppm after 1 day. For the solutions with a molar ratio of 2.00:1 and 3.00:1 appearance of such a peak is delayed till 3 days after synthesis. In case of the 2.00:1 solution a peak is observed at -535 ppm and at -546 ppm, while the 3.00:1 solution only exhibits a peak at -546 ppm. For all solutions, the observed peak onsets evolve to clear signals within 10 days. From this point on, the peaks continuously grow and no retardation is observed up to 136 days after synthesis. Note that for the

0.75:1 solution, a second peak appears 17 days after synthesis at -545 ppm. Thus, the V(IV) species present in the solutions significantly oxidize to V(V) as a function of time ageing (days).

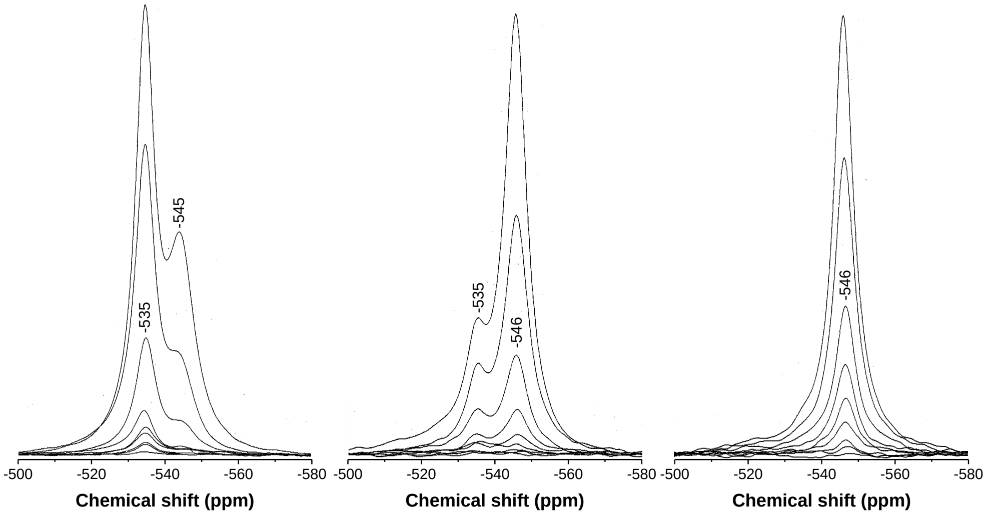

Figure 3.6: ^{51}V-NMR spectra of the solutions with a molar ratio of 0.75:1 (left, vertical scale = 2500), 2.00:1 (middle, vertical scale = 5000) and 3.00:1 (right, vertical scale = 7500). The spectra are plotted with an increasing age after synthesis (1, 2, 3, 6, 10, 17, 31, 73 and 136 days).

The signal evolution of the two chemical shifts observed differs for each solution, for example after a time ageing of 136 days:

1. The ^{51}V-NMR spectra of the 0.75:1 solution is dominated by the peak at -535 ppm which can be assigned, according to Ehde et al., to oxalato-VO_2^+ (i.e. $[VO_2(C_2O_4)_2]^{3-}$)[106]. In this complex, the vanadium(V) ion is chelated by two bidentate oxalate ligands and two oxygen atoms forming the dioxovanadate(V) center. An alternative assignment could be HVO_4^{2-} but this species is typically observed in other solution circumstances (i.e. 8.5 ≤ pH ≤ 11 and [V] ≤ 10 mM).[58, 80] The second peak at -545 ppm manifests as a shoulder of the oxalato-VO_2^+ peak and can be assigned to a dinuclear citrato-VO_2^+ complex (either as $[V_2O_4(C_6H_5O_7)_2]^{4-}$ or as $[V_2O_4(H_2O)_2(OH)(C_6H_5O_7)]^{3-}$).[70] Both citrato-$VO_2^+$ complexes are featured by two VO_2^+ centers allied by a double V-O-V bridge into a $[O_2V<O,O>VO_2]$ unit.[29, 65, 70, 71] The bridging oxygen originates from citrate's α-hydroxyl functionality or from the hydroxo ligand. Thus, the oxidized vanadium(V) species in the 0.75:1 solution are dominated by the presence of oxalato-VO_2^+. Based on the peak height, its molar excess with respect to the citrato-VO_2^+ is about 2.5:1.

2. In the ^{51}V-NMR spectra of the aged 2.00:1 solution, the opposite holds true. The

peak at -546 ppm, assigned to the dinuclear citrato-VO_2^+, dominates while the peak at -535 ppm, assigned to oxalato-VO_2^+, appears as a shoulder. Here, the oxidized vanadium(V) species are mainly citrato-VO_2^+ with an estimated molar excess of 3.0:1.

3. The ^{51}V-NMR spectra of the aged 3.00:1 solution do not show a peak associated with oxalato-VO_2^+ species. The only peak observed corresponds to dinuclear citrato-VO_2^+ at a chemical shift of -546 ppm.

Thus, so far it seems that all solutions exhibit a vanadium(IV) to vanadium(V) oxidation and that the initial dominating chelation in the VO_2^+ complexes (observed by EPR in the previous paragraph) remains also the dominating chelation in the VO_2^+ complexes upon time ageing. The 0.75:1 solution shows oxalato-VO_2^+ complexes as the dominating species shortly after its synthesis (EPR) and the dominating presence of oxalato-VO_2^+ complexes after 136 days of time ageing (^{51}V-NMR). On the other hand, the 3.00:1 solution exhibits only citrato-VO_2^+ complexes shortly after its synthesis and only citrato-VO_2^+ complexes after 136 days of time aging.

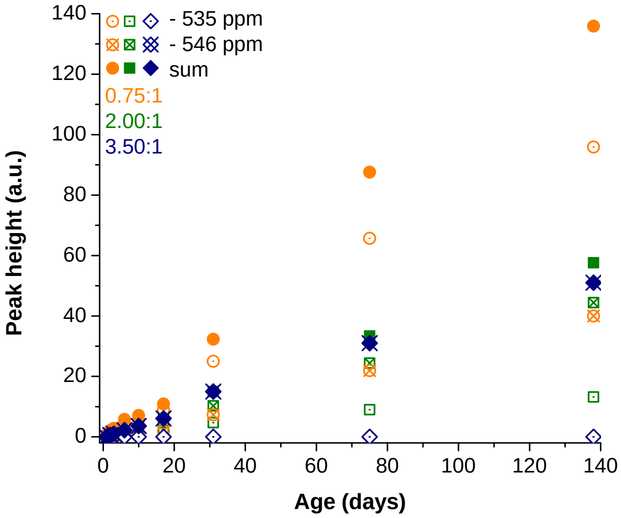

Figure 3.7: Evolution of the peak height (at -535 ppm, -546 ppm and their sum) in the ^{51}V-NMR spectra (plotted with a vertical scale of 1000) recorded on the solutions with a molar ratio (citrate:VO^{2+}) of 0.75:1, 2.00:1 and 3.50:1 as a function of ageing time. All solutions were stored in closed NMR tubes filled with air. Note that for the 3.50:1 solution, no signal is observed at -535 ppm which leads to the coincidence of the sum and -546 ppm data points.

To compare the oxidation rates of the above described solutions, the peak heights are plotted as a function of ageing time in Figure 3.7. As mentioned earlier, during the first 17 days, the vanadium(IV) oxidation is rather limited and comparing the oxidation rates is rather speculative. However between an age of 17 and 136 days, clear differences can be observed in the oxidation rate between the studied solutions. The total oxidation rate (indicated by the sum) is clearly the highest for the 0.75:1 solution with the dominating presence of oxalato-VO^{2+} complexes. The total oxidation rate for the 2.00:1 and 3.00:1 solution is rather similar with a slightly higher oxidation rate for the 2.00:1 solution. Interestingly, comparing the three solutions at a certain age (i) a large difference can be observed for the peak height associated with the oxalato-VO$_2^+$ complex (-535 ppm) and (ii) a quite similar height is observed for the peak associated with the citrato-VO$_2^+$ complex (-546 ppm). Thus difference in the total oxidation rate (i.e. highest for the 0.75:1 solution and lowest for the 3.00:1 solution) is only determined by the oxidation rate of the oxalato-VO$_2^+$ complexes which has the highest concentration in the 0.75:1 solution and the lowest concentration in the 3.00:1 solution. The citrato-VO^{2+} oxidation rate is independent of its concentration and has a marginal effect on the difference in the total oxidation rate.

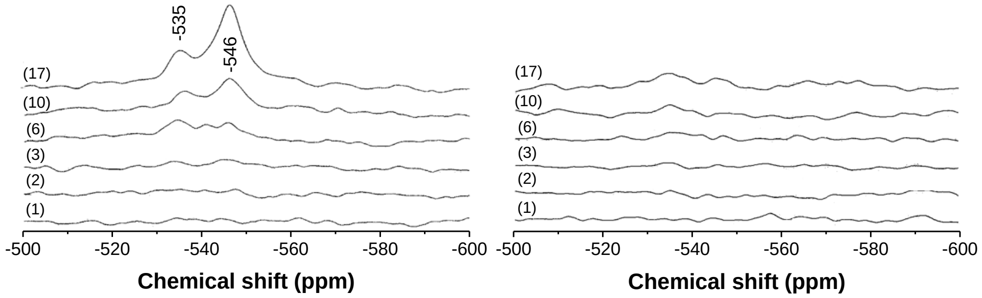

Figure 3.8: ^{51}V-NMR spectra of a 2.00:1 citrate:VO^{2+} solution after 1, 2, 3, 6, 10 and 17 days of synthesis. Left: spectra of a solution conserved in a closed NMR tube under air. Right: spectra of an identical solution but for which the dissolved O_2 was removed by intensive N_2 bubbling, followed by conservation in a closed NMR tube filled with N_2.

To identify the oxidizing agent, the aging of the 2.00:1 solution is studied (i) as conserved in a closed NMR tube filled with air and (ii) after evacuation of the dissolved O_2 by intensive N_2 bubbling and conservation in a closed NMR tube filled with N_2. The ^{51}V-NMR spectra of the 2.00:1 solution kept under air and N_2 are given in Figure 3.8. From these spectra it is clear that the peaks associated with oxalato-VO$_2^+$ and citrato-VO$_2^+$ complexes appear earlier under air and that their rate of growth is higher under air. This suggests that the dissolved O_2 – which is either present directly after the synthesis or replenished from the ambient – causes the vanadium(IV) oxidation. A possible reduction mechanism of dissolved O_2 into H_2O_2 is suggested by Pourbaix et al. and is characterized by a reduction potential between 0.1 V and 0.5 V (vs. SHE) depending on the p_{O_2}:[H_2O_2] ratio.[43]

In summary, the stability of oxalato-VO^{2+} and citrato-VO^{2+} complexes, present as dominating species in aqueous solutions with low (0.75:1) and higher (2.00:1 to 3.00:1) citrate:VO^{2+} molar ratio is studied. All complexes react with the dissolved O_2 in a redox reaction causing the oxidation of the vanadium(IV) into the vanadium(V). The onset of oxidation is observed during the first week, but no resolved difference is observed between both complexes. After 17 days, the oxidation rate is the highest for the solution with the oxalato-VO^{2+} complexes as dominating species. For solutions in which the citrato-VO^{2+} complexes dominate (2.00:1 and 3.00:1), no further difference in oxidation rate is detected. After a significant ageing time (e.g. 136 days) the ratio of the VO_2^+ complexes present in the aged solution (i.e. oxalato-VO_2^+ versus citrato-VO_2^+), as observed by ^{51}V-NMR, reflects the initial VO^{2+} complexes (i.e. oxalato-VO^{2+} versus citrato-VO^{2+}), as observed by EPR, present shortly after their synthesis. Finally, the reactivity of VO^{2+} complexes can be drastically retarded by evacuation of dissolved O_2 and subsequent storage under a N_2 ambient.

3.4 Conclusions

Aqueous solutions of oxalato- and citrato-VO^{2+} complexes are successfully prepared and the ligand exchange reaction is investigated as a function of the molar ratio of citrate to $[VO(C_2O_4)_2]^{2+}$ via EPR (CW and HYSCORE) and FTIR spectroscopy. At a low molar ratio (i.e. 0.75:1), monomeric cis-oxalato-VO^{2+} complexes occur with a distorted square pyramidal geometry. As the amount of citrate increases, oxalate is gradually exchanged for citrate leading to a VO^{2+} complex with a mixed oxalate/citrate ligation (1.5:1) or an exclusive citrato ligation (2:1 or higher). In the latter case, both mono- and dimeric citrato complexes are observed. However, the monomeric citrato complex dominates (abundance $\geq$ 80 %) and is characterized by sixfold chelation of the vanadium(IV) ion by a RCO_2^- ligation at the equatorial positions and a H_2O/R-OH ligation at the axial position. The oxalato-VO^{2+} and citrato-VO^{2+} complexes show a different redox reactivity towards the dissolved O_2 in the aqueous solution. During the first week after synthesis, a non-resolved onset of oxidation is observed for both complexes. After 17 days, the oxidation rate is the highest for the oxalato-VO^{2+} complexes. If citrato-VO^{2+} complexes dominate, no further difference between the oxidation rates is detected as more citrate is present in the solution. The reactivity of the VO^{2+} complexes can be drastically retarded by evacuation of the dissolved O_2 and subsequent storage in a N_2 ambient.

Part II

UNDERSTANDING THE THERMAL DECOMPOSITION PATHWAY OF THE AMMONIUM-CITRATO/OXALATO-VO^{2+} GEL

Chapter 4

Thermal decomposition of the solution's constituents

In this part the thermal decomposition pathway of the ammonium-citrato/oxalato-VO^{2+} gel, obtained by drying of the associated aqueous solution at 60 °C, is discussed. As stated in the objectives and targeted to state a relation between the composition of the VO^{2+} complexes and the vanadium oxide stoichiometry/phase formation, it is important to understand these thermally-induced transformations. The thermal decomposition pathway of the ammonium-citrato/oxalato-VO^{2+} gel, obtained by evaporation of the precursor solution, will be studied via (i) simultaneous Thermogravimetric - Differential Scanning Calorimetry (TG-DSC), (ii) hyphenated Thermogravimetric - Mass Spectrometry (TG-MS) and (iii) ex-situ analysis of the remaining product by Fourier Transform Infrared (FTIR) spectroscopy. For convenience, this part is divided in three chapters with to goal the understand the thermal decomposition pathway:

- Constituents of the aqueous citrato/oxalato-VO^{2+} solutions
- Ammonium-oxalato-VO^{2+} gel
- Ammonium-citrato-VO^{2+} gel

This chapter will focus on the analysis of the thermal decomposition pathway of the solution's constituents: citric acid, oxalic acid, the metal-free ammonium citrate and the metal free ammonium oxalate.

4.1 Citric acid

Figure 4.1 shows the thermal decomposition profile of citric acid in air, studied at a heating rate of 10 °C min^{-1}. Citric acid's weight loss can be divided into two regions: (i) between 100 °C and 288 °C and (ii) between 300 °C and 450 °C. The first decomposition step accounts for a weight loss of about 93 % and is associated with a decrease in the heat flow with respect to its background value. The decreased heat flow suggests a sequence of decomposition reactions with an overall endothermic nature. The maximum decomposition rate is observed at 228 °C. In the second step, the remaining 7 % is decomposed in an exothermic reaction, as evidenced by the increased heat flow. This final weight loss is more gradual and has a maximum decomposition rate at about 425 °C.

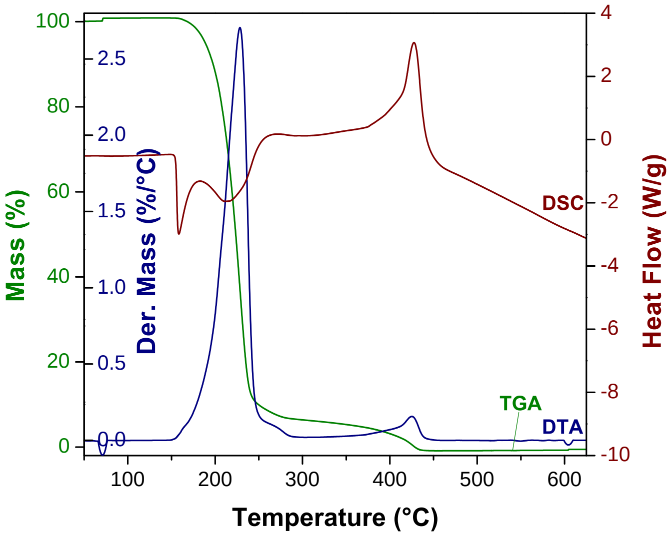

Figure 4.1: TGA (Mass %), DTA (Der. Mass) and DSC (Heat Flow) analysis of citric acid studied in dry air at a heating rate of 10 °C min^{-1}.

Citric acid's decomposition mechanism is detailed studied by Rajendran et al. and Van Werde et al. via HT-DRIFT (High Temperature - Diffuse Reflectance Infrared Fourier Transform) spectroscopy and on-line coupled TG-EG (ThermoGravimetric - Evolved Gas) analysis.[86, 107, 108] Figure 4.2 shows citric acid's endothermic decomposition mechanism. This decomposition occurs through a sequence of endothermic dehydroxylation and decarboxylation reactions sequentially forming aconitic acid, itaconic acid, itaconic anhydride and citraconic anhydride.[86, 108] The first dehydroxylation, i.e. citric acid's transformation to the unsaturated aconitic acid, already occurs at 150 °C and corresponds to the sharp decrease in the heat flow, emphasizing the strong endothermic nature of thus dehydroxylation. This aconitic acid is next subjected to a decarboxylation and a second dehydroxylation reaction forming the itaconic anhydride. This transformation is expected at about 165 °C. As the temperature increases to 180 °C, the double bound rearranges and the citraconic anhydride is formed. Both anhydride compounds evaporate above 210 °C in dry air which ends the sequence of citric acid's endothermic decomposition reactions. Finally, between 300 °C and 450 °C, with a decomposition rate maximum at 425 °C, the remaining thermo stable compounds (i.e. 7 %) exothermally decompose into H_2O and CO_2.[86, 107–109]

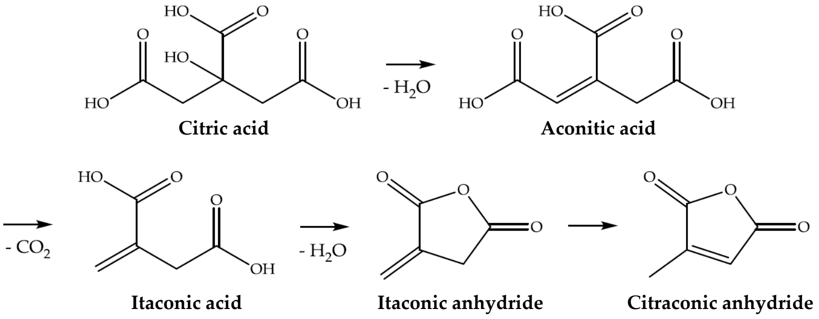

Figure 4.2: Schematic representation of the thermal, endothermic decomposition of citric acid at a heating rate of ~ 10 °C min^{-1}. The mechanism is based on references [86, 108].

4.2 Metal ion free ammonium citrate gel

As evident from the thermal profile in Figure 4.3, the metal ion free ammonium citrate is thermally more stable and the final oxidative decomposition step occurs at a higher temperature (~ 515 °C).[108] Similar to the thermal decomposition of the citric acid, the first set of decomposition reactions (i.e. ≤ 350 °C) are endothermic and non-oxidative while the second set of decomposition reactions (i.e. ≥ 350 °C) are exothermic and oxidative.

Below 100 °C, a small weight loss is sometimes observed and is ascribed to the evaporation of residual water remaining after the drying of the aqueous solution. At 155 °C, the dehydroxylation of the α-hydroxyl functionality occurs, forming ammonium aconitate from the ammonium citrate. Simultaneously, the ammonium carboxylate groups present in the gel convert to carboxylic acid and NH_3 (Equation 4.1), forming citric acid and aconitic acid.[86]

$$R\text{–}CO_2^- \cdots H^+\text{–}NH_3 \longrightarrow R\text{–}CO_2H + NH_3 \tag{4.1}$$

Between 160 °C and 220 °C, the largest weight loss is observed with its maximum decomposition rate at 180 °C. In this step, CO_2 is released during the endothermic and non-oxidative decarboxylation of the formed carboxylic acid groups resulting in the itaconic acid. Additionally the second, non-oxidative and endothermic dehydroxylation reactions occurs in this temperature interval forming the itaconic and

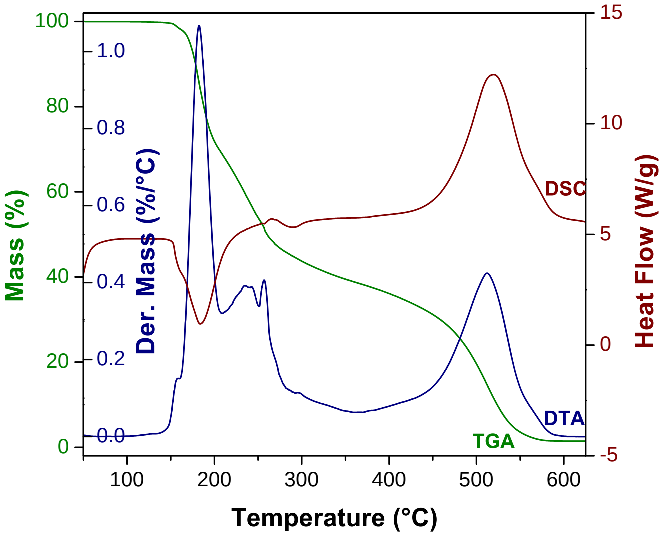

Figure 4.3: TGA (Mass %), DTA (Der. Mass) and DSC (Heat Flow) analysis of the metal ion free ammonium citrate gel studied in dry air.

citraconic anhydride. These anhydrides evaporate at ~ 235 °C and result in a small weight loss.

Besides these dehydroxylation and decarboxylation reactions, also solid primary amides are formed (around 170 °C) probably originating from the reaction between NH_3 and carboxylic acid groups. These amides evaporate around 260 °C and are typically detected as the $NH_2{-}C(OH){=}CH_2^+$ fragment.[110] Between 270 °C and 400 °C a continuous, small weight loss, assigned to a further decarboxylation or evaporation of the few remaining carboxylic acid groups or amides, is observed.

In an oxidative ambient, several exothermic decomposition reactions appear starting from 400 °C. These exothermic oxidation reactions coincide and are characterized by a maximum decomposition rate at 510 °C. As a temperature of 600 °C is reached, all organic fragments are decomposed and no further weight loss is observed. A first reaction is the dehydration of an amide to an aliphatic nitrile which either evaporates or further reacts to hydrogen cyanide (HCN). Besides the evaporation of the aliphatic nitrile, HCN and NH_3, also NO_2 is formed by oxidation of the remaining nitrogen-containing compounds. In a second reaction all residual organics burn and a significant amount of CO_2 is released.

4.3 Oxalic acid dihydrate

Figure 4.4 shows the weight loss, its derivative and the associated heat flow of oxalic acid dehydrate upon heating at 10 °C min^{-1}. Note that the entire decomposition pathway is associated with a decreased heat flow, suggesting that the pathway is entirely endothermic. The thermal decomposition proceeds through two steps. (i) The first weight loss occurs between room temperature and 110 °C with its maximum decomposition rate around 92 °C. In this step a weight loss of 29 % is observed. Assuming that the first step is only associated with the evaporation of the hydrate molecules, its number per formula unit corresponds to 2. (ii) The second weight loss proceeds between 110 °C and 200 °C and corresponds to the decomposition of the remaining product with a weight percentage 71 %. The maximum decomposition rate occurs around 190 °C. Muraishi et al have studied the thermal behavior of various dicarboxylic acids and confirm the one step decomposition of hydrate-free oxalic acid between 110 °C and 200 °C.[111] In this temperature range, oxalic acid is transformed to formic acid (HCO_2H) with the release of CO_2. This formic acid subsequently decomposes into CO and H_2O. In an oxidative atmosphere, the CO is further oxidized to CO_2, resulting in the following over-all, oxidative decomposition reaction of oxalic acid (Equation 4.2).

$$2\,C_2H_2O_4 + O_2 \longrightarrow 4\,CO_2(g) + 2\,H_2O(g) \tag{4.2}$$

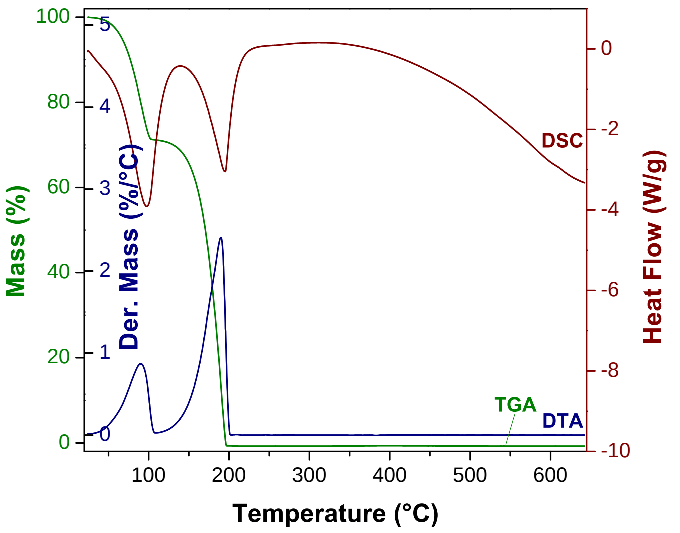

Figure 4.4: TGA (Mass %), DTA (Der. Mass) and DSC (Heat Flow) analysis of oxalic acid dihydrate studied in dry air at a heating rate of 10 °C min^{-1}.

4.4 $(NH_4)_2C_2O_4$ precipitate

In the synthesis of the aqueous, oxalate-poor citrato-VO^{2+} solution, $(NH_4)_2C_2O_4$ crystals precipitate (section 2.3). FTIR analysis showed that these crystals are VO^{2+}-free (Figure 2.13). In this section, these dried crystals are grinded and used in the thermal decomposition study of the VO^{2+}-free ammonium oxalate.

The thermal decomposition pathway of $(NH_4)_2C_2O_4 \cdot xH_2O$ is studied in dry air and in N_2. Figure 4.5 shows its weight loss, the derivative of its weight loss and the associated heat flow as a function of temperature. All the curves (i.e. weight loss, derivative of the weight loss and the heat flow) are identical for the analysis of $(NH_4)_2C_2O_4 \cdot xH_2O$ in dry air and in N_2. This suggests that the entire thermal decomposition pathway is non-oxidative. Also note that the final weight (e.g. at 500 °C) is 0 % which indicates that the $(NH_4)_2C_2O_4 \cdot xH_2O$ is completely transformed into gaseous species during the thermal decomposition. The decomposition pathway itself consist of two dominating steps. A first weight loss (of 12.9 %) is observed between 60 °C and 110 °C with its its maximum decomposition rate at 95 °C. The second weight loss is observed between 160 °C and 240 °C and accounts for a weight loss of 85.1 %. The maximum decomposition rate of this step is observed at 230 °C. The remaining mass (i.e. 2.0 %) is gradually removed from the sample between 240 °C and 500 °C.

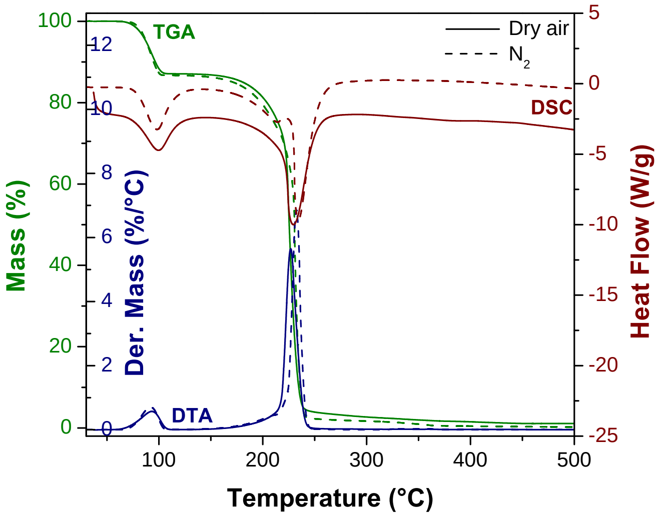

Figure 4.5: TGA (Mass %), DTA (Der. Mass) and DSC (Heat Flow) analysis of the dried $(NH_4)_2C_2O_4$ precipitate, originated from the synthesis of the citrato-VO^{2+} solution. The analysis is performed in dry air and in N_2 at a heating rate of 10 °C min^{-1}.

To elucidate the exact decomposition pathway of the $(NH_4)_2C_2O_4$ precipitate in both dry air and N_2, mass fragments of the evolved gasses are followed as a function of the temperature. Figures 4.6 and 4.7 show the significant mass fragments[1] evolved during the thermal decomposition of the $(NH_4)_2C_2O_4$ in dry air and in N_2 respectively. A tentative assignment of these mass fragments is given in Table 4.1.

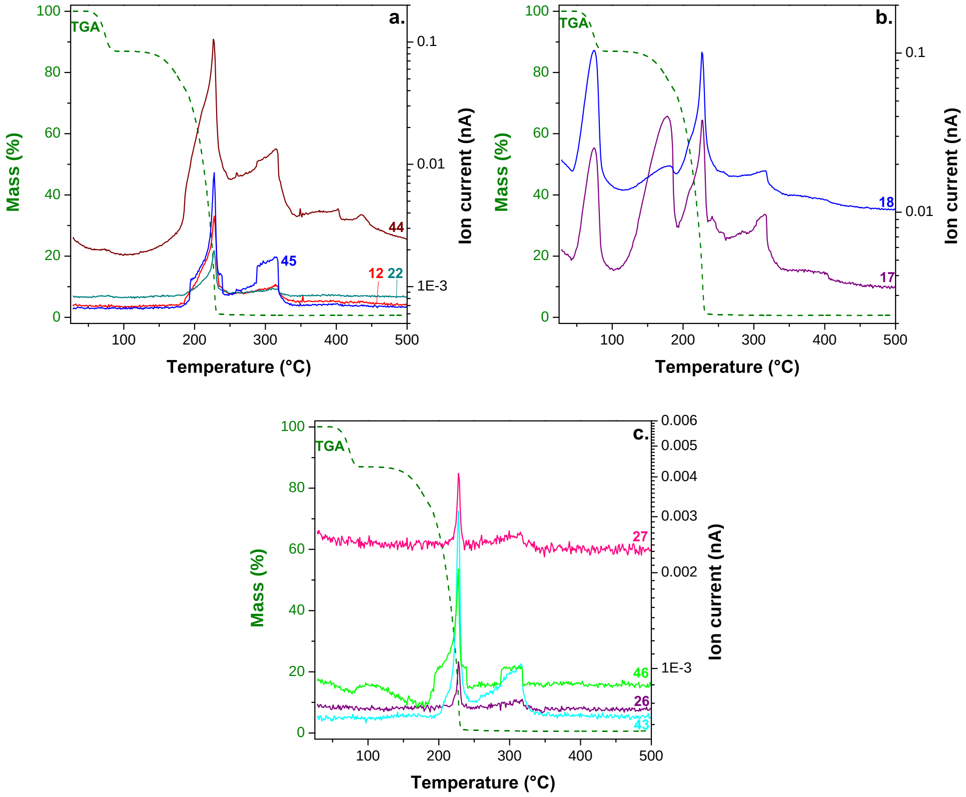

Figure 4.6: TGA-MS profile in dry air of $(NH_4)_2C_2O_4 \cdot xH_2O$ at a heating rate of 10 °C min^{-1}: fragments related to the carboxylate groups (a.), to H_2O and/or NH_4^+ (b.) and to the interaction between carboxylic acid groups and NH_3 (c.). Only the relevant fragments in the m/e = 5-70 region are shown (Ion currents). Note that each sub-figure has its own Ion current scale.

In dry air, the first weight loss with its maximum decomposition rate at 95 °C results in the increase of the mass fragments m/e = 17 (OH^+ or $NH_3^{+\cdot}$) and m/e = 18 ($H_2O^{+\cdot}$ or NH_4^+). These mass fragments originate from water molecules. Assuming that

---

[1] The mass fragments labeled as *significant* are the only mass fragments which exhibit a significant temperature-dependent ion current. The other fragments in the indicate region are detected as well, but no significant temperature-dependence is observed. This expression will be, systematical, used in this work.

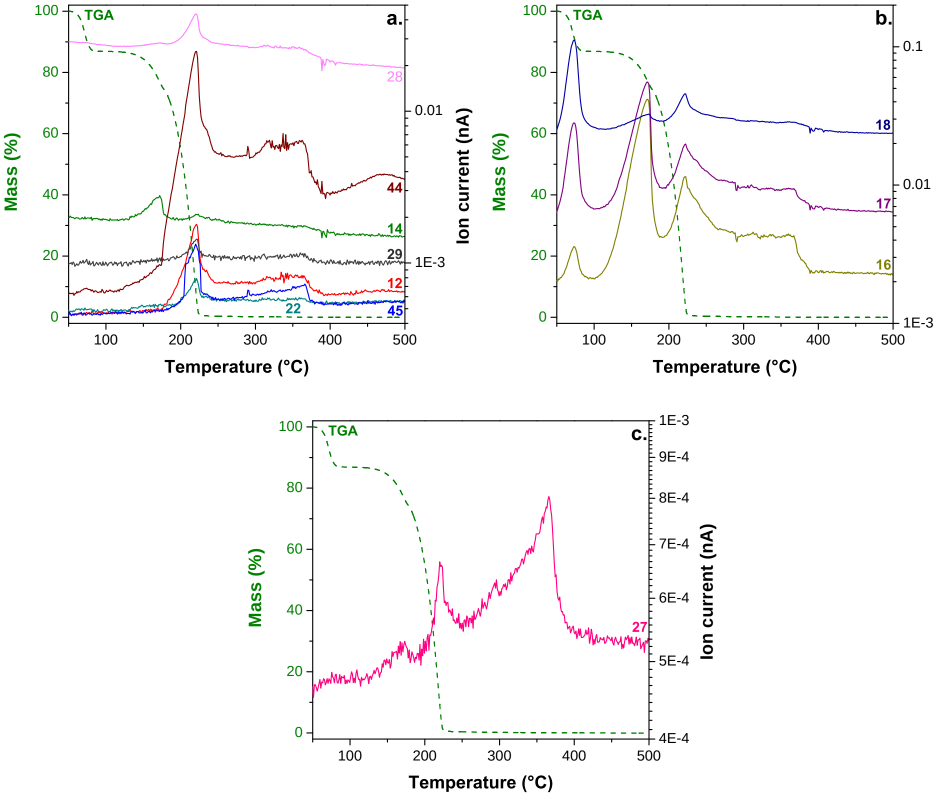

Figure 4.7: TGA-MS profile in N_2 of $(NH_4)_2C_2O_4 \cdot xH_2O$ at a heating rate of 10 °C min^{-1}: fragments related to the carboxylate groups (a.), to H_2O and/or NH_4^+ (b.) and to the interaction between carboxylic acid groups and NH_4^+ (c.). Only the relevant fragments in the m/e = 5-70 region are shown (Ion currents). Note that each sub-figure has its own Ion current scale.

the first and second weight loss corresponds to the volatilization of water molecules (with a molar mass of x 18.02 g mol^{-1}) and the non-hydrated ammonium oxalate (with a molar mass of 124.12 g mol^{-1}) respectively, the average number of hydrate molecules per $(NH_4)_2C_2O_4 \cdot xH_2O$ molecule is calculated: x = 1.04.

During the second, dominating decomposition step between 160 °C and 240 °C in dry air and N_2, the mass fragments associated with the release of H_2O and NH_3 remain (i.e. m/e = 17, 18 in dry air and m/e = 16, 17, 18 in N_2). Additionally, a strong increase in the mass fragment m/e = 44 ($CO_2^{+\cdot}$) can be observed in both dry air and N_2. This mass fragments is unambiguously related to the emission of CO_2. The increase in its ion current with respect to the background value is four times higher in dry air than in N_2 (0.103 nA in dry air and 0.024 nA in N_2). Besides the dominating CO_2 mass fragment (i.e. $CO_2^{+\cdot}$), also the mass fragments m/e = 22 and 45 are observed and

m/e	Fragments
12	$C^{+\cdot}$
14	CO^{++}
16	$O^{+}, O_2^{++}, NH_2^{+}$
17	$OH^{+}, NH_3^{+\cdot}$
18	$H_2O^{+\cdot}, NH_4^{+}$
22	CO_2^{++}
26	CN^{+}
27	$HCN^{+\cdot}$
28	$CO^{+\cdot}$
29	$^{13}CO^{+\cdot}$
43	$HNCO^{+\cdot}, C_2H_5N^{+}$
44	$CO_2^{+\cdot}$
45	$^{13}CO_2^{+\cdot}$
46	NO_2^{+}

Table 4.1: Significant mass fragments in the TGA-MS of the dried $(NH_4)_2C_2O_4 \cdot xH_2O$ precipitate. The tentative assignments are based on reference [86, 94, 108, 110, 112].

ascribed to the evolution of CO_2 by its assignment to CO_2^{++} and $^{13}CO_2^{+\cdot}$ respectively. In addition, a small increase in the mass fragment m/e = 12 ($C^{+\cdot}$) is observed. Only in N_2 the mass fragments m/e = 14, 28 and 29, assigned to CO^{++}, $CO^{+\cdot}$ and $^{13}CO^{+\cdot}$ respectively, arise. These fragments originate from the release of CO between 160 °C and 240 °C. Also, little amounts of the mass fragments m/e = 27, 43 and 44 are formed and are possibly due to gaseous species originated from the rearrangement of the ammonium carboxylate groups in the $(NH_4)_2C_2O_4 \cdot xH_2O$.

In conclusion, the two-step thermal decomposition pathway of the $(NH_4)_2C_2O_4{\cdot}xH_2O$ can be ascribed as follows:

1. Evaporation of the water ligands or a further drying of the precipitate at $\sim$ 95 °C with the release of H_2O and NH_3.
2. The actual $(NH_4)_2C_2O_4$ is transformed into gaseous species with its maximum decomposition rate at 225 °C. Based on the evolved mass fragments the following sequence of non-oxidative reactions can be suggested[92]:
    - The transformation of $(NH_4)_2C_2O_4$ to $H_2C_2O_4$ and gaseous NH_3,
    - The decomposition of $H_2C_2O_4$ to H_2CO_3 and gaseous CO,
    - The disintegration of H_2CO_3 into gaseous H_2O and gaseous CO_2.

In N_2, all the gaseous species are observed by the presence of the mass fragments m/e = 14 (CO^{++}), 16 (NH_2^{+}), 17 (OH^{+} and $NH_3^{+\cdot}$), 18 ($H_2O^{+\cdot}$ and NH_4^{+}), 22 (CO_2^{++}), 28 ($CO^{+\cdot}$), 29 ($^{13}CO^{+\cdot}$), 44 ($CO_2^{+\cdot}$) and 45 ($^{13}CO_2^{+\cdot}$). However, in dry air, the fragments associated with the release of CO are not observed, but the ion currents of the mass fragments associated with CO_2 are quadrupled. By the abundant presence of O_2 in dry air, the CO might be further oxidized towards CO_2 explaining the absence of CO and the increase in the emission of CO_2.

4.5 Conclusion

In this chapter, the thermal decomposition pathway of the major solution's constituents are described. These insights are of importance during the elaboration on the thermal decomposition pathway of the ammonium-citrato-VO^{2+} or ammonium-oxalato-VO^{2+} gel in the following chapters.

Chapter 5

Thermal decomposition of ammonium-oxalato-VO^{2+}

Before elaborating on the thermal decomposition pathway of the ammonium-oxalato-VO^{2+} gel, the species, possibly present in the gel are listed. As indicated in Figure 2.2 and in the experimental section (section C.1.3), the pH value of the ammonium-oxalato-VO^{2+} solution equals 7. Sine this value largely exceeds oxalic acid's pKa_2 value (i.e. 4.2[72]), all carboxylic acid groups are assumed deprotonated into carboxylate groups. These carboxylate groups interact, electrostatically, with the present VO^{2+} or NH_4^+ cations. This yields the following chelating possibilities for the oxalate ion:

- a bidentate chelation with one VO^{2+} ion: oxalato-VO^{2+},
- a bidentate chelation with one NH_4^+ ion: oxalato-NH_4^+,
- a bridging between two VO^{2+} ions: μ-oxalato-$(VO^{2+})_2$,
- a bridging between two NH_4^+ ions: μ-oxalato-$(NH_4^+)_2$,
- a bridging between one VO^{2+} ion and one NH_4^+ ion: μ-oxalato-(NH_4^+,VO^{2+}).

5.1 Weight loss and heat flow

Figure 5.1 shows the thermal decomposition profile of the ammonium-oxalato-VO^{2+} gel heated at 10 °C min^{-1} in a dry air and N_2. In both conditions, the weight loss occurs through a sequence of steps. Up to 250 °C, the thermal decomposition pathway consists of two steps with its maximum decomposition rate around 153 °C and 235 °C, respectively. Both steps are characterized by a decrease in the heat flow with respect to its background level. Therefore, both steps are considered as non-oxidative and endothermic. Besides, a slightly higher weight loss in dry air, the

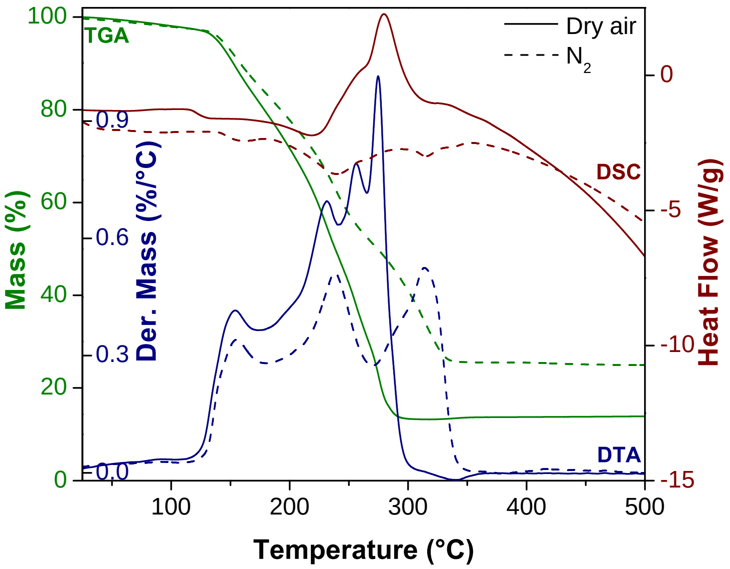

Figure 5.1: TGA (mass %), DTA (mass derivative) and DSC (heat flow) analysis of the ammonium-oxalato- VO^{2+} gel in dry air and N$_2$.

thermal decomposition pathway in dry air and N$_2$ is similar. The characteristics of the second weight loss (maximum decomposition rate at 235 °C, endothermic and non-oxidative) are identical to those of the hydrate-free $(NH_4)_2C_2O_4$ species (Figure 4.5). This suggests that the μ-oxalato-$(NH_4^+)_2$ species, present in the ammonium-oxalato-VO^{2+} gel, are stable during the first decomposition step and decompose in a single step around 235 °C. As the temperature increases (i.e. above 250 °C), a significant diversification is observed between the thermal decomposition pathway in dry air and N$_2$.

- In dry air, exothermic and oxidative weight losses are observed between 250 °C and 300 °C. This region is characterized by a first, local decomposition rate maximum at 256 °C and a second, local decomposition rate maximum at 275 °C. Above, 300 °C, no further weight loss occurs. About 14 % if the initial weight remains.
- In N$_2$, no exothermic decomposition is observed within the studied temperature interval. The significant weight loss is observed between 250 °C and 350 °C with a single decomposition rate maximum at 322 °C. No further weight loss is observed as the temperature exceeds 350 °C. 25 % of its initial weight remains.

To elucidate the exact decomposition mechanism in an oxidative and inert atmosphere of the ammonium-oxalato-VO^{2+} gel, the evolved gasses are analyzed using an online coupled mass spectrometer in the following sections.

5.2 Thermal decomposition from room temperature to 250 °C

Figures 5.2 and 5.3 show the mass fragments derived from the evolved gasses during the thermal decomposition of the ammonium-oxalato-VO^{2+} gel in dry air and He, respectively. In Table 5.1 the significant mass fragments are tentatively assigned. During the first, non-oxidative, endothermic weight loss around 153 °C, a strong increase in the ion current of the mass fragments $m/z = 17$ (OH^+ or $NH_3^{+\cdot}$), $m/z = 18$ ($H_2O^{+\cdot}$ or NH_4^+) and $m/z = 44$ ($CO_2^{+\cdot}$) is observed in dry air and in He. In He, an increase in the ion current of the mass fragment $m/z = 16$ (NH_2^+) is detected as well. These fragments can be assigned to H_2O, NH_3 and CO_2. Additionally, the modest increase in the ion current of the mass fragments $m/z = 12$ ($C^{+\cdot}$), $m/z = 22$ (CO_2^{++}) and $m/z = 45$ ($^{13}CO_2^{+\cdot}$) support the tentatively assigned release of CO_2. The NH_3 originates from the rearrangement of an ammonium carboxylate group into a carboxylic acid group (Equation 5.1). The formed carboxylic acid group is subsequently subjected to a decarboxylation resulting in a formato-VO^{2+} interaction (Equation 5.2).

m/e	Dry air	N_2	Tentative assignment
12	x	x	$C^{+\cdot}$
13		x	CN^{++}
15		x	NO^{++}
16		x	O^+, O_2^{++}, NH_2^+
17	x	x	$OH^+, NH_3^{+\cdot}$
18	x	x	$H_2O^{+\cdot}, NH_4^+$
22	x	x	CO_2^{++}
26	x	x	CN^+
27	x	x	$HCN^{+\cdot}$
30		x	NO^+
32		x	O_2^+
43	x	x	$HNCO^{+\cdot}$
44	x	x	$CO_2^{+\cdot}$
45	x	x	$^{13}CO_2^{+\cdot}$
46	x	x	NO_2^+

Table 5.1: Mass fragments which exhibit significant changes in the TGA-MS of the dried ammonium-oxalate-VO^{2+} gel. The tentative assignments are based on references [86, 94, 108, 110, 112].

$$VO^{2+}\cdots{}^{-}OOC{-}COO^{-}\cdots NH_4^+ \longrightarrow VO^{2+}\cdots{}^{-}OOC{-}COOH + NH_3(g) \qquad (5.1)$$

$$VO^{2+}\cdots{}^{-}OOC{-}COOH \longrightarrow VO^{2+}\cdots{}^{-}OOCH + CO_2(g) \qquad (5.2)$$

Alternatively, the carboxylic acid group can react with NH_3 to form an amide with the emission of H_2O (Equation 5.3).

$$VO^{2+}\cdots{}^{-}OOC{-}COOH + NH_3 \longrightarrow VO^{2+}\cdots{}^{-}OOC{-}CONH_2 + H_2O(g) \qquad (5.3)$$

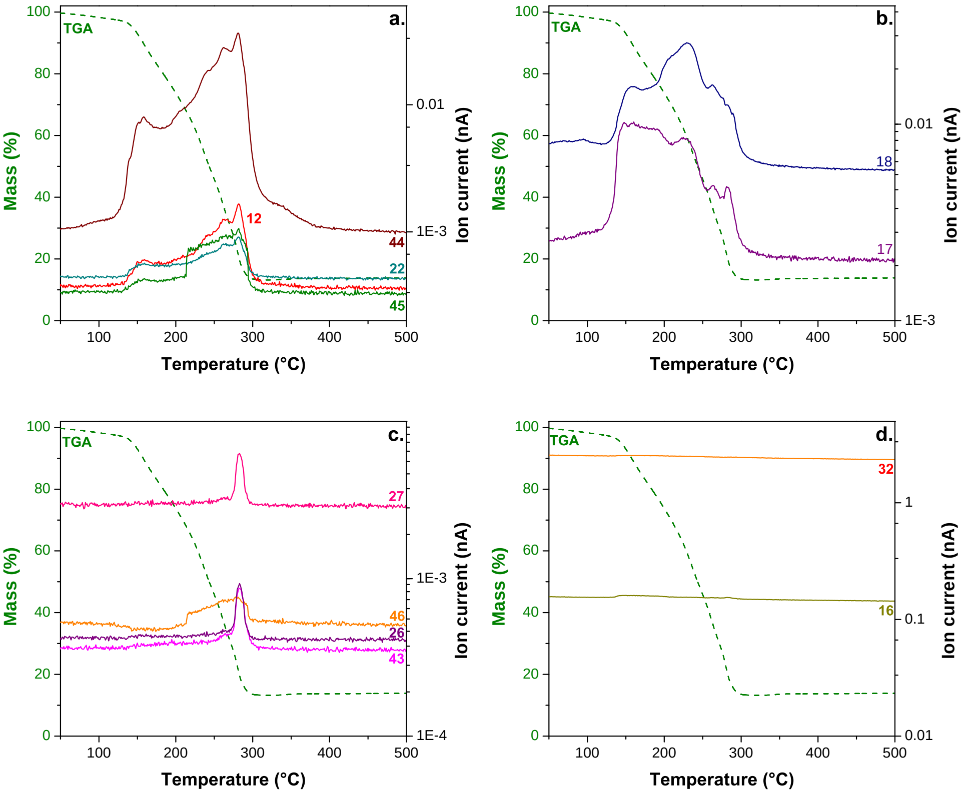

Figure 5.2: TGA-MS profile of the ammonium-oxalato-VO^{2+} gel recorded in dry air at a heating rate of 10 °C min^{-1}: fragments related to the carboxylate groups (a.), to H_2O and/or NH_4^+ (b.), to the interaction between carboxylic acid groups and NH_3 (c.) and to the ambient (d.). Only the relevant fragments in the m/e = 5-120 region are shown (Ion currents). Note that each sub-figure has its own Ion current scale. A tentative assignment is given in Table 5.1

As the temperature increases up to 235 °C, the second weight loss occurs. During this decomposition step, a further increase in the ion current of the mass fragments assigned to NH_3 (m/z = 17, 18), H_2O (m/z = 17, 18) and CO_2 (m/z = 12, 22, 44, 45) is observed. This decomposition step can be ascribed to the aforementioned non-oxidative and endothermic decomposition of the μ-oxalato-$(NH_4^+)_2$ species, via oxalic acid, into volatile NH_3, H_2O and CO (Equations 5.4 and 5.5).[92] Obviously, in the presence of O_2, the CO is further oxidized to CO_2.

$$(NH_4)_2C_2O_4 \longrightarrow C_2O_4H_2 + 2\,NH_3(g) \tag{5.4}$$

$$C_2H_2O_4 \longrightarrow CO(g) + H_2O(g) \tag{5.5}$$

In conclusion, all ammonium carboxylate groups present in the ammonium-oxalato-VO^{2+} gel are systematically decomposed between T_{Room} and 250 °C. The decomposition reactions are non-oxidative and endothermic and lead to the emission of NH_3, H_2O, CO and CO_2. The following species remain at 250 °C: oxalato-VO^{2+}, μ-oxalato-$(VO^{2+})_2$, formato-VO^{2+} and oxamato-VO^{2+}.[1]

5.3 Thermal decomposition from 250 °C to 500 °C

5.3.1 Oxidative pathway

Between 250 °C and 300 °C, a single decomposition step is observed in dry air with its decomposition rate maximum at 275 °C. Figure 5.2 shows a further increases in the ion currents of the mass fragments associated with the evolution of CO_2 to their maximum value (i.e. m/z = 12, 22, 44 and 45), suggesting a large emission of CO_2 in this temperature interval. Note that, despite a significant decrease in the ion current of the mass fragments m/z = 17 (OH^+ or $NH_3^{+\cdot}$) and m/z = 18 ($H_2O^{+\cdot}$ or NH_4^+) occurs, their ion current still remains at a level well above its background. Clearly the emission of H_2O and NH_3 is diminishing. Additionally, small peaks in the ion currents of the mass fragments m/z = 26 (CN^+), m/z = 27 ($HCN^{+\cdot}$), m/z = 43 ($HNCO^{+\cdot}$) and m/z = 46 (NO_2^+) are observed.

A first decomposition reaction around 275 °C is related to rearrangement of the amide functionality in oxamato-VO^{2+} to a nitrile functionality and the release of H_2O (Equation 5.6).

$$VO^{2+}\cdots {}^{-}OOC{-}CONH_2 \longrightarrow VO^{2+}\cdots {}^{-}OOC{-}C{\equiv}N + H_2O(g) \tag{5.6}$$

The mass fragments m/z = 26, 27 and 43 are associated with the release of such nitrile groups. The residual carboxylate groups are simultaneously burned to CO_2. Alternatively, the amide or nitrile functionality can directly burn, resulting in volatile NO_2 which is detected as NO_2^+ (m/z = 46) by the mass spectrometer. With these reactions, the ligands in the formato-VO^{2+} and oxamato-VO^{2+} species are decomposed. The oxalato-VO^{2+} and μ-oxalato-$(VO^{2+})_2$ species remain. In an oxidative ambient, the oxalate is subjected to an exothermic burning completely converting it to volatile CO_2.

---

[1] No insights in the interaction of the amide group with a VO^{2+} ion are obtained: the oxamato ligand can be a monodentate via the carboxylate group, bidentate or bridging (i.e. μ-oxamato-$(VO^{2+})_2$).

Thus during the exothermic and oxidative step around 275 °C, the remaining formato-VO^{2+}, oxamato-VO^{2+}, oxalato-VO^{2+} and μ-oxalato-$(VO^{2+})_2$ are fully decomposed with the release of mainly H_2O, CO_2 and NO_2. Additionally, during the decomposition in air, the formation of the V-O bonds takes place resulting in V_2O_5.

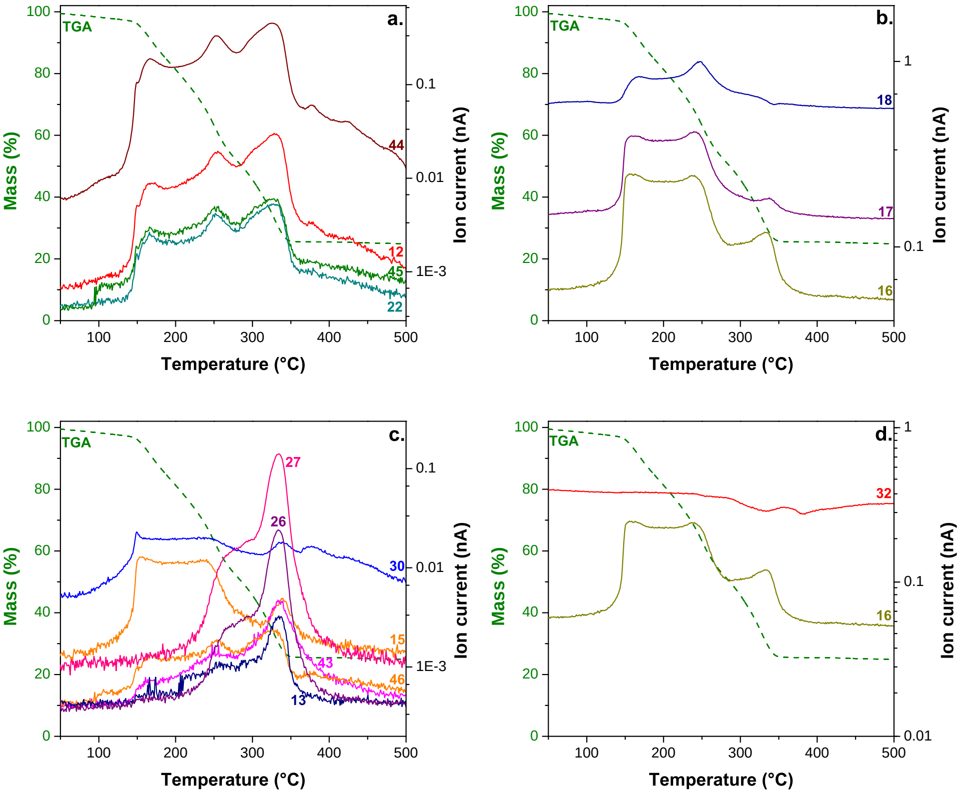

Figure 5.3: TGA-MS profile of the ammonium-oxalato-VO^{2+} gel recorded in He at a heating rate of 10 °C min^{-1}: fragments related to the carboxylate groups (a.), to H_2O and/or NH_4^+ (b.), to the interaction between carboxylic acid groups and NH_3 (c.) and to the ambient (d.). Only the relevant fragments in the m/e = 5-120 region are shown (Ion currents). Note that each sub-figure has its own Ion current scale. A tentative assignment is given in Table 5.1

5.3.2 Non-oxidative pathway

In the He ambient, a decreased amount of O_2 is available. A comparison between the ion current at room temperature of the m/e = 32 mass fragment in Figures 5.2d. and 5.3d. indicates a concentration of 2–3 %. Due to this decreased O_2 concentration, the thermal decomposition pathway above 250 °C differs. The largest weight loss is now observed between 300 °C and 350 °C (Figure 5.1) with its decomposition rate maximum at 322 °C. This weight loss is associated with a decrease in the heat flow, indicating an endothermic process. Firstly, the amide rearrangement (Equation 5.6) and the nitrile release is observed by the increase in the ion current of the mass fragments m/z = 13 (CN^{++}), m/z = 26 (CN^{+}), m/z = 27 ($HCN^{+\cdot}$) and m/z = 43 ($HNCO^{+\cdot}$). The value to which these ion currents increase is at least one order in magnitude higher than in dry air. Additionally, an increase in the ion current of the mass fragment m/z = 13 can be observed in He, while in dry air this ion current remained at its background level. Thus, the decomposition pathway of the amide rearrangement and the nitrile emission occurs more in He than in dry air. Secondly, a significant increase in the ion current of the mass fragments m/z = 15 (NO^{++}) and m/z = 30 (NO^{+}) is detected in He. The ion current of the mass fragments associated with the evolution CO_2 (i.e. m/z = 12, 22, 44 and 45) increase as well. Simultaneously, a decrease in the ion current of the mass fragments m/z = 32 (O_2^{+}) is observed in Figure 5.3d. This indicates that, even in the He ambient with a reduced O_2 concentration, an oxidative decomposition of the amide/nitrile groups and of the remaining organic matrix occurs. Since Figure 5.1 shows a higher final weight at 500 °C in N_2, the organic matrix is certainly not entirely decomposed. The residual sample still contains compounds that are thermally stable in the reduced O_2 ambient. These compounds account for ~ 44 w/w% of the residual sample.

In conclusion, the thermal decomposition pathway in He favors the formation of amide and nitrile functionalities and the release of their associated mass fragments. Additionally, the little amount of O_2 present in this He ambient is consumed for the formation of NO and CO_2, derived from the oxidative decomposition of such amide/nitrile functionalities and of the residual matrix, respectively. At 500 °C, the sample still contains compounds that are thermally stable in the reduced O_2 ambient (~ 44 w/w% of the residual sample).

5.4 Conclusion

The thermal decomposition pathway of the ammonium-oxalato-VO^{2+} gel is conscientiously studied in air and N_2 (or He). The largest weight loss is observed below 250 °C. This weight loss corresponds to the non-oxidative and endothermic decomposition of all the ammonium carboxylate groups with the release of NH_3, H_2O and CO_2. At 250 °C, the oxalato-VO^{2+}, μ-oxalato-$(VO^{2+})_2$, formato-VO^{2+} and oxamato-VO^{2+} species remain. Above 250 °C, a differentiation is observed between the decomposition pathway in an oxidative (dry air) and a non-oxidative (N_2 or He) ambient.

- In an oxidative ambient, an exothermic and oxidative decomposition step occurs around 275 °C. The remaining VO^{2+} species are fully decomposed with the release of mainly H_2O, CO_2 and NO_2. Additionally, the formation of the V-O bonds takes place resulting in V_2O_5. No weight loss is observed above 300 °C leading to a final weight of 11 %.

- In a non-oxidative ambient, no exothermic reactions are observed and the major decomposition step is delayed to 322 °C. The thermal decomposition pathway favors the formation of amide and nitrile functionalities and the release of their associated mass fragments. Additionally, the little amount of O_2 present is consumed for the formation of NO and CO_2, derived from the oxidative decomposition of such amide/nitrile functionalities and of the residual matrix, respectively. At 500 °C, the sample still contains compounds that are thermally stable in the reduced O_2 ambient (~ 44 w/w% of the residual sample).

With aforementioned insights, the thermal study of the ammonium-citrato-VO^{2+} gel can begin, knowing that: (i) the aqueous citrato-VO^{2+} solution probably contains oxalate residues and (ii) the decomposition profile is expected to be more complicated due to the larger ligand.

Chapter 6

Thermal decomposition of ammonium-citrato-VO^{2+}

During the synthesis of the ammonium-citrato-VO^{2+} solution (Figure 2.2 in Chapter 2), citric acid and NH_3 are added to the solution in a 2/1 molar ratio w.r.t. VO^{2+} and to obtain a solution with a pH value of 7, respectively. In Chapter 2, the structure of the citrato-VO^{2+} complex has been studied using Electron Paramagnetic Resonance spectroscopy.

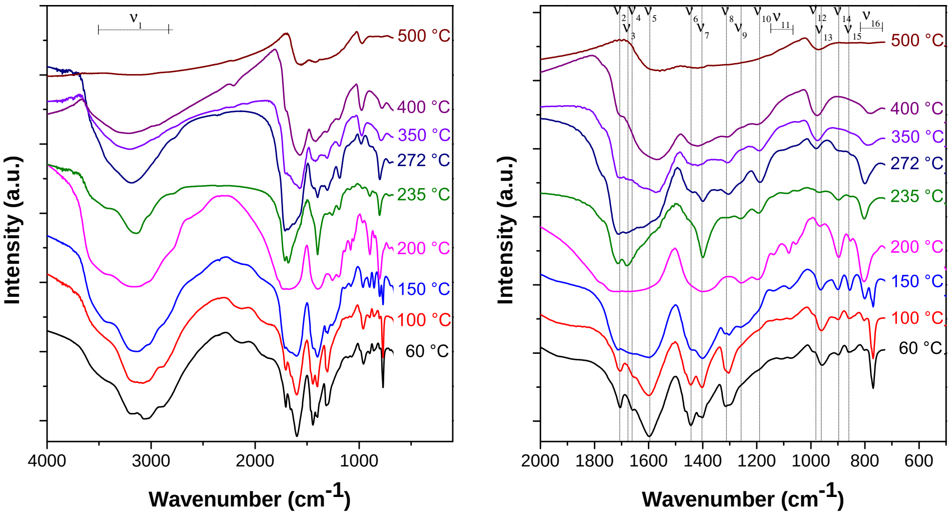

Figure 6.1: FTIR spectra of the ammonium-citrato-VO^{2+} gel, obtained after drying at 60 °C, heated in dry air (100 mL min^{-1}) for 30 minutes at various temperatures. (left: spectra from 4000 cm^{-1} to 600 cm^{-1}, right: spectra from 2000 cm^{-1} to 600 cm^{-1}) A tentative assignment is given in Table 6.1.

It is shown that the citrato-VO^{2+} complex occupies a distorted octahedral geometry with a four carboxylate ligation at the equatorial positions and a fifth carboxylate ligation at the axial position w.r.t. to the V=O axis. Thus each VO^{2+} ion is chelated by 5 carboxylate groups. However 6 carboxylate groups have been added to the solution per VO^{2+} ion, indicating that every sixth carboxylate group is available for the formation of an ammonium-carboxylate bridge between two or three VO^{2+} complexes. Note that α-hydroxyl functionality (possibly protonated) does not chelate the VO^{2+} and is considered a free hydroxyl group.

The FTIR spectrum of the ammonium-citrato-VO^{2+} gel, obtained by drying at 60 °C, in Figure 6.1 confirms the presence of the aforementioned groups or interactions. A detailed assignment of the main vibrations is listed in Table 6.1. The C=O vibration mode and O-C=O deformation, both associated with carboxylic acid groups (i.e. -COOH), are observed at 1710 cm^{-1} and 1303 cm^{-1}, respectively. The presence of carboxylate groups, originating from oxalate of citrate ligands and interacting with either NH$_4^+$ or VO^{2+}, is suggested by the symmetric and asymmetric vibration modes occurring at 1643 cm^{-1}, 1601 cm^{-1}, 1440 cm^{-1} and 1405 cm^{-1}. Note that the $\nu_s(CO_2^-)$ at 1405 cm^{-1} coincides with the ammonium deformation (i.e. $\delta(NH_4^+)$).[75, 92–94] The vanadyl unit is observed by its stretch vibration at 954 cm^{-1} and its V-O-V skeleton vibration at 803 cm^{-1}.[95, 113]

Vibration	Wavenumber (cm^{-1})	(Assignment)	
ν_1	3600 – 2800 (broad)	ν(O-H)	O-H stretching in H_2O
ν_1	3600 – 2800 (broad)	ν(N-H)	N-H stretching in NH_4^+
ν_1	3600 – 2800 (broad)	ν(C-H)	C-H stretching in CH_2
ν_2	1710	ν(C=O)	C=O stretching in COOH or in anhydride
ν_3	1676	ν(C=O)	C=O stretching in $CONH_2$
ν_4	1643	$\nu_{as}(CO_2^-)$	Asymmetric CO_2^- stretching with VO^{2+} or VO_2^+
ν_5	1601	$\nu_{as}(CO_2^-)$	Asymmetric CO_2^- stretching with NH_4^+
ν_6	1440	$\nu_s(CO_2^-)$	Symmetric CO_2^- stretching with NH_4^+
ν_7	1405	$\nu_s(CO_2^-)$	Symmetric CO_2^- stretching with VO^{2+} or VO_2^+
ν_7	1405	$\delta(NH_4^+)$	NH_4^+ deformation
ν_7	1405	$\nu_s(CON)$	C-N stretching in $CONH_2$
ν_8	1303	δ(O-C=O)	O-C=O deformation
$\nu_{9,10}$	1260 and 1195	ν(C-O)	C-O stretching in anhydride ether, doublet
ν_{11}	1110 and 1070	ν(C-O)	C-O stretching in C-OH, doublet
ν_{12}	980	$\nu(V^{5+} = O)$	V^{5+}=O stretching
ν_{13}	954	$\nu(V^{4+} = O)$	V^{4+}=O stretching
ν_{14}	897	$\delta_\gamma(C - H)$	C-H out-plane deformation in terminal methylene
ν_{15}	875	δ(C-O)	C-O out-of-plane deformation
ν_{16}	803	ν(V-O-V)	V-O-V skeleton vibration

Table 6.1: Band assignments of the main vibrations (expressed in cm^{-1}) observed in the FTIR spectra of the dried ammonium-citrato-VO^{2+} gel heated at various temperatures for 30 minutes in dry air. Note that the carboxylate vibrations can originated from carboxylate groups associated with oxalate or citrate. The assignments are based on references [75, 92–94, 113].

Additionally, a broad band in the FTIR spectrum is observed between 3600 cm^{-1} and 2800 cm^{-1} which is assigned to $\nu(O-H)$, $\nu(N-H)$ and $\nu(C-H)$ associated with residual H_2O, NH_4^+ and citrate's CH_2 group respectively. This band is broadened by H-bridge formation in the gel. The presence of oxalate residues in the ammonium-citrato-VO^{2+} gel is expected as well.

6.1 Weight loss and heat flow

The thermal decomposition profile of the ammonium-citrato-VO^{2+} precursor gel, given in Figure 6.2, is studied up to 625 °C in an oxidative (dry air) and inert (N_2) ambient.

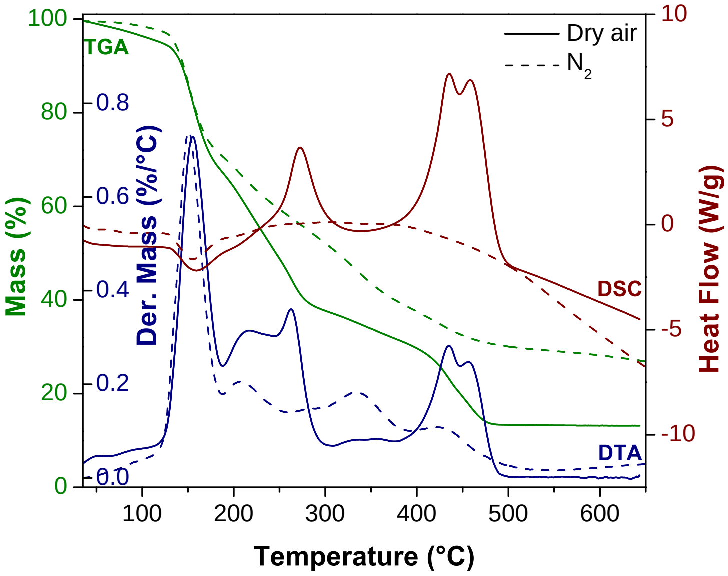

Figure 6.2: TGA (Mass %), DTA (Der. Mass) and DSC (Heat Flow) analysis of the citrato-VO^{2+} gel, obtained by drying of the aqueous citrato-VO^{2+} solution at 60 °C. The analyses are performed in dry air and in N_2.

In both conditions, the weight loss occurs though a sequence of steps. Up to 245 °C, the thermal decomposition pathway is very similar in dry air and N_2. The decomposition consists of non-oxidative and endothermic steps, as suggested by the decrease in the heat flow with respect to its background level. Above 245 °C, a diversification is observed between the thermal decomposition pathway in dry air and N_2.

- In dry air, a first oxidative and exothermic process takes place between 245 °C and 300 °C with its decomposition rate maximum at 270 °C. Note that the ammonium-oxalate-VO^{2+} gel exhibits a decomposition rate maximum at 275 °C as well, suggesting that this decomposition step stems from the decomposition of the residual ammonium-oxalate-VO^{2+} in the ammonium-citrato-VO^{2+} gel. The second oxidative and exothermic process is observed between 400 °C and 500 °C with local decomposition rate maxima at 433 °C and 457 °C. As the temperature reaches 500 °C, no further weight loss is observed leading to a total weight loss of 87 % in dry air.

- In N_2, no exothermic decomposition is observed within the studied temperature interval. From 245 °C to 480 °C, a gradual weight loss is observed with a small increase in the decomposition rate around 337 °C and 425 °C. This gradual weight loss accounts for about 30 %. The step around 325 °C is also observed in the thermal decomposition of the ammonium-oxalate-VO^{2+} gel in an inert ambient which further confirms the presence of residual oxalates in the ammonium-citrato-VO^{2+} gel. As the temperature further increase up to 625 °C, an additional and continuous weight loss of about 5 % is observed.

In order to describe the reactions occurring during the thermal decomposition of the ammonium-citrato-VO^{2+} gel, the evolved gasses and the remaining solid are analyzed using an online coupled mass spectrometer and by ex-situ FTIR spectroscopy respectively. Figures 6.3 and 6.4 show the profile of the significant mass fragments detected during the thermal decomposition of the ammonium-citrato-VO^{2+} gel in dry air and He, respectively. A tentative assignment of these mass fragments is listed in Table 6.2. The FTIR spectra of the solids obtained after heating of the ammonium-citrato-VO^{2+} gel in dry air at various temperatures and the tentative assignments of its main vibrations are given in Figure 6.1 and Table 6.1, respectively.

6.2 Thermal decomposition from room temperature to 245 °C

The small weight loss below 100 °C is associated with the onset of evolution of the m/z = 17 (OH^+, $NH_3^{+\cdot}$) and m/z = 18 ($H_2O^{+\cdot}$, NH_4^+) mass fragments as observed in Figures 6.3 and 6.4. Since the onset of the mass fragment m/z = 16 (NH_2^+) is not observed in He, it is plausible to assume that the evolution of the mass fragments m/z = 17 and 18 is caused by the evaporation of water. In this temperature range, the FTIR spectra of the remaining product (Figure 6.1) does not change, suggesting that the ammonium bridged network of citrato-VO^{2+} complexes is not affected. Therefore, this first weight loss is only caused by a further drying of the gel with the evaporation of H_2O.

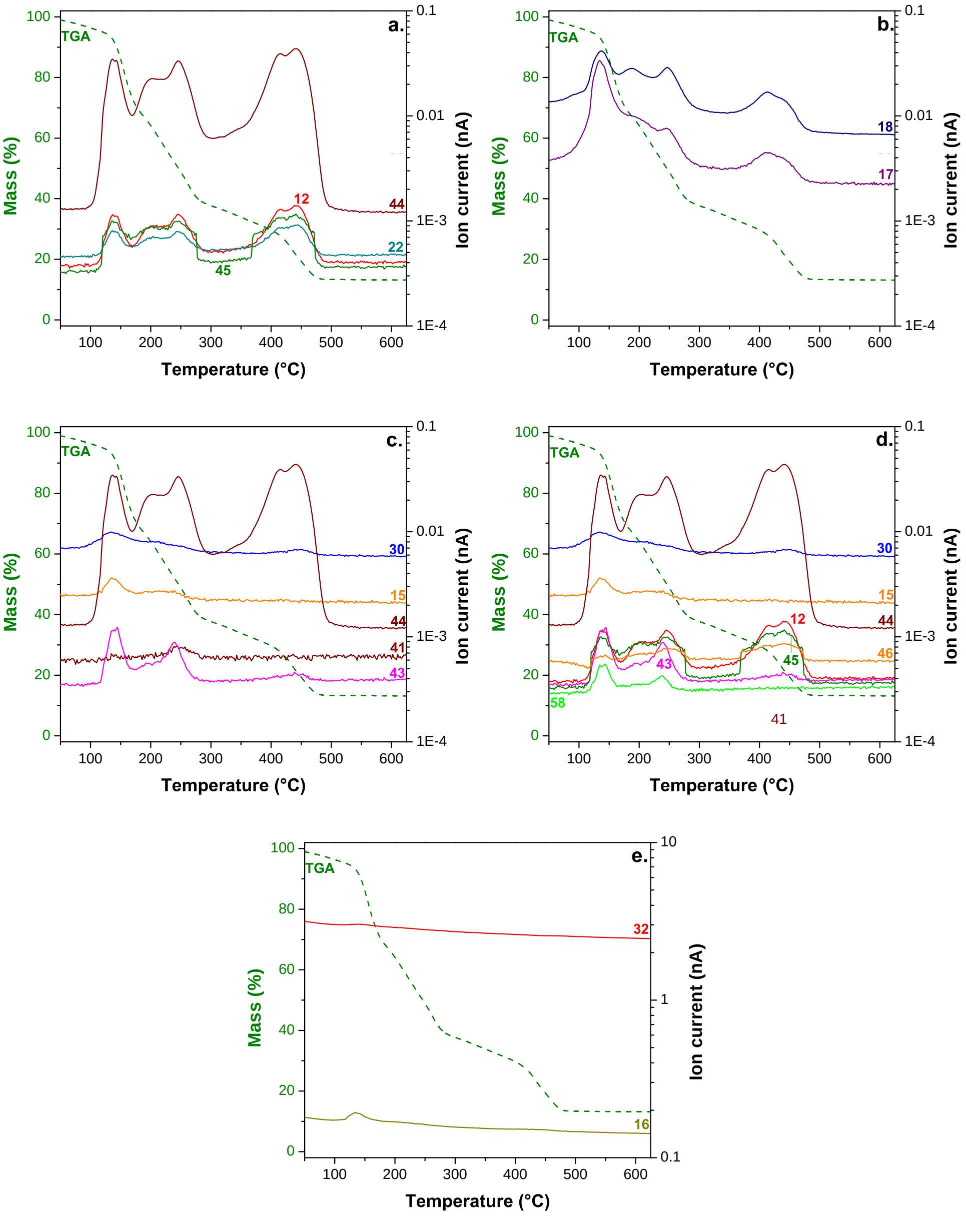

Figure 6.3: TGA-MS profile of the ammonium-citrato-VO^{2+} gel, obtained by drying of the citrato-VO^{2+} solution at 60 °C, recorded in dry air at a heating rate of 10 °C min^{-1}: fragments related to the carboxylate groups (a.), to H_2O and/or NH_4^+ (b.), to the interaction between carboxylic acid groups and NH_3 (c.) and to the citrate's skeleton (d.) and to the ambient (e.). Only the relevant fragments in the m/e = 5-120 region are shown (Ion currents). Note that each sub-figure has its own Ion current scale. A tentative assignment is given in Table 6.2

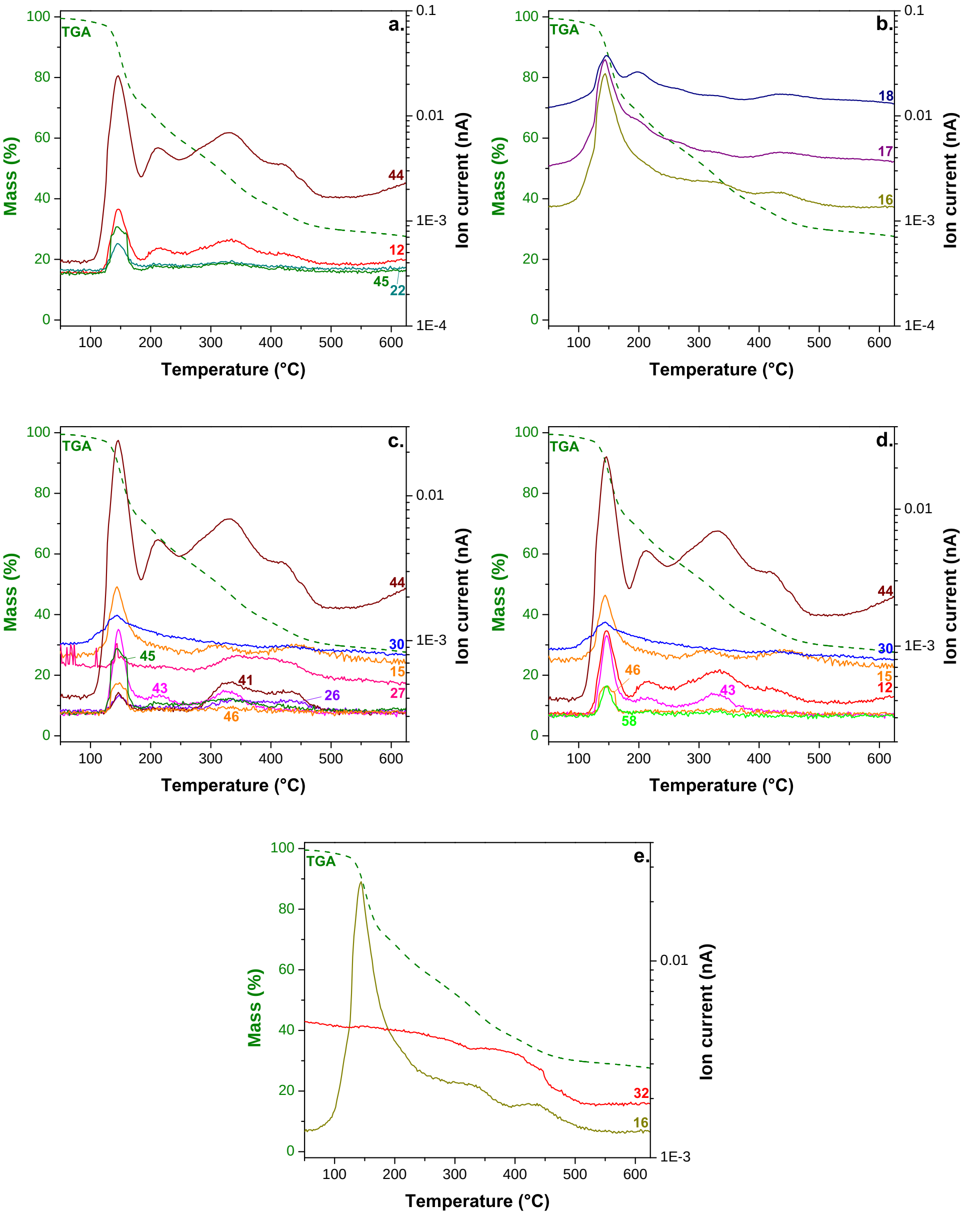

Figure 6.4: TGA-MS profile of the ammonium-citrato-VO^{2+} gel, obtained by drying of the citrato-VO^{2+} solution at 60 °C, recorded in He at a heating rate of 10 °C min^{-1}: fragments related to the carboxylate groups (a.), to H_2O and/or NH_4^+ (b.), to the interaction between carboxylic acid groups and NH_3 (c.) and to the citrate's skeleton (d.) and to the ambient (e.). Only the relevant fragments in the m/e = 5-120 region are shown (Ion currents). Note that each sub-figure has its own Ion current scale. A tentative assignment is given in Table 6.2

m/e	dry air	N_2	Tentative assignment
12	x	x	$C^{+\cdot}$
15	x	x	NO^{++}, CH_3^+
16	x	x	O^+, O_2^{++}, NH_2^+
17	x	x	$OH^+, NH_3^{+\cdot}$
18	x	x	$H_2O^{+\cdot}, NH_4^+$
22	x	x	CO_2^{++}
26		x	CN^+
27		x	$HCN^{+\cdot}$
30	x	x	$NO^+, C_2H_6^+, H_2N{=}CH_2^+$
32	x	x	O_2^+
41	x	x	$H_2C{=}C{=}NH^{+\cdot}$
43	x	x	$HNCO^{+\cdot}, C_2H_7^+$
44	x	x	$CO_2^{+\cdot}, H_2N{-}C{=}O^+, C_3H_8^+$
45	x	x	$^{13}CO_2^{+\cdot}$
46	x	x	$NO_2^+, C_2H_5OH^{+\cdot}$
58	x	x	$C_3H_6O^{+\cdot}$

Table 6.2: Mass fragments which exhibit significant changes in the TGA-MS of the dried ammonium-citrato-VO^{2+} gel. The tentative assignments are based on references [86, 94, 108, 110, 112].

Between 100 °C and 190 °C, a strong weight loss (i.e. about 29 %) can be seen in the thermal decomposition profile of the ammonium-citrato-VO^{2+} gel. This weight loss is identical in dry air and He and is associated with a decrease in the heat flow to a value below its background level. This suggests an endothermic and non-oxidative nature of this decomposition step. In Figures 6.3 and 6.4, a further increase in the ion current of the mass fragments m/z = 17 (OH^+, $NH_3^{+\cdot}$) and m/z = 18 ($H_2O^{+\cdot}$, NH_4^+) is visible. In addition, a strong increase in the ion current of the mass fragment m/z = 16 (NH_2^+) is observed in He. The evolution of these mass fragments suggest a strong emission of NH_3 and H_2O. After a short delay, mass fragments associated with the evolution of CO_2 appear in the MS curves: m/z = 12 ($C^{+\cdot}$) and m/z = 22 (CO_2^{++}), m/z = 44 ($CO_2^{+\cdot}$) and m/z = 45 ($^{13}CO_2^{+\cdot}$). For the dominating CO_2-related fragment (i.e. m/z = 44) the ion current almost increases with two orders in magnitude. This is, in comparison to the other significant mass fragments, a large release. In addition a small increase in the ion current (i.e. below 1 pA) of the mass fragments m/z = 15 (CH_3^+), m/z = 30 ($H_2N{=}CH_2^+$), m/z = 41 ($H_2C{=}C{=}NH^{+\cdot}$), m/z = 43 ($HNCO^{+\cdot}$), m/z = 46 ($C_2H_5OH^{+\cdot}$) and m/z = 58 ($C_3H_6O^{+\cdot}$) is observed.

In the FTIR spectra of the powders obtained after heating at 100 °C, 150 °C and 200 °C in air (Figure 6.1), the following observations can be made:

- The vibration modes associated with the ammonium-carboxylate groups at 1440 cm^{-1} and $\delta(O - C = O)$ at 1303 cm^{-1} disappear.
- The symmetric stretching mode associated with VO^{2+}-carboxylate groups at 1405 cm^{-1} or the V^{4+}=O center ($\nu(V^{4+} = O)$ at 954 cm^{-1}) are invariant.

- Changes occur in the frequency region between 1550 cm^{-1} and 1750 cm^{-1}. Instead of resolved peaks, a plateau with a rather continuous intensity is observed at 150 °C and 200 °C. This region can cover the $\nu(C = O)$ of a carboxylic acid or an amide group, the $\nu_{as}(CO_2^-)$ of a carboxylate interacting with VO^{2+} (1643 cm^{-1}) or with NH_4^+ (1601 cm^{-1}) and the $\nu(C = C)$ of a terminal methylene.
- The presence of a terminal methylene groups is proven by the presence of its out-of-plane deformation at 897 cm^{-1}.

Combining both observations - (i) the emission of certain gasses detected as an increase in the ion current of its associated mass fragments and (ii) the changes in FTIR spectra of the formed compounds - and previous reports on the thermal decomposition of an ammonium-citrato-Zn^{2+} gel by Van Werde et al.[86] leads to the following conclusions on this non-oxidative and endothermic decomposition step[1]:

1. Similar to the decomposition of pure citric acid, citrate's α-hydroxyl functionality is subjected to a dehydroxylation which releases H_2O and results in a double bond (i.e. C=C) transforming the citrate into an aconite. The stretch vibration of such a double bond is located around 1650 cm^{-1} which is unresolved in the FTIR spectra.
2. The ammonium carboxylate groups rearrange towards carboxylic acid groups (Equation 6.1) with the release of NH_3.

$$\mathrm{R{-}COO^-\cdots H{-}NH_3^+ \longrightarrow R{-}COOH + NH_3(g)} \tag{6.1}$$

3. The formed carboxylic acid groups can further react with NH_3 to form amides and emit H_2O (Equation 6.2).

$$\mathrm{R{-}COOH + NH_3 \longrightarrow R{-}CONH_2 + H_2O(g)} \tag{6.2}$$

4. By combining the dehydroxylation of citrate's α-hydroxyl functionality and the rearrangement of the ammonium-carboxylate groups, unsaturated carboxylic acid and unsaturated amides can be formed. An ordinary carboxylic acid group and such an unsaturated carboxylic acid group is subjected to a further decarboxylation with the emission of CO_2, forming a terminal methyl or a terminal methylene group (Equations 6.3 and 6.4), respectively.

$$\mathrm{(R_1)(R_2)(R_3)C{-}CH_2{-}COOH \longrightarrow (R_1)(R_2)(R_3)C{-}CH_3 + CO_2(g)} \tag{6.3}$$

$$\mathrm{(R_1)(R_2)C{=}CH{-}COOH \longrightarrow (R_1)(R_2)C{=}CH_2 + CO_2(g)} \tag{6.4}$$

---

[1] Note that in the following equations, for simplicity, the insignificant groups are abbreviated as R or R_i. For each equation R and R_i can be different and the R_i partition only indicates that the insignificant groups are not necessarily identical.

5. Alternatively, two neighboring carboxylic acid groups can interact and form an anhydride during a nucleophilic acyl substitution with the emission of H_2O (Equation 6.5).[114] The presence of such an anhydride is suggested by C-O-C stretch vibration at 1260 cm^{-1} and 1195 cm^{-1} in the FTIR spectra at 200 °C.

$$R_1COOH + R_2COOH \longrightarrow R_1C(=O){-}O{-}(O=)CR_2 + H_2O(g) \qquad (6.5)$$

So far, the origin of the observed H_2O, NH_3 and CO_2 emission has been suggested by rearranging citrate's α-hydroxyl functionality, carboxylic acid groups and ammonium-carboxylate groups. The following groups or species remain: itaconate in which each carboxylate group interacts with a VO^{2+} ion, terminal methyl ($-CH_3$), terminal methylene ($= CH_2$), saturated amide ($-CONH_2$), unsaturated amide ($= C - CONH_2$) and anhydride ($-C(= O) - O - (O =)C-$). Note that in this temperature interval, also the first step in the decomposition pathway of oxalate residues occur: the formation of carboxylic acid and amide groups by a rearrangement of the ammonium carboxylate groups and the decarboxylation of the formed carboxylic acid groups.

As the temperature further increases, a next weight loss is observed between 190 °C and 245 °C. This weight loss occurs in dry air and in He, and is associated with a small decrease in the heat flow. The MS spectra show only a slight increase in the ion current of the mass fragments associated with H_2O, NH_3 and CO_2 in dry air and in He: m/z = 12 ($C^{+\cdot}$), m/z = 17 (OH^+, $NH_3^{+\cdot}$), m/z = 18 ($H_2O^{+\cdot}$, NH_4^+), m/z = 22 (CO_2^{++}), m/z = 44 (CO_2^+) and m/z = 45 ($^{13}CO_2^+$). The FTIR spectra of the powders obtained at 200 °C and 235 °C exhibit only differences in the region 1350–1450 cm^{-1} and 1550–1750 cm^{-1}. Only the carboxylate vibrations associated with the VO^{2+} ion remain at 235 °C: $\nu_{as}(CO_2^-)$ at 1643 cm^{-1} and $\nu_s(CO_2^-)$ at 1405 cm^{-1}. No indications for carboxylate vibrations associated with the ammonium ion are detected. In addition, the C=O stretch vibration in an amide group (1676 cm^{-1}) and in an anhydride group (1710 cm^{-1}) are clearly observable in the FTIR spectrum of the powder obtained after heating at 235 °C. These observation correspond to the non-oxidative and endothermic decomposition of the oxalato-NH_4^+ species, via oxalic acid, into the volatile NH_3, H_2O and CO_2 (Equations 5.4 and 5.5). Note that the FTIR spectra show a shift of the vanadyl vibration from 954 cm^{-1} to 980 cm^{-1} as the temperature increases from 200 °C to 272 °C. This suggest the oxidation onset of vanadium(IV) to vanadium (V). At 235 °C, the wavenumber is intermediate indicating the presence of both vanadium(IV) and vanadium(V)

Summarizing, the sequence of reactions below 245 °C decomposes the organic matrix consisting of ammonium carboxylate groups, carboxylic acid groups and ammonium oxalate residues. The carboxylate groups, coordination the VO^{2+} ion, are still unaffected. However, the VO^{2+} ion itself oxidizes to a VO_2^+ ion. The following groups remain at 245 °C: itaconate in which each carboxylate group interacts with a VO_2^+ ion, terminal methylene, (un)saturated amide, anhydride, oxalato-VO_2^+, μ-oxalato-$(VO^{2+})_2$, formato-VO_2^+ and oxamato-VO_2^+. As indicated earlier, the thermal decomposition pathway in dry air and He differs from 245 °C on. In dry air, an oxidative pathway is followed with exothermic peaks in the heat flow. Contrarily, a non-oxidative pathway is followed in He without significant heat flow features. Both pathways will be discussed in the next sections.

6.3 Thermal decomposition from 245 °C to 625 °C

6.3.1 Oxidative pathway

Between 245 °C and 300 °C the first weight loss, related to an oxidative and exothermic decomposition process, is observed with its maximum decomposition rate at 270 °C (Figure 6.2). The mass spectrum in Figure 6.3 shows a local increase in the ion current of the mass fragments assigned to the release of H_2O, NH_3 (m/z = 17, 18) and CO_2 (m/z = 12, 22, 44, 45). Additionally, a small peak in the ion current of the mass fragments m/z = 43 ($HNCO^{+\bullet}$) and m/z = 46 (NO_2^+) is observed. The FTIR spectra of the powders obtained at 235 °C and 272 °C (Figure 6.1) are almost identical. A subtitle decrease in the intensity of the peaks associated with the asymmetric and symmetric carboxylate stretch vibrations in the interaction with the VO_2^+ ion at 1643 cm^{-1} and 1405 cm^{-1} is observed. This intensity decrease is relative to the invariant intensity of neighboring peaks. Aforementioned observations could suggest that:

1. Some carboxylate groups in the direct vicinity of a VO_2^+ ion burn with the release CO_2 and H_2O.
2. Some of the present amide groups further rearrange into nitrile functionalities with the release of H_2O.
3. The formed nitrile groups decompose into the volatile isocyanic acid (HNCO).
4. Few nitrogen containing groups, i.e. amides or nitriles, oxidize and release NO_2.

This oxidative decomposition pathway is feasible for the citrate and oxalate residues. For an ammonium-citrato-Zn^{2+} gel this pathway is only suggested at higher temperatures (between 400 °C and 500 °C).[86] However, this temperature range fits perfectly with the oxidative decomposition of the oxalato-VO_2^+, μ-oxalato-$(VO^{2+})_2$, formato-VO_2^+ and oxamato-VO_2^+, studied in Chapter 5. Thus it is acceptable to assume that the oxidative decomposition step between 245 °C and 300 °C almost completely corresponds to the decomposition of the oxalate residues. In addition, Figure 5.1 shows that no further decomposition of oxalate residues can be expected above 300 °C suggesting that all oxalate residues are fully decomposed at 300 °C. At this point in the oxidative decomposition of the ammonium-citrato-VO^{2+} gel only the following species remain: carboxylate groups - originating from the citrate ligand - in the direct vicinity of a VO_2^+ ion, terminal methylene, (un)saturated amide and anhydride functionalities.

Finally, between 380 °C and 500 °C, the last decomposition steps are observed with their decomposition rate maxima at 435 °C and 456 °C (Figure 6.2). These decomposition steps result in a strong increase in the heat flow suggesting the presence of very exothermic reactions. The mass spectrum shows a strong increase in the ion current of the mass fragments associated with the emission of CO_2 (i.e. m/z = 12, 22, 44 and 45). Each of these ion currents reach its highest level in the entire studied temperature interval, emphasizing the large release of CO_2. Additionally, the evolution of H_2O and NH_3 is observed by the increase in the ion current associated with the mass fragments m/z = 17 and m/z = 18. A strong increase in the mass fragment m/z = 46 (NO_2^+) suggests a large evolution of NO_2 as well. Interestingly, no fragments associated with the non-oxidative decomposition of nitrile groups are observed: m/z = 26 (CN^+) and m/z = 27 ($HCN^{+\cdot}$). The FTIR spectra of the powders obtained at 350 °C, 400 °C and 500 °C show a disappearance of all organic groups as the temperature increases. The peaks associated with anhydride vibrations - $\nu(C=O)$, $\nu(C-O-C)$ and $\nu(C-O-C)$ at 1710 cm^{-1}, 1260 cm^{-1} and 1195 cm^{-1} respectively - which could persist until 400 °C, are not longer present at 500 °C. The peaks associated with carboxylate groups interacting with VO_2^+ at 1643 cm^{-1} and 1405 cm^{-1} disappear from 400 °C to 500 °C. The C-H out-of-plane deformation of the terminal methylene, $\delta_\gamma(C-H)$, at 897 cm^{-1} is already vanished at 350 °C. The only vibration left at 500 °C, is the vanadyl stretch vibration, $\nu(V^{5+}=O)$, at 980 cm^{-1}.

The observations in the MS and FTIR spectra suggest that all organics burn and emit CO_2, H_2O and/or NO_2.

1. The (un)saturated amide and nitrile groups react with O_2 and form NO_2 rather than their non-oxidative rearrangement and the emission of nitrile-based fragments.

2. The anhydride functionalities can either burn with the release O_2 and H_2O or evaporate.[86] Typical fragments assigned to the evaporation of anhydride species, m/z = 68 ($C_4H_4O^+$) and m/z = 112 ($C_5H_4O_3^+$), are not detected. This suggests that such an evaporation is unlikely and that the anhydride species are rather burned.

3. The carboxylate groups in the direct vicinity of a VO_2^+ ion and the terminal methylene burn to CO_2 and H_2O.

4. During decomposition in air, the formation of the V-O bonds takes place.

The obtained powder at 625 °C is crystalline and is identified as orthorhombic V_2O_5 according to JCPDS 03-0206[96] (Figure 6.5).

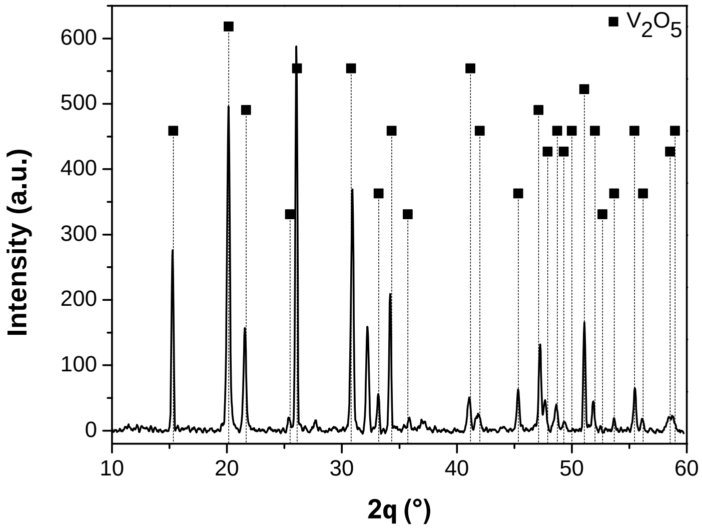

Figure 6.5: X-Ray Diffraction of the ammonium-citrato-VO^{2+} gel after a thermal treatment till 625 °C in dry air. The assignments are based on JCPDS 03-0206 of orthorhombic V_2O_5.[96]

In conclusion, during the oxidative decomposition pathway between 245 °C and 625 °C the following reactions occur. Firstly, the onset of VO^{2+}/VO$_2^+$ oxidation is already observed at 200 °C and is fully carried out at 272 °C. Around 272 °C, oxalate residues interacting with the VO$_2^+$ ion (oxalato-VO$_2^+$, μ-oxalato-(VO^{2+})$_2$, formato-VO$_2^+$ and oxamato-VO$_2^+$) completely oxidize to H_2O, CO_2 and NO_2. No indication of oxalate residues are found above 300 °C. Between 400 °C and 500 °C, species and groups related to the citrate ligand (carboxylate groups in the direct vicinity of a VO$_2^+$ ion, terminal methylene, (un)saturated amide and anhydride functionalities) burn with the strong emission of H_2O, CO_2 and NO_2. During this temperature interval V-O bonds are formed and V_2O_5 crystallization occurs.

6.3.2 Non-oxidative pathway

In an inert atmosphere, the decomposition pathway of the ammonium-citrato-VO^{2+} gel is quite different at higher temperatures (i.e. above 245 °C). So far the organic matrix - consisting of the α-hydroxyl, ammonium carboxylate groups and carboxylic acid groups - is decomposed by a series of endothermic and non-oxidative steps including dehydroxylation and decarboxylation. In contrast, the carboxylate groups - coordination the VO^{2+} ion - are still unaffected. The following groups or species are still present at 245 °C: itaconate in which each carboxylate group interacts with a VO^{2+} ion, terminal methylene, (un)saturated amide, anhydride, oxalato-VO$_2^+$, μ-oxalato-(VO^{2+})$_2$, formato-VO^{2+} and oxamato-VO^{2+}.

Between 245 °C and 380 °C a weight loss of about 16 % is seen with its decomposition rate maximum at 325 °C. This weight loss is accompanied with an increase in the ion current of the mass fragments associated with the evolution of CO_2 (m/z = 12, 44 and 45). The ion current of the mass fragment m/z = 15 shows local maximum at 325 °C. Since the terminal methyl group is already volatilized around 150 °C (CH_3^+), the assignment of this mass fragment to NO^{++} is plausible. Both CO_2 and NO are the result of a minor oxidation of carboxylate and amide groups. This is confirmed by the dip in the ion current of the O_2 mass fragment (m/z = 32). At 325 °C, a small increase in the ion current of mass fragments associated with the emission of NH_3 and H_2O is observed (m/z = 16, 17, 18). These fragments can arise from amide rearrangements and nitrile emissions as is observed by the increase in the ion current of the mass fragments m/z = 26 (CN^+), m/z = 27 ($HCN^{+\bullet}$) and m/z = 43 ($HNCO^{+\bullet}$). Because of the large similarities with the non-oxidative decomposition of the ammonium-oxalato-VO^{2+} gel around 325 °C in He, these decomposition steps are assigned to the final decomposition of oxalate species (i.e. oxalato-VO_2^+, μ-oxalato-$(VO^{2+})_2$, formato-VO^{2+} and oxamato-VO^{2+}) present in the ammonium-citrato-VO^{2+} gel. Note that Figure 5.1 shows no further weight loss as the temperature exceeds 350 °C, thus all oxalate residues are assumed to be fully decomposed at this temperature. At this point only the following species remain: carboxylate groups - originating from the citrate ligand - in the direct vicinity of a VO^{2+} ion, terminal methylene, (un)saturated amide and anhydride functionalities.

As the temperature further increase towards 500 °C, the mass curve further decreases and an additional decomposition step can be observed between 380 °C and 500 °C with its decomposition rate maximum at 425 °C. The mass spectrum shows a plateau in the ion current of the mass fragments m/z = 26 (CN^+) and m/z = 27 ($HCN^{+\bullet}$) between 300 °C and 450 °C. This suggests that nitrile formation already occurs during the final oxalate removal and its fragmentation continuous until 450 °C. Nitriles can be formed by the rearrangement of a primary amide (equation 6.6). This nitrile is subjected to two types of dissociation reactions: (i) cleavage of the C_α-CN with a β-H (Equation 6.7) and the emission of HCN and (ii) cleavage of the C_β-C_α bond with a γ-H and the emission of $H_2C{=}C{=}NH$ in a McLafferty rearrangement (Equation 6.8).[110] The increased ion current of the mass fragments m/z = 26 (CN^+), m/z = 27 ($HCN^{+\bullet}$) and m/z = 41 ($H_2C{=}C{=}NH^{+\bullet}$) support both nitrile rearrangements in an inert atmosphere.

$$RC({=}O)NH_2 \longrightarrow RC{\equiv}N + H_2O(g) \tag{6.6}$$

$$RRHC{-}CH_2{-}C{\equiv}N \longrightarrow RRC{=}CH_2 + HCN(g) \tag{6.7}$$

$$RCH{=}C(R){-}CH_2{-}C{\equiv}N \longrightarrow RC{\equiv}C(R) + CH_2{=}C{=}NH(g) \tag{6.8}$$

Around 425 °C, a dip in the ion current of mass fragment associated with O_2 (m/z = 32, O_2^+) is observed. Simultaneously a slight increase in the ion current, associated with the emission of CO_2 (m/z = 12, 22, 44 and 45) and NO (m/z = 15, 30), occurs. This indicates that the low amount of O_2 present in the He atmosphere is consumed in the oxidative decomposition of residual organics. Obviously, nitrogenous groups only partially oxidize to NO and not to NO_2 (an increase in the mass fragment m/z = 46, NO_2^+, is not detected). As the temperature further increases (i.e. from 500 °C to 625 °C), almost all mass fragments fall to their initial background level. The final weight obtained at 625 °C in N_2 (Figure 6.2) equals 27 %. This is 14 % more than could be obtained in dry air. Thus the organic matrix is certainly not entirely decomposed. The residual sample still contains compounds that are thermally stable in the reduced O_2 ambient. These compounds account for ~ 51 w/w% of the residual sample.

6.4 Conclusion

The thermal decomposition pathway of the ammonium-citrato-VO^{2+} gel is conscientiously studied in air and N_2 (or He). The largest weight loss is observed below 245 °C. This weight loss firstly corresponds to the release of residual water and ammonia from the precursor gel. Secondly, a sequence of non-oxidative and endothermic processes take place in which the organic matrix (i.e. α-hydroxyl groups, ammonium carboxylate groups and carboxylic acid groups) is decomposed through a series of dehydroxylation and decarboxylation reactions with the release of NH_3, H_2O and CO_2. Above 245 °C, the thermal decomposition pathway of the ammonium-citrato-VO^{2+} gel depends on the ambient.

- In oxidative conditions (i.e. dry air) all thermo stable compounds formed during the previous decomposition steps and the direct coordination sphere of the vanadium ion are decomposed with the formation of mainly H_2O, NH_3, CO_2 and NO_2. Mass fragments suggesting amide formation are detected as well, but with a marginal ion current. Finally, the formation of the V-O bonds takes place and V_2O_5 crystallization occurs.
- In an inert atmosphere, the decomposition of oxalate residues extends up to 325 °C (as was already observed during the decomposition study of the ammonium-oxalato-VO^{2+} in Chapter 5). Next, amide functionalities form and convert to nitrile groups with the release of H_2O. These nitrile groups subsequently rearrange and emit HCN or $H_2C{=}C{=}N$. Due to the unintended presence of O_2 in the inert atmosphere also minor oxidative burnings of thermo stable compounds are observed. The residual sample, obtained at 625 °C, still contains compounds that are thermally stable. These compounds account for ~ 51 w/w% of the residual sample.

Part III

RELATING THE AQUEOUS PRECUROS CHEMISTRY TO THE VANADIUM OXIDE STOICHIOMETRY AND PHASE FORMATION

Chapter 7

Review: solution deposition route for vanadium oxide formation

Since the composition and structure of the VO^{2+} complexes, present in the aqueous solution, and their thermal decomposition pathway are understood, the actual vanadium oxide formation can be explored. Prior to this study, a brief literature elaboration on the technological importance of nanostructured vanadium oxides and a description of the selected solution-based deposition (i.e. *Chemical Solution Deposition*) and processing route will be given in this Chapter.

As discussed earlier, vanadium forms a variety of vanadium oxides (Figure 1). This variety includes single valence oxides (such as VO, V_2O_3, VO_2 and V_2O_5) and mixed valence oxides either belonging to the Magnéli phases, $V_nO_{2n\text{-}1}$, or the Wadsley phases, $V_{2n}O_{5n\text{-}2}$.[1–4] Some of these vanadium oxides with a specific structure and crystallinity are intensively investigated as candidate active materials in future technological devices.

7.1 VO_2 M1

7.1.1 The metal-to-insulator transition (MIT)

The mixed valance oxides from the Magnéli series, with a stoichiometry defined in Equation 7.1, take an intermediary position between the vanadium dioxide (VO_2) and the vanadium sesquioxide (V_2O_3).[4]

$$V_nO_{2n-1} = V_2O_3 + (n-2)VO_2 \tag{7.1}$$

The crystal structures of the Magnéli phases consist of rutile- and corundum-type building blocks.[2, 4] Except for V_7O_{13}, which behaves metallic at all temperatures [115], each Magnéli phase undergoes a semiconductor-to-insulator transition[1] (MIT) at a critical temperature, as given in Table 7.1. Each MIT of the listed vanadium oxides is accompanied by a structural phase transition and a change in its electrical and optical properties.[4, 5, 116]

Compound	n	T_{MIT} (°C)
VO	1	-150
V_2O_3	2	-105
V_3O_5	3	157
V_4O_7	4	-23
V_5O_9	5	-138
V_6O_{11}	6	-103
V_7O_{13}	7	
V_8O_{15}	8	-203
V_9O_{17}	9	-195
VO_2	∞	68

Table 7.1: Examples of mixed valance vanadium oxides belonging to the Magnéli series, V_nO_{2n-1}. The last column gives the transition temperature, T_{MIT}, of these vanadium oxides if a transition is theoretically predicted or experimentally observed.[3–5, 116]

Among the Magnéli vanadium oxides, only VO_2 demonstrates a transition temperature close to T_{Room} (68 °C in bulk crystals). The MIT causes an abrupt change in electrical resistivity (factor in the order of 10^4 - 10^5) and in its near-infrared optical properties in the 0.8 – 2.2. μm region (e.g. a transmittance of $\sim$ 70 % and $\sim$ 15 % at 20 °C and 80 °C, respectively).[3, 6, 7, 17, 18, 22, 23, 117–128] The MIT is mostly triggered by a temperature change. However, another approach to trigger the MIT is by applying an electrical field to a VO_2-based two- or three-terminal structure (i.e. a simple electronic switch or a gated electronic switch).[129–134]. In addition, Baum et al. and Cavalleri et al. have shown that the MIT occurs on a nanosecond timescale.[135, 136] These unique properties make VO_2 an excellent candidate for ultra fast thermal, optical and electronic switching and sensing applications in future technological devices such as intelligent windows, non-volatile memories, transistors and sensors.[5–7, 116, 131, 137–139]

The VO_2 MIT is accompanied by a structural phase transition (SPT) from a tetragonal or rutile (R) ($P4_2/mnm$) to monoclinic (M1) ($P2_1/c$) structure.[135, 137, 138, 140, 141] Recent studies suggest the involvement of an additional monoclinic (M2) (C2/m) phase near the MIT. It is claimed that both monoclinic phases have similar electrical properties, which explains the ignorance concerning the M2 phase in older literature. The VO_2 SPT from the rutile, via the M2 monoclinic, to the M1 monoclinic phases is

---

[1] This semiconductor-to-metal transition is more commonly named *metal-to-insulator*, abbreviated as *MIT*. The assignment of insulator to the low temperature phase is rather inaccurate since the band gap of e.g. VO_2 amounts 0.6 to 0.7 eV.

shown in Figure 7.1. In each structure, the vanadium atoms form chains in which each vanadium atom is surrounded by six oxygen atoms in a distorted octahedral geometry. In the high temperature, rutile phase all chains are straight and periodic. Whereas in the low temperature, monoclinic M1 phases every vanadium atom in the chain is dimerized and the chain is slightly tilted. Going from the rutile phase to the monoclinic M1 phase, the following structural changes occur[138, 140–142]:

- Every two vanadium atoms pair along the c-axis, resulting in an alternating short and long V-V interaction distance.
- The interaction axis of two paired vanadium atoms tilt with respect to the c-axis.

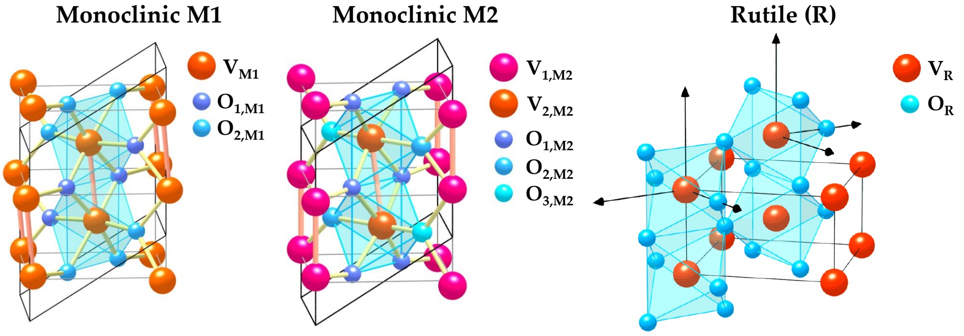

Figure 7.1: Crystal structure of the monoclinic M1, monoclinic M2 and rutile phases involved in the SPT of VO_2.[140]

7.1.2 Modulating the MIT parameters

The VO_2 metal-to-insulator transition is extremely sensitive to small changes in the intrinsic and extrinsic parameters such as the stoichiometry, crystallinity, morphology, film thickness, underlying surface and dopants. The effect of some of these parameters on the transition is summarized in Figure 7.2 and in Tables 7.2, 7.3, 7.4 and 7.5. Figure 7.2A shows an idealized transition curve during a triangular temperature sweep. The transition temperature in a forward sweep (i.e. heating), $\overrightarrow{T}_{MIT}$, rarely coincides with the one in the backward sweep (i.e. cooling), $\overleftarrow{T}_{MIT}$, which results in an hysteresis characterized by its width. $\overrightarrow{T}_{MIT}$ is typically higher than $\overleftarrow{T}_{MIT}$. The low temperature, semiconducting state is featured by:

- a higher electrical resistance, inconsistently expressed as *resistance* (Ω), *resistivity* (Ω.cm), conductance (S) or conductivity ($\nicefrac{S}{cm}$) in literature,
- a higher optical transmission in the 2000 μm – 2500 μm region, inconsistently expressed as % *transmittance* or % *reflectance* in literature.

The quantity conversion requires additional - often not available - information about the synthesized VO_2 such as the film thickness. Therefore, the literature comparison depicted in Figures 7.2B, 7.2C and 7.2D does not include the electrical or optical characteristics and is limited to the transition temperature and the hysteresis width.

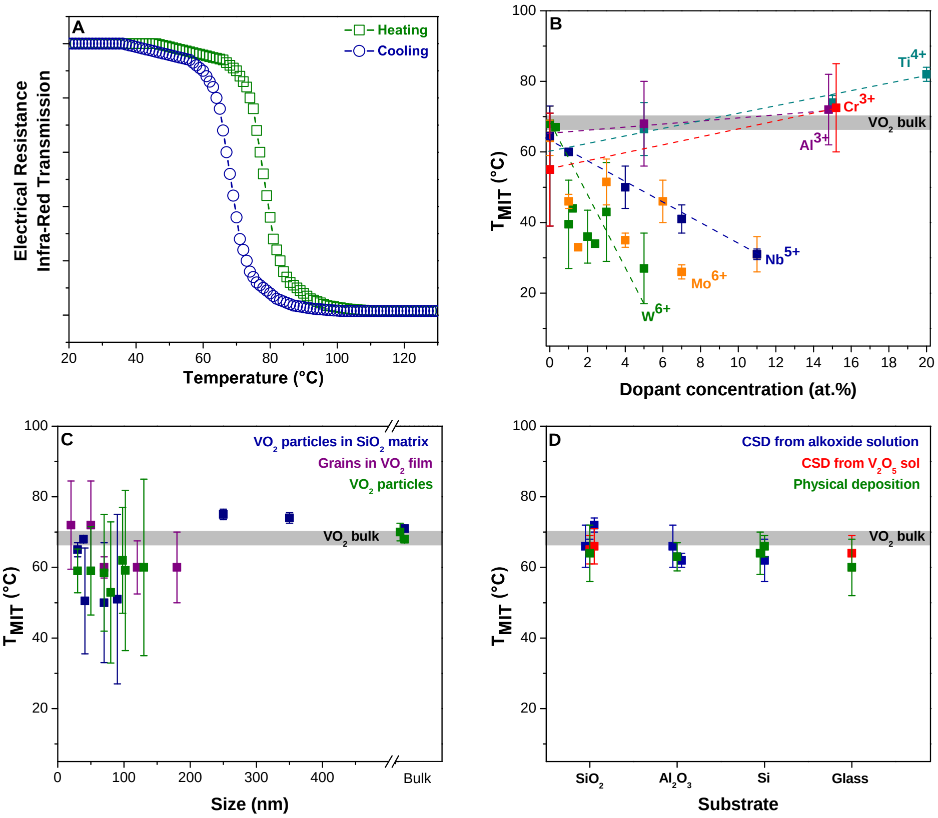

Figure 7.2: Idealized MIT curve during a triangular temperature sweep (A); and effect of the dopant concentration (B), morphology (C), synthesis method (D) and substrate (D) on the transition temperature (T_{MIT}). The symbols and bars in curves B, C and D correspond to the average T_{MIT} (i.e. average between T_{MIT} during heating and T_{MIT} during cooling) and the hysteresis width. CSD corresponds to chemical solution deposition. All data points are specified in Tables 7.2, 7.3, 7.4 and 7.5 and are based on references [7, 8, 15, 22, 23, 117, 119, 121–125, 129, 139, 143–150].

The transition temperature of VO_2 (i.e. 68 °C) is too high for many practical applications. Figure 7.2B shows that this transition temperature can be modulated significantly by doping of the VO_2 film. Among the studied dopants, high valent cations, such as W^{6+}, Mo^{6+} and Nb^{5+}, decrease the transition temperature while low valent cations, such as Al^{3+}, Cr^{3+} and Ti^{4+}, increase the transition temperature. Just as the ongoing discussion on the nature of the VO_2 MIT and SPT, the explanation for the shifting of the transition temperature by the addition of dopants is still unrevealed.

Figure 7.2C focuses on the influence of the morphology (i.e. grains size in a closed film or particle size) on the transition. It seems that, in general, small particles (with a size below 150 nm) are characterized by a slightly lower transition temperature and a broad hysteresis width (i.e. more than 20 °C). The lowering of the transition temperature with maximum 10 °C can be considered as negligible with respect to dominating hysteresis broadening. Kang et al. suggest that each grain or nanoparticle exhibits its own MIT characterized by a certain transition temperate and hysteresis width dependent on the particle or grain size. An analyzed area consists of many grains or nanoparticles and the observed transition curve can be constructed as the sum of the elementary transition curves, resulting in broadened hysteresis width.[150]

The last graph, Figure 7.2D, shows the contribution of the substrate and deposition technique on the VO_2 transition temperature and the hysteresis width. No significant difference is observed between the studied substrates (SiO_2, Al_2O_3, Si or glass) and deposition techniques. In all cases, the transition temperature of the films approaches the transition temperature of bulk VO_2 (i.e. 68 °C). With respect to bulk VO_2, the hysteresis curve is slightly broadened, but not to the extent of the hysteresis broadening observed for particles of granular films. This is consistent with statements of Nag et al. who claim an intermediate hysteresis width for thin films.[7–9, 17, 18] In addition, it is demonstrated that VO_2 thin films and nanoparticles tend to survive the stress generated during repeated cycles of SPT better then bulk VO_2.[7–9, 17, 18]

Synthesis method	Phase transformation	Dopant	$\overrightarrow{T}_{MIT}$	$\overleftarrow{T}_{MIT}$	Δ T$_{MIT}$	Semiconductor (electrical or *optical* quantity)	Metal	Reference
CSD of V_2O_5 sol on glass	$V_2O_5 \xrightarrow{CO/CO_2} VO_2$	0 %	69	59	10	$1.3\ 10^{-5}$ S	$6.0\ 10^{-3}$ S	[122]
CSD of V_2O_5 sol on glass	$V_2O_5 \xrightarrow{CO/CO_2} VO_2$	1 % Mo^{6+} %	47	45	2	$2.5\ 10^{-4}$ S	$1.5\ 10^{-2}$ S	[122]
CSD of V_2O_5 sol on glass	$V_2O_5 \xrightarrow{CO/CO_2} VO_2$	4 % Mo^{6+} %	36	34	2	$6.3\ 10^{-4}$ S	$1.3\ 10^{-2}$ S	[122]
CSD of V_2O_5 sol on glass	$V_2O_5 \xrightarrow{CO/CO_2} VO_2$	7 % Mo^{6+} %	27	25	2	$1.5\ 10^{-3}$ S	$1.2\ 10^{-3}$ S	[122]
CSD of $VO(OR_a)_3/R_aOH$ solution on Al_2O_3	$V_2O_5 \xrightarrow{\text{low } p_{O_2}} VO_2$	0 %	68	?	?	0.1 $^{S}/_{cm}$	$2.0\ 10^{3}$ $^{S}/_{cm}$	[119, 147]
CSD of $VO(OR_a)_3/R_aOH$ solution on Al_2O_3	$V_2O_5 \xrightarrow{\text{low } p_{O_2}} VO_2$	0.3 % W^{6+}	67	?	?	1.0 $^{S}/_{cm}$	$1.0\ 10^{3}$ $^{S}/_{cm}$	[119, 147]
CSD of $VO(OR_a)_3/R_aOH$ solution on Al_2O_3	$V_2O_5 \xrightarrow{\text{low } p_{O_2}} VO_2$	0.6 % W^{6+}	57	?	?	1.0 $^{S}/_{cm}$	$1.0\ 10^{3}$ $^{S}/_{cm}$	[119, 147]
CSD of $VO(OR_a)_3/R_aOH$ solution on Al_2O_3	$V_2O_5 \xrightarrow{\text{low } p_{O_2}} VO_2$	1.2 % W^{6+}	44	?	?	5.0 $^{S}/_{cm}$	$5.0\ 10^{2}$ $^{S}/_{cm}$	[119, 147]
CSD of $VO(OR_a)_3/R_aOH$ solution on Al_2O_3	$V_2O_5 \xrightarrow{\text{low } p_{O_2}} VO_2$	2.4 % W^{6+}	34	?	?	2.0 $^{S}/_{cm}$	$5.0\ 10^{2}$ $^{S}/_{cm}$	[119, 147]

Table 7.2: Literature overview of VO_2 MIT curves and the effect of dopants (and their concentration in at.%) on the transition curve. The optical quantity is always measured at a value between 2000 μm and 2500 μm. The following abbreviations are used: $\overrightarrow{T}_{MIT}$ (T$_{MIT}$ during heating), $\overleftarrow{T}_{MIT}$ (T$_{MIT}$ during cooling), Δ T$_{MIT}$ (hysteresis width), CSD (chemical solution deposition), S (Siemens), R_a (C_3H_7) and Transm. (transmittance).

Synthesis method	Phase transformation	Dopant	$\overrightarrow{T}_{MIT}$	$\overleftarrow{T}_{MIT}$	Δ T_{MIT}	Semiconductor	Metal	Reference
						(electrical or *optical* quantity)		
Sputtering on V-coated SiO_2	Direct VO_2	0 %	73	56	17	*37 % Transm.*	*5 % Transm.*	[148]
Sputtering on V-coated SiO_2	Direct VO_2	3 % W^{6+}	50	36	14	*35 % Transm.*	*5 % Transm.*	[148]
Sputtering on V-coated SiO_2	Direct VO_2	5 % W^{6+}	32	22	10	*30 % Transm.*	*5 % Transm.*	[148]
Sputtering on V-coated SiO_2	Direct VO_2	3 % Mo^{6+}	58	45	13	*42 % Transm.*	*5 % Transm.*	[148]
Sputtering on V-coated SiO_2	Direct VO_2	6 % Mo^{6+}	52	40	12	*42 % Transm.*	*5 % Transm.*	[148]
Sputtering on V-coated SiO_2	Direct VO_2	11 % Mo^{6+}	36	26	10	*37 % Transm.*	*12 % Transm.*	[148]
Sputtering on V-coated SiO_2	Direct VO_2	4 % Nb^{5+}	56	44	12	*52 % Transm.*	*7 % Transm.*	[148]
Sputtering on V-coated SiO_2	Direct VO_2	7 % Nb^{5+}	45	37	8	*25 % Transm.*	*7 % Transm.*	[148]
Sputtering on V-coated SiO_2	Direct VO_2	11 % Nb^{5+}	34	30	4	*14 % Transm.*	*7 % Transm.*	[148]
CSD of $VO(OR_a)_3/R_aOH$ solution on glass	$V_2O_5 \xrightarrow{5\,\%\,H_2} VO_2$	0 %	78	46	32	*50 % Transm.*	*2 % Transm.*	[7, 117, 149]
CSD of $VO(OR_a)_3/R_aOH$ solution on glass	$V_2O_5 \xrightarrow{5\,\%\,H_2} VO_2$	5 % Ti^{4+}	74	58	16	*50 % Transm.*	*2 % Transm.*	[7, 117, 149]
CSD of $VO(OR_a)_3/R_aOH$ solution on glass	$V_2O_5 \xrightarrow{5\,\%\,H_2} VO_2$	15 % Ti^{4+}	78	70	8	*52 % Transm.*	*10 % Transm.*	[7, 117, 149]
CSD of $VO(OR_a)_3/R_aOH$ solution on glass	$V_2O_5 \xrightarrow{5\,\%\,H_2} VO_2$	20 % Ti^{4+}	85	82	3	*40 % Transm.*	*10 % Transm.*	[7, 117, 149]
CSD of $VO(OR_a)_3/R_aOH$ solution on glass	$V_2O_5 \xrightarrow{5\,\%\,H_2} VO_2$	1 % W^{6+}	53	32	21	*40 % Transm.*	*2 % Transm.*	[7, 117, 149]
CSD of $VO(OR_a)_3/R_aOH$ solution on glass	$V_2O_5 \xrightarrow{5\,\%\,H_2} VO_2$	2 % W^{6+}	43	28	15	*35 % Transm.*	*5 % Transm.*	[7, 117, 149]
CSD of $VO(OR_a)_3/R_aOH$ solution on glass	$V_2O_5 \xrightarrow{5\,\%\,H_2} VO_2$	5 % Al^{3+}	80	57	23	*50 % Transm.*	*2 % Transm.*	[7, 117, 149]
CSD of $VO(OR_a)_3/R_aOH$ solution on glass	$V_2O_5 \xrightarrow{5\,\%\,H_2} VO_2$	15 % Al^{3+}	83	61	22	*46 % Transm.*	*20 % Transm.*	[7, 117, 149]
CSD of $VO(OR_a)_3/R_aOH$ solution on glass	$V_2O_5 \xrightarrow{5\,\%\,H_2} VO_2$	15 % Cr^{3+}	78	66	12	*62 % Transm.*	*20 % Transm.*	[7, 117, 149]

Table 7.3: Literature overview of VO_2 MIT curves and the effect of dopants (and their concentration in at.%) on the transition curve. The optical quantity is always measured at a value between 2000 μm and 2500 μm. The following abbreviations are used: $\overrightarrow{T}_{MIT}$ (T_{MIT} during heating), $\overleftarrow{T}_{MIT}$ (T_{MIT} during cooling), Δ T_{MIT} (hysteresis width), CSD (chemical solution deposition), S (Siemens), R_a (C_3H_7) and Transm. (transmittance).

Synthesis method	Morphology	Size (nm)	$\overrightarrow{T}_{MIT}$	$\overleftarrow{T}_{MIT}$	Δ T$_{MIT}$	Semiconductor (electrical or *optical* quantity)	Metal	Reference
Vanadium implanting in SiO_2 host	VO_2 particles in SiO_2	40	75	35	40	*1.00 R. Transm.*	*0.80 R. Transm.*	[125]
Vanadium implanting in SiO_2 host	VO_2 particles in SiO_2	70	68	33	35	*1.00 R. Transm.*	*0.68 R. Transm.*	[125]
Vanadium implanting in SiO_2 host	VO_2 particles in SiO_2	90	66	35	31	*1.00 R. Transm.*	*0.65 R. Transm.*	[125]
CSD of $VO(OR_b)_3/Si(OR_b)_3/$ solution on glass	VO_2 particles in SiO_2	30	69	61	8	*22 % Transm.*	*15 % Transm.*	[121]
CSD of $VO(OR_b)_3/Si(OR_b)_3$ solution on glass	VO_2 particles in SiO_2	40	69	67	2	*28 % Transm.*	*14 % Transm.*	[121]
CSD of $VO(OR_b)_3/Si(OR_b)_3$ solution on glass	VO_2 particles in SiO_2	250	77	72	5	*34 % Transm.*	*14 % Transm.*	[121]
CSD of $VO(OR_b)_3/Si(OR_b)_3$ solution on glass	VO_2 particles in SiO_2	350	77	72	5	*40 % Transm.*	*11 % Transm.*	[121]
CSD of $VO(OR_b)_3/Si(OR_b)_3$ solution on glass	VO_2 particles in SiO_2	950	73	71	2	*55 % Transm.*	*10 % Transm.*	[121]
ACSD of V_2O_5/N_2H_4/HCl/PVP solution on SiO_2	VO_2 particles	30	65	53	12	*73 % Transm.*	*21 % Transm.*	[139, 150]
ACSD of V_2O_5/N_2H_4/HCl/PVP solution on SiO_2	VO_2 particles	50	76	41	35	*70 % Transm.*	*15 % Transm.*	[139, 150]
ACSD of V_2O_5/N_2H_4/HCl/PVP solution on SiO_2	VO_2 particles	70	75	42	33	*71 % Transm.*	*17 % Transm.*	[139, 150]
ACSD of V_2O_5/N_2H_4/HCl/PVP solution on SiO_2	VO_2 particles	80	73	33	40	*63 % Transm.*	*13 % Transm.*	[139, 150]
ACSD of V_2O_5/N_2H_4/HCl/PVP solution on SiO_2	VO_2 particles	100	82	37	45	*69 % Transm.*	*19 % Transm.*	[139, 150]
ACSD of V_2O_5/N_2H_4/HCl/PVP solution on SiO_2	VO_2 particles	130	85	35	50	*69 % Transm.*	*16 % Transm.*	[139, 150]
Pulsed laser deposition on Si and oxidative PDA	Grained VO_2 film	10	56	58	2	*0 % Refl.*	*55 % Refl.*	[8]
Pulsed laser deposition on Si and oxidative PDA	Grained VO_2 film	70	63	57	6	*0 % Refl.*	*62 % Refl.*	[8]
Pulsed laser deposition on Si and oxidative PDA	Grained VO_2 film	120	68	52	16	*0 % Refl.*	*67 % Refl.*	[8]
Pulsed laser deposition on Si and oxidative PDA	Grained VO_2 film	180	70	50	20	*0 % Refl.*	*67 % Refl.*	[8]
CSD of $VO(acac)_2/CH_3OH$ on quartz	Grained VO_2 film	20	85	59	26	*90 % Transm.*	*40 % Transm.*	[144]
CSD of $VO(acac)_2/CH_3OH$ on quartz	Grained VO_2 film	50	90	54	36	*83 % Transm.*	*40 % Transm.*	[144]

Table 7.4: Literature overview of VO_2 MIT curves and the effect of the morphology (and its characteristic size) on the transition curve. The optical quantity is always measured at a value between 2000 μm and 2500 μm. The following abbreviations are used: $\overrightarrow{T}_{MIT}$ (T$_{MIT}$ during heating), $\overleftarrow{T}_{MIT}$ (T$_{MIT}$ during cooling), Δ T$_{MIT}$ (hysteresis width), CSD (chemical solution deposition), ACSD (aqueous chemical solution deposition), R. Transm. (relative transmission), R$_b$ (C_2H_5), Transm. (transmittance), PVP (polyvinylpyrrolidone), PDA (post deposition anneal), and Refl. (reflectance).

Synthesis method	Substrate	Phase transformation	$\overrightarrow{T}_{MIT}$	$\overleftarrow{T}_{MIT}$	Δ T$_{MIT}$	Semiconductor	Metal	Reference
						(electrical or *optical* quantity)		
CSD of VO(OR$_a$)$_3$/R$_a$OH solution	Al_2O_3	$V_2O_5 \xrightarrow{\text{low } p_{O_2}} VO_2$	64	60	4	10^5 Ω	1.0 Ω	[23, 147]
CSD of VO(OR$_a$)$_3$/R$_a$OH solution	SiO_2	$V_2O_5 \xrightarrow{\text{low } p_{O_2}} VO_2$	73	71	2	10^5 Ω	10^2 Ω	[23, 147]
CSD of VO(OR$_a$)$_3$/R$_a$OH solution	SiO_2	$V_2O_5 \xrightarrow{\text{Reducing atmosphere}} VO_2$	68	64	4	10^3 Ω	5.0 10^{-1} Ω	[22]
CSD of VO(OR$_a$)$_3$/R$_a$OH solution	SiO_2	$V_2O_5 \xrightarrow{\text{Reducing atmosphere}} VO_2$	68	64	4	*60 % Transm.*	*2 % Transm.*	[22]
CSD of VO(OR$_a$)$_3$/R$_a$OH solution	Al_2O_3	$V_2O_5 \xrightarrow{\text{Reducing atmosphere}} VO_2$	64	62	2	10^4 Ω	5.0 10^{-1} Ω	[22]
CSD of VO(OR$_a$)$_3$/R$_a$OH solution	Al_2O_3	$V_2O_5 \xrightarrow{\text{Reducing atmosphere}} VO_2$	64	62	2	*60 % Transm.*	*0 % Transm.*	[22]
CSD of V_2O_5/alcohol solution	SiO_2	$V_2O_5 \xrightarrow{N_2} VO_2$	72	60	12	20 Ω.cm	0.2 Ω.cm	[143]
CSD of V_2O_5/alcohol solution	SiO_2	$V_2O_5 \xrightarrow{N_2} VO_2$	72	60	12	*100 % Transm.*	*50 % Transm.*	[143]
CSD of V_2O_5/alcohol solution	Al_2O_3	$V_2O_5 \xrightarrow{N_2} VO_2$	72	60	12	30 Ω.cm	0.2 Ω.cm	[143]
CSD of V_2O_5/alcohol solution	Al_2O_3	$V_2O_5 \xrightarrow{N_2} VO_2$	72	60	12	*100 % Transm.*	*50 % Transm.*	[143]
CSD of V_2O_5/alcohol solution	SiO_2	$V_2O_5 \xrightarrow{N_2} VO_2$	68	56	12	20 Ω.cm	0.1 Ω.cm	[143]
CSD of V_2O_5/alcohol solution	SiO_2	$V_2O_5 \xrightarrow{N_2} VO_2$	68	56	12	*100 % Transm.*	*65 % Transm.*	[143]
CSD of V_2O_5 sol	Glass	$V_2O_5 \xrightarrow{CO/CO_2} VO_2$	69	59	10	1.3 10^{-5} S	6 10^{-3} S	[122]
CSD of V_2O_5 sol	SiO_2	$V_2O_5 \xrightarrow{4\,\%\, H_2} VO_2$	69	61	8	10^6 Ω	10^3 Ω	[145]
CSD of V_2O_5 sol	SiO_2	$V_2O_5 \xrightarrow{\text{low } p_{O_2}} VO_2$	71	61	10	3.0 Ω.cm	10^{-3} Ω.cm	[146]
Sputtering	Glass	Direct VO_2	68	52	16	1.5 10^{-5} S	6 10^{-3} S	[123]
Sputtering	SiO_2	Direct VO_2	72	56	16	*37 % Transm.*	*5 % Transm.*	[148]
Pulsed laser deposition	Al_2O_3	Direct VO_2	67	59	8	10^6 Ω	1.0 Ω	[129]
Atomic layer deposition	Si	Direct VO_2	70	58	12	10^{-1} Ω.cm	10^{-3} Ω.cm	[15]

Table 7.5: Literature overview of VO_2 MIT curves and the effect of the synthesis method and substrate on the transition curve. The optical quantity is always measured at a value between 2000 μm and 2500 μm. The following abbreviations are used: $\overrightarrow{T}_{MIT}$ (T$_{MIT}$ during heating), $\overleftarrow{T}_{MIT}$ (T$_{MIT}$ during cooling), Δ T$_{MIT}$ (hysteresis width), CSD (chemical solution deposition), R. Transm. (relative transmission), R$_a$ (C_3H_7) and Transm. (transmittance).

7.2 Intercalation vanadium oxides

The layered oxides of vanadium – i.e. V_2O_5, V_6O_{13}, VO_2 (monoclinic *B phase*), V_4O_{10} and V_3O_8 – have received a lot of attention during the last decade(s) as candidate cathode materials for lithium batteries. Figure 7.3 shows the structures of these vanadium oxides and the intercalated lithium atoms for which the layered lattice acts as a perfect host.[10]

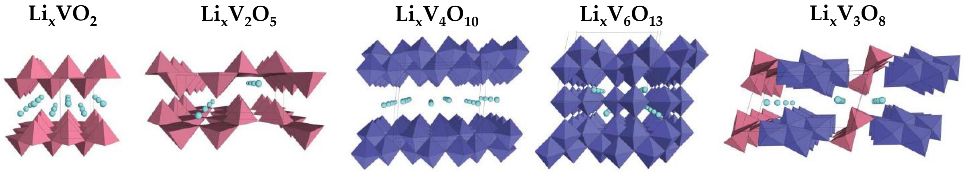

Figure 7.3: Structures of layered and lithiated vanadium oxides: Li_xVO_2, $Li_xV_2O_5$, $Li_xV_4O_{10}$, $Li_xV_6O_{13}$ and $Li_xV_3O_8$. The VO_5 square pyramids, VO_6 octahedra and Li atoms are represented in pink, blue and turquoise, respectively.[10]

The vanadium pentoxide, V_2O_5, is mostly investigated and its intercalation mechanism is well documented.[151] As shown in Figure 7.3, orthorhombic V_2O_5 consists of layers of edge and corner sharing VO_5 square pyramids. The electrochemical lithium intercalation of V_2O_5 is associated with several phases depending on the amount of intercalated lithium. Figure 7.4 presents the evolution of the $Li_xV_2O_5$ phases with the amount of intercalated lithium, the cycling of the ω phase and structural representation of $\delta - LiV_2O_5$ and $\gamma - Li_2V_2O_5$. The α, ϵ and δ phases exist for $x < 1$ and show a V_2O_5-type of structure with a small distortion of the layers. For these phases, the original, lithium-free V_2O_5 can be recovered upon lithium deintercalation. However if x exceeds 1 and the steep potential drop is observed, the initial V_2O_5 phase can no longer be recovered. Instead, a structure associated with the γ phase is formed. In this structure, the layers are not planar, but parallel crenelated. This γ phase can be, reversibly, cycled in the range $0 < x < 2$ without changing the γ-type structure. Upon further intercalation (i.e. $x = 3$), a new irreversible ω-phase with a rock-salt type structure is formed. This ω phase can be intercalated and deintercalated for $0.5 < x < 2.5$.[10, 13, 152]

Since the elucidation of the electrochemical behavior of V_2O_5, various vanadium oxides are synthesized and investigated as host for Li atoms. The V_6O_{13} is such a studied candidate cathode material. The structure of monoclinic V_6O_{13} contains slightly distorted VO_6 octahedra joined by edge sharing into single and double zigzag chains and linked together by additional edge sharing into single and double sheets of octahedra. The single and double sheets alternate and are interconnected by corner sharing into a three−dimensional framework.[12, 153] The reversible insertion of lithium into the cavities of the V_6O_{13} structure was first demonstrated by Murphy et

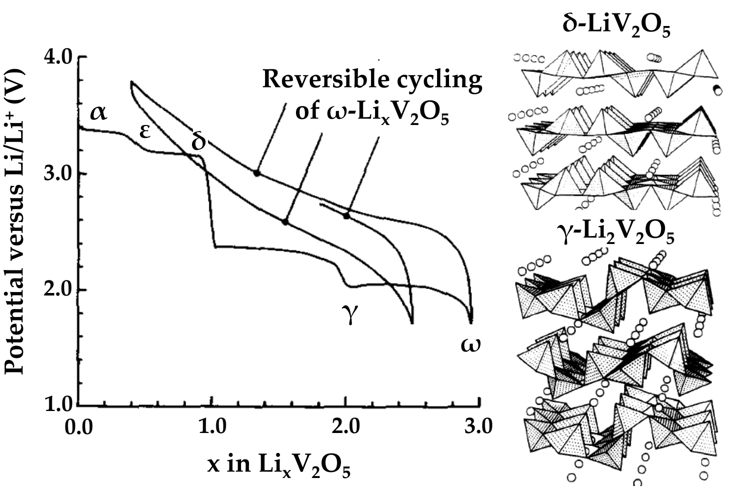

Figure 7.4: Evolution of the $Li_xV_2O_5$ phases with the amount of intercalated lithium, the cycling of the ω phase and structural representation of $\delta - LiV_2O_5$ and $\gamma - Li_2V_2O_5$.[13]

al. and further studied by West et al. V_6O_{13} can accommodate up to 8 lithium atoms. The intercalation of lithium proceeds through several phase changes, as illustrated by the discharge curve in Figure 7.5. After the first three intercalation plateaus (i.e. at 2.8 V, 2.6 V and 2.5 V), every site with a fivefold oxygen coordination is occupied by lithium atoms. The resulting structure is similar to the initial V_6O_{13} structure, but expanded by 7.6 % in the direction of the layers (c-axis). If the intercalation continues (i.e. x > 3), a second intercalation plateau is observed at 2.1 V and the lithium atoms are rearranged occupying the square planar and the square pyramidal sites of the V_6O_{13} lattice. This results in a re-contraction of the unit cell along the c-axis and an expansion of 5.6 % along the b-axis. These phase transitions make it very difficult to obtain a good cyclability.[12, 152–155]

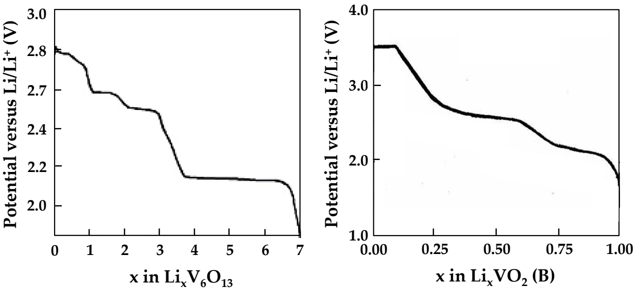

Figure 7.5: Discharge curve of V_6O_{13} and VO_2 B showing the potential decrease as a function of the amount of intercalated lithium. Both curves are adapted from reference [155, 156].

As shown in Figure 7.3, the VO_2 B structure consists of VO_5 square pyramids which share corners of the base to form a sheet. In contrast to popular V_2O_5, the lithium intercalation in VO_2 B is less studied. Zachau−Christiansen et al. showed the first discharge curve of Li_xVO_2 B (Figure 7.5). Li_xVO_2 B exhibits a relatively smooth discharge curve upon lithium intercalation. A first potential plateau is observed at 2.5 V and is associated with the intercalation of 0.25 to 0.50 atoms of lithium per formula unit. A second potential plateau is present at 2.0 V and corresponds to the intercalation of $\sim$ 0.8 atoms of lithium per formula unit. In the region $0 < x < 1$, Li_xVO_2 B, the intercalation is fully reversible.[156]

7.3 Overview of solution-based routes for the formation of vanadium oxides

The most common solution-based routes are listed by Van den Rul et al. and Schwartz et al. who classify them based on (i) their gel-forming mechanism and (ii) the involvement of the metal cations in the gel structuring.[21, 33].

7.3.1 Metallo-organic decomposition route

In this precursor route, each metallo-organic compound is dissolved separately in a non-interacting solvent. The solutions are then combined to yield a new solution which reflects the stoichiometry of the desired metal oxide. The starting compounds – mostly carboxylates with a long aliphatic group or β-diketonates (such as acetylacetonates) – are water insensitive and do not exhibit hydrolysis or condensation. Actually, this solution is a simple mixture of the starting compounds and does not feature gel formation upon drying. Obviously, this precursor route is straightforward, but often associated with cracking of the deposited film during the film processing. In these cases the non-interacting solvent and the extended metallo-organics are replaced by polar solvent and smaller metallo-organics, respectively.[21, 33]

Pan et el. and Zhang et al. prepared a homogeneous sol by dissolving vanadyl acetylacetonate ($VO(acac)_2$) in methanol with a vanadium concentration of $\sim$ 0.125 M. Homogeneous films are obtained after spin coating on glass or on Si. The wet film is subsequently dried at 60 or 80 °C and annealed in a N_2 ambient at 500–600 °C. They directly obtain crystalline VO_2 M1 with a thickness of 20–30 nm per cycle.[144, 157]

7.3.2 Alkoxide sol-gel route

In the alkoxide sol-gel route, molecular alkoxide compounds polymerize into a three-dimensional network which, subsequently, converts to a xerogel by removing the alkanol solvent. The starting compound is typically a metal alkoxide ($M(OR)_n$) or a mixture of a metal salt and a metal alkoxide in an alcohol. Such a compound hydrolyzes readily in the presence of water and forms a partially hydrolyzed monomer

($M(OR)_{n\text{-}h}(OH)_h$) as given in Equation 7.2. These partially hydrolyzed monomers condensate via alkolation, alkoxolation, olation or oxolation reactions into oligomers. Figure 7.6 schematically shows these possible condensation mechanisms. Further condensation of these oligomers results in large clusters and eventually in a three-dimensional network by aggregation of these clusters.[21, 39]

$$M(OR)_n + hH_2O \longrightarrow M(OR)_{n-h}(OH)_h + hR(OH) \tag{7.2}$$

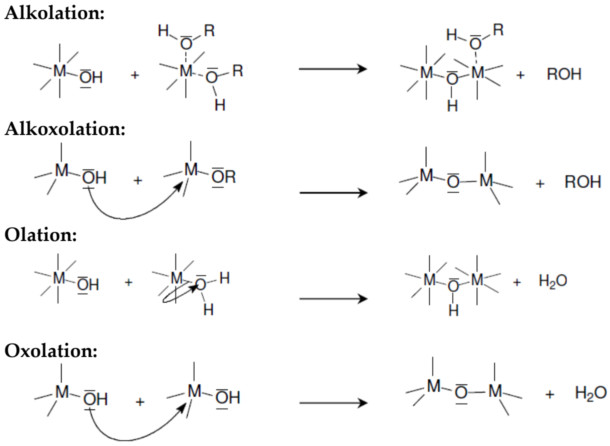

Figure 7.6: Possible mechanism for the condensation of partially hydrolyzed monomers towards oligomers.[21]

Alkoxides are very reactive to ambient humidity, which implies the use of inconvenient experimental circumstances (i.e. inert atmosphere and glove box). Nonetheless, this alkoxide-based sol-gel route is the most commonly applied chemical solution route for the formation of vanadium oxides. Typical vanadium alkoxide starting compounds are the vanadium(V) oxytriisopropoxide $VO(C_3H_7O)_3$ and the vanadium(V) oxytriethoxide $VO(C_2H_5O)_3$, dissolved in isopropanol or ethanol. Chae et al.[23, 118, 147], Béteille et al.[117, 149], Hanlon et al.[122], Chen et al.[121] and Partlow et al.[22] used these vanadium alkoxide solutions in the formation of nanostructured vanadium oxides on glass, on SiO_2 and on Al_2O_3. In all the mentioned studies, V_2O_5 is first prepared by drying and heating of the deposited film in air at temperatures around 80 °C and between 400 °C and 700 °C, respectively. The formed V_2O_5, either amorphous or crystalline, is subsequently reduced to VO_2 (B or M1 phase) in a H_2, CO/CO_2 or low p_{O_2} ambient.[7, 22, 23, 117, 118, 121, 122, 147, 149, 158]

7.3.3 Aqueous solution-gel route

In the aqueous solution-gel route, the metal cation reacts with chelating α-hydroxy-carboxylato ligands to form α-hydroxy-carboxylato metal ion complexes in water.

These complexes (i) prevent undesired hydrolysis of the metal cation and (ii) inhibit precipitation upon water evaporation during the film deposition step via the formation of a cross linked three-dimensional network.[21, 33] Citrate is typically chosen as chelating agent and has resulted in stable solutions containing among others Ti^{4+}, Zr^{4+}, Nb^{5+}, Ta^{5+}, Gd^{3+}, Ln^{3+} and Zn^{2+}. These solutions are used successfully for the preparation of mono- and multimetal oxide compounds such as $SrBi_2Nb_2O_9$, ZnO, $(Nb_{1\text{-}x}Ta_x)_2O_5$ and TiO_2.[61, 62, 85, 86]

Even though the aqueous vanadium chemistry and its complexation by a chelating α-hydroxy-carboxylato ligand such as citrate, is frequently studied (see Chapter 1), its employment as an aqueous solution-gel precursor for the formation of vanadium oxide nanostructures is scarcely reported. It seems that the interest for the vanadium complexes is to be found in medical and biochemical applications. Hardy et al. performed preliminary work on the synthesis of an aqueous citrato-peroxo-dioxovanadate(V) precursor solution.

7.3.4 Polymer complex controlled route

In the polymer complex controlled route, the formation of a three-dimensional network made by an organic polymer, in which the metal cations are distributed, is aimed for. This polymer-based network can be:

- in-situ formed if a gel of coordinated metal cations is built during the polymerization of monomers or oligomers,
- formed by the direct interaction of the metal cations with the polymer.

The *Pechini route* is a typical example of such an in-situ polymer complex controlled route. In this Pechini route, carboxylic acids (e.g. citric acid) and carboxylate metal ion complexes (e.g. citrato complexes) are dissolved in ethylene glycol. The heating of this solution induces an esterification of the $-OH$ function of the ethylene glycol and the $-COOH$ or $-COO^-$ group of the acid or the metal ion complex. The formed ester-based species contain, in turn, an $-OH$ and a COOH or COO^- functionality. In this way, a polymer-based network of metal cations is sequentially built. A similar gel structure is obtained by the direct dissolution of a metal coordinating polymer and a metal salt. In this case, the polymer is not in-situ formed, but metal cations are still attached to the polymer.

Gao et al. have reported such a polymer-complex controlled route for the formation of crystalline VO_2 M1. In their approach, $VOCl_2$ and polyvinylpyrrolidone (PVP) are dissolved in water. In comparison to the PVP-free solution, a strong increase in the stability of the solution (from days to months) is observed and ascribed to the interaction between the polymer and the oxovanadate(IV) ion. They claim that in PVP the nitrogen of the amide group partially donates its free electron pair to the neighboring carbonyl group. This results in a negatively charged carbonyl group and a positively charged amine group which electrostatically interact with the oxovanadate(IV) ions present. This PVP-based oxovanadate(IV) solution is employed for the formation of a crystalline VO_2 M1 film by spin coating of the solution on fused silica, drying at 60 °C and a final anneal at 600 °C in an N_2 ambient.[139, 150, 159] Interestingly, the PVP does not only assist in the stability of the precursor solution and in the gel formation upon solvent evaporation, but is also indispensable in the formation of VO_2 M1. They assign this observation to the formation of in-situ reductive gasses which (i) could prevent vanadium(IV) from oxidazing or (ii) could reduce vanadium(V) if formed during one of the previous deposition or processing steps. The reductive gasses originate from the thermal degradation of PVP.[159]

7.3.5 Viscosity controlled route

In an alternative polymer based approach, a non-interacting polymer can be introduced in the - metal cation containing - solution. Here, the increased viscosity upon solvent evaporation guarantees the spatial fixation and homogeneous distribution of the metal cations in the gel structure.[21]

7.3.6 Colloidal or particulate sol-gel route

In this route, colloidal particles, with a diameter of 1–100 nm, are formed and dispersed in a liquid medium to form a sol. During the solvent evaporation (i.e. the gelation), this sol converts to a gel in which the particle interaction is electrostatically and/or sterically controlled. The obtained, particulate gel consists of aggregates or colloidal particles dispersed down to the nanometer scale.[21]

Dachaun et al. report the synthesis of a brownish V_2O_5 sol by pouring molten V_2O_5 into water at room temperature (i.e. quenching of the V_2O_5 melt). This V_2O_5 sol is subsequently used for the formation of nanostructured, crystalline V_2O_5 via chemical deposition and processing steps (i.e. spin coating - drying - thermal treatment at 400 °C in air).[25] In more recent work, this V_2O_5 sol is also employed for the formation of VO_2 by adding a reductive step in an H_2, N_2, CO/CO_2 or low p_{O_2} ambient to the processing sequence.[122, 145, 146, 160, 161]

7.4 Chemical Solution Deposition and processing

Chemical solution deposition (CSD) routes have already been successfully employed for more than 25 year in the preparation of amorphous or crystalline, electronic, metal oxide, thin films.[2] This route is based on the deposition of a wet, thin film on a

---

[2] Note that the *CSD* name does not specify the solution used. In this work, an aqueous solution containing citrato/oxalato-VO^{2+} complexes is systematically used as precursor solution.

substrate and its subsequent conversion to a metal oxide film through a sequence of thermal steps.[33] Figure 7.7 shows a flowchart of a typical CSD process, if spin coating is chosen as the coating technique.

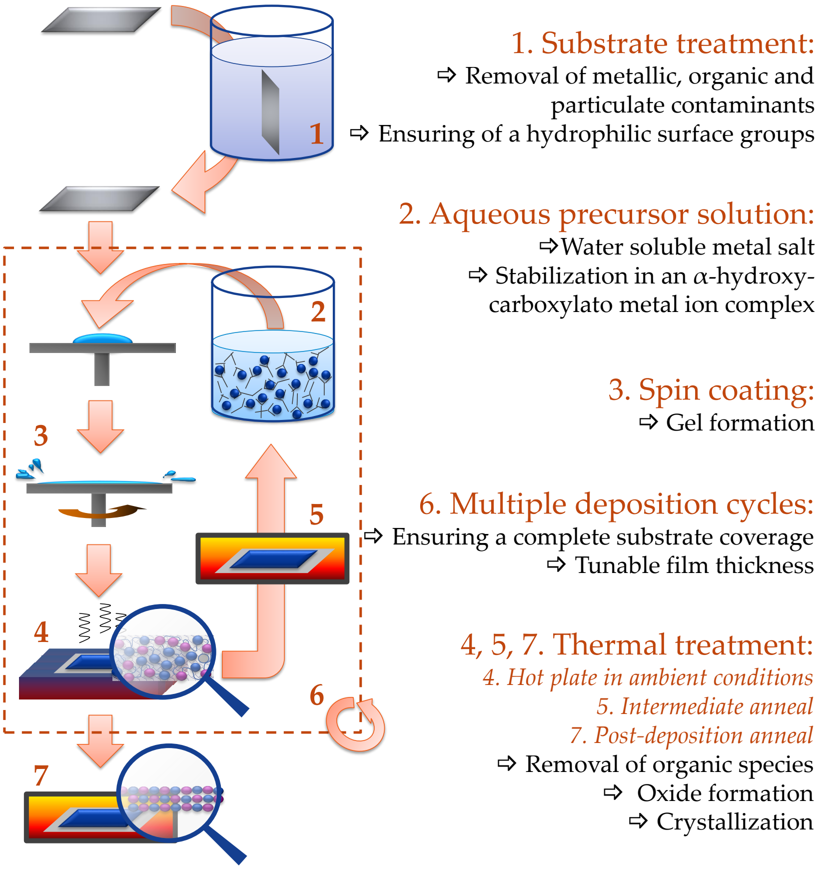

Figure 7.7: Flowchart of a typical CSD process if (i) the precursor is an aqueous solution containing α-hydroxy-carboxylato metal ion complexes and (ii) spin coating is chosen as the coating technique. The CSD flowchart is expanded by pre-deposition substrate treatment. On the right-hand site, the experimental manipulation and the most important objectives of each manipulation are given. This scheme is designed by IMO-IPC research group at the Hasselt University and is based on references [21, 33].

The shown CSD flowchart is expanded by a pre-deposition substrate treatment. Note that some steps (e.g. a thermal treatment) overlap and can be applied multiple times. In each step of the CSD route, the step parameters – which will influence the final metal oxide and its properties – can be tuned. This is the strength of the CSD process, but simultaneously also the difficulty. Nevertheless, the CSD route is a fast, rather cheap and experimentally easy method for the formation of metal oxide films with specific materials and functional properties.

7.4.1 Substrate treatment

Via the CSD process, the aqueous precursor is deposited and transformed into a metal oxide. The first interaction of the aqueous solution and the substrate is crucial. If the aqueous solution does not sufficiently attach to the substrate – because of surface contamination or hydrophobic surface groups – the obtained film will exhibit artifacts and inhomogeneities. Possible surface contaminants are organic impurities, adsorbed molecules, anions, metals and particulates originating from the substrate production, transportation, packaging and dust collection.[162] Thus, a pre-deposition substrate treatment (or *cleaning*), aiming to remove these contaminants and to ensure hydrophilic surface groups, is necessary for a successful CSD process. It is important to realize that such a substrate treatment could cause other effects: the introduction of new contaminants, surface modification (e.g. etching and roughening) and surface reactions.[162]

In this work, two treatments have been applied: a wet treatment (i.e. the *sulfuric acid peroxide mixture / ammonia peroxide mixture, SPM/APM* route) and dry treatment (i.e. the *UV/O_3* route). The principles of both treatments will be briefly discussed below. Experimental details can be found in Appendix C.

Wet treatment: SPM/APM

The first step - SPM - consists of a mixture of H_2SO_4 and H_2O_2 and is often named *Piranha solution*. In this solution, the oxidative *Caro's acid* is formed as shown in Equation 7.3.

$$\mathrm{H_2SO_4 + H_2O_2 \longrightarrow H_2SO_5 + H_2O} \tag{7.3}$$

Due to the strong oxidative properties of this mixture, organic contaminants are removed from the substrate (Equations 7.4, 7.5 and 7.6). In addition, metallic contaminants are removed by the SPM treatment. The SPM might (i) leave residual sulfates behind if the substrate is not properly rinsed and (ii) could cause oxidation of a bare Si surface (obtained e.g. after an HF dip).[162]

$$\textit{Dissolution}:\quad \mathrm{H_2SO_4 + C_xH_y(s) \longrightarrow H_2SO_4 + C_xH_y(aq)} \tag{7.4}$$

$$\textit{Decomposition}:\quad \mathrm{(4x{+}y)H_2SO_5 + 2\,C_xH_y(aq) \longrightarrow (4x{+}y)H_2SO_4 + 2\,xCO_2(g) + yH_2O} \tag{7.5}$$

$$\textit{Decomposition}:\quad \mathrm{H_2SO_4 + C_xH_y(aq) \xrightarrow{H_2O_2} H_2O + C_xH_{y-1}SO_3H(aq)} \tag{7.6}$$

In the second step - APM - a mixture of H_2O, H_2O_2 and NH_3 is made. This mixture consists of several components, each responsible for the removal of a specific contaminant or a specific surface modification. The H_2O_2 is responsible for the formation of the hydrophilic Si−OH surface groups by oxidation of the hydrophobic Si−H surface groups. The APM is capable of removing particulates from the substrates by etching of the Si or SiO_2 surface. This etching directly indicates the major problem during an APM treatment: roughening of surface by etching. Etch rates of 0.7 $^{nm}/_{min}$ and 0.1 $^{nm}/_{min}$ are suggested for Si and SiO_2, respectively.[162]

In conclusion, the consecutive SPM and APM treatment removes organic, metallic and particulate contaminants and results in hydrophilic, Si−OH surface groups.

Dry treatment: UV/O_3

The UV/O_3 treatment is a softer surface treatment and focuses on the removal of organic contaminants. During the treatment, the produced O_3 is converted to the intermediate atomic oxygen. This atomic oxygen is very reactive and easily oxidizes organic contaminants.[21]

7.4.2 Aqueous precursor solution

Despite, the discussion concerning the possible precursor solutions in section 7.3, a few comments must be given on the requirements for the solution chemistry to ensure its successful implementation in the CSD route[33]:

- Except for the metal cation, each element in the solution must be released into the gas phase without undesired thermo-stable residues during one of the applied thermal treatments.
- The formation of a gel upon water evaporation during the coating is aimed for and requires the formation of a three-dimensional network.
- The solution must feature a significant stability (towards precipitation or other ageing effects).
- The solution should exhibit a good wetting to the substrate to assure a homogeneous film without thickness variation or island formation.

7.4.3 Spin coating

Spin coating is a popular technique to deposit ultra thin (~ 10 nm) to relatively thick (~ 5 μm), continuous coatings on flat substrates.[84]

The basic principle of this spin coating is the equilibrium between (i) the centrifugal force applied on the deposited liquid, leading to a thinning of the layer, and (ii)

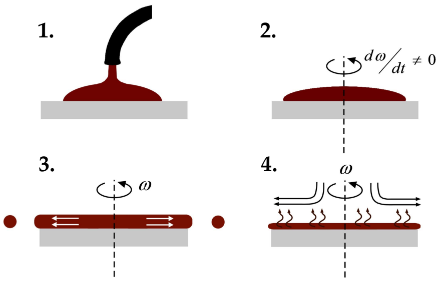

Figure 7.8: Schematic of the different stages during a spin coat process: dispensation (a), acceleration (b), spin off (c) and evaporation (d).[163]

the viscous force which increases upon evaporation of the solvent during the spin coating, counteracting the layer thinning.[84]

The spin coating process is depicted in Figure 7.8 and consists of a sequence of steps[33, 84, 162, 163]:

1. Dispersion of an excess of the precursor solution on the substrate.
2. Acceleration of the substrate until the desired spinning speed is achieved. During this step already ~ 95 % of the liquid is spun off the substrate.
3. Spin off during constant speed rotation. In this step, the film thins by the centrifugal force and fluid dynamics on the liquid layer present. The thinning during this spin off step is proportional to the spinning speed ω (rpm) and the film viscosity η (Equation 7.7).

$$\mathrm{t}_{\text{spin off}} \propto \omega^{-1/2}\eta^{1/3} \tag{7.7}$$

4. Evaporation during constant speed rotation. In this step, the film further thins by evaporation of the solvent (Equation 7.8).

$$\mathrm{t}_{\text{evaporation}} \propto \omega^{-1/2} \tag{7.8}$$

5. After a pre-defined time, the spinning stops and a homogenous film with a reproducible thickness is obtained.

7.4.4 Repeated coating

The deposition cycle (i.e. sequence of spin coating - hot plate treatment - intermediate anneal) is often repeated to ensure a complete substrate coverage and to tune the final film thickness. If the precursor solution does not affect (e.g. etching) the previously deposited film, multiple deposition cycles result in thicker films. In this context, the notions *layer* and *film* can be distinguished: a layer is the deposit after one cycle and a film is the entire stack of layers after the total number of cycles. The *as deposited film* refers to the final x-layered film, obtained after x cycles in which each cycle consist of the deposition step, the hot plate step and the intermediate anneal. Thus the *as deposited film* is the film just before the post deposition anneal (i.e. step 7 in Figure 7.7).

Note that the surface on which the aqueous precursor is applied changes as well: (i) for the first layer, this surface is the substrate surface, (ii) if the substrate is not yet fully covered, the surface consists of substrate and film areas and (iii) after a full coverage of the substrate by the deposited film, the surface equals the top surface of the deposited layer. Thus, changing the deposition surface might affect the wetting properties of the aqueous precursor solution.

7.4.5 Thermal treatment

To obtain the desired crystalline, oxide phase the spin coated gel is subjected to a number of thermally induced transformations. Firstly, the residual solvent - entrapped in the pores of the gel - is removed upon heating. If an aqueous precursor is used, these residual H_2O molecules are typically released between T_{Room} to ~ 100 °C. Secondly, the organic moieties, originating from e.g. the counter ion in the metal salt or from the α-hydroxyl-carboxylate compounds, are thermally removed as volatile species as well.[33, 84]. A detailed study of such thermally induced transformations is given in Chapters 5 and 6.

Thirdly, the formation of the oxide phase is aimed for. Here, the gel network is rearranged by reorganization of a variety of bonds and by the elimination of the free volume in the film. During this process M−O−C and M−O−H bonds are broken and the associated organic species are removed as volatile compounds. In addition, the formation of M−O−M bonds takes place and the desired oxide arises. Fourthly, if the formed oxide phase is still amorphous, a further transformation (i.e. crystallization) takes place to form the crystalline oxide compound.

A *two-step* approach is commonly employed to complete the transformation of the as-deposited gel film into the crystalline oxide film. The first step takes place at lower temperatures (200-400 °C) and often in ambient conditions (i.e. on hot plates). The second step is a high temperature step (> 400 °C) in a controlled ambient (e.g. inert furnace). During the entire sequence of thermal steps, the film shrinks by the removal of the organic moieties and the rearrangement into the crystalline oxide phase. The thickness reduction varies between 50 and 80 % and is associated with the nature of the precursor.[33, 84]

In the formation of nanostructured VO_2 and intercalation VO_x, typically an additional, reduction step is added. Commonly, V_2O_5 is first formed and subsequently reduced in a H_2, CO/CO_2, NH_3 or low p_{O_2} ambient to form the desired oxide (e.g. VO_2 or V_6O_{13}).[7, 22, 23, 117, 118, 121–123, 139, 143, 145, 147, 149, 150, 160, 164]

7.5 Thermodynamic considerations

7.5.1 Film crystallization

Films, originating from a chemical precursor solution, are typically amorphous after the thermal treatment intended to remove the organic species. The crystallization occurs within the amorphous layer and can be described by the traditional nucleation and growth principles.[33] Figure 7.9A. shows the driving force (i.e. the decrease in the film's Gibbs free energy difference, ΔG) for the crystallization of an amorphous film. The transformation of the amorphous film into a crystalline film is governed by the nucleation of crystallites and their subsequent growth. A nucleation event can occur within the amorphous film (i.e. homogeneous nucleation) or at the interface of the amorphous film and its substrate (heterogeneous nucleation).

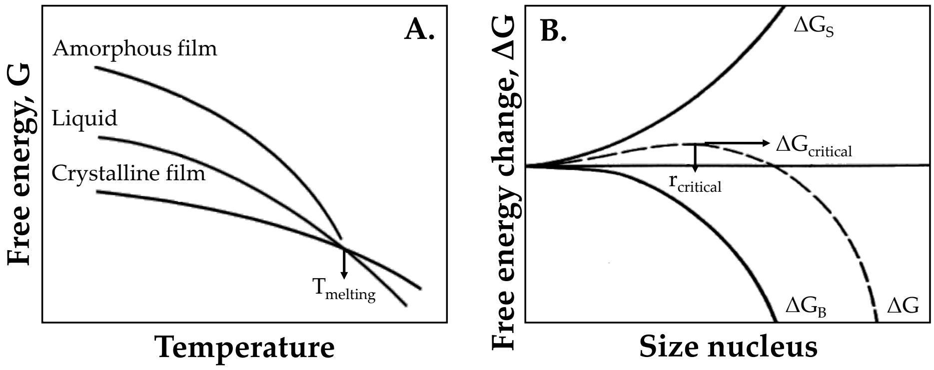

Figure 7.9: Schematic diagram of the Gibbs free energy, G, or the Gibbs free energy change, ΔG. (A.) G as a function of temperature for an amorphous film, its associated liquid and its associated crystalline film. (B.) ΔG, ΔG_B and ΔG_S as a function of the nucleus size with the indication of the critical nucleus size and its critical Gibbs free energy. The Figures are adapted from references [33, 165].

In the case of homogeneous nucleation, the Gibbs free energy change (ΔG) is determined by two terms: the bulk Gibbs free energy change (ΔG_B) and the surface Gibbs free energy change (ΔG_S) (Equation 7.9). Assuming a spherical particle with radius r and defining (i) the surface energy between the nucleis or crystallite and the amorphous matrix as γ_{ca} and (ii) Gibbs free energy difference per unit volume associated with the transformation of an amorphous to crystalline film as ΔG_v, Equation 7.10 evolves. Based on Equation 7.10, the energy barrier ($\Delta G_{critical}$) for homogeneous nucleation and the associated critical nucleus size ($r_{critical}$) is derived as the maximum value of ΔG (i.e. $\frac{d\Delta G}{dr} = 0$) leading the expression 7.11 and 7.12. Additionally, the rate of nucleation (J) follows the typical Arrhenius behavior as a function of the temperature (T) and Boltzmann's constant (k_B) (Equation 7.13).[33, 165]

$$\Delta G = \Delta G_S + \Delta G_B \tag{7.9}$$

$$\Delta G = 4\,\pi r^2 \gamma_{ca} + \frac{4}{3}\pi r^3 \Delta G_v \tag{7.10}$$

$$\mathrm{r}_{\mathrm{critical}} = -\frac{2\gamma_{ca}}{\Delta G_v} \tag{7.11}$$

$$\Delta G_{critical} = \frac{16\pi\gamma_{ca}^3}{3(\Delta G_v)^2} = \frac{4\pi r_{critical}^2}{3} \tag{7.12}$$

$$\mathrm{J} = \mathrm{A} \cdot exp\left(-\frac{\Delta G_{critical}}{k_B T}\right) \tag{7.13}$$

In the case of heterogeneous nucleation, an additional function (i.e. f(θ)) – related to the contact angle between the nucleus with the heterogeneous surface (θ) – is included in Equations 7.9, 7.10, 7.12 and 7.13 leading to a alternative expression (Equation 7.14) for the heterogeneous nucleation energy barrier ($\Delta G^{hetero}_{critical}$). For an hemispherical nucleus, the contact angle function is elaborated in Equation 7.15. The contact angle is related to the surface energies between (i) crystallite and amorphous matrix (γ_{ca}), (ii) crystallite and surface (γ_{cs}) and (iii) surface and amorphous matrix (γ_{sa}) via Equation 7.16.[33, 165]

$$\Delta G^{hetero}_{critical} = \mathrm{f}(\theta)\frac{16\pi\gamma_{ca}^3}{3(\Delta G_v)^2} \tag{7.14}$$

$$\mathrm{f}(\theta) = \frac{2 - 3cos\theta + cos^3\theta}{4} \tag{7.15}$$

$$\gamma_{sa} = \gamma_{cs} + \gamma_{ca}\cos\theta \tag{7.16}$$

Note that f(θ) $\leq$ 1 indicates that the energy barrier for heterogeneous nucleation is lower or equal to the barrier for homogeneous nucleation. Although the direct implementation of previous thermodynamic principles is not straightforward, some key ideas are given by Schwartz et al.[33] If little energy is available for nucleation (i.e. at lower temperatures), heterogeneous nucleation is favored and the number of nucleation events (determined by the nucleation rate) is limited. This typically leads to crystalline films with columnar morphology. If plenty energy is available (i.e. at higher temperatures), homogeneous nucleation becomes as probable as heterogeneous nucleation. In this situation, there is more than sufficient energy to overcome the energy barrier for all (including less energetically favorable) nucleation events, resulting in a large number of nucleation events.. This typically results in polycrystalline films with approximately equal sizes.

7.5.2 Solid state dewetting

Solid state dewetting or microstructural instability is the phenomenon where a metastable film, especially if the film is very thin (~ 10 to 100 nm), breaks up and forms islands if heated at sufficiently high temperatures. This process is driven by the minimization of surface energy and occurs via surface diffusion well below the melting temperature.[166] Since the dewetting process requires the formation and growth of holes in the film, it is largely governed by the temperature (facilitating ion diffusion) and the film thickness. Thompson reviewed a model for the surface energy minimization during such a hole formation and growth starting from grain boundaries in a grained film.[166]

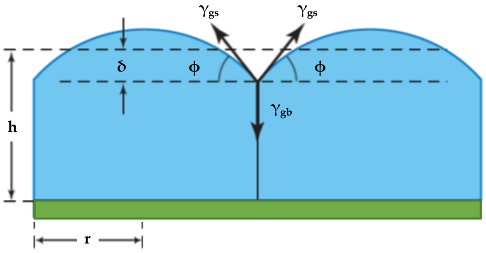

Figure 7.10: Schematic cross-sectional view of a grained film.[166]

Figure 7.10 gives a cross-sectional view of a grained film. Assuming a homogeneous system, the grained film is defined by:

- the grain radius (r),
- the initial film thickness before grain formation and with a perfect planar film surface (h),
- the groove depth (δ) with respect to the initial planar film surface,
- the grain surface energy (γ_{bs}),
- the grain boundary energy (γ_{gb}) and
- the angle at the groove's end (ϕ).

At the point where the grain boundary and the surface meet, an equilibrium settles (Equation 7.17) leading to an expression for the groove's end angle and depth (Equations 7.18 and 7.19). If the groove's depth (δ) is larger than the initial film thickness (h), the groove will contact the substrate and initiate dewetting.[166]

$$\gamma_{gb} = 2\,\gamma_{gs}\sin\phi \tag{7.17}$$

$$\phi = \sin^{-1}\left(\frac{\gamma_{gb}}{2\gamma_{gs}}\right) \tag{7.18}$$

$$\delta = \mathrm{r}\frac{2 - 3cos\phi + cos^3\phi}{3sin^3\phi} \tag{7.19}$$

Since each grain boundary has a different energy, not all grain boundaries will form holes. Hole formation is most likely at higher energy grain boundaries. The number of holes increases if (i) the initial film thickness (h) and the grain surface energy (γ_{gs}) are small and (ii) the grain boundary energy (γ_{gb}) and grain size (r) are large.[166] In addition it has been demonstrated that, the groove depth is greater at grain boundary triple junctions in comparison to the groove depth at the boundary between two grains. Hence, at the triple junctions hole formation occurs most likely first.[167]

Chapter 8

Tuning the CSD route for the formation of vanadium oxides

As defined in milestone 3 of this work, vanadium oxide formation – using the chemical solution deposition route and subsequent processing – is aimed for. Therefore, each step and parameter of CSD route is investigated in this Chapter with the formation of VO_2 M1, VO_2 B, V_6O_{13} and V_2O_5 intended. The temperatures of the hot plate steps, the intermediate anneal conditions and the multiple deposition cycle will be key parameters. This chapter is divided in two sections. In the first section, it is aimed to retain the vanadium +IV oxidation state to allow the direct formation of VO_2 and V_6O_{13}. An elaborate study on the processing temperature and O_2 partial pressure will be carried out. The content of this section is published in reference [74]. The second part will focus on the formation of V_2O_5 and a re-oxidation of the vanadium +IV oxidation state is allowed.

8.1 The CSD route for the formation of VO_2 and V_6O_{13}

8.1.1 Preventing V(IV) re-oxidation

During the deposition process, the spin coated precursor solution should convert to a stable and well adhering oxide layer. This is typically realized by a thermal treatment. From the thermal decomposition studies, it is clear that oxidative conditions should be limited to prevent V(IV)/V(V) re-oxidation. To study a possible V(IV) oxidation and the residual organics in the deposited layer, single layered films are spin coated on SiO_2 and subsequently heated at various temperatures in ambient air on hot plates. The obtained films are analyzed by GATR-FTIR spectroscopy (Figure 8.1).

As was shown in the thermal decomposition study performed on the ammonium-citrato-VO^{2+} gel in Chapter 6; the excess of ammonium citrate, ammonium oxalate

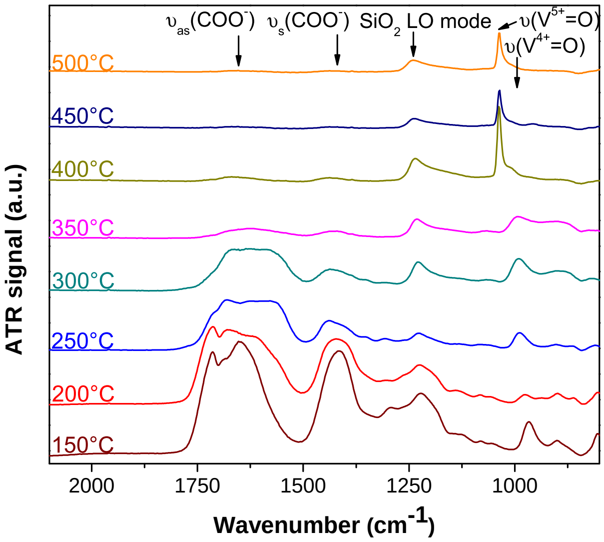

Figure 8.1: GATR-FTIR spectra of deposited films with their possible IR assignments as function of temperature in ambient conditions for a single spin coated layer on 1.2 nm SiO_2.

and the citrato-VO^{2+} complex – which are deposited from the precursor solution onto the SiO_2 substrate – decompose between 150 °C and 450 °C. Their decomposition is indicated by the disappearance of the carboxylate stretch vibrations between 1700 cm^{-1} and 1400 cm^{-1}. Furthermore, a shift in the vanadyl stretch vibration, $\nu(V = O)$, from 976 cm^{-1} to 1020 cm^{-1} is observed as a function of the temperature. This shift corresponds to the oxidation of V(IV) to V(V) and the corresponding change in V=O bond distance (1.60 Å for V(IV)=O and 1.58 Å for V(V)=O).[113, 168] Three stages can be distinguished in the temperature range between 150 °C and 450 °C:

- a non-oxidative stage up to 200 °C with preservation of V(IV),
- a transition stage, with the occurrence of both V(IV) and V(V) between 250 °C and 400 °C and
- a strong oxidative stage above 400 °C, comprising the complete transformation to V(V).

Thus, to prevent oxidation of V(IV) in ambient air during the thermal treatment process, the hot plate temperature should not exceed 200 °C.

After single layer deposition and thermal treatment in ambient air at only 200 °C the film still contains vanadium species with the preferred +IV oxidation state. To obtain thicker films and to ensure complete substrate coverage after the full film

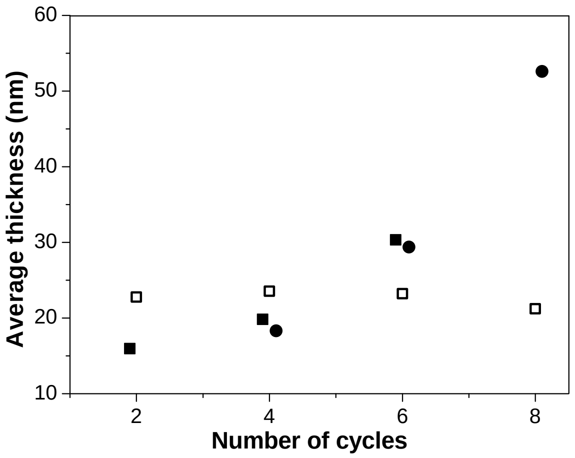

Figure 8.2: Average thickness as function of the number of deposition cycles with (filled) and without (open) an intermediate anneal (400 °C, 0.1 % O_2, 10 minutes). Film thicknesses are determined by ellipsometry (□,■) and X-SEM (●).

processing, including the final anneal steps, multiple layers should be deposited by repeating the deposition cycle. Figure 8.2 shows the thickness of the deposited film for a different number of deposition cycles, each with a thermal treatment of 200 °C in ambient conditions, with or without a subsequent intermediate annealing. Clearly, for a higher number of deposition cycles no significant thickness increase is observed if no intermediate anneal is carried out. It has to be concluded that during the next deposition cycle the previously deposited layer is re-dissolved in the freshly applied precursor solution. Thus the film has to be rendered less soluble in the precursor solution prior to deposition of the subsequent layer. Therefore, the thermal treatment, in this case a non-oxidative intermediate anneal, should be carried out at an as high as possible temperature in order to allow maximal precursor decomposition, however still avoiding V(IV) oxidation. The TGA curves of the citrato-VO^{2+} precursor gel obtained in air or N_2 (Chapter 6) show a similar weight loss of 30 % up to 400 °C. The main difference is the observed V(IV) oxidation in air at higher temperatures, which is absent in N_2. Thus the preferential temperature for the intermediate anneal is 400 °C.

Initially, a fully inert (N_2) intermediate anneal is applied. However, a disadvantage of this approach is the formation of a less hydrophilic surface, as suggested by the high contact angle (± 47 °) for a single spin coated layer on SiO_2 after an intermediate anneal at 400 °C in N_2 (Figure 8.3).

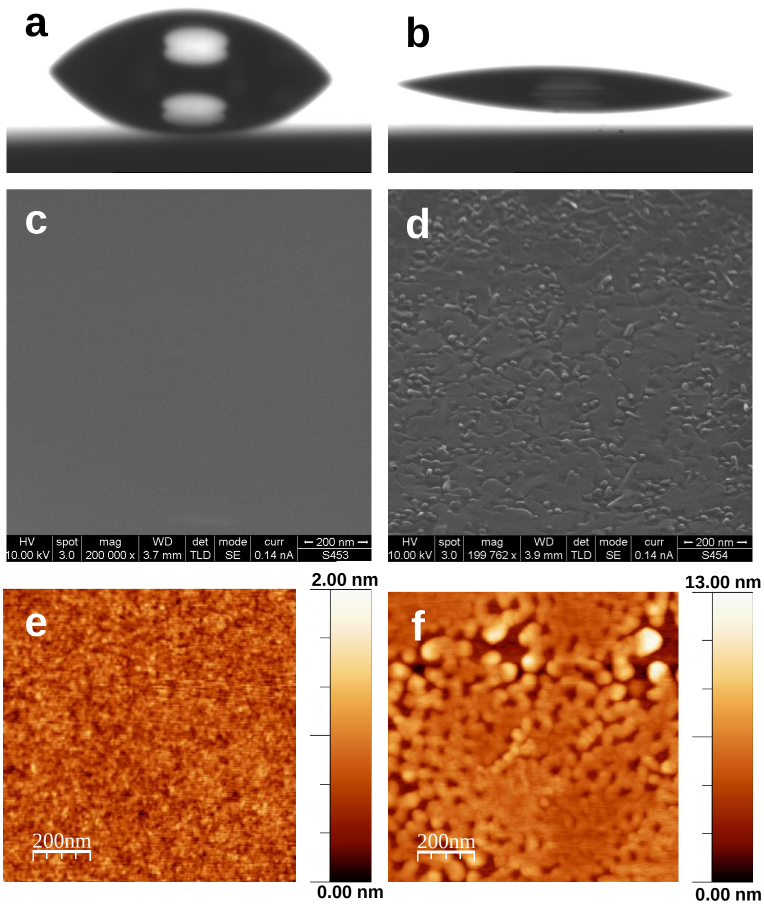

Figure 8.3: Surface analysis of a single spin coated layer on 1.2 nm SiO_2 with an intermediate anneal (10 minutes, 400 °C) in N_2 (a, c, e) or in 0.1 % O_2 (b, d, f): Contact angle measurements with water (a and b), SEM images (c and d) and AFM images (e and f).

Peak position (cm^{-1})	N_2	0.1 % O_2	Assignment
2925	22	5	$\nu_{as}(C-H)$ in CH_2
2850	118	3	$\nu_s(C-H)$ in CH_2
1590	31	12	$\nu_{as}(COO^-)$ in COO^-/VO^{2+}
1400	5	7	$\nu_s(COO^-)$ in COO^-/VO^{2+}
1240	100	100	SiO_2 LO mode
976	1	9	$\nu(V(IV)=O$ in VO^{2+}

Table 8.1: Normalized peak areas of baseline corrected GATR-FTIR spectra of a single spin coated layer on 1.2 nm SiO_2 with an intermediate anneal in N_2 or 0.1 % O_2 (400 °C, 10 minutes). The normalization is performed with respect to the SiO_2 longitudinal optical mode. The assignments are based on references [75, 168, 169]

We ascribe the hydrophobicity of the film to the presence of organic residues which remain present after non-oxidative dehydroxylation and decarboxylation reactions during the N_2 intermediate anneal as shown by the GATR-FTIR band assignments in Figure 8.4 and Table 8.1. This hydrophobic nature is in contrast to pure vanadium oxides, such as V_2O_5, VO_2 and V_6O_{13}, which are vanadyl (V=O) surface terminated and therefore can be expected to be hydrophilic.[170] As a consequence, the wetting of the aqueous solution is unfavorable and the second layer becomes inhomogeneous. Thus by tolerating a very small O_2 percentage during the intermediate anneal, allowing the oxidative removal of the surface organics without compromising the V(IV) oxidation state, better wetting properties are expected.

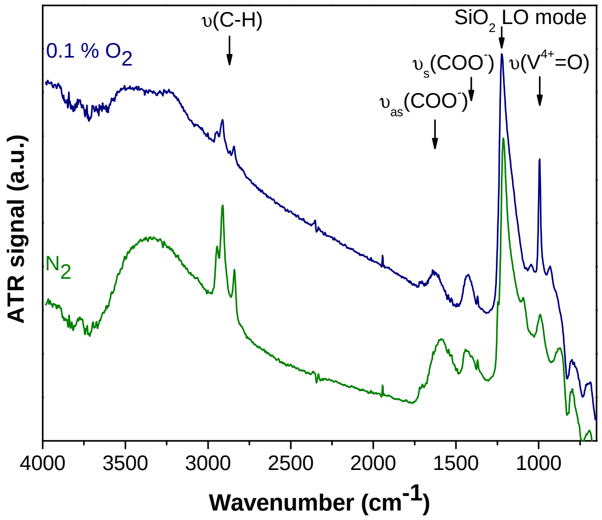

Figure 8.4: GATR-FTIR spectra with possible IR assignments of a single spin coated layer on 1.2 nm SiO_2, followed by an intermediate anneal in N_2 or in 0.1 % O_2 (400 °C, 10 minutes).

The effect of the O_2 percentage during such an intermediate anneal at 400 °C on the possible V(IV)/V(V) oxidation is illustrated in Figure 8.5 using GATR-FTIR spectroscopy. Due to the strong Al_2O_3 longitudinal optical mode at 930 cm^{-1}[171], the expected V(IV)=O stretch vibration below 0.3 % O_2 is not visible. However, already at 0.3 % O_2, a small V(V)=O stretch vibration at 1020 cm^{-1} is observed indicating V(IV)/V(V) oxidation. To avoid this oxidation, the following conditions are now chosen for the intermediate anneal: 400 °C and 0.1 % O_2. Such a film is characterized by a lower contact angle (± 18 °) (Figure 8.3b), indicating an enhanced surface wetting. Applying these intermediate anneal conditions, all sequentially deposited layers result in homogeneous films.

Table 8.1 compares and assigns the normalized peak areas of GATR-FTIR spectra

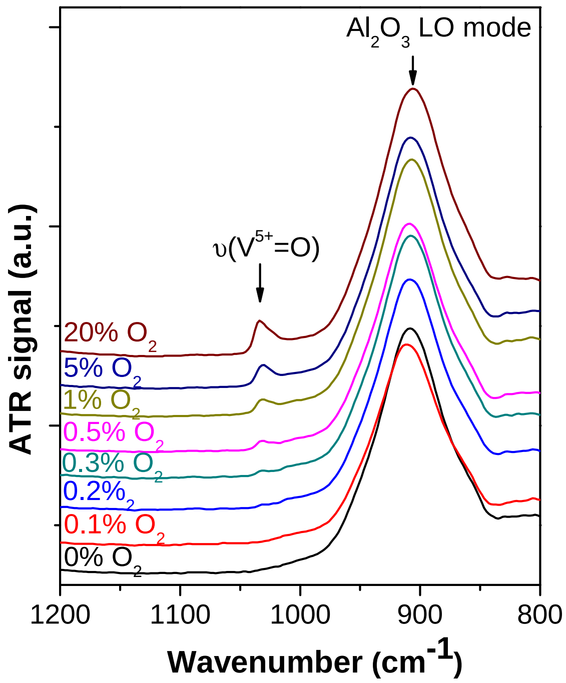

Figure 8.5: GATR-FTIR vibrations as function of the O_2 percentage during the intermediate anneal (400 °C, 10 minutes) for a single spin coated layer on 10 nm Al_2O_3.

obtained from a single spin coated layer on SiO_2 after an intermediate anneal in N_2 or 0.1 % O_2 (400 °C, 10 minutes). Because of non-oxidative dehydroxylation and decarboxylation reactions occurring in both N_2 and 0.1 % O_2 no traces of the excess of ammonium citrate are found, as can be seen by the absence of the $\nu_{as}(COO^-)$ in COO^-/NH_4^+ at about 1703 cm^{-1}. However, a decrease in the normalized peak areas of $\nu_{as}(C-H)$ in $-CH_2$, $\nu_s(C-H)$ in $-CH_2$ and $\nu_{as}(COO^-)$ in COO^-/VO^{2+} for 0.1 % O_2, in comparison to N_2, is observed due to the oxidative decomposition of the citrato ligands already in 0.1 % O_2. This supports the hypothesis that hydrophobicity can be partially ascribed to the presence of surface organics or, rephrased, that a more hydrophilic surface can be formed by the removal of these surface organics. Additionally, the significant increase of the normalized peak area of $\nu(V(IV)=O)$ indicates an enhanced presence of V=O groups, as was reported by Surnev et al. for several vanadium oxides, such as V_2O_5, V_6O_{13} and VO_2.[170] Moreover, the 0.1 % O_2 environment changes the morphology and surface roughness, as shown in Figures 8.3c, 8.3d, 8.3e and 8.3f by SEM and AFM. The obtained layer starts to break up, resulting in an incompletely closed layer with an RMS roughness around 1.5 nm. This higher surface roughness could, in combination with an increased availability of the vanadyl surface groups, explain the better surface wetting[172, 173] and lower contact angle after an intermediate anneal in 0.1 % O_2. Additionally, the thickness after the intermediate anneal (Figure 8.2) clearly linearly increases as a function of the number of deposition cycles.

In conclusion, by applying an intermediate anneal in 0.1 % O_2 (400 °C, 10 minutes) between subsequent depositions, it is possible to prepare films with different thicknesses starting from an aqueous citrato(-oxalato)-oxovanadate(IV) precursor. This has been shown for various substrates such as SiO_2 and Al_2O_3.

8.1.2 Phase formation on SiO_2

The synthesized aqueous citrato-oxalato-VO^2 and citrato-VO^{2+} solutions will be used for the formation of crystalline vanadium oxides on SiO_2 substrates. Multiple thermal treatments, studied in the previous paragraph, are applied to convert the spin coated precursor solution into a stable and well adhering oxide film. (i) The first thermal step is a hot plate treatment at 90 °C for 2 minutes in ambient conditions. During this step, water is evaporated and the precursor solution adheres to the substrate. (ii) Secondly, an intermediate anneal is applied at 400 °C for 10 minutes in a 0.1 % O_2 ambient. This intermediate anneal enables the subsequent deposition of layers without affecting the previously deposited layer and the V(IV) oxidation state, resulting in a film with an adjustable thickness.

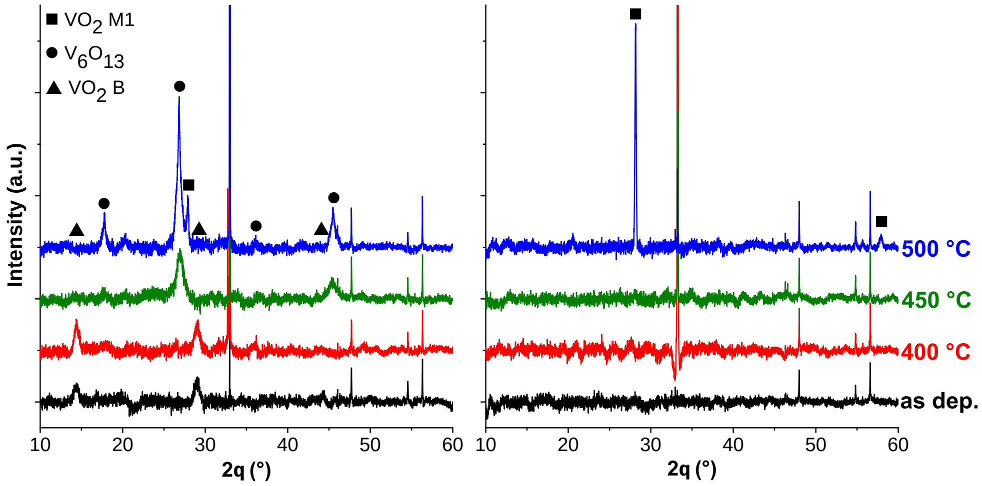

Figure 8.6: XRD pattern of films spin coated from the aqueous citrato-oxalato-VO^{2+} (left) and citrato-VO^{2+} (right) solution on 200 nm SiO_2 after an intermediate anneal of 400 °C (as dep.) and a post deposition anneal at 400 °C, 450 °C or 500 °C. All anneals are performed in a 0.1 % O_2 ambient for 10 minutes. The assignments are based on JCPDS 71-4821, 78-0983 and 81-2392 of, respectively, monoclinic VO_2 (M1), monoclinic V_6O_{13} and monoclinic VO_2 (B).[96]

Figure 8.6 shows the XRD patterns of four layered vanadium oxide films deposited on SiO_2 from the aqueous citrato-oxalato-VO^{2+} and citrato-VO^{2+} solution. For the citrato-oxalato-VO^{2+} solution, the initial four layered film (labeled *As deposited*) in Figure 8.6) already shows an onset for monoclinic VO_2 B phase formation, indicated by the presence of the (001) and (002) diffraction peak at 14.4 °2θ and 29.0 °2θ, respectively (JCPDS 81-2392)[96]. After applying a post deposition anneal at 400 °C in a 0.1 % O_2 ambient, the integrated area of the diffraction peaks at 14.4 °2θ and 29.0 °2θ slightly increases, suggesting growth of the amount of crystalline material. After an anneal at 450 °C in a 0.1 % O_2 ambient, the diffraction peaks associated with monoclinic VO_2 disappear and diffraction peaks corresponding to monoclinic V_6O_{13} arise at 26.8 °2θ (003) and 45.9 °2θ (005) (JCPDS 78-0983)[96]. As the temperature further increases to 500 °C, the integrated area of the diffraction peak at 26.8 °2θ increases and additional diffraction peaks for monoclinic V_6O_{13} are being observed at 17.8 °2θ (002) and 36.0 °2θ (004), suggesting an increased amount of crystalline material and a strongly textured film. Additionally, the Full Width at Half Maximum of the V_6O_{13} diffraction peak at 26.8 °2θ decreases (from 0.87 °2θ at 450 °C to 0.47 °2θ at 500 °C), indicating an increase of the V_6O_{13} crystallite size. Besides the diffraction peaks associated with crystalline, monoclinic V_6O_{13}, also a peak at 27.9 °2θ is observed after the anneal at 500 °C. This latter peak can be assigned to the (220) diffraction peak of monoclinic VO_2 M1 (JCPDS 71-4821)[96]. Thus, the aqueous citrato-oxalato-VO^{2+} solution, containing ammonium oxalate, can result in a crystalline VO_2 B film after an intermediate anneal at 400 °C, which further evolves to V_6O_{13} after an additional post deposition anneal at 450 °C or 500 °C. This VO_2 B to V_6O_{13} transformation was suggested by (i) Murphy et al. who studied the conversion of V_2O_5, V_6O_{13} and VO_2 B powders in a reducing ambient.[12] (ii) Premkumar et al. who studied the sequential oxidation of VO_2 B films on SiO_2 and Al_2O_3 to V_6O_{13} and to V_2O_5 as function of temperature (between 400 °C and 500 °C) in a similar low p_{O_2} ambient or as function of the p_{O_2} at 500 °C.[16] Both studies support our observed transformation of crystalline VO_2 B to crystalline V_6O_{13} as function of temperature.

The crystallization behavior of four layered films deposited from the citrato-VO^{2+} solution, is also given in Figure 8.6 and clearly differs from its citrato-oxalato-VO^{2+} variant. Since the XRD pattern of the initial four layered film does not show any diffraction, this film is considered amorphous. After a post deposition anneal at 400 °C or 450 °C, for 10 minutes in a 0.1 % O_2 ambient, the film stays amorphous. As the temperature increase to 500 °C, crystallization into the VO_2 monoclinic (M1) phase is observed, as evidenced by the diffraction peaks at 27.9 °2θ (110) and 57.6 °2θ (220). No additional peaks are observed in the XRD pattern, suggesting that the film consists of phase pure, monoclinic VO_2 M1. The crystallization of an amorphous vanadium oxide layer into monoclinic VO_2 M1 on SiO_2 in a low p_{O_2} ambient at temperatures around 500 °C is in agreement with previous reports.[9, 16]

In conclusion, the aqueous citrato-oxalato-VO^{2+} solution results in the formation of VO_2 B and V_6O_{13} films, while the citrato-VO^{2+} solution leads to VO_2 M1 films. This suggests that ammonium oxalate, present in the deposited film up to 207 °C, relates to VO_2 B crystallization during the heating stage of the intermediate anneal.

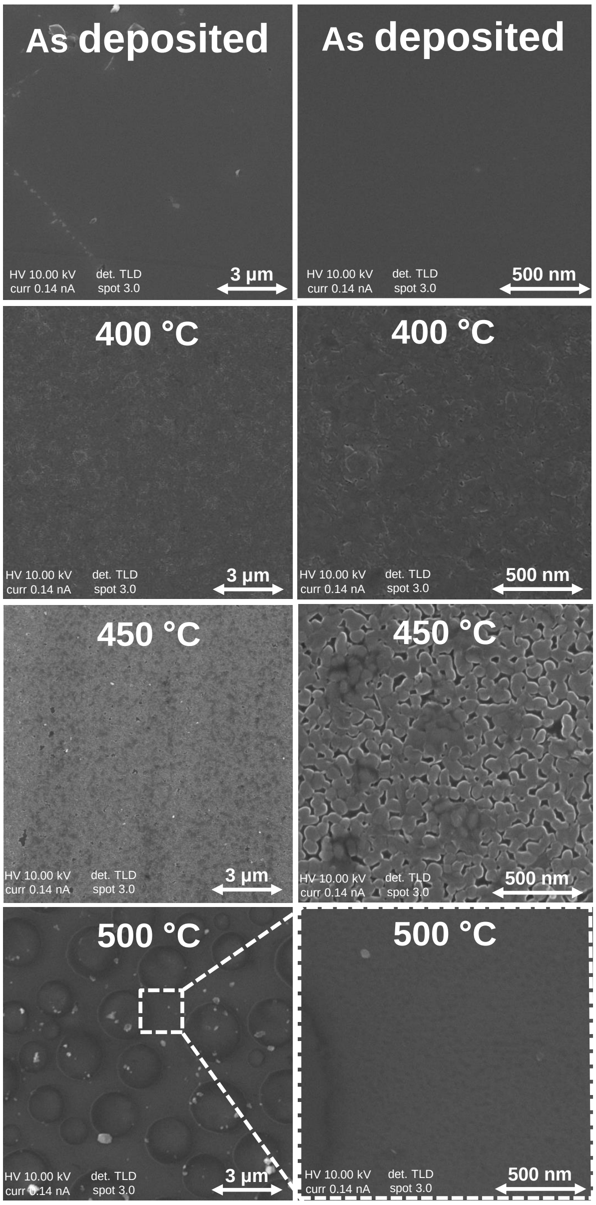

Figure 8.7: SEM images of films spin coated from the aqueous citrato-VO^{2+} solution on 200 nm SiO_2 after an intermediate anneal of 400 °C (as deposited) and a post deposition anneal at 400 °C, 450 °C or 500 °C. All anneals are performed in a 0.1 % O_2 ambient for 10 minutes.

8.1.3 Morphology of VO_2 M1 on SiO_2

The morphology of vanadium oxide films deposited from the aqueous citrato-VO^{2+} solution on SiO_2 is studied by SEM in Figure 8.7. The as deposited film obtained after an intermediate anneal at 400 °C in 0.1 % O_2, shows a continuous and featureless morphology, as expected for an amorphous film. The films annealed at 400 °C and 450 °C become discontinuous and the VO_2 starts to agglomerate into islands. As the temperature increases to 500 °C and crystallization into the monoclinic VO_2 M1 phase occurs (Figure 8.6), the films' morphology changes into randomly distributed particles. The formation of VO_2 particles from a thin (< 20 nm), amorphous and continuous film deposited on SiO_2, is consistent with previous observations reported by Suh et al. and Nag et al.[7, 8] Solid state dewetting of the metastable VO_2 film and the subsequent Ostwald ripening into VO_2 particles at sufficiently high temperatures was their suggested explanation. This process is, thermodynamically, driven by surface energy minimization and can occur via surface diffusion well below the film's melting temperature, especially when the film is very thin.[166] Obviously the film thickness and the surface energy of the substrate - and hence the chemical composition of the substrate - are in this case determining parameters.[166] An image analysis is performed on these VO_2 particles to determine their size. The particle size is distributed between 0.68 μm and 2.76 μm, with an average of 1.78 μm and a standard deviation of 0.46 μm. The total substrate coverage amounts to 48 %. The change in the VO_2 morphology on SiO_2 as function of the anneal conditions is well documented in literature and is systematically associated with the VO_2 M1 crystallization process.[9, 16, 23] As mentioned earlier, VO_2 M1 particles formed on an insulating SiO_2 substrate are, recently, becoming more interesting because of their enhanced performance compared to continuous VO_2 films.[7, 9, 17, 18]

8.1.4 Elemental composition & carbon contamination

The entire procedure for the formation of VO_2 or V_6O_{13} aims to maintain the vanadium +IV oxidation state throughout the entire sequence of solution deposition and film processing. Therefore, the oxidative power (determined by temperature, time and O_2 partial pressure) of each step is limited, as is thoroughly studied in section 8.1. However, the question rises if carbon remains in the film after a thermal treatment with such a limited oxidative power. In this context, the elemental composition of a few samples (description see Table 8.2) are analyzed by Energy-dispersive X-ray spectroscopy (EDX). Figure 8.8 shows the EDX spectra of samples EDX 1, EDX 2 and EDX 3. In all the samples, the signals of Al and Si are assigned to the silicon substrate with 10 nm Al_2O_3. Assuming that the Al amount in the sample volume during EDX analysis remains unchanged, the peak integration of the Al signal is used as a reference in the following qualitative discussion.

Sample	Deposition cycle	Number of cycles	Post deposition anneal
EDX 1	(1) 90 °C, 2 min in ambient air	1	-
EDX 2	(1) 90 °C, 2 min in ambient air (2) 190 °C, 2 min in ambient air	1	-
EDX 3	(1) 90 °C, 2 min in ambient air (2) 190 °C, 2 min in ambient air (3) 400 °C, 10 min in 0.1 % O_2	4	450 °C, 10 min in 0.1 % O_2

Table 8.2: Description used for EDX analysis. All the films are deposited by means of spin coating (3000 rpm, 30 s, 1000 rpm/s) using the citrato-oxalato-VO^{2+} solution onto small pieces (± 6 cm^2) of p-type Si with 10 nm Al_2O_3, cleaned in a sulfuric acid peroxide mixture and ammonia peroxide mixture.[174]

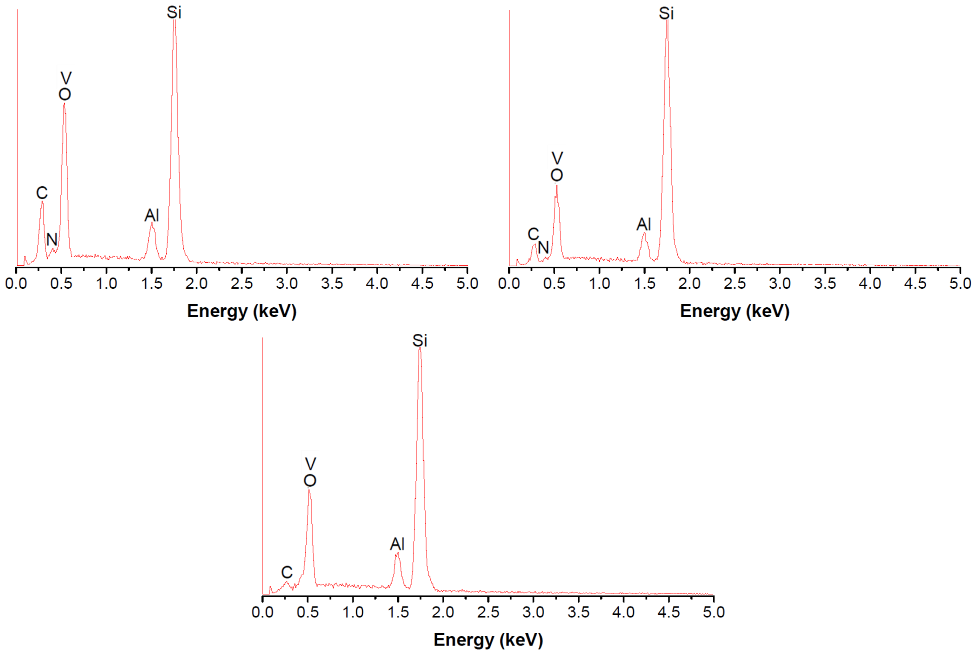

Figure 8.8: Energy-dispersive X-ray spectra of sample EDX 1 (top, left), EDX 2 (top, right) and EDX 3 (bottom), recorded on FEI Quanta 200-FEG SEM using a Si(Li) detector.

In sample EDX 1, a large amount of carbon and a small amount of nitrogen are observed. This single layered film has just received a thermal treatment of 90 °C in ambient air during which only the remaining water of the aqueous precursor is evaporated from the sample. At this stage the citrato-VO^{2+} complexes, which are cross-linked by ammonia groups, are not yet affected. This explains the amount of carbon and nitrogen observed in sample EDX 1. If the temperature increases to 190 °C in ambient air (sample EDX 2), the carbon signal strongly decreases and the nitrogen signal disappears in the noise level. As indicated in the discussion of the thermal decomposition pathway of the citrato(-oxalato)-VO^{2+} gel, only non-oxidative decomposition occurs up to 190 °C. The non-oxidative decomposition pathway consists mainly of two reactions: decarboxylation and dehydroxylation, in which NH_3, H_2O and CO_2 are released. Additionally, a weight loss of about 30 % between 90 °C and 190 °C is observed (Chapter 6). The removal of NH_3, H_2O and CO_2 during this non-oxidative decomposition pathway explains the decrease in the carbon and nitrogen signal observed in Figure 8.8. Moreover, a decrease in the un-resolved vanadium and oxygen signal in Figure 8.8 is observed and can be explained by the removal of oxygen as H_2O and CO_2 from the sample.

Sample EDX 3 has received an additional thermal treatment of 400 °C in a 0.1 % O_2 environment. The deposition cycle is repeated four times and a post deposition anneal is performed at 450 °C in 0.1 % O_2. Thus, in this sample a fourfold of material is deposited. Nevertheless the carbon signal in Figure 8.8 further decreases due to the continuation of the non-oxidative decomposition pathway up to 275 °C and due to a limited amount (since there is only 0.1 % O_2 available) of oxidative burnings starting at 275 °C. However, no significant decrease in the un-resolved vanadium and oxygen signal is observed in Figure 8.8. This could be explained by the combination of the fourfold of the vanadium amount in the sample and the decrease in the oxygen amount due to the additional removal of H_2O and CO_2 in the non-oxidative decomposition pathway.

In conclusion, the initial amounts of nitrogen and carbon originating from the aqueous citrato(-oxalato)-VO^{2+} gel are step-wise removed from the sample during the non-oxidative pathways as NH_3, CO_2 and H_2O. However, due to a limited amount of oxidative burnings in the 0.1 % O_2 environment, traces of carbon remain present in the films even after a post deposition anneal at 450 °C. Within the detection limit (estimated at about 0.1 w/w%) of the EDX analysis, no traces of other contaminants are found in the analyzed samples.

8.2 The CSD route for the formation of V_2O_5

In contrast to the previous section, the re-oxidation of vanadium(IV) to vanadium(V) during the film processing is required for the formation of crystalline V_2O_5. This section will focus on the formation of such crystalline V_2O_5 by (i) the deposition of the aqueous citrato-VO^{2+} precursor solution on SiO_2 or Al_2O_3 via spin coating and (ii) the subsequent film processing.

8.2.1 Conversion of the ammonium-citrato-VO^{2+} gel into V_2O_5

For this study, the aqueous citrato-VO^{2+} precursor solution is spin coated on SiO_2 and treated on a first hot plate at 90 °C for 2 minutes (static air). Depending on the final anneal temperature, a second hot plate treatment at 200 °C for 2 minutes and a third hot plate treatment at 400 °C for 2 minutes were carried out. In all cases, the highest hot plate temperature did not exceed the final anneal temperature. This final anneal was performed on a hot plate as well (2 minutes).

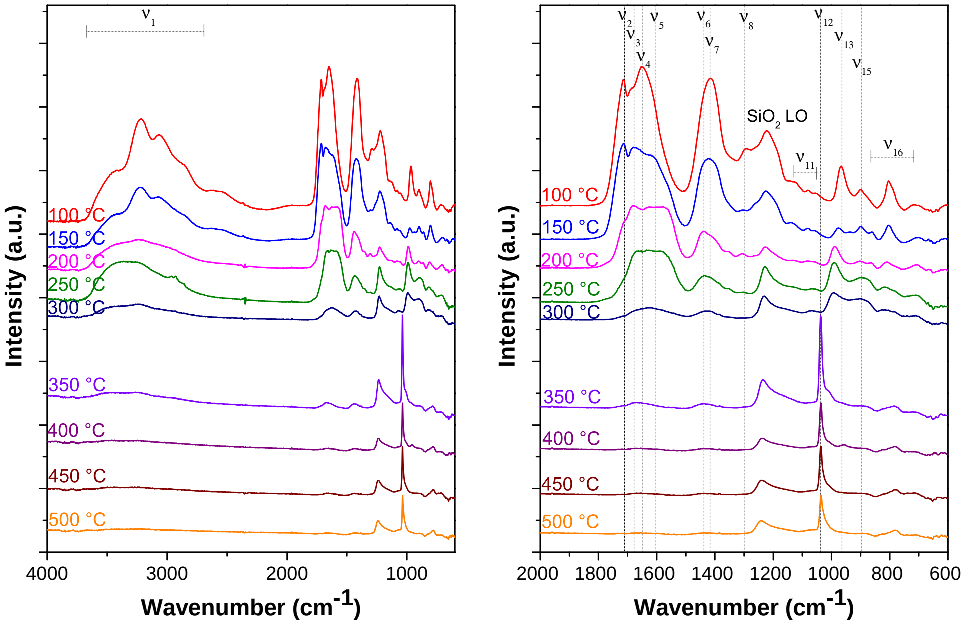

Figure 8.9: GATR-FTIR spectra of single layers, spin coated from the aqueous citrato-VO^{2+} precursor solution, on SiO_2. The spectra are given as a function of the final anneal temperature performed on hot plate for 2 minutes in dry air. Left: spectra from 4000 cm^{-1} to 600 cm^{-1}. Right: spectra from 2000 cm^{-1} to 600 cm^{-1}). The peaks are tentatively assigned in Table 8.3.

The change in the organic matrix - composed by the ammonium-citrato-VO^{2+} complexes and the oxalate residues - during the film processing is analyzed as function of the temperature during the final thermal treatment in dry air by GART-FTIR spectroscopy (Figure 8.9). Note that the band and peak assignments are identical to those assigned during the thermal decomposition study of the ammonium-citrato-VO^{2+} gel in air (Figure 6.1 and Table 6.1 in Chapter 6). Here, the observations in the temperature-dependent GATR-FTIR spectra are briefly discussed. For a full elaboration on the observed vibrations is referred to Chapter 6.

Vibration	Wavenumber (cm^{-1})	(Assignment)	
ν_1	3600 – 2800 (broad)	ν(O-H)	O-H stretching in hydrated H_2O
ν_1	3600 – 2800 (broad)	ν(N-H)	N-H stretching in NH_4^+
ν_1	3600 – 2800 (broad)	ν(C-H)	C-H stretching in CH_2
ν_2	1710	ν(C=O)	C=O stretching in COOH or in anhydride
ν_3	1678	ν(C=O)	C=O stretching in $CONH_2$
ν_4	1650	$\nu_{as}(CO_2^-)$	Asymmetric CO_2^- stretching with VO^{2+} or VO_2^+
ν_5	1600	$\nu_{as}(CO_2^-)$	Asymmetric CO_2^- stretching with NH_4^+
ν_6	1438	$\nu_s(CO_2^-)$	Symmetric CO_2^- stretching with NH_4^+
ν_7	1410	$\nu_s(CO_2^-)$	Symmetric CO_2^- stretching with VO^{2+} or VO_2^+
ν_7	1410	$\delta(NH_4^+)$	NH_4^+ deformation
ν_7	1410	$\nu_s(C-N)$	C-N stretching in $CONH_2$
ν_8	1296	δ(O-C=O)	O-C=O deformation
$\nu_{9,10}$	(A)	ν(C-O)	C-O stretching in anhydride ether, doublet
ν_{11}	1110 and 1070	ν(C-O)	C-O stretching in C-OH, doublet
ν_{12}	1035	$\nu(V^{5+}=O)$	V^{5+}=O stretching
ν_{13}	990	$\nu(V^{4+}=O)$	V^{4+}=O stretching
ν_{14}	903	$\delta_\gamma(C-H)$	C-H out-plane deformation in terminal methylene
ν_{15}	880	δ(C-O)	C-O out-of-plane deformation
ν_{16}	803	ν(V-O-V)	V-O-V skeleton vibration

Table 8.3: Band assignments of the main vibrations (expressed in cm^{-1}) observed in the GATR-FTIR spectra of a single layer, spin coated on SiO_2. This single layer is heated at various temperatures, on hot plates, for 2 minutes in dry air. Note that the carboxylate vibrations can originated from carboxylate groups associated with citrate or oxalate residues. Around 1245 cm^{-1}, the SiO_2 longitudinal optical vibration mode is observed, coinciding with other, possible vibration modes (A). The assignments are based on references [75, 92–94, 113].

After a heating at 100 °C, the ammonium-citrato-VO^{2+} network is unaffected and the vanadium ion still has the IV oxidation state. As the temperature increases to 200 °C and the major non-oxidative and endothermic decomposition steps are passed, the GATR-FTIR spectra change significantly. These changes indicate structural modifications of the species present in the deposited film.

- The vanadyl vibration starts shifting towards 1035 cm^{-1}, indicating the onset of VO^{2+}/VO_2^+ oxidation.

- The ammonium-carboxylate groups transform to carboxylic acid or amide functionalities.

- The carboxylic acid functionalities subsequently decarboxylate resulting in terminal methyl or methylene groups.

In contrast to the ammonium-citrato-VO^{2+} gel, the commencement of anhydride species is not visible in the GATR-FTIR spectrum. Possibly, their ether stretch vibration coincides with longitudinal optical mode of the SiO_2 substrate between 1180 cm^{-1} and 1280 cm^{-1}. Thus, up to 200 °C, the infra-Red characteristics of the deposited film and powder are very similar. Hence, the non-oxidative decomposition pathway studied on powders is also valid for the deposited film. As the temperature increases and the oxidative part of the decomposition pathway of the residual ammonium-citrato-VO^{2+} network is reached, the GATR-FTIR characteristics evolve. Between 200 °C and 350 °C, the vanadyl vibrations further shifts confirming the continuing VO^{2+}/VO_2^+ oxidation. At 350 °C, the final position and shape of the peak assigned to the $\nu(V^{5+} = O)$ is set. At this temperature, the peak height is strongly increases while its full-width-at-half maximum narrows. Both observations stem from a better (long-range) order in the obtained vanadium oxide material which could be due to crystallization. Already at 400 °C, no vibrations associated with the residual organic matrix persist. This indicates that the carboxylate groups in the direct vicinity of a VO_2^+ ion, the terminal methylene group, the (un)saturated amide functionalities and the anhydride species already burn before 400 °C. Thus this oxidative decomposition occurs about 100 °C earlier than anticipated based on the thermal decomposition pathway of its powder variant. Such an offset can be explained by the combining effect of (i) a different heating setup: tube furnace with a continuous air flow (powder) hot plate in static air (film), (ii) a possible thermal gradient within the powder determined by its sample volume (a few mm^3) and its expected absence within the deposited film (about 20 nm thick[97]) and (iii) a different heat transfer: via the ambient (powder) and via the substrate (film).

8.2.2 V_2O_5 crystallization and morphology

The V_2O_5 crystallization is studied by in-situ HT-XRD in air on a single layered film deposited from the aqueous ammonium-citrato-VO^{2+} precursor solution onto 10 nm Al_2O_3 (Figure 8.10, left). The deposited film remains amorphous up to 315 °C. At 315 °C, the onset of V_2O_5 crystallization is observed by the emerging peak distributed around 20.3 °2θ (001) (JCPDS 03-0206[96]). This temperature corresponds well with temperature interval (300 °C to 350 °C) in which an increased (long-range) order is suggested by GATR-FTIR spectroscopy (Figure 8.9).

As discussed in Chapter 6 and based on GATR-FTIR spectroscopy (Figure 8.9), in this temperature interval the residual organic matrix is burned as well. It can be concluded that V_2O_5 crystallization only occurs if the majority of the organic matrix is removed. As the temperature increases up to 500 °C, the integrated intensity of the peak distributed around 20.3 °2θ enlarges, suggesting a further crystallization and an increase in the amount of crystalline material. At 500 °C, this integrated intensity is maximal. Note that within the studied 2θ interval (from 12.5 °2θ to 32.5 °2θ) only the peak around 20.3 °2θ is detected for the deposited layer. The crystalline V_2O_5 powder (Figure 6.5, shown in Chapter 6) exhibits additional XRD peaks at 15.4 °2θ (020), 21.8 °2θ (110), 26.1 °2θ (101) and 30.8 °2θ (310) (JCPDS-03-0206[96]). The single XRD peak demonstrates a preferred c-axis oriented crystallization of the V_2O_5. Its corresponding (002) peak is expected at 41.3 °2θ. This (002) peak is observed in a room temperature XRD pattern of a layer anneal at 600 °C in air (ex-situ XRD), covering an interval of 40 °2θ (Figure 8.10, right). Between 550 °C and 670 °C, the full-width-at-half-maximum of the (001) peak around 20.3 °2θ decreases without a significant change in its integrated intensity. This is assigned to a grain growth of the c-axis oriented crystals. At 670 °C, V_2O_5 melts[72] and the (001) peak disappears.

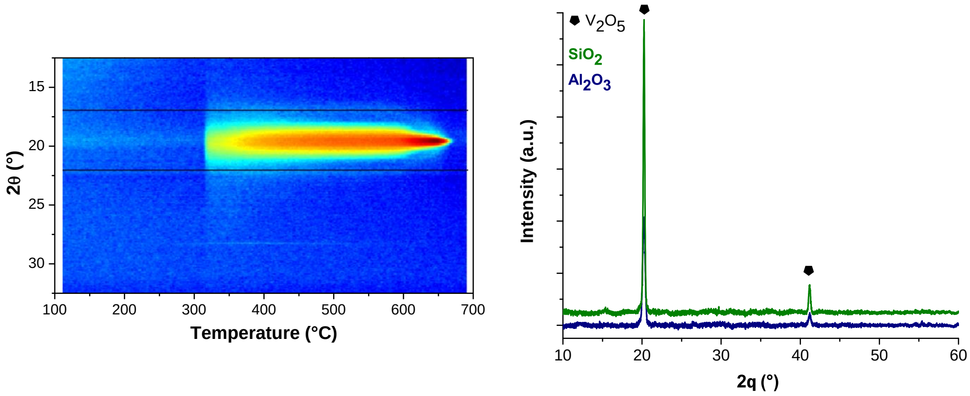

Figure 8.10: Left: In-situ HT-XRD – obtained in dry air – of a single layer, spin coated from the aqueous citrato-VO^{2+} precursor solution on 10 nm Al_2O_3. Right: XRD pattern of four layered films, spin coated from the aqueous citrato-VO^{2+} precursor solution on 1.2 nm SiO_2 or 10 nm Al_2O_3, after a final anneal at 600 °C in dry air. The assignment to crystalline V_2O_5 is based on JCPDS 03-0206.[96].

The microstructure of the films, obtained by deposition of the ammonium-citrato-VO^{2+} precursor solution on Al_2O_3, after a final anneal in air at 400 °C, 500 °C or 600 °C is examined by (cross-sectional) SEM (Figure 8.11). At 400 °C a rough, but closed film with a thickness of about 20 nm is obtained. On the surface elongated structures seem to emerge. At 500 °C, these elongated structures are clearly more developed. The cross-sectional SEM image visualizes that the initial film is completely broken for the formation of these rod-like structures. The dimensions of such a rod vary, with exception of its width (or *height*), clearly exceeds 100 nm which explains the breaking of a 20 nm thick film for formation of rods. The presence of these one-directional rods confirms the preferred c-axis crystallization of V_2O_5. As the temperature further increases to 600 °C, the crystallites grow as proposed during the HT-XRD analysis (Figure 8.10, left). Additionally, some parts of the surface are no longer covered by rods but by continuous layer. A partial melting of the V_2O_5 nanostructures already at 600 °C and its subsequent quenching in a glassy layer could explain this surface coverage.

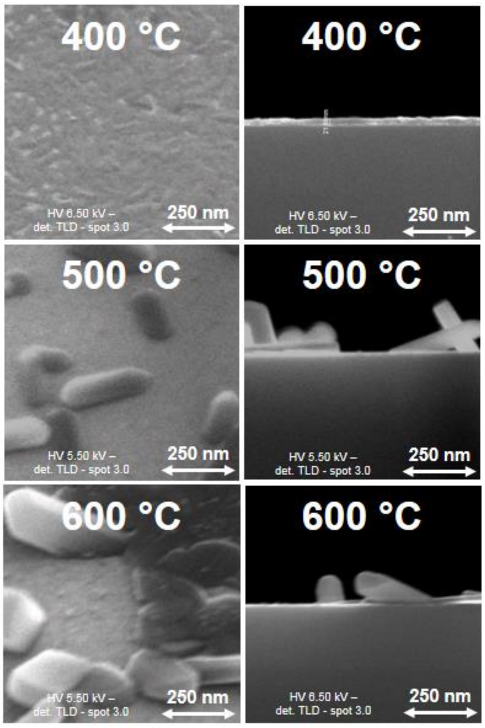

Figure 8.11: SEM images of four layered films spin coated from the aqueous ammonium-citrato-VO^{2+} precursor solution on 10 nm Al_2O_3 and after a final thermal treatment at 400 °C, 500 °C or 600 °C in air (hot plates).

8.2.3 V_2O_5 reduction in 5 % H_2

A first attempt to reduce the V_2O_5 film, in an 5 % H_2 ambient, into VO_2 (M1) is shown in Figure 8.12. As is seen by the diffraction peak at 20.3 2θ, the starting material is indeed V_2O_5 with a preferred (001) orientation. Already at 349 °C, a second crystalline phase appears with a diffraction peak at 21.3 2θ. According JCPDS 71-2248, this peak is assigned as the (202) peak of orthorhombic V_4O_9.[96] Between 349 °C and 469 °C, both vanadium oxide phase coexists. At 438 °C, the V_2O_5 phase disappears and the onset of crystalline VO_2 (B) is seen by the (001) and (002) diffraction peaks at 14.7 2θ and 29.4 2θ (JCPDS81-2392).[96] Between 438 °C and 469 °C, the V_4O_9 and VO_2 B phase coexist. As the temperature exceeds 469 °C, only crystalline VO_2 (B) remains. As the temperature further increases (up to 600 °C), the VO_2 (B) disappears and an amorphous film is obtained. Thus, the following temperature-dependent pathway for the V_2O_5 reduction is obtained (Equation 8.1):

$$V_2O_5 \longrightarrow V_4O_9 \longrightarrow VO_2(B) \longrightarrow \text{amorphous film} \qquad (8.1)$$

The suggested reduction pathway, with the intermediate formation of V_4O_9, is in line

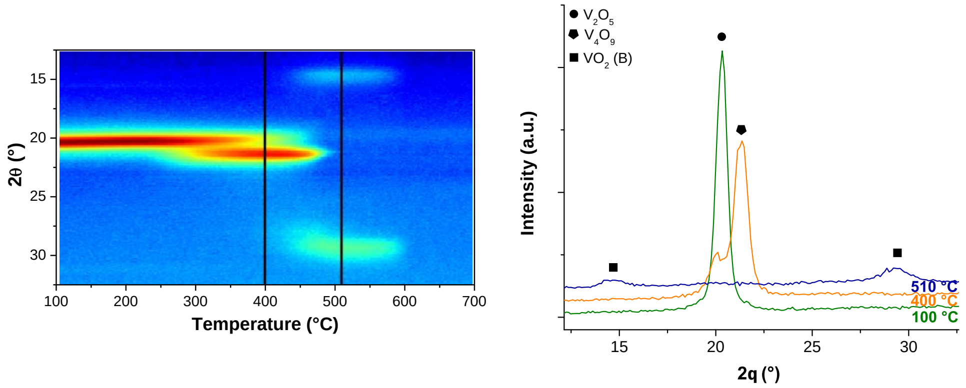

Figure 8.12: Left: In-situ HT-XRD recorded on a four layered film obtained by spin coating from the aqueous citrato-VO^{2+} solution 10 nm Al_2O_3. After each layer, the sample is treated at 100 °C, 200 °C and 400 °C in static air (hot plates) for 2 minutes. The final film is annealed at 550 °C for 10 minutes in air. The in-situ HT-XRD is performed in 5 % H_2 (in He) with a heating rate of 1 $°Cs^{-1}$. Right: Sections of the HT-XRD analysis at 100 °C, 400 °C and 510 °C. The assignment of crystalline V_2O_5, V_4O_9 and VO_2 (B) is based on JCPDS 03-0206, 71-2248 and 81-2392, respectively.[96].

with the observations of Murphy et al.[12] This indicates that the direct formation of VO_2 (M1) from V_2O_5 in H_2-based ambient is not straightforward.

8.3 Conclusion

A new aqueous synthesis route for the preparation of crystalline VO_2 and V_6O_{13} films by controlling the vanadium oxidation state throughout the entire deposition process is presented. An intermediate anneal in 0.1 % O_2 (400 °C, 10 minutes) is added to the film processing to allow sub 100 nm thickness adjustment without compromising the vanadium +IV oxidation state. The enhanced surface hydrophilicity is explained by an increased surface roughness and the larger availability of surface vanadyl groups. Both, aqueous precursor solutions - i.e. citrato-oxalato-VO^{2+} and the citrato-VO^{2+} - are successfully used for the preparation of crystalline vanadium oxide nanostructures on SiO_2, after a final anneal at 500 °C in a 0.1 % O_2 ambient. The citrato-oxalato-VO^{2+} precursor solution results in a monoclinic V_6O_{13} film. The citrato-VO^{2+} precursor solution forms monoclinic VO_2 M1 particles with an average size of 1.78 μm and a substrate coverage of 48 %.

Contrarily, in an oxidative ambient (i.e. air), the precursor solution is also suitable for the formation of crystalline V_2O_5 on SiO_2 and Al_2O_3. The removal of the organic matrix, its crystallization is studied via GATR-FTIR spectroscopy, in-situ HT-XRD and SEM. In contrast to its powder variant, the organic matrix already decomposed at 400 °C in air. Besides the temperature offset, the thermal decomposition pathway is considered identical. At 315 °C the onset of V_2O_5 crystallization is observed. As the temperature increases, the preferred c-axis oriented crystallization pushes through which results in elongated nano-rods. From 650 °C, all V_2O_5 melts and all peaks disappear from the HT-XRD pattern. The obtained crystalline V_2O_5 film does not lead to VO_2 (M1) in a reductive H_2 ambient. Instead, V_4O_9 and VO_2 (B) are obtained between 349 °C and 469 °C and between 438 °C and 600 °C, respectively. If the temperature exceeds 600 °C, the film becomes amorphous.

Chapter 9

Vanadium oxide phase formation

In the previous Chapter, a procedure for the transformation of the amorphous gel into a crystalline vanadium oxide – without affection the vanadium IV oxidation state – is presented. In addition, an intermediate anneal in 0.1 % O_2 ambient is introduced to ensure films with a tunable thickness. This Chapter will investigate the relation between the vanadium oxide phase formation and the (i) the precursor chemistry, (ii) the selected substrate and (iii) the thermal budget. Section 9.2 is part of a manuscript, submitted for publication.

Reference conditions

The aqueous citrato-oxalato-VO^{2+} solution, with a citrate:VO^{2+} ratio of 2:1, is spin coated (3000 rpm, 30 seconds, 1000 $^{rpm}/_{s}$) onto small pieces (± 6 cm^2) of p-type Si with 200 nm SiO_2, cleaned in a sulfuric acid peroxide mixture and ammonia peroxide mixture. A hot plate treatment is carried out on each deposited layer at 90 °C for 2 minutes. An intermediate anneal is performed in a rapid thermal anneal system (Accutherm AW-610) with an isothermal period of 10 minutes at 400 °C in an 0.1 % O_2 ambient. The deposition cycle (spin coating - hot plate - intermediate anneal) is repeated four times. A post deposition anneal is performed in the same rapid thermal anneal system in the 0.1 % O_2 ambient.

Parameters

1. The following **substrates** are studied, all the other reference conditions are maintained:
    - SiO_2, Al_2O_3 and TiO_2 as semiconductor substrate for VO_2 M1 and its future electrical evaluation. The TiO_2 could act as a template for the epitaxial growth of the high-temperature VO_2 rutile phase.

- Pt and TiN as metallic substrate for VO_2 (B), V_6O_{13} and V_2O_5 and their future electrochemical evaluation.

2. An **anneal time** of 10 and 30 minutes is studied. The 30 minutes anneal is expected to increase the amount of crystalline material by its benefit on the crystallite growth time.

3. The **number of deposition cycles** is varied between 1 and 10, leading to films with a different film thickness. The different film thickness could influence (i) the crystallization temperature, as was studied by Hardy et al. on $BaZr_{0.8}Ti_{0.2}O_3$ obtained via CSD from an aqueous precursor solution[60] or (ii) the film's morphology by influence the solid state dewetting (Section 7.5.2).

4. The effect of the **precursor chemistry** on the vanadium oxide phase formation is studied by comparing the precursor solutions studied in Chapter 3. In these solutions the citrate:VO^{2+} ratio varies: 0.75:1, 1.50:1, 3.00:1 and 4.50:1. For these solutions, the excess of ammonium oxalate is removed via precipitation (see Chapter 2).

Four vanadium oxides, with a specific stoichiometry and crystallinity, will be encountered: monoclinic VO_2 (B), monoclinic VO_2 (M1)[1], monoclinic V_6O_{13} and orthorombic V_2O_5. The diffraction peak assignment in this chapter is systematically based on JCPDS 81-2392, 82-0661, 78-0983 and 03-0206, respectively.[96] For simplicity, no further reference to one of these JCPDS diffractograms will made in this Chapter.

9.1 Substrate, anneal conditions and film thickness

9.1.1 Substrate – observations

On **SiO_2** and **TiO_2**, the initial four layered film (Figure 9.1, labeled as *as dep.*) already exhibits diffraction peaks associated with monoclinic VO_2 (B) at 14.5 °2θ (001), 29.1 °2θ (002) and 44.3 °2θ (003). An additional post deposition anneal at 400 °C does not significantly change the XRD pattern. Though, the onset of the most intense peak of monoclinic V_6O_{13} is seen at 26.9 °2θ. As the temperature increases to 450 °C (for SiO_2) or to 500 °C (for TiO_2), the peaks corresponding to monoclinic VO_2 (B) disappear and new diffraction peaks appear at 8.9 (001), 17.8 (002), 36.0 (004) and 45.5 (005) °2θ, indicating the presence of monoclinic V_6O_{13}. In addition, the diffraction peak at 26.9 (003) °2θ further evolves with an increase in its integrated area. At 500 °C and 550 °C, the diffraction peaks assigned to crystalline monoclinic V_6O_{13} remain. However, each peak has an increased integration area and decreased FWHM, stemming from the increase in crystalline material and the crystallite growth.

---

[1] This phase is the low temperature variant of rutile VO_2 (R). Obviously, during thermal treatment rutile VO_2 (R) is formed which transforms into VO_2 (M1) upon cooling.

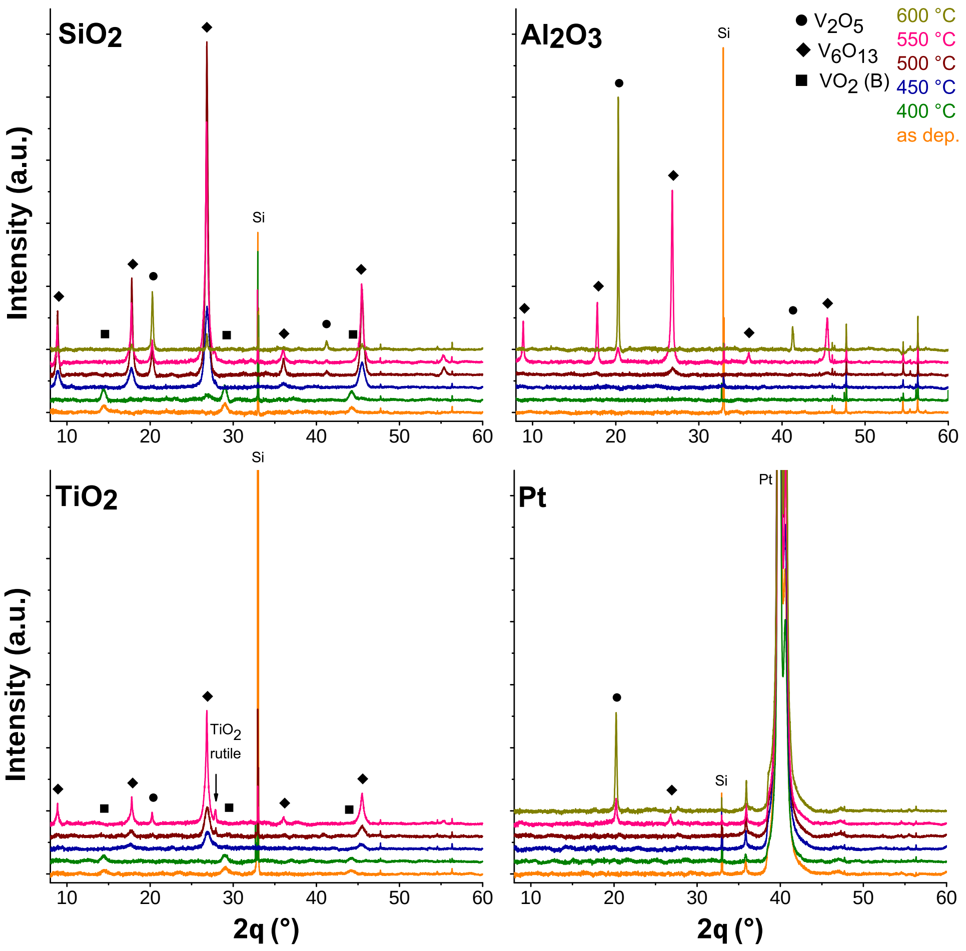

Figure 9.1: XRD pattern of four layered films spin coated from the aqueous citrato-oxalato-VO^{2+} on SiO$_2$ (left, top), γ-Al$_2$O$_3$ (right, top), TiO$_2$ (left, bottom) or Pt (right, bottom) with an intermediate hot plate step at 90 °C in air (2 minutes), an intermediate anneal at 400 °C (as dep.) and a post deposition anneal at 400 °C, 450 °C, 500 °C, 550 °C or 600 °C. All anneals are performed in a 0.1 % O$_2$ ambient for 10 minutes.

Note that the XRD patterns indicate the presence of a strongly textured film (i.e. 001, 002, 003, 004 and 004). Already at 500 °C (for SiO$_2$) and 550 °C (for TiO$_2$), a secondary phase is observed by the emerging peaks at 20.3 °2θ and 41.3 °2θ. These peaks are assigned to orthorhombic V$_2$O$_5$ with the (001) and (002) reflections. Finally, at 600 °C, the peaks associated with crystalline V$_6$O$_{13}$ diminish and the diffraction peaks assigned to orthorhombic V$_2$O$_5$ enlarge. Note that TiO$_2$ itself crystallizes at 500 °C into rutile TiO$_2$, as is seen by the appearance of the (011) diffraction peak at 27.7 °2θ (JCPDS 21-1276[96]).

On **γ-Al$_2$O$_3$**, the vanadium oxide phase formation differs from those observed on SiO_2 and TiO_2. The initial four layered film or films that underwent a post deposition anneal up to 450 °C are clearly amorphous. The onset of the monoclinic V_6O_{13} phase formation, indicated by the appearance of the (003) diffraction peak, is observed at 500 °C. As the temperature increases further to 550 °C, the integrated area of this diffraction peak increases and additional diffraction peaks indicating monoclinic V_6O_{13} are observed at 8.9 (001), 17.8 (002), 36.0 (004) and 45.5 (005) °2θ. This suggests an increased amount of crystalline material and a strongly textured film. Already at 550 °C, orthorhombic V_2O_5 with a preferential (001) orientation is observed. This secondary V_2O_5 phase becomes the dominant phase at 600 °C and the diffraction peaks of the V_6O_{13} phase completely disappear. From 550 °C to 600 °C, the V_2O_5 amount of crystalline material and the crystallite size increase.

The vanadium oxide crystallization further modifies on **Pt**. The initial four layered film and the films that underwent a post deposition anneal up to 500 °C are clearly amorphous. At 550 °C, crystalline V_2O_5 emerges as demonstrated by the (001) diffraction peak. The second most intense peak of crystalline V_2O_5 is expected around 41.3 °2θ (002) and coincides with the very intense and broad Pt diffraction peak centered around 39.8 °2θ (111) (JCPDS 01-1190[96]). At 550 °C, the V_2O_5 phase is accompanied by a V_6O_{13} secondary phase. This secondary phase disappears at 600 °C and orthorombic V_2O_5 is the only crystalline phase present.

Temperature	SiO_2	γ-Al$_2$O$_3$	TiO_2	Pt
as deposited	VO_2 (B)	amorphous	VO_2 (B)	amorphous
400 °C	VO_2 (B)	amorphous	VO_2 (B)	amorphous
450 °C	V_6O_{13}	amorphous	V_6O_{13}	amorphous
500 °C	V_6O_{13} (primary) V_2O_5 (secondary)	V_6O_{13}	V_6O_{13}	amorphous
550 °C	V_6O_{13} (primary) V_2O_5 (secondary)	V_6O_{13} (primary) V_2O_5 (secondary)	V_6O_{13} (primary) V_2O_5 (secondary)	V_2O_5 (primary) V_6O_{13} (secondary)
600 °C	V_2O_5	V_2O_5	-	V_2O_5

Table 9.1: Summary of the vanadium oxide crystallization on SiO_2, γ-Al$_2$O$_3$, TiO_2 and Pt. Each film is obtained by fourfold repetition of the deposition cycle and a final anneal, performed at various temperatures in the 0.1 % O_2 atmosphere (10 minutes).

Table 9.1 summarizes the vanadium oxide phase formation on the studied substrates. The following trends are observed: (i) As the temperature increases, the vanadium oxidation state increases in an oxidative trend: VO_2 (B), V_6O_{13} and V_2O_5. (ii) The crystalline substrates are more resistive to crystallization and do not form a crystalline film below 450 °C (γ-Al$_2$O$_3$) or 500 °C (Pt). (iii) All substrates exhibit crystalline V_2O_5 (as secondary or primary phase) at 550 °C, accompanied with V_6O_{13}. At 600 °C, all films contain phase pure V_2O_5. In the next parameter studies, only SiO_2 and γ-Al$_2$O$_3$ are considered as examples of an amorphous and a crystalline substrate, respectively.

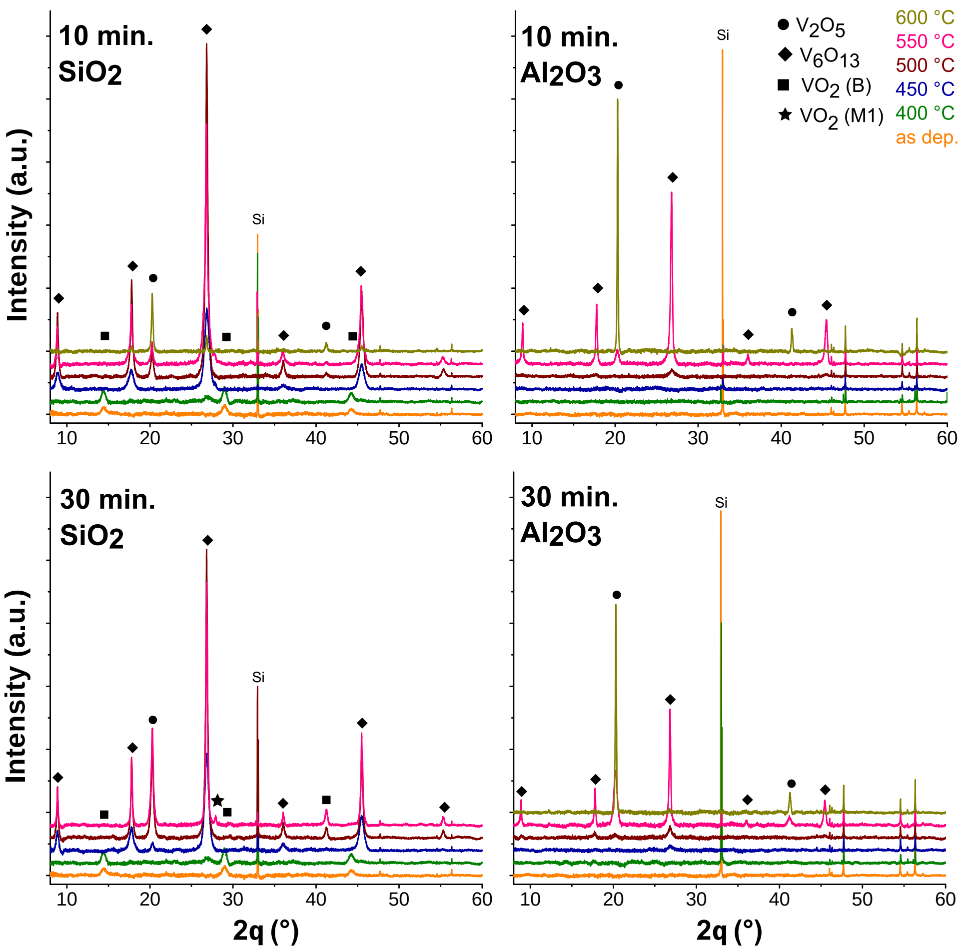

Figure 9.2: XRD pattern of four layered films spin coated from the aqueous citrato-oxalato-VO^{2+} solution on SiO_2 (left) and γ-Al_2O_3 (right) with an intermediate hot plate step at 90 °C in air (2 minutes), an intermediate anneal at 400 °C (10 minutes, as dep.) and a post deposition anneal at 400 °C, 450 °C, 500 °C, 550 °C or 600 °C for 10 minutes (top) or 30 minutes (bottom). All anneals are performed in a 0.1 % O_2 ambient.

9.1.2 Anneal time – observations

The influence of the anneal time (10 or 30 minutes) is studied on SiO_2 and γ-Al_2O_3, as given by the XRD patterns in Figure 9.2. For both substrates, the studied anneal time has not a large influence on the vanadium oxide crystallization. Below 450 °C, no difference at all is observed. From 450 °C on, the following sequence is shifted towards lower temperature on both SiO_2 and γ-Al_2O_3: (i) V_6O_{13} onset, (ii) phase pure V_6O_{13} with an increased amount of crystalline material and a larger crystallite size,

(iii) V_6O_{13} with a secondary V_2O_5 phase and (iv) the disappearance of V_6O_{13} and the dominance of crystalline V_2O_5. Due to the minor effect of the anneal time (within the studied interval, i.e. 10 – 30 minutes), the anneal time in the following studies is limited to 10 minutes.

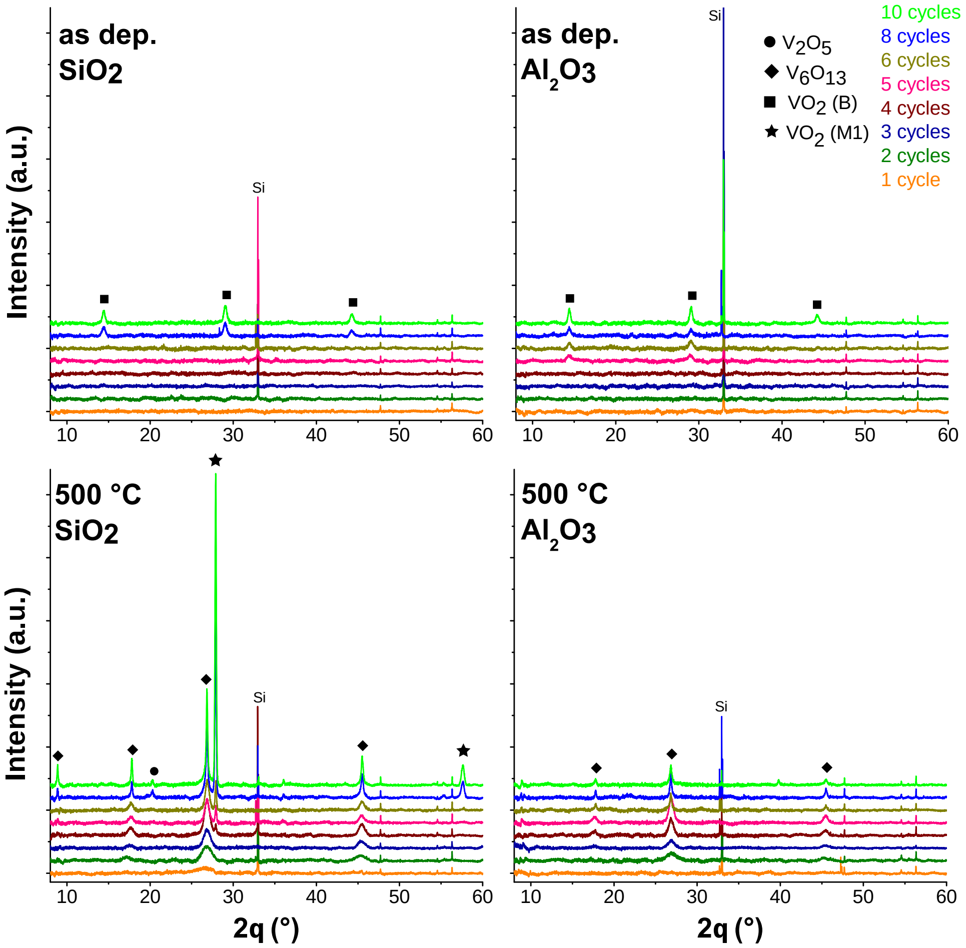

Figure 9.3: XRD pattern of films spin coated from the aqueous citrato-oxalato-VO^{2+} solution on SiO_2 (left) and γ-Al_2O_3 (right) with an intermediate hot plate step at 90 °C in air (2 minutes), an intermediate anneal at 400 °C in 0.1 % O_2 (10 minutes, top) and a post deposition anneal at 500 °C in 0.1 % O_2 (10 minutes, bottom). The number of deposition cycles is varied between 1 and 10.

9.1.3 Film thickness – observations

To analyze the effect of the film thickness on the vanadium oxide phase formation, the number of deposition cycles is varied between 1 and 10. In Chapter 8, it is shown that the film thickness increases with the number of deposition cycles, leading to growth per cycle of ± 5 nm. Figure 9.3 displays the XRD patterns, obtained from spin coated films on SiO_2 and γ-Al_2O_3 without and with a post deposition anneal at 500 °C, as a function of the number of deposition cycles.

As deposited

A total stack of four or less layers results in an amorphous film. As the number of cycles exceeds four, crystallization occurs and VO_2 (B) is formed on both substrates. Accompanied with the transformation from an amorphous film to a crystalline film (i.e. VO_2 (B)), its morphology changes as well.

Figure 9.4 demonstrates the morphology change as a function of the number of deposition cycles on γ-Al_2O_3. After 1 cycle, the film is still amorphous and the SEM image displays a full coverage of the substrate. As the number of cycles increases to 4, just before VO_2 (B) crystallization is observed in Figure 9.3, the morphology changes. Two zones seem to cover the substrate. The first zone appears lighter in the SEM image and clearly exhibits features related to substrate coverage. The second zone appears more dark in the SEM image and, at this point, does not show any characteristics. After six layers, crystallization into VO_2 (B) is observed and the morphology differentiation between the two zones remains. The features, such as grains and roughening, in the lighter zone become more distinct. Though they are not very well resolved in the SEM image and probably less abundantly present, similar features emerge in the more dark zone, indicating that the substrate is fully covered. It is plausible to assign the lighter zone to the presence of crystalline VO_2 (B) and the darker zone to a still amorphous part of the film.

After 500 °C

The influence of the number of cycles or film thickness on the crystallization is more pronounced after a final anneal at 500 °C. On both substrates, one cycle is insufficient to induce crystallization. The onset of V_6O_{13} crystallization on SiO_2 could be argumented because of the increased signal intensity between 25 °2θ and 28 °2θ. Starting from two cycles, V_6O_{13} crystallization is observed on both substrates. On γ-Al_2O_3, phase pure V_6O_{13} is formed for films obtained after multiple cycles ranging between 2 and 10. Crystallization into phase pure V_6O_{13} is also observed on SiO_2 for films obtained after 2 or 3 cycles. As the number of cycles exceeds 3, a small peak, assigned to VO_2 (M1), emerges at 27.8 °2θ (011). As the number of cycles increases, on both substrates, the amount of crystalline material and the crystallite size increase. Note that the peaks on SiO_2 have a larger peak area in comparison to γ-Al_2O_3, indicating the crystallization is enhanced on SiO_2. The small peak, associated with crystalline VO_2 (M1), at 27.8 °2θ further grows on SiO_2 if the number of cycles increases. Furthermore, for a film obtained after 6 cycles, this VO_2 (M1) peak even becomes dominating. After 8 cycles, a second peak corresponding to crystalline VO_2

(M1) is detected at 57.5 °2θ (022). Thus, on SiO_2, a film obtained after 8 or 10 layers crystallizes into primary VO_2 (M1) with V_6O_{13} as secondary phase after a final anneal at 500 °C.

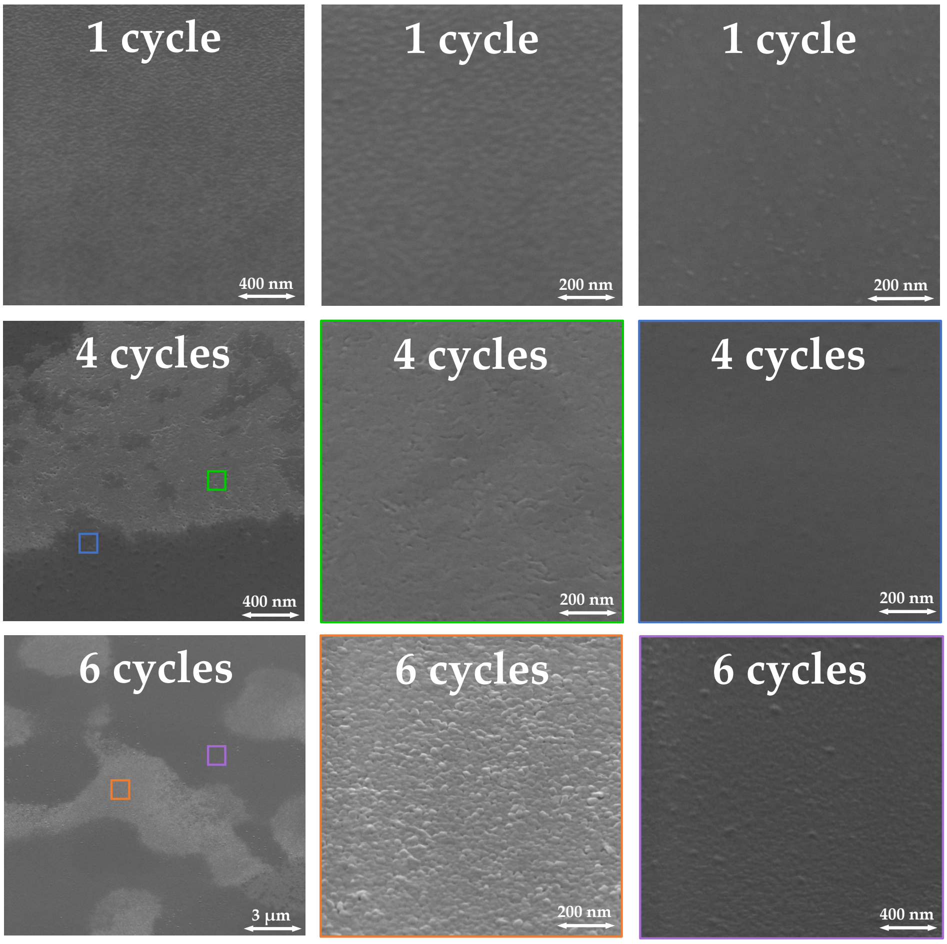

Figure 9.4: SEM images of films spin coated from the aqueous citrato-oxalato-VO^{2+} solution on γ-Al_2O_3 with an intermediate hot plate step at 90 °C in air (2 minutes), an intermediate anneal at 400 °C in 0.1 % O_2 (10 minutes). The number of deposition cycles is 1, 4 or 6.

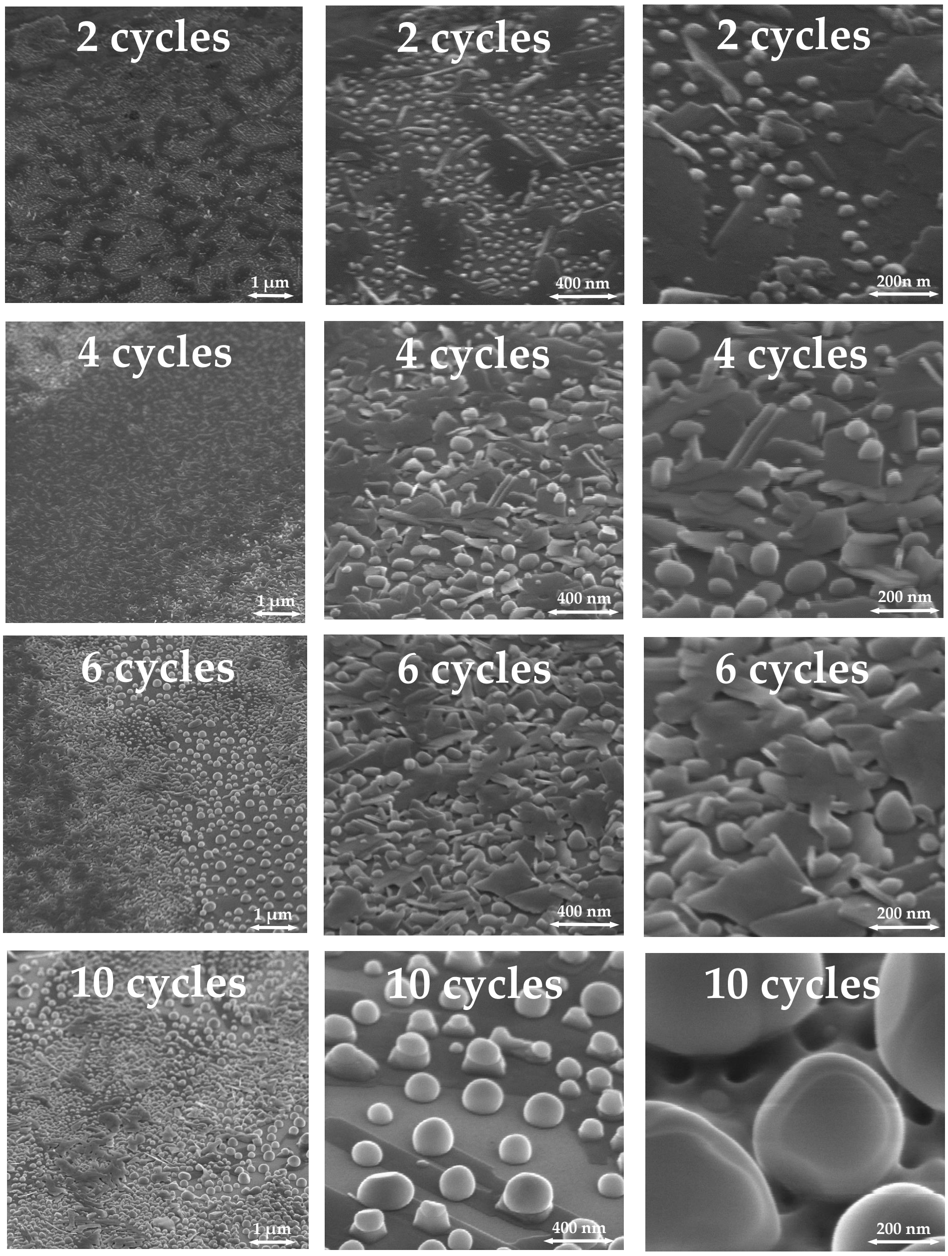

Figure 9.5: SEM images of films spin coated from the aqueous citrato-oxalato-VO^{2+} solution on SiO_2 with an intermediate hot plate step at 90 °C in air (2 minutes), an intermediate anneal at 400 °C in 0.1 % O_2 (10 minutes) and a final anneal at 500 °C in 0.1 % O_2 (10 minutes). The number of deposition cycles is 2, 4, 6 or 10.

The morphology of the deposited films, after a final anneal at 500 °C, also changes as a function of the number of cycles. Figure 9.5 shows SEM images of the films obtained on SiO_2 with 2, 4, 6 and 10 cycles. After 2 cycles, where the onset of V_6O_{13} crystallization is observed, two features can be distinguished. Parts of the substrate are fully covered by a closed film, while other parts are covered by separate rod-like or (hemi-)spherical particles. As the number of cycles increases, more parts of the film break up and particles with both shapes remain present. As the number of cycles increases to 10, and VO_2 (M1) is dominantly present with the V_6O_{13} secondary phase, the particle density increases and the (hemi-)spherical particles predominate.

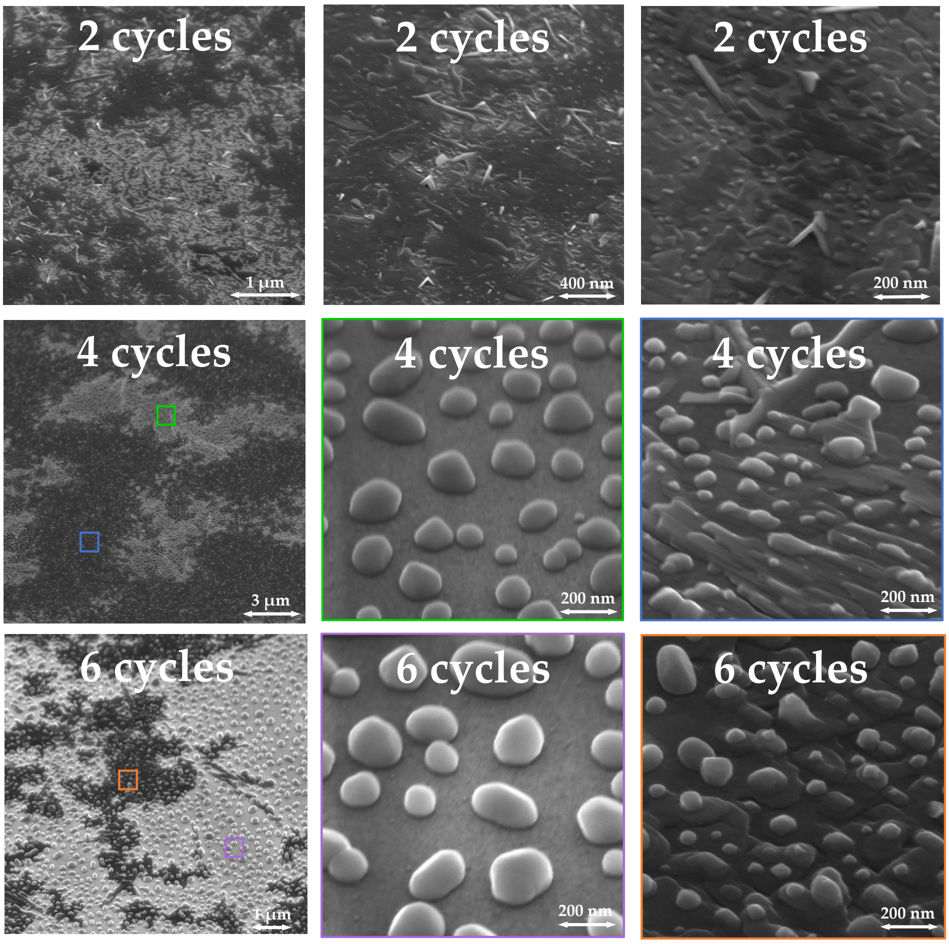

Figure 9.6: SEM images of films spin coated from the aqueous citrato-oxalato-VO^{2+} solution on γ-Al_2O_3 with an intermediate hot plate step at 90 °C in air (2 minutes), an intermediate anneal at 400 °C in 0.1 % O_2 (10 minutes) and a final anneal at 500 °C in 0.1 % O_2 (10 minutes). The number of deposition cycles is 2, 4 or 6.

On γ-Al_2O_3 the similar morphology trend is observed (Figure 9.6). At the onset of V_6O_{13} crystallization (2 cycles), the film breaks up into rod-like and spherical particles. Also here, the extent to which the film breaks up is directly related to the amount of crystalline, V_6O_{13}, material.

In summary, crystallization only occurs (or is only detected) if a minimal amount of material is deposited onto the substrate (i.e. the equivalent of 2 cycles). On SiO_2, phase pure V_6O_{13} is formed if 2 or 3 cycles are performed. For 4, 5 and 6 cycles, both V_6O_{13} and VO_2 (M1) are equally formed. As the number of cycles exceeds 6 (i.e. 8 or 10), VO_2 (M1) becomes the dominating phase. The VO_2 (M1) crystallization is accompanied by a breaking of the film into (hemi-) spherical particles. On γ-Al_2O_3 similar observations are made. However, no traces of VO_2 (M1) are found and in this case, the formation of similar (hemi-) spherical particles is related to V_6O_{13} crystallization. The formation of VO_2 particles from a thin ($\leq$ 20 nm), amorphous and continuous film deposited on SiO_2, is consistent with previous observations reported by Suh et al. and Nag et al. [7, 8] Solid state de-wetting of the metastable VO_2 film and the subsequent Ostwald ripening into VO_2 particles was the explanation they suggested.[166] Despite, the substrate effect is previously discussed by Chae et al., Vernardou et al. and Premkumar et al., no clear explanation is put forward.[7, 16, 23]

9.1.4 Hypothesis

This section aims to explain the trends observed in the vanadium oxide phase formation. Since the system is rather complex and very sensitive towards small experimental fluctuations, it is intended to present some ideas on the observed trends, rather than giving a detailed understanding of each result obtained with a specific set of experimental conditions.

In general, three stages are passed during the vanadium oxide phase formation as a function of temperature. Note that the anneal time (within the studied interval) does not significantly influence these stages. At mildest anneal conditions, monoclinic VO_2 (B) crystallizes with a low amount of crystalline material. At this point, the grained film completely covers the substrate. During the intermediate anneal conditions, the monoclinic VO_2 (B) transforms into monoclinic V_6O_{13}. At this stage, monoclinic VO_2 (M1) appears as a secondary phase. The morphology changes from a grained film covering the substrate to a structure partially consisting of a grained, substrate covering film and (hemi-)spherical particles. If more material is provided by e.g. a thicker film, the amount of crystalline material increases for both phases (i.e. V_6O_{13} and VO_2 (M1)). This increase is the largest for VO_2 (M1), that becomes the primary phase for films obtained after 6 or more cycles. The morphology changes as well if more material is provided: the grained substrate covering film is almost fully converted to the (hemi-)spherical particles. Finally, after the anneal with the strongest conditions (i.e. highest temperature), the V_6O_{13} starts to transform into orthorhombic V_2O_5, while the VO_2 (M1) phase remains. This leads to a structure with V_6O_{13}, V_2O_5

and VO_2 (M1). Note that on γ-Al_2O_3 and Pt (i.e. the crystalline surfaces), the first stage (i.e. VO_2 (B)) is not observed and the formation of VO_2 (M1) does not occur during the second stage. Additionally, the particle formation during the second stage is more pronounced on γ-Al_2O_3 in comparison to SiO_2

Temperature-dependent VO_2 (B), V_6O_{13} and V_2O_5 conversions

This transformation is already observed by (i) Murphy et al. who studied the conversion of V_2O_5, V_6O_{13} and VO_2 (B) in a reducing ambient[12] and by (ii) Premkumar et al. who studied the sequential oxidation of VO_2 (B) films on SiO_2 and Al_2O_3 to V_6O_{13} and to V_2O_5 as function of temperature in a similar low pO_2[16]. Both studies support our observed transformations of VO_2 (B) to V_6O_{13} and to V_2O_5 as function of temperature. Figure 9.7 schematically shows the structures of these vanadium oxides. According to Katzke et al., VO_2 (B), V_6O_{13} and V_2O_5 belong to a homologeous series of oxygen deficient structures originating from the same fcc structure with a decreased number of oxygen vacancies, respectively.[2] Due to these oxygen vacancies, the fcc lattice destabilizes and a monoclinic shear deformation emerges.[2, 12] Note that Katkze et al. and Leroux et al. have compared the structures of VO_2 (B) and VO_2 (M1) and claim (i) that both structures significantly differ and belong to a different homologeous series each with its own parent structure and (ii) their interconversion is very unlikely and requires a significant re-ordering of the vanadium and oxygen atoms in the lattice which can only be realized by the destruction of the VO_2 (B) lattice and re-construction into the VO_2 (M1) lattice.[2, 175] Thus, the appearance of VO_2 (M1) has nothing to do with the VO_2 (B), V_6O_{13} and V_2O_5 conversions.

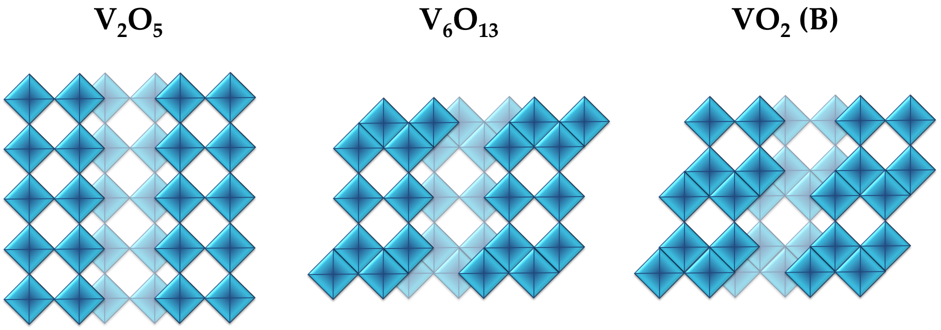

Figure 9.7: Schematic view of the V_2O_5, V_6O_{13} and VO_2 (B) structures constructed from idealized MO_6 octahedra. Based on references [2, 12].

Nucleation behavior

As discussed by Equations 7.14 and 7.15, the energy barrier for heterogeneous nucleation is lower than the energy barrier for homogeneous nucleation. If this is combined with a film thickness of about 20 nm, it is plausible to assume that nucleation preferentially occurs at the interface of the amorphous film and the substrate. Indeed, crystallization occurs much more early on SiO_2 than on γ-Al_2O_3. If crystallization would be induced by homogenous nucleation, no significant difference between both substrates is expected. Thus crystallization is most likely initiated by heterogeneous nucleation. In this context, nucleation is energetically favored on the amorphous SiO_2, compared to the crystalline γ-Al_2O_3, suggesting that surface energy between the nucleus and the surface (i.e.γ_{cs}) is the lowest for SiO_2. The nuclei formed on SiO_2 at a low temperature further grow and convert to V_6O_{13} and V_2O_5 as the temperature increases. On γ-Al_2O_3 the higher energy barrier for heterogeneous nucleation is only overcome at a higher temperature directly leading to nuclei for formation of crystalline V_6O_{13}.

Since monoclinic VO_2 (B) and rutile VO_2 (R) are not structurally related and their interconversion is very unlikely, their associated crystallites are likely originating from different nuclei. Because, VO_2 (B) and VO_2 (M1) crystallize at significantly different temperatures, the pathway of progressive nucleation[2] is suggested. Indeed during the nucleation and growth of VO_2 (B), only a limited amount of the amorphous film crystallizes (low diffraction peaks with small integrated areas) leaving plenty of material behind for the retarded nucleation into VO_2 (M1). Also for the VO_2 (M1) nucleation, the energy barrier for heterogeneous nucleation is the lowest for SiO_2, explaining why VO_2 (M1) is detected on SiO_2. Possibly, VO_2 (M1) nucleation can occur on γ-Al_2O_3 at a higher temperature (e.g. 600 °C). However, at this temperature already significant diffraction peaks with a large integrated area are observed, (i) suggesting that the majority of the amorphous material is already crystallized and (ii) inhibiting the formation of new nuclei.

Proceeding on the hypothesis of heterogeneous nucleation and in comparison to γ-Al_2O_3, SiO_2 exhibits a lower energy barrier for nucleation which leads a higher amount of nuclei and, after growth, to a higher density of small grains. On γ-Al_2O_3, less nuclei emerge which results in a film with a lower grain density and larger grains. In the context of solid state dewetting - for films with an equal thickness (h), grain boundary energy (γ_{gb}) and grain surface energy (γ_{gs}) - the condition for film breaking is identical. Obviously, if the grains are larger (as is the case on γ-Al_2O_3) this condition is more easily met. This might explain why for the same amount of deposition cycles (i.e. 4 and 6), the solid state dewetting (and particle formation) is more pronounced on γ-Al_2O_3 in comparison to SiO_2. Alternatively, the condition for solid state dewetting is more easily fulfilled if the amount of deposition cycles (and thus the film thickness h) increases, as is observed on SiO_2 and γ-Al_2O_3

---

[2] During progressive nucleation, not all nuclei are formed at the same time or temperature. Some clusters nucleate while other are already growing. The opposite is instantaneous nucleation in which all nuclei are formed at the same time or temperature.

9.2 Precursor chemistry

The aqueous solutions containing oxalato-VO^{2+} (i.e. solutions with a citrate:VO^{2+} ratio of 0.75:1 and 1.50:1, see Chapter 3) and citrato-VO^{2+} complexes (i.e. the solutions with a citrate:VO^{2+} ratio of 3.00:1 and 4.50:1, see Chapter 3) are used – within one week after their synthesis – for the preparation of crystalline vanadium oxides on 200 nm SiO_2, using the CSD route developed in Section 8.1.

Figure 9.8 shows the XRD patterns of the obtained four layered vanadium oxide films. For the oxalato-VO^{2+} solution (molar ratio 0.75:1), the initial four layered film (labeled *as dep.* in Figure 9.8) already shows crystalline features corresponding to the monoclinic VO_2 B phase as indicated by the (001), (002) and (003) diffraction peaks at 14.4 °2θ, 29.0 °2θ and 44.1 °2θ respectively. After an additional anneal at 400 °C, the diffraction peaks associated with VO_2 (B) remain without a significant change in their integrated area. If the temperature increases to 450 °C, the peaks associated with monoclinic VO_2 (B) completely disappear, but new peaks corresponding to monoclinic V_6O_{13} appear at 17.8 °2θ (002), at 26.9 °2θ (003) and at 45.5 °2θ (005). As the temperature further increases to 500 °C, the V_6O_{13} diffraction peaks sharpen and their FWHM decreases, indicating an increase of the V_6O_{13} crystallite size. Note that both VO_2 (B) and V_6O_{13} exhibit reflections corresponding to parallel crystallographic planes perpendicular to the c-axis. At 500 °C, an additional diffraction peak is observed at 27.8 °2θ which is assigned as the (110) diffraction peak of monoclinic VO_2 (M1).

The aqueous solution with a molar ratio of 1.50:1 results in a similar temperature-dependent vanadium oxide phase formation: VO_2 (B) at 400 °C, V_6O_{13} at 450 °C, and V_6O_{13} and VO_2 (M1) at 500 °C. At all studied temperatures, the integrated area of the diffraction peaks associated with VO_2 (B) and V_6O_{13} is smaller than those obtained from the 0.75:1 solution. No significant difference is observed in the VO_2 (M1) diffraction peak at 500 °C. The temperature-dependent phase formation is clearly different if the dominating oxalato-VO^{2+} species in the solution are exchanged by the citrato-VO^{2+} species (i.e. solutions with a molar ratio of 3.00:1 and 4.50:1). The solution with a molar ratio of 3.00:1 leads to an amorphous four layered film without VO_2 (B) characteristics directly after the intermediate anneal. If an additional anneal at 400 °C (10 minutes) is applied, small peaks associated with VO_2 (B) can be distinguished from the background at 29.0 and 44.1 °2θ. Similar to solutions with a molar ratio of 0.75:1 and 1.50:1, the VO_2 (B) diffraction peaks are replaced by V_6O_{13} diffraction peaks at 450 °C. Note that only the peaks at 26.9 °2θ can be distinguished and that their intensity is much lower than the ones observed for the oxalato-VO^{2+} containing solutions at 450 °C. As the temperature further increases to 500 Â°C, a strong crystallization occurs with appearance of intense diffraction peaks associated with monoclinic V_6O_{13} – (002) peak at 17.8 °2θ, (003) peak at 26.9 °2θ, (004) peak at 36.2 °2θ and (005) peak at 45.5 °2θ – and monoclinic VO_2 (M1) – (220) peak at 27.8 °2θ. An additional diffraction peak is observed at 20.3 °2θ and is ascribed to orthorhombic V_2O_5.

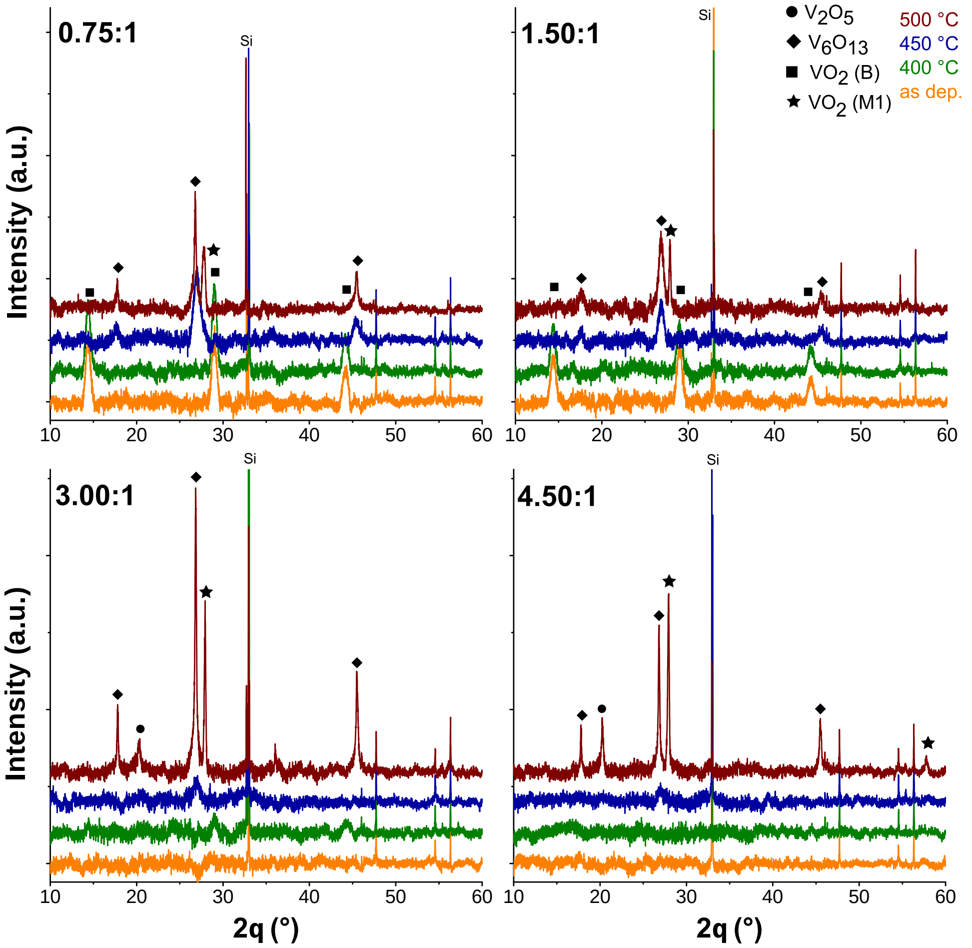

Figure 9.8: XRD pattern of four layered films spin coated from the aqueous VO^{2+} solutions – with a citrate:VO^{2+} molar ratio of 0.75:1, 1.50:1, 3.50:1 and 4.5:1 – on 200 nm SiO_2 after an intermediate anneal of 400 °C and a post deposition anneal at 400 °C, 450 °C or 500 °C. All anneals are performed in a 0.1 % O_2 ambient for 10 minutes. The assignments are based on JCPDS 82-0661, 78-0983, 81-2392 and 03-0206 of monoclinic VO_2 (M1), monoclinic V_6O_{13}, monoclinic VO_2 (B) and orthorhombic V_2O_5. The vertical scale is decreased by factor 4 in comparison to the other XRD patterns in this Chapter.

The temperature-dependent phase formation from the solution with a molar ratio of 4.50:1 exhibits similar features as the one from the 3.00:1 solution. However, the VO_2 (B) phase formation is not observed and the intensity of the V_6O_{13} peaks at 450 °C is decreased. Moreover, the intensity of the diffraction peak associated with VO_2

(M1) at 27.8 °2θ is increased and a second diffraction peak associated with VO_2 M1 is observed at 57.9 °2θ (220). Thus, as the molar ratio of citrate to VO^{2+} increases in the solution and the dominance of oxalato-VO^{2+} complexes is exchanged for citrato-VO^{2+} complexes: (i) crystallization is delayed from 400 °C to 500 °C, (ii) the formation of VO_2 (B) is no longer observed and (iii) enhanced V_6O_{13} and VO_2 (M1) crystallization is observed at 500 °C.

1. Schwartz et al. suggest that crystallization of solution deposited films only occurs if the organic moieties are thermally removed from the film.[33] Thermal analyses, preformed in a low p_{O_2} ambient, indeed indicate that this final removal occurs at 350 and 400 °C for the oxalato-VO^{2+} (Chapter 5) and citrato-VO^{2+} (Chapter 6) complexes, respectively. Both temperatures shortly precede the observed crystallization from the oxalato-VO^{2+} solution (i.e. 450 °C) and the citrato-VO^{2+} solution (500 °C).
2. The formed VO_2 (B) easily transforms into V_6O_{13} and V_2O_5 as the processing temperature increases Section 9.1.4). According to Katzke et al., VO_2 (B), V_6O_{13} and V_2O_5 belong to a homologous series of oxygen deficient structures originating from the same structure with a decreased number of oxygen vacancies, respectively.[2] Thus the transformation of VO_2 (B) to V_6O_{13} and V_2O_5 is caused by filling of the oxygen vacancies at higher temperatures.
3. Thirdly, VO_2 (M1) is not an oxygen deficient structure but belongs to a different homologous series originating from a hexagonal-closed-packed bilayer structure. This VO_2 (M1) typically crystallizes from an amorphous matrix at 500 °C in a low p_{O_2} ambient.

In conclusion, the solutions with the dominance of oxalato-VO^{2+} complexes form the oxygen deficient, crystalline VO_2 (B) already at 400 °C because its final thermal decomposition already occurs at 350 °C. Once VO_2 (B) is formed, it can only transform into V_6O_{13} and V_2O_5 by filling of the oxygen vacancies at higher temperatures. The solution with the dominance of citrato-VO^{2+} complexes initially results in an amorphous film, because the final decomposition step only occurs at 450 °C. As a consequence, crystallization only appears at 500 °C and is associated with a simultaneous VO_2 (M1) and V_6O_{13} crystallization.

9.3 TiN $\cdots$ a different story

TiN was initially chosen as a metallic substrate which would allow electrochemical evaluation of the layered vanadium oxides (i.e. VO_2 (B), V_6O_{13} and V_2O_5). As will be seen in this section, the TiN not only acts as a substrate but actively participates in the phase formation. This is the reason why TiN is not included in the substrate discussion above, but discussed separately.

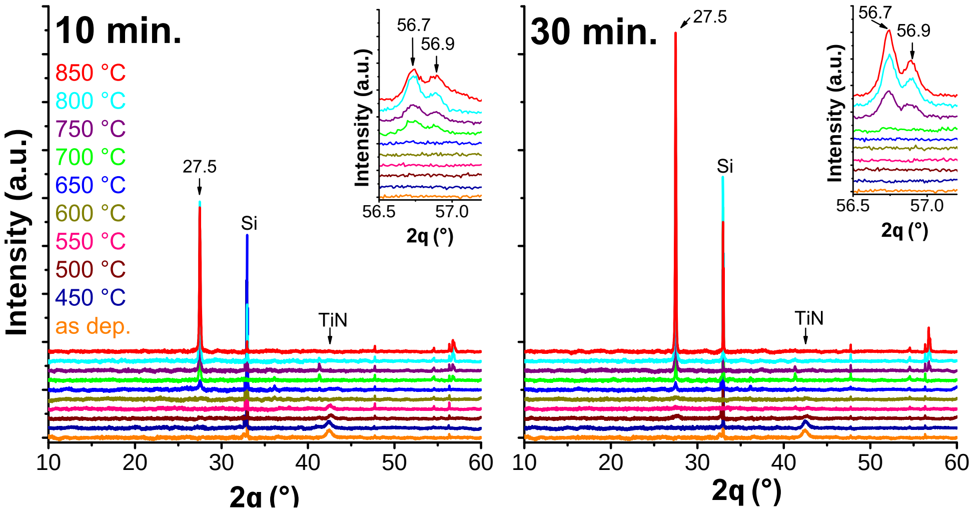

Figure 9.9: XRD pattern of four layered films spin coated from the aqueous citrato-oxalato-VO^{2+} (molar ratio of citrate:VO^{2+} = 2:1) on 70 nm TiN with an intermediate hot plate step at 90 °C in air (2 minutes), an intermediate anneal at 400 °C in 0.1 % O_2 (10 minutes, as dep.) and a post deposition anneal at temperatures ranging between 450 °C and 850 °C in 0.1 % O_2. The anneal time of this final anneal is either 10 minutes (left) or 30 minutes (right).

9.3.1 Observations

The vanadium oxide phase formation and the associated morphology, starting from the aqueous oxalato-citrato-VO^{2+} solution, is studied on TiN as well. Figure 9.9 shows the XRD patterns obtained of four layered films after a final anneal in 0.1 % O_2 at temperatures ranging between 450 °C and 850 °C with an anneal time of 10 or 30 minutes. Firstly, the as deposited film only demonstrates a diffraction peak associated with crystalline TiN substrate around 42.5 °2θ (011). This diffraction peak disappears as the temperature increases. Crystalline TiN can endure up to 550 °C or up to 450 °C in 0.1 % O_2 for an anneal time of 10 or 30 minutes, respectively. Secondly, starting from 650 °C, a diffraction peak occurs at 27.5 °2θ.

Oxide	JCPDS	Reflection	Position (°2θ)
Rutile TiO_2	21-1276	(011)	27.5
		(022)	56.6
High temperature, rutile VO_2	44-0253	(011)	27.7
		(022)	57.1
Low temperature, monoclinic VO_2 (M1)	82-0661	(011)	27.8
		(022)	57.5

Table 9.2: Overview of the most important XRD reflections of rutile TiO_2, rutile VO_2 and monoclinic VO_2 (M1)

As indicated by Table 9.2, this peak can be assigned to the (011) reflection of monoclinic VO_2 (M1), of rutile VO_2 or of rutile TiO_2. Theoretically, the rutile VO_2 is only present if the actual temperature exceeds 68 °C, which makes its assignment rather unlikely. As the temperature further increases, the peak intensity drastically increases, suggesting a strong increase in crystalline material. Additionally, starting from 700 °C (anneal of 10 minutes) or from 750 °C (30 minutes), two new diffraction peaks appear at 56.7 °2θ and at 56.9 °2θ which can be tentatively assigned to the (022) reflection of rutile TiO_2 and monoclinic VO_2 (M1) or rutile VO_2, respectively. Also here, the assignment to rutile VO_2 is rather unlikely. However, its theoretical reflection position better fits the observed value than monoclinic VO_2 (M1). This suggests that during the anneal, (i) TiN oxidizes to TiO_2 and (ii) crystallization into rutile VO_2 takes place. As the sample cools down and the XRD measurement is performed at T_{Room} , the rutile VO_2 transforms into the monoclinic VO_2 (M1).

To gain more insights, the morphology of the total stack (i.e. TiN or TiO_2 substrate and four layered films annealed at various temperatures in 0.1 % O_2 for 30 minutes) is examined in Figures 9.10 and 9.11. At 550 °C or 600 °C, when no signs of crystalline TiN remain and no indications are seen for crystalline VO_2 or TiO_2, the amorphous film covers the entire substrate and grain formation emerges. Since, TiN is already lost below 550 °C the diffusion of O_2 through pin holes or its direct contact at uncovered parts of the substrate is excluded. As the temperature increases to 650 °C, and the onset of VO_2 (M1) and TiO_2 crystallization is demonstrated, the grains evolve and become clearly visible. At this point the grains are reasonably small and have an average size of 90 nm. From Figure 9.11 it is clear that the grains further grow, via Ostwald ripening, as the temperature increases. Note that during this ripening, the grains partially rip off and spherical particles arise. E.g. at 850 °C, the average particle size exceeds 400 nm.

9.3.2 Hypothesis

It is well known that TiN coatings thermally oxidize to TiO_2 starting between 350 °C and 450 °C in an O_2 based environment.[176–179]. These studies are, generally, performed on TiN with a ± 1:1 stoichiometry. This TiN features a diffraction peak at 37.3 °2θ, assigned to the (111) reflection and firstly oxidizes to anatase TiO_2 with the dominating (004) reflection at 37.8 °2θ. These studies are not consistent with our observations. However, recent reports of Deng et al. study the oxidation behavior of N-doped TiO_2, via in-situ HT-XRD, of samples with a different N:Ti ratios in He and air. (i) N-deficient TiN samples (with N content of 10 at. %) clearly exhibit the (200) reflection of TiN at 47.5 °2θ. (ii) Starting from 625 °C and in He, these N-deficient TiN samples transform to rutile TiO_2 with a primary (022) reflection at 27.5 °2θ and a less intense, secondary (002) reflection at 39.0 °2θ. (iii) Their oxidation in air leads to anatase TiO_2 at 475 °C which transforms into rutile TiO_2 at 700 °C.[180] This study suggests that the used TiN substrate is N-deficient and that the 0.1 % O_2 rather

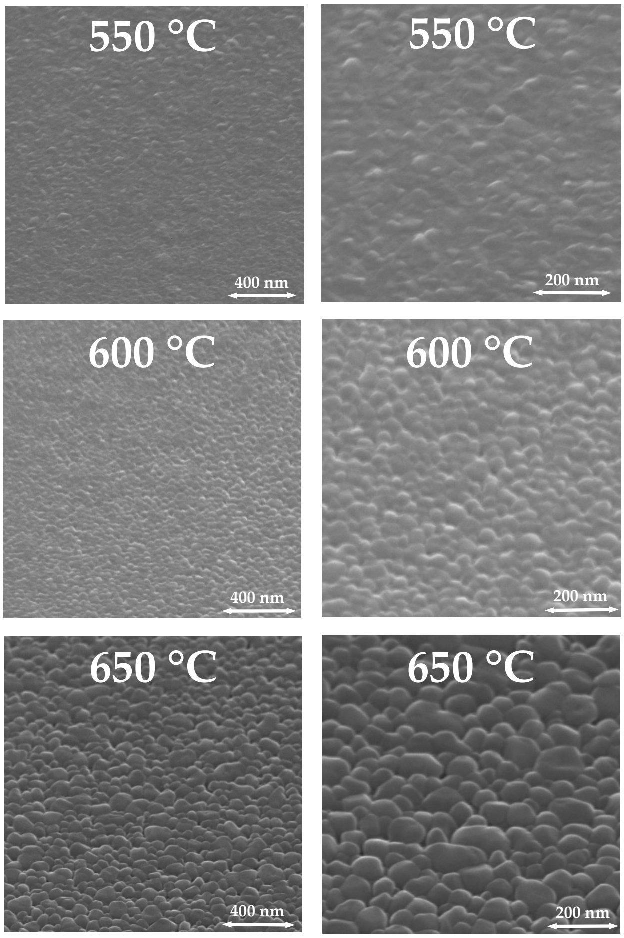

Figure 9.10: SEM images of four layered films spin coated from the aqueous citrato-oxalato-VO^{2+} (molar ratio of citrate:VO^{2+} = 2:1) on 70 nm TiN with an intermediate hot plate step at 90 °C in air (2 minutes), an intermediate anneal at 400 °C in 0.1 % O_2 (10 minutes) and a final anneal at 550 °C (top), 600 °C (middle) or 650 °C (bottom) in 0.1 % O_2 (30 minutes).

approaches the He and not the air atmosphere. Indeed, careful inspection of the TiN substrate synthesis (i.e. Ionized Metal Plasma synthesis) elucidates a N-deficient $TiN_{0.6}$ stoichiometry. Additionally, AFM images of the in He treated N-deficient TiN show the formation of separated TiO_2 particles, with an average size of 300 nm and a rather low surface coverage, on a SiO_2 surface.[180] Also these observations are in line with our results, based on the SEM images in Figures 9.10 and 9.11. Our high surface coverage could be explained by the thicker, initial TiN layer (70 nm versus 25 nm in the work of Deng et al.). In summary, the N-deficient TiN substrate transforms,

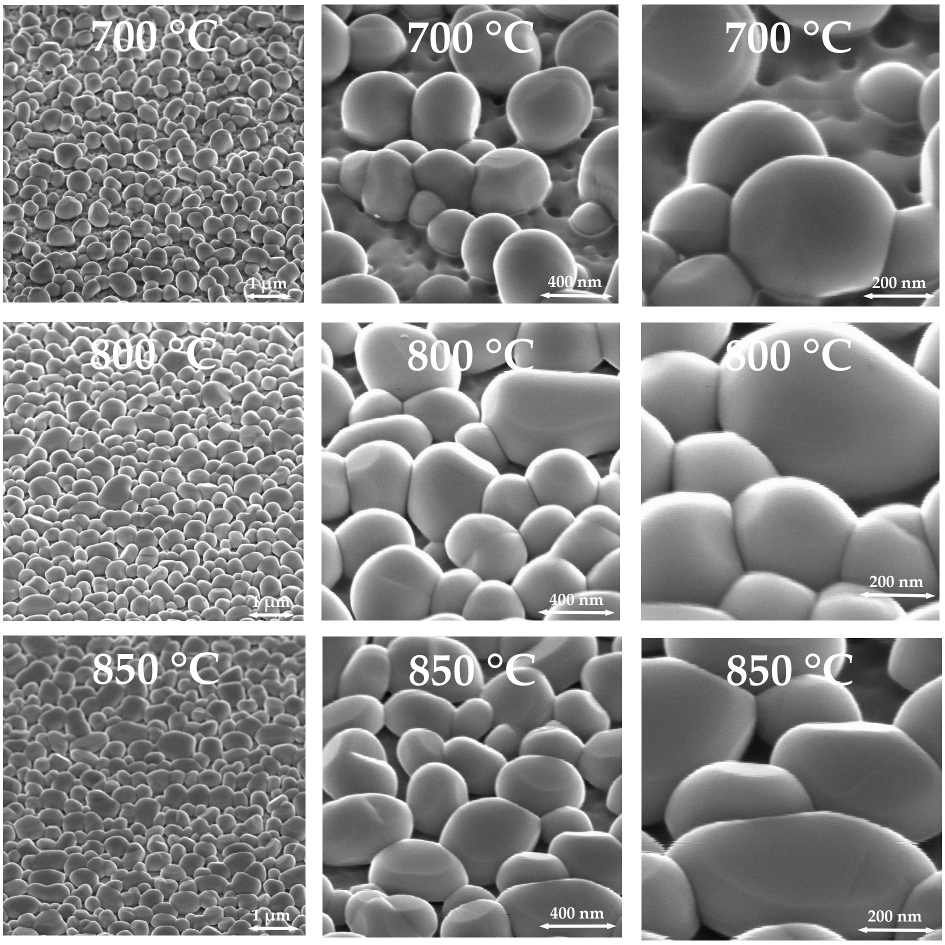

Figure 9.11: SEM images of four layered films spin coated from the aqueous citrato-oxalato-VO^{2+} (molar ratio of citrate:VO^{2+} = 2:1) on 70 nm TiN with an intermediate hot plate step at 90 °C in air (2 minutes), an intermediate anneal at 400 °C in 0.1 % O_2 (10 minutes) and a final anneal at 700 °C (top), 800 °C (middle) or 850 °C (bottom) in 0.1 % O_2 (30 minutes).

at 625 °C and in O_2-poor atmosphere, into rutile TiO_2 particles with a preferred (011) orientation.

Muraoka et al. and Abreu et al. compare the epitaxial growth of rutile VO_2, above its phase transition temperature, on a TiO_2 (001) and a TiO_2 (011) surface.[181, 182] They demonstrate the exclusive, epitaxial growth of (i) rutile TiO_2 with a preferred (001) orientation on a rutile TiO_2 (001) surface and (ii) rutile TiO_2 with a preferred (011) orientation on a rutile TiO_2 (011) surface. The last one is in a full agreement with the observed VO_2 crystallization with the (011) and (022) diffraction peaks.

Combining both argumentations, it is plausible to hypothesize that during the final anneal (in a O_2-poor atmosphere) the N-deficient TiN transforms into rutile TiO_2 particles with a preferred (011) orientation which acts as an in-situ formed surface for the epitaxial growth of rutile VO_2. In this hypothesis the VO_2 covers the entire surface of the TiO_2 particles leading to composite core-shell particles with a TiO_2 core and VO_2 shell. Obviously, during cooling, the rutile VO_2 transforms, via the well-known structural phase transition, into monoclinic VO_2. This hypothesis is the perfect starting point for further work to (i) prove the core-shell TiO_2/VO_2 structure via physical characterization such as TEM, (ii) to analyze its metal-to-insulator transition which would be very straightforward since the SiO_2 layer, buried beneath the initial TiN, has a thickness of about 100 nm and (iii) to optimize particle density by tuning the TiN thickness or the VO_2 thickness by changing the amount of deposition cycles prior to the final anneal.

9.4 Conclusion

The vanadium oxide phase formation is analyzed through an extended parameter study and related to the nucleation behavior. As was expected from the complicated vanadium-oxygen phase diagram (Figure 1), the vanadium oxide phase formation is not straightforward and each parameter in the CSD process influences this vanadium oxide phase formation. In general, three stages are passed during the vanadium oxide phase formation as a function of temperature.

1. At mildest anneal conditions, monoclinic VO_2 (B) crystallizes on the amorphous substrates (SiO_2 and TiO_2). The monoclinic VO_2 (B) crystallites originate from the progressive, heterogeneous nucleation at the interface between the amorphous layer and the substrate. VO_2 (B) crystallization is not observed on the crystalline substrates (γ-Al_2O_3 and Pt) which is probably due to their increased surface energy, inhibiting heterogeneous nucleation. At this point, the grained film completely covers the substrate.

2. During the intermediate anneal conditions, the monoclinic VO_2 (B) transforms into monoclinic V_6O_{13} which is caused by filling of the oxygen vacancies in the lattice. Additional, monoclinic VO_2 (M1) appears as a secondary phase and originates from different nuclei formed at the interface. Nevertheless VO_2 (B) nucleated earlier, had the opportunity to grow and transform into V_6O_{13}, plenty amorphous material is available for the formation of the rutile VO_2 (R) nuclei. This rutile VO_2 (R) nucleation is heterogeneous and is only observed on the substrates with a low surface energy (i.e. SiO_2). The morphology changes from a grained film covering the substrate to a structure partially consisting of a grained, substrate covering film and (hemi-)spherical particles. This phenomenon is related to the solid state dewetting of films and preferentially occurs

on films with a low density of large grains as is the case on γ-Al_2O_3 (explaining the extended dewetting on γ-Al_2O_3 in comparison to SiO_2) and on films with higher initial thickness (explaining the extended dewetting after 6, 8 or 10 deposition cycles in comparison to less deposition cycles).

3. Finally, after the anneal with the strongest conditions (i.e. highest temperature), the V_6O_{13} starts to transform into orthorombic V_2O_5, while the VO_2 (M1) phase remains leading to a structure with V_6O_{13}, V_2O_5 and VO_2 (M1).

The aqueous solutions containing oxalato-VO^{2+} and citrato-VO^{2+} complexes lead to a different vanadium oxide phase formation on SiO_2. The solutions with the dominance of oxalato-VO^{2+} complexes form the oxygen deficient, crystalline VO_2 (B) already at 400 °C because its final thermal decomposition already occurs at 350 °C. Once VO_2 (B) is formed, it can only transform into V_6O_{13} and V_2O_5 by filling of the oxygen vacancies at higher temperatures. The solution with the dominance of citrato-VO^{2+} complexes initially results in an amorphous film, because the final decomposition step only occurs at 450 °C. As a consequence, crystallization only appears at 500 °C and is associated with a simultaneous VO_2 (M1) and V_6O_{13} crystallization. This is one of the key achievements in this doctoral research: the structure and chelation of the VO^{2+} complexes, present in the aqueous solution, directly relates to the vanadium oxide phase formation through their thermal decomposition pathway.

On the N-deficient TiN an alternative phase formation pathway is followed. During the final anneal (in a O_2-poor atmosphere) the TiN transforms into rutile TiO_2 particles with a preferred (011) orientation which acts as an in-situ formed surface for the epitaxial growth of rutile VO_2. This hypothesis could be the starting point of further work to (i) prove the core-shell TiO_2/VO_2 structure, (ii) to analyze its metal-to-insulator transition and (iii) to optimize particle or grain density.

Conclusions

The main objective of this work was to obtain fundamental insights in the aqueous vanadium precursor chemistry and in their relation to the vanadium oxide stoichiometry/phase formation, obtained via a solution deposition route. Here, the main achievements per milestone will be summarized.

Acquiring insights in the aqueous citrato/oxalato-VO^{2+} solution chemistry: synthesis, structure and stability

Defined goal

Firstly, a detailed literature study on the behavior of vanadium ions and their coordination with citrato ligands in water was required. Secondly, our aim was to synthesize mononuclear citrate-VO^{2+} complexes without inserting a high amount of citrate or thermally non-decomposable species. In addition, the prevention of the secluded, dimeric structure – by the formation of ammonium carboxylate interactions, bridging two or more citrato-VO^{2+} complexes into a network – was targeted. From a fundamental scientific perspective, it was interesting to study and understand each step, and the associated chemical transformations, during this synthesis. The structure and stability of the final citrato-VO^{2+} complexes, present in the aqueous solution, would be explored in particular.

Achievements

The review of the aqueous vanadium chemistry indicates that:

- Vanadium can occur with three different oxidation states in the aqueous solution (i.e. +III, +IV and +V). The conversion from one to another oxidation state must be anticipated, especially when other components (such as citric acid or H_2O_2) are introduced in the aqueous solution.
- In the absence of an additional chelating compound (such as citric acid), the vanadium(V) ion easily hydrolyzes. This hydrolyzed species is subsequently subjected to condensation reactions leading to pH-dependent polynuclear species such as tri-, tetra-, penta- or decavandates.

- Condensation can be prevented by forming citrato complexes in the aqueous solution. Citrato-VO_2^+ complexes are typically observed as dinuclear complexes with a very stable $(VO_2)_2\,(\mu_2 - O)$ unit, formed by the deprotonated α-hydroxyl functionality of the citric acid/citrate. The associated geometry is a square pyramidal with the free V=O bond in the axial position. Citrato-VO^{2+} complexes are also observed as dinuclear complexes with a very stable $(VO)_2(\mu_2 - O)$ unit. Here, the associated geometry is pH-dependent and can be a square pyramidal with the V=O bond at the axial position (pH ~ 5) or a distorted octahedral with the V=O bond at the first axial position and a carboxylate group at the second axial position (pH ~ 8). Mononuclear complexes are only observed if a high amount of citrate is added to the solution (i.e. m.r. 100:1).

A new method for the synthesis of an aqueous solution containing oxalato-VO^{2+}, citrato-oxalato-VO^{2+} or citrato-VO^{2+} complexes is developed and each step in its synthesis is studied in detail by various spectroscopic techniques such as ^{51}V-NMR and EPR spectroscopy. During synthesis, cyclic tetravanadate(V) is converted into VO^{2+} using oxalic acid as an acidifier and reducing agent. The subsequent complexation of the VO^{2+} ion with citrato complexing agents occurs as a ligand exchange reaction with chelating oxalato ligands. A successful procedure, based on the limited solubility of $(NH_4)_2C_2O_4$ in water, is developed for the removal of the oxalate excess (which was necessary for a complete VO_2^+/VO^{2+} reduction).

As a function of the molar ratio of citrate to the reduced $[VO(C_2O_4)_2]^{2+}$ species, the following complexes are obtained and identified. At a low molar ratio (i.e. 0.75:1), monomeric cis-oxalato-VO^{2+} complexes occur with a distorted square pyramidal geometry. As the amount of citrate increases, oxalate is gradually exchanged for citrate leading to a VO^{2+} complex with a mixed oxalate/citrate ligation (1.5:1) or an exclusive citrato ligation (2:1 or higher). In the latter case, both mono- and dimeric citrato complexes are observed. However, the monomeric citrato complex dominates (abundance > 80 %) and is characterized by sixfold chelation of the vanadium(IV) ion by a RCO_2^- ligation at the equatorial positions and a H_2O/R-OH ligation at the axial position. The oxalato-VO^{2+} and citrato-VO^{2+} complexes show a different redox reactivity towards the dissolved O_2 in the aqueous solution. During the first week after synthesis, a non-resolved onset of oxidation is observed for both complexes. After 17 days – in closed NMR tube filled with air and at room temperature – the oxidation rate is the highest for the oxalato-VO^{2+} complexes. If citrato-VO^{2+} complexes dominate, no further difference between the oxidation rates is detected as more citrate is present in the solution. The reactivity of the VO^{2+} complexes can be drastically retarded by evacuation of the dissolved O_2 and subsequent storage in a N_2 ambient.

Understanding the thermal decomposition pathway of the ammonium-citrato/oxalato-VO^{2+} gel

Defined goal

The formation of a vanadium oxide, starting from an aqueous vanadium precursor solution, via the chemical solution deposition route, requires the, thermally-induced, transformation of the precursor gel into the oxide. Hence, it was important to understand the thermal decomposition pathway of the precursor gel and its containing complexes. In addition, this fundamental understanding would aid in determining the initial processing conditions and in establishing the relation between the precursor composition and the vanadium oxide stoichiometry/phase formation. Thus the thermal decomposition pathway of the ammonium-oxalato-VO^{2+} gel and ammonium-citrato-VO^{2+} gel had to be studied in air and in N_2 (or He).

Achievements

In the thermal decomposition pathway of both gels, the largest weight loss is observed at 250 °C. This weight loss corresponds to the non-oxidative and endothermic decomposition of the α-hydroxyl groups, ammonium carboxylate groups and carboxylic acid groups with the release of NH_3, H_2O and CO_2. Above 250 °C, the pathway depends on the ambient (air versus N_2/He) and on the composition of the complexes in the gel (oxalato- versus citrato-VO^{2+}).

1. Ammonium-oxalato-VO^{2+}
    - In an oxidative ambient, an exothermic and oxidative decomposition step occurs around 275 °C. The remaining VO^{2+} species are fully decomposed with the release of mainly H_2O, CO_2 and NO_2. Additionally, the formation of the V-O bonds takes place resulting in V_2O_5. No weight loss is observed above 300 °C leading to a final weight of 11 %.
    - In a non-oxidative ambient, no exothermic reactions are observed and the major decomposition step is delayed to 322 °C. The thermal decomposition pathway favors the formation of amide and nitrile functionalities and the release of their associated mass fragments. Additionally, the little amount of O_2 present is consumed for the formation of NO and CO_2, derived from the oxidative decomposition of such amide/nitrile functionalities and of the residual matrix, respectively. At 500 °C, the sample still contains compounds that are thermally stable in the reduced O_2 ambient (~ 44 w/w% of the residual sample):
2. Ammonium-citrato-VO^{2+}
    - In oxidative conditions all thermo stable compounds formed during the previous decomposition steps and the direct coordination sphere of the

vanadium ion are decomposed with the formation of mainly H_2O, NH_3, CO_2 and NO_2. Mass fragments suggesting amide formation are detected as well, but with a marginal ion current. Finally, the formation of the V-O bonds takes place and V_2O_5 crystallization occurs.

- In an inert atmosphere, the decomposition of oxalate residues extends up to 325 °C. Next, amide functionalities form and convert to nitrile groups with the release of H_2O. These nitrile groups subsequently rearrange and emit HCN or $H_2C{=}C{=}N$. Due to the unintended presence of O_2 in the inert atmosphere also minor oxidative burnings of thermo stable compounds are observed. The residual sample, obtained at 625 °C, still contains compounds that are thermally stable. These compounds account for ~ 51 w/w% of the residual sample.

Relating the aqueous precursor chemistry to the vanadium oxide stoichiometry and phase formation

Defined goal

Once the composition and structure of the VO^{2+} complexes, present in the aqueous solution, and their thermal decomposition pathway would be understood, the actual vanadium oxide formation could be explored. Each step and parameter of the chemical solution deposition route had to be investigated with the formation of VO_2 (M1), VO_2 (B), V_6O_{13} and V_2O_5 targeted. Next, the vanadium oxide stoichiometry and phase formation would be investigated and related to the composition and thermal decomposition pathway of the VO^{2+} complexes present in the aqueous solution.

Achievements

A full procedure for the preparation of crystalline vanadium oxide films by controlling the vanadium oxidation state throughout the entire deposition process is presented. An intermediate anneal in 0.1 % O_2 (400 °C, 10 minutes) needs to be added to the film processing to allow sub 100 nm thickness adjustment without compromising the vanadium +IV oxidation state. All aqueous solutions are successfully used for the preparation of crystalline vanadium oxide nanostructures.

The vanadium oxide stoichiometry and phase formation is directly related to the aqueous precursor chemistry and to the parameters of the chemical solution deposition route:

1. The deposition of an aqueous solution with the dominance of citrato-VO^{2+} complexes on SiO_2 and the subsequent processing in an 0.1 % O_2 ambient is recommended for the formation of **VO_2 (M1)** (e.g. for its MIT property). This solution initially results in an amorphous film, because the final decomposition step only occurs at 450 °C. VO_2 (M1) crystallization occurs at 500 °C and is

accompanied by a V_6O_{13} secondary phase. If a four layered film is deposited, particles are obtained after an anneal at 500 °C with an average size of 1.78 μm and a substrate coverage of 48 %.

2. If **VO_2 (B)**, **V_6O_{13}** or **V_2O_5** is targeted (e.g. as candidate cathode material), the citrate-VO^{2+} complexes must be replaced by oxalato-VO^{2+} complexes. An aqueous solution with the dominance of oxalato-VO^{2+} complexes forms the oxygen deficient, crystalline VO_2 (B) already at 400 °C because its final thermal decomposition already occurs at 350 °C. Once VO_2 (B) is formed, it can only transform into V_6O_{13} and V_2O_5 by filling of the oxygen vacancies at higher temperatures. The temperature-dependent VO_2 (B), V_6O_{13} and V_2O_5 transformation and their morphology can be tuned by changing the substrate and processing conditions:

    - The entire transformation sequence is followed on the amorphous substrates (SiO_2 and TiO_2) due to the progressive and heterogeneous nucleation of VO_2 (B) crystallites at the interface between the amorphous layer and the substrate. The crystalline substrates (γ-Al_2O_3 and Pt) are more resistive to crystallization and VO_2 (B) phase formation is not observed.
    - As the temperature increases, the morphology changes from a grained film to a structure consisting of a grained film and (hemi-)spherical particles. This phenomenon is related to the solid state dewetting of films and preferentially occurs on polycrystalline films with a low density of large grains as is the case on γ-Al_2O_3 and on films with higher initial thickness.

3. If the films are treated in an oxidative ambient (i.e. air), all precursor solutions form crystalline **V_2O_5**. The removal of the organic matrix and its crystallization is studied via GATR-FTIR spectroscopy and in-situ HT-XRD. In contrast to its powder variant, the organic matrix already decomposes at 400 °C in air. Despite the temperature offset, the thermal decomposition pathway is identical. At 315 °C the onset of V_2O_5 crystallization is observed. As the temperature increases, the preferred c-axis oriented crystallization pushes through which results in elongated nano-rods. From 650 °C, V_2O_5 melts and all peaks disappear from the HT-XRD pattern.

On the N-deficient TiN an alternative phase formation pathway is followed. During the final anneal (in a O_2-poor atmosphere) the TiN transforms into rutile TiO_2 particles with a preferred (011) orientation which acts as an in-situ formed surface for the epitaxial growth of rutile VO_2. This hypothesis could be the starting point of further work to (i) prove the core-shell TiO_2/VO_2 structure, (ii) to analyze its metal-to-insulator transition and (iii) to optimize particle or grain density.

Outlook

At this point several aqueous solutions containing oxalato-VO^{2+}, citrato-oxalato-VO^{2+} or citrato-VO^{2+} complexes are synthesized and investigated. In addition, the vanadium oxide stoichiometry and phase formation are related to the precursor chemistry.

This work shows the important relation between the precursor chemistry and the oxide formation (in a reduced O_2 ambient). It would be very interestingly if one could generalize this key point by (i) studying alternative chelating agents for which a different thermal decomposition pathway is expected and (ii) transferring our observations to a citrato/oxalato precursor system with a different metal cation.

Another follow-up study could focus on the implementation and functional characterization of these VO_2 (M1), VO_2 (B), V_6O_{13} and V_2O_5, as active component in future technological devices. This would first require an optimization of the morphology and the realization of closed films without pin-holes. An increased film thickness – by a higher VO^{2+} concentration or a higher number of deposition cycles – could be the starting point. Moreover, in the context of VO_2 (M1):

- The effect of dopants on the MIT can be investigated by the preparation of doped-VO_2 (M1) films or particles. The preparation and analysis of multimetal ion solutions containing VO^{2+} complexes and Ti^{4+}, Al^{3+}, W^{6+}, Mo^{6+} or Nb^{5+} complexes will be required.
- The obtained VO_2 (M1) nanoparticles could be incorporated in a SiO_2 matrix which promises enhanced functional properties.

Finally, the collaboration framework could be explored for a more detailed analysis of some of the metal-ion precursors available in the IMO-IPC research group. E.g. complexes with a specific manganese, cobalt or chromium ion could be structurally analyzed via EPR spectroscopy. Alternatively, complexes with a specific lithium or aluminum ion could be investigated via NMR spectroscopy.

Scientific contributions

Publications

N. Peys, H. Damm, S. Gielis, K. Schellens, C. De Dobbelaere, G. Rampelberg, C. Detavernier, S. De Gendt, A. Hardy, M.K. Van Bael (2014) *Thermal decomposition study of an ammonium-oxalato/citrato-*VO^{2+} *solution-gel precursor for* V_2O_5 *formation*, manuscript in preparation.

N. Peys, S. Maurelli, G. Reekmans, C. De Dobbelaere, P. Adriaensens, S. Van Doorslaer, S. De Gendt, A. Hardy, M.K. Van Bael (2014) *Oxalato- and citrato-*VO^{2+} *complexes in an aqueous solution: spectroscopic study, reactivity and use as aqueous precursor for vanadium oxide phase formation*, manuscript submitted.

N. Peys, P. Adriaensens, S. Van Doorslaer, S. Gielis, E. Peeters, C. De Dobbelaere, S. De Gendt, A. Hardy, M.K. Van Bael (2014) *Aqueous citrato-oxovanadate(IV) solutions for* VO_2*: synthesis, spectroscopic investigation and thermal analysis*, accepted for publication in Dalton Transactions.

K. Elen, B. Capon, C. De Dobbelaere, D. Dewulf, **N. Peys**, C. De Detavernier, A. Hardy, M. K. Van Bael (2014) *Transparent conducting oxide films of group V doped titania prepared by aqueous chemical solution deposition*, Thin Sold Films, http://dx.doi.org/10.1016/j.tsf.2013.05.104.

B. Souvereyns, C. De Dobbelaere, K. Elen, A. Kelchtermans, **N. Peys**, J. D'Haen, H. Van den Rul, V. Meynen, P. Cool, A. Hardy, M.K. Van Bael (2013) *Hydrothermal synthesis of a concentrated and stable dispersion of* TiO_2 *nanoparticles*, Chemical Engineering Journal, 223, 135–144.

N. Peys, Y. Ling, D. Dewulf, S. Gielis, C. De Dobbelaere, D. Cuypers, P. Adriaensens, S. Van Doorslaer, S. De Gendt, A. Hardy, M.K. Van Bael (2013) V_6O_{13} *films by control of the oxidation state from aqueous precursor to crystalline phase*, Dalton Transactions, 42(4), 959–968.

N. Chiodarelli, Y.L. Li, D.J. Cott, S. Mertens, **N. Peys**, M. Heyns, S. De Gendt, G. Groeseneken, P.M. Vereecken (2011) *Integration and electrical characterization of carbon nanotube via interconnects*, Microelectronic Engineering, 88, 837–843.

D. Dewulf, **N. Peys**, S. Van Elshocht, G. Rampelberg, C. Detavernier, S. De Gendt, A. Hardy, M.K. Van Bael (2011) *Interfacial reactions of Gd- and Nb-oxide based high-k layers deposited by aqueous chemical solution deposition*, Microelectronic Engineering, 88, 1338–1341.

N. Chiodarelli, K. Kellens, D.J. Cott, **N. Peys**, K. Arstila, M. Heyns, S. De Gendt, G. Groeseneken, P.M. Vereecken (2010) *Integration of Vertical Carbon Nanotube Bundles for Interconnects*, Journal of the Electrochemical Society, 157(10), K211–K217.

A. Hardy, S. Van Elshocht, D. Dewulf, S. Clima, **N. Peys**, C. Adelmann, K. Opsomer, P. Favia, H. Bender, I. Hoflijk, T. Conard, A. Franquet, H. Van den Rul, J.A. Kittl, S. De Gendt, M.K. Van Bael, J. Mullens (2010) *Properties of Ultrathin High Permittivity, $(Nb_{1-x}Ta_x)_2O_5$ Films Prepared by Aqueous Chemical Solution Deposition*, Journal of the Electrochemical Society, 157(1), G13–G19.

J. Swerts, **N. Peys**, L. Nyns, A. Delabie, A. Franquet, J. W. Maes, S. Van Elshocht, S. De Gendt (2010) *Impact of Precursor Chemistry and Process Conditions on the Scalability of ALD HfO_2 Gate Dielectrics*, Journal of the Electrochemical Society, 157, G26 (2010).

Oral presentations

N. Peys, S. Gielis, C. De Dobbelaere, S. De Gendt, A. Hardy, M.K. Van Bael, (2013), *An aqueous process for the formation of VO_2 (M1) and V_6O_{13} films*, Materials Science & Technology 2013, Montreal, Canada, October 27–31, 2013.

N. Peys, S. Gielis, C. De Dobbelaere, S. Van Doorslaer, S. De Gendt, A. Hardy, M.K. Van Bael (2013) *Vanadium oxide nanostructure formation by an aqueous deposition route: from precursor solution to crystalline phase*, Materials Research Society Spring meeting 2013, San Francisco, USA, April 1–5, 2013.

N. Peys, S. Van Doorslaer, P. Adriaensens, S. De Gendt, A. Hardy, M.K. Van Bael (2012) *Acquiring insights in the synthesis of an aqueous citrato-oxovanadate(IV) precursor by Magnetic Resonance techniques*, Conference for Young Belgian Magnetic Resonance Scientists 2012, Spa, Belgium, November 25–26, 2012.

N. Peys, S. Gielis, A. Hardy, S. De Gendt, M.K. Van Bael (2012) *VO_2 films synthesized by an aqueous deposition route: From precursor solution to crystalline phase*, imec PhD Days 2012, Heverlee, Belgium, November 19–21, 2012.

N. Peys, S. Gielis, D. Dewulf, A. Hardy, S. De Gendt, M.K. Van Bael (2012) *Aqueous citrato-oxovanadate(IV) precursor for the deposition of VO_x nanostructures*, Chemisty Conference for Young Scientists 2012, Blankenberge, Belgium, March 1–2 March, 2012.

D. Dewulf, C. De Dobbelaere, **N. Peys**, H. Damm, S. Van Elshocht; S. De Gendt, A. Hardy, M.K. Van Bael (2012) *Impact of the precursor system on* Nb_2O_5 *thin films: comparing citric and tartaric acid*, Chemisty Conference for Young Scientists 2012, Blankenberge, Belgium, March 1–2, 2012.

N. Peys, D. Dewulf, S. Gielis, A. Hardy, S. De Gendt, M.K. Van Bael (2011), *New aqueous vanadium precursor for the deposition of* VO_x *nanostructures by systematically controlling the vanadium oxidation state*, imec PhD Days 2011, Heverlee, Belgium, November 22–24, 2011.

N. Pavlovic, C. De Dobbelaere, **N. Peys**, J. D'Haen, A. Volodin, C. Van Haesendonck, A. Hardy, M.K. Van Bael (2011) $BiFeO_3$ *thin films: between decomposition and phase stability*, COST, Conference for Young Scientists, The Nineth Students' Meeting 2011, Novi Sad, Serbia, November 16–18, 2011.

S. Gielis, **N. Peys**, D. Dewulf, C. De Dobbelaere, N. Pavlovic, S. Van Elshocht, S. De Gendt, P.M. Vereecken, A. Hardy, M.K. Van Bael (2011) *Aqueous chemical solution deposition of* $LuFeO_3$ *thin films in view of energy storage applications*, COST, Conference for Young Scientists, The Nineth Students' Meeting 2011, Novi Sad, Serbia, November 16–18, 2011.

N. Peys, K. Schellens, C. De Dobbelaere, D. Dewulf, S. Gielis, P. Adriaensens, P. M. Vereecken, S. De Gendt, A. Hardy, M.K. Van Bael (2011) *New synthesis route for* VO_2*(B) nanolayers by controlling the vanadium oxidation state throughout the entire process*, European Materials Research Society Fall Meeting 2011, Warsaw, Poland, September 19–23, 2011.

D. Dewulf, **N. Peys**, C. De Dobbelaere, S. Gielis, S. Van Elshocht, S. De Gendt, A. Hardy, M.K. Van Bael (2011) *Aqueous Chemical Solution Deposition as a tool for new high-k materials*, European Materials Research Society Fall Meeting 2011, Warsaw, Poland, September 19–23, 2011.

K. Schellens, C. De Dobbelaere, **N. Peys**, J. D'Haen , A. Hardy , M.K. Van Bael (2011) *Solution deposited c-axis preferred orientation AZO thin films using a novel solvent method*, 12th Conference of the European Ceramic Society 2011, Stockholm, Sweden, June 19–23, 2011.

A. Hardy, D. Dewulf, **N. Peys**, S. Van Elshocht, S. De Gendt, M.K. Van Bael (2011) *Material's chemistry behind the dielectric properties of ultrathin high-k oxides prepared by aqueous chemical solution deposition*, Electronic materials for applications 2011, Florida, USA, January 18–20, 2011.

P.M. Vereecken, N. Chiodarelli, A. Romo-Negreira, C. Santini, *N. Peys*, D.J. Cott, M.H. van der Veen, A. Verhulst, K. Arstila, G. Groeseneken, M.M. Heyns, S. De Gendt (2009) *Integration of CNT/Cu hybrid interconnects for BEOL: new possibilities for ECD*, 215th Electro Chemical Society Meeting 2009, San Francisco, USA, May 24–29, 2009.

Poster presentations

N. Peys, S. Gielis, A. Hardy, S. De Gendt, M.K. Van Bael (2012) *VO_2 films synthesized by an aqueous deposition route: From precursor solution to crystalline phase*, imec PhD Days 2012, Heverlee, Belgium, November 19–21, 2012.

N. Peys, S. Gielis, D. Dewulf, A. Hardy, S. De Gendt, M.K. Van Bael (2012) *Effect of the O_2 content and temperature on the formation of VO_x nanostructures in an ACSD process*, Summer school, Microelectronics for Society – More than Moore expands More Moore 2012, Bad Honnef, Germany, June 10-16, 2012.

S. Gielis, **N. Peys**, D. Dewulf, N. Pavlovic, S. Van Elshocht, S. De Gendt, A. Hardy, M.K. Van Bael (2012) *Aqueous chemical solution deposition of $LuFeO_3$ thin high-k films*, Summer school, Microelectronics for Society – More than Moore expands More Moore 2012, Bad Honnef, Germany, June 10-16, 2012.

N. Peys, D. Dewulf, S. De Gendt, A. Hardy, M.K. Van Bael (2011) *Aqueous chemical solution deposition of V_2O_5 and VO_2 thin films for novel memory components*, 12th Conference of the European Ceramic Society 2011, Stockholm 2011, Sweden, June 19-23, 2011.

N. Peys, D. Dewulf, S. Gielis, A. Hardy, S. De Gendt, M.K. Van Bael (2011) *New aqueous vanadium precursor for the deposition of VO_x nanostructures*, imec PhD Days 2011, Heverlee, Belgium, November 22-24, 2011.

S. Gielis, **N. Peys**, S. Van Elshocht, S. De Gendt, P.M. Vereecken, A. Hardy, M.K. Van Bael (2011) *Aqueous chemical solution deposition of $LuFeO_3$ thin films for high energy density systems*, imec PhD Days 2011, Heverlee, Belgium, November 22-24, 2011.

K. Elen, B. Capon, C. De Dobbelaere, D. Dewulf, **N. Peys**, C. Detavernier, A. Hardy, M.K. Van Bael (2011) *Group 5 doped anatase films prepared by aqueous chemical solution deposition*, European Materials Research Society Fall Meeting 2011, Warsaw, Poland, September 19–23, 2011.

S. Gielis, **N. Peys**, D. Dewulf, C. De Dobbelaere, N. Pavlovic, H. Damm, S. Van Elshocht, S. De Gendt, P.M. Vereecken, A. Hardy, M.K. Van Bael (2011) *Aqueous chemical solution deposition of $LuFeO_3$ thin films in view of energy storage applications*, European Materials Research Society Fall Meeting 2011, Warsaw, Poland, September 19–23, 2011.

N. Pavlovic, C. De Dobbelaere, *N. Peys*, J. D'Haen, A. Volodin, C. Van Haesendonck, A. Hardy, M.K. Van Bael (2011) *From aqueous solution to multiferroic thin films*, European Materials Research Society Fall Meeting 2011, Warsaw, Poland, September 19–23, 2011.

D. Dewulf, **N. Peys**, A. Hardy, S. Van Elshocht, G. Rampelberg, C. Detavernier, S. De Gendt, M.K. Van Bael (2011) *Interlayer formation of thin high-k layers deposited on different substrates by aqueous CSD*, 17th Conference on Insulating Films on Semiconductors, Grenoble, France, June 21-24, 2011.

N. Peys, C. De Dobbelaere, D. Dewulf, A. Hardy, S. De Gendt, M.K. Van Bael (2010) *Aqueous chemical solution deposition of* V_2O_5 *and* VO_2 *thin films*, imec PhD Days 2010, Heverlee, Belgium, November 23-25, 2010.

D. Dewulf, **N. Peys**, S. Van Elshocht, S. De Gendt, A. Hardy, M.K. Van Bael (2010) *Insight in Gd(III)-Nb(V)-oxides: high-k materials screened by aqueous CSD*, Electroceramics 2010, Trondheim, Norway, June 13-16, 2010.

N. Peys, D. Dewulf, K. Schellens, K. Martens, J. D'Haen, S. De Gendt, A. Hardy, M.K. Van Bael (2010) *Development of an aqueous vanadium precursor for the chemical solution deposition of* V_2O_5 *films*, Vlaams Jongeren Congres 2010, Blankenberge, Belgium, 1-2 March 2010. **Awarded with best poster award in the field of Inorganic Chemistry.**

Appendix A

Magnetic Resonance Spectroscopy

In this chapter, a brief introduction in two, complementary, Magnetic Resonance Spectroscopic techniques will be given: (i) Nuclear Magnetic Resonance (NMR) Spectroscopy with a focus on ^{51}V−NMR Spectroscopy and (ii) Electron Paramagnetic Resonance (EPR) Spectroscopy. Both techniques allow structural investigation of the vanadium species present in the aqueous solution and can be considered complementary since ^{51}V−NMR and EPR probe vanadium(V) and vanadium(IV) species, respectively.

A.1 Magnetic resonance

Before applying NMR and EPR on a vanadium nucleus or species, some general theoretical principles on magnetic resonance are discussed. A quantum mechanical description of the magnetic resonance phenomena can be found in the textbooks of Atkins and Friedman: *Molecular Quantum Mechanics*[50]. Its practice on NMR and EPR is discussed by Friebolin in his book *Basic One- and Two-Dimensional NMR Spectroscopy*[183] and by Weil and Bolton in their book *Electron paramagnetic resonance: elementary theory and practical applications*[184], respectively. These works are used as references in the following section.

A.1.1 Angular momentum and magnetic moment

The rotational motion of a particle is typically described by its angular momentum $\vec{j}$, which is expressed as the cross product of its position vector $\vec{r}$ and its linear momentum $\vec{p}$ in Equation A.1.

$$\vec{j} = \vec{r} \times \vec{p} \tag{A.1}$$

By introducing the moment of inertia I in Equation A.2, the rotational energy of this particle can then be expressed as function of the angular momentum (Equation A.3).

$$\mathrm{I} = \mathrm{mr}^2 \tag{A.2}$$

$$\mathrm{E} = \frac{\vec{j}^{\,2}}{2I} \tag{A.3}$$

If this particle is charged, its rotation results in a magnetic moment $\vec{\mu}$ which is proportional to the angular momentum of the considered particle by the g-factor and the magnetogyric ratio γ, as given in Equation A.4. The magnetogyric ratio is particle specific and is defined as the ratio of its charge q to its mass m (Equation A.5).

$$\vec{\mu} = \mathrm{g}\gamma\vec{j} \tag{A.4}$$

$$\gamma = \frac{q}{2m} \tag{A.5}$$

For a further elaboration of the angular momentum and the associated magnetic moment, three situations must be distinguished: (i) the orbital angular momentum $\vec{l}$ which describes the rotation of a free electron in an orbit around the nucleus, (ii) the intrinsic electron angular momentum or electron spin $\vec{s}$ which describes the rotation of a free electron around its own axis and (iii) the intrinsic nuclear angular momentum or nuclear spin $\vec{I}$ which sums the individual intrinsic angular momenta of the core particles $\vec{i}_i$.

Orbital angular momentum $\vec{l}$ and its magnetic moment $\vec{\mu_l}$

Consider an electron, with mass $\mathrm{m_e}$ and charge $-e$, free to move over the surface of a sphere with radius r. Assuming a zero potential energy of this electron, its Hamiltonian is stated in Equation A.6. In this Hamiltonian, ∇^2 corresponds to the *Laplacian operator* and expresses a second order differential either in Cartesian or in spherical polar coordinates.

$$\mathrm{H} = -\frac{\hbar^2}{2m}\nabla^2 \tag{A.6}$$

Further elaboration of this Hamiltonian can be found in the textbook of Atkins and Friedman.[1] The obtained solutions are the *Spherical harmonics*, $\mathrm{Y}_{\mathrm{l,m_l}}(\theta,\phi)$, in which the labels l and $\mathrm{m_l}$ refer to the angular momentum quantum number and the magnetic quantum number. The possible values for both l and $\mathrm{m_l}$ are listed in Equation A.7. Expressions for the Spherical harmonics can be found in Table A.1.

---

[1] The following boundary conditions are assumed by Atkins and Friedman. (i) The particle is confined to the surface of the sphere with a fixed radius, r, and the r itself is considered as a constant. (ii) The cyclic boundary condition states that $\Phi(\phi + 2\,\pi) = \Phi(\phi)$.

$$l = 0, 1, 2, ... \quad and \quad m_l = l, l-1, ..., -(l-1), -l \tag{A.7}$$

l	$\mathrm{m_l}$	$\mathrm{Y_{l,m_l}}(\theta,\phi)$
0	0	$\frac{1}{2}\pi^{1/2}$
1	0	$\frac{1}{2}\left(\frac{3}{\pi}\right)^{1/2}\cos(\theta)$
	± 1	$\mp\frac{1}{2}\left(\frac{3}{2\pi}\right)^{1/2}\sin(\theta)\exp(\pm i\phi)$
2	0	$\frac{1}{4}\left(\frac{5}{\pi}\right)^{1/2}\left(3\cos^2(\theta)-1\right)$
	± 1	$\mp\frac{1}{2}\left(\frac{15}{2\pi}\right)^{1/2}\cos(\theta)\sin(\theta)\exp(\pm i\phi)$
	± 2	$\frac{1}{4}\left(\frac{15}{2\pi}\right)^{1/2}\sin^2(\theta)\exp(\pm 2i\phi)$

Table A.1: Examples of Spherical harmonics.[50]

The energies, $\mathrm{E_{l,m_l}}$, of the considered particle are confined to the values given in Equation A.8. Since for a given value of l, $2\mathrm{l}+1$ values are possible for m_l, each energy level is $2\mathrm{l}+1$ degenerate. The projection of the orbital angular momentum on an arbitrary z-axis $\mathrm{l_z}$ is given in Equation A.9

$$\mathrm{E_{l,m_l}} = l(l+1)\frac{\hbar}{2I} \tag{A.8}$$

$$\mathrm{l_z} = \mathrm{m_l}\hbar \tag{A.9}$$

Substitution of the orbital magnetic momentum in Equation A.4 results in the orbital magnetic moment $\overrightarrow{\mu_l}$ where $\mathrm{g_l}$ and γ_e correspond to the g-factor for an electron in an orbital rotation (i.e. $\mathrm{g_l} = 1$) and the magnetogyric ratio of the electron (Equations A.10, A.11). $\mu_{l,z}$ corresponds to the projection of the magnetic moment at an arbitrary z-axis (Equation A.12). Here, the Bohr magneton can be presented (Equation A.13) which elaborates the expression for the orbital magnetic moment in Equation A.12.

$$\overrightarrow{\mu_l} = \mathrm{g_l}\gamma_e\overrightarrow{l} = \gamma_e\overrightarrow{l} \tag{A.10}$$

$$\gamma_e = -\frac{e}{2m_e} \tag{A.11}$$

$$\mu_{l,z} = \gamma_e\mathrm{m_l}\hbar = -\mu_B\mathrm{m_l} \tag{A.12}$$

$$\mu_B = \frac{e\hbar}{2m_e} = 9.274 \times 10^{-24}\frac{J}{T} \tag{A.13}$$

Tables A.2 and A.3 summarize the main expressions for the orbital angular momentum, $\overrightarrow{l}$, and its associated magnetic moment, $\overrightarrow{\mu}_l$.

Electron spin $\vec{s}$

The rotation of an electron around its own axis results in an intrinsic angular momentum or spin, $\vec{s}$. In contrast to the orbital rotation of the electron (and its orbital angular momentum), the rotation of an electron around its own axis does not have to satisfy the same boundary conditions as those for an electron rotating on the surface of a sphere. Consequently, the spin quantum number s and spin magnetic quantum number m_s differ from those associated with the orbital angular momentum. Its confined values are given in Equation A.14. The projection of the spin on an arbitrary z-axis is defined in Equation A.15

$$s = \frac{1}{2} \quad \textit{and} \quad m_s = \pm\frac{1}{2} \tag{A.14}$$

$$s_z = m_s\hbar \tag{A.15}$$

By analogy with the orbital magnetic moment, an electron spin magnetic $\vec{\mu}_s$ moment arises from the rotation of the electron around its own axis. The experimental determination of this electron spin magnetic moment indicates that the magnetic moment is twice the value expected from Equation A.4. The expression found for the electron spin magnetic moment is given in Equation A.16. γ_e and g_e correspond to the magnetogyric ratio of the electron and the electron g-factor ($g_e = 2.002319304$), respectively.

$$\vec{\mu_s} = g_e\gamma_e\vec{s} \tag{A.16}$$

The quantized component of the electron spin magnetic moment is expressed in equation A.17.

$$\mu_{s,z} = g_e\gamma_e m_s\hbar = -g_e\mu_B m_s \tag{A.17}$$

Tables A.2 and A.3 summarize the main expressions for the electron spin, $\vec{s}$, and its associated magnetic moment, $\vec{\mu}_s$.

Since a system usually posses more than one electron, the total spin can be considered as the sum of the spin of each electron. For a system with one unpaired electron, this leads to a spin state (S = ½). For a system with more unpaired electrons, a spin state S > ½ is obtained (e.g. Fe(III) with 5 unpaired electrons, S = 5⁄2).

Nuclear spin $\vec{I}$

Since a nucleus consists of a collection of core particles (i.e. neutrons and protons), its angular momentum or spin is considered as the sum of the intrinsic angular momenta of each core particle in the considered nucleus (Equation A.18). The quantum number of the spin of a single proton or a single neutron is identical to the quantum number of a free electron (i.e. 1/2).

$$\overrightarrow{I} = \sum \overrightarrow{i}_i \tag{A.18}$$

Despite Equation A.18, it is not straightforward to calculate the nuclear spin of certain nuclei due to the lack of information on the direction of each angular momentum in a collection of protons and neutrons. For this purpose tables can be consulted.[183] However, a few trends can be observed in these tables:

- Nuclei with an odd mass number will have a half-integer spin: $^n/_2$,
- Nuclei with an even mass number will have an integer spin: n,
- Nuclei with an even number of protons and an even number of neutrons have zero nuclear spin.

The electrical charge of nuclei with a spin quantum number I = $^1/_2$ is spherically and homogeneously distributed. The NMR spectrum of these nuclei consists of sharp lines. Nuclei with a spin quantum number I > $^1/_2$ have an ellipsoidal charge distribution which results in an electrical quadrupole moment (e.g. -4.8 fm^2 for a ^{51}V nucleus). This electrical quadrupole can be viewed as two back-to-back electrical dipoles. These nuclei typically result in broad lines in the NMR spectrum.

For the determination of the nuclear magnetic moment, $\overrightarrow{\mu_I}$, a similar caution is desirable. The magnetic moment of a free proton or a free neutron is expressed in Equations A.19 and A.20. The g-factor of a free proton and a free neutron is symbolized by g_p (g_p = 5.5856912) and g_n ($g_n = -3.8260837$), respectively.

$$Proton : \overrightarrow{\mu_{i,p}} = \mathrm{g_p}\gamma_p \overrightarrow{i}_p \tag{A.19}$$

$$Neutron : \overrightarrow{\mu_{i,n}} = \mathrm{g_n}\gamma_n \overrightarrow{i}_n \tag{A.20}$$

The presence of a magnetic moment at a neutron suggests that there is an internal structure involving the movement of charged particles. Just as the nuclear angular momentum, it is not straightforward to calculate the nuclear magnetic moment using Equations A.19 and A.20. Therefore, its nuclear magnetic moment is typically determined using Equation A.21 and tables which include the gyromagnetic constant and g-factor of the protons and neutrons present (e.g. 26.75 $\frac{rad}{Ts}$ and 7.05 10^7 $\frac{rad}{Ts}$ for a ^{1}H and a ^{51}V nucleus, respectively).[183]

$$\overrightarrow{\mu_I} = \gamma_n \overrightarrow{I} \tag{A.21}$$

Tables A.2 and A.3 summarize the main expressions for the nuclear spin, $\overrightarrow{I}$, and its associated magnetic moment, $\overrightarrow{\mu}_I$.

	Quantum number	Magnetic quantum number	Orientations	Magnitude	Z component
Orbital angular momentum $\overrightarrow{l}$	l = 0, 1, 2, ...	m_l = l, (l - 1), ..., - (l - 1) and - l	2l + 1	$\sqrt{l(l+1)}\hbar$	$m_l\hbar$
Electron intrinsic angular momentum or electron spin $\overrightarrow{s}$	s = $\frac{1}{2}$	$m_s = \pm \frac{1}{2}$	2s + 1	$\sqrt{s(s+1)}\hbar$	$m_s\hbar$
Nuclear intrinsic angular momentum or nuclear spin $\overrightarrow{I}$	I= 0, $\frac{1}{2}$, 1, $\frac{3}{2}$, 2, ...	m_I = I, (I - 1), ..., - (I - 1) and - I	2I + 1	$\sqrt{I(I+1)}\hbar$	$m_I\hbar$

Table A.2: Angular momentum of a rotating free electron and nucleus.

	Expression	Orientations	Magnitude	Z component
Orbital magnetic moment $\overrightarrow{\mu_l}$	$\overrightarrow{\mu_l} = \gamma_e \overrightarrow{l}$	2l + 1	$- \sqrt{l(l+1)}\mu_B g_l$	$- \mu_B g_l m_l$
Electron spin magnetic moment $\overrightarrow{\mu_s}$	$\overrightarrow{\mu_s} = g_e \gamma_e \overrightarrow{s}$	2s + 1	$- \sqrt{s(s+1)}\mu_B g_e$	$- \mu_B g_e m_s$
Nuclear spin magnetic moment $\overrightarrow{\mu_I}$	$\overrightarrow{\mu_I} = \gamma_n \overrightarrow{I}$	2I + 1	$\sqrt{I(I+1)}\hbar\gamma$	$\hbar\gamma m_I$

Table A.3: Magnetic moment of a rotating free electron and nucleus.

A.1.2 Energy in an external magnetic field

Despite the elaborate study on the orbital angular momentum and its associated magnetic moment, only the electron and nuclear spin, and their associated magnetic moment are of interest for *Magnetic Resonance Spectroscopy*, respectively in EPR and NMR Spectroscopy. Thus only the electron and nuclear spin will be considered.

In the absence of an external magnetic field, all the spin states, defined by their magnetic quantum number and conceptualized by their z component, are degenerated. The presence of an external magnetic field $\overrightarrow{B_0}$ lifts this degeneracy which results in the splitting of the spin states. This is known as the *Zeeman effect*: the *Electron Zeeman effect* and the *Nuclear Zeeman effect* for the splitting of the electron spin states and the nuclear spin states, respectively. The energy is then expressed as the scalar product of the magnetic moment and the external magnetic field (Equation A.22).

$$\mathrm{E_m} = -\overrightarrow{\mu}\overrightarrow{B_0} \tag{A.22}$$

By convention, this magnetic field is applied along the z-axis and, as a consequence, its z component equals its magnitude. Thus the energy, $\mathrm{E_m}$, is further elaborated and this results in a general expression (Equation A.23). This general expression results in Equation A.24 for the electron spin and in equation A.25 for the nuclear spin.

$$\mathrm{E_m} = -\mu_z \mathrm{B_0} \tag{A.23}$$

$$\textit{Free electron spin}: \quad \mathrm{E_{m_s}} = \mathrm{m_s g_e} \mu_B \mathrm{B_0} \quad \textit{with} \quad \mathrm{m_s} = \pm\frac{1}{2} \tag{A.24}$$

$$\textit{Free nuclear spin}: \quad \mathrm{E_{m_I}} = -\mathrm{m_I}\gamma\hbar B_0 \quad \textit{with} \quad \mathrm{m_I} = 0, \frac{1}{2}, 1, \frac{3}{2}, \ldots \tag{A.25}$$

Figure A.1 shows energy level schemes for either an electron with s = 1/2 or a nucleus with I = 1/2, I = 1 and I = 3/2. Note that for an electron only s = 1/2 is possible, while for the nucleus other values for I are allowed. Based on these energy values, the energy difference between two adjacent levels is calculated in equations A.26 and A.27.

$$\textit{Free electron spin}: \quad \Delta E = \mathrm{g_e}\mu_B \mathrm{B_0} \tag{A.26}$$

$$\textit{Free nuclear spin}: \quad \Delta E = \gamma\hbar B_0 \tag{A.27}$$

These energy differences are clear if s = 1/2 and if I = 1/2. But what happens if more than two energy levels are available, i.e. if I ≥ 1? The answer is provided by quantum mechanics and states that only those transitions with a change in the magnetic quantum number equal to 1 are allowed (i.e. $\Delta m = \pm 1$). In fact, this corresponds to the transition between two adjacent energy levels with an energy given in equation A.27.

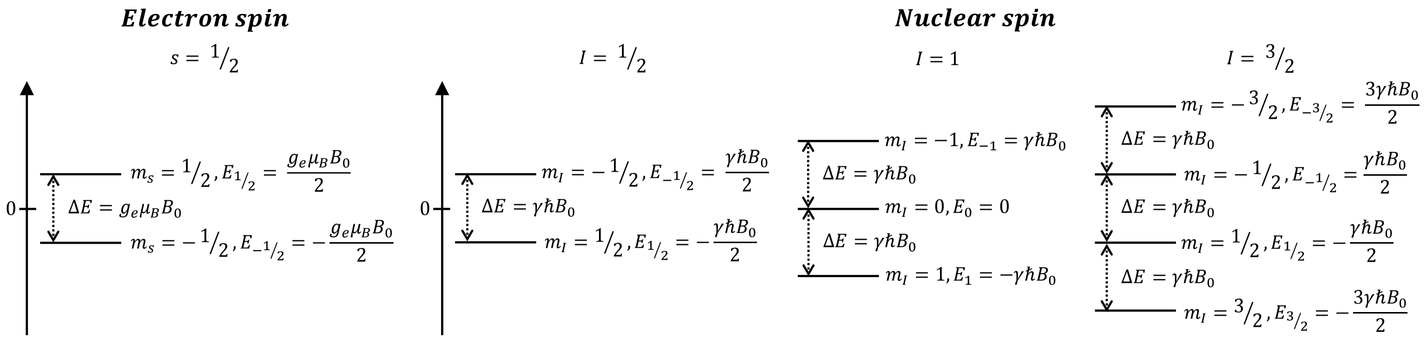

Figure A.1: Examples of energy level schemes.

A.1.3 Gyromagnetic effect and precession

In a classical description, the external magnetic field (applied along the z-axis) causes a circular motion of the electron or nucleus around the orientation axis of the external magnetic field (i.e. z-axis) in a plane perpendicular to this orientation axis (i.e. gyromagnetic effect, see Figure A.2). This circular motion is called *precession*. The angular velocity of this precession equals to the resonance or Larmor frequency. Besides its frequency, this precession is characterized by the angle of the precession cone θ. In classic mechanics, all values for this angle are allowed. However, quantum mechanics learns that only certain discrete values are possible (see number of orientations in Table A.3).

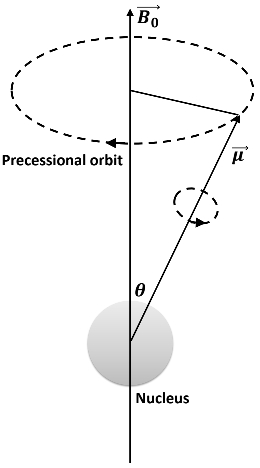

Figure A.2: Precession of a nucleus in the presence of an external magnetic field with strength B_0.

A.1.4 Population and macroscopic magnetization

A real system consists of a collection of electrons (or nuclei) and the magnetic moment of each electron (or each nuclei) occupies one of the different energy states. At thermal equilibrium, the magnetic moments are distributed over the different energy levels according to the *Boltzmann distribution*. This distribution is given in Equation A.28 in which k_B and T stand for the Boltzmann constant (i.e. $k_B = 1.381 \cdot 10^{-23}\ J/K$) and the temperature.

$$N_j = N \frac{e^{\left(-\frac{E_j}{k_B T}\right)}}{\sum_j e^{\left(-\frac{E_j}{k_B T}\right)}} \tag{A.28}$$

N is equal to the number of magnetic moments in the collection. E_j and N_j correspond to energy of the considered spin state and its population. If an ensemble of electron spins with s = 1/2 or an ensemble of nuclear spins with I = 1/2 is considered, the Boltzmann distribution is used to determine the population differences between both spin states (Equation A.29).

$$\frac{N_{high\ energy\ state}}{N_{low\ energy\ state}} = \exp\left(-\frac{\Delta E}{k_B T}\right) \tag{A.29}$$

In NMR, the energy difference between both spin states is very small, leading to only a small excess in the low energy state (e.g. 68 ppm at 9.4 T for a collection of ^{1}H nuclei). IN EPR, the energy difference between both spin states is larger which results in smaller population of the high energy state and increases the sensitivity of an analysis. In both NMR and EPR, the population difference results in (i) a macroscopic, longitudinal magnetization in the z direction, $\overrightarrow{M_0}$, with the same orientation and direction as the applied magnetic field and (ii) no net, transverse magnetization in the xy plane. This magnetization is shown in Figure A.3.

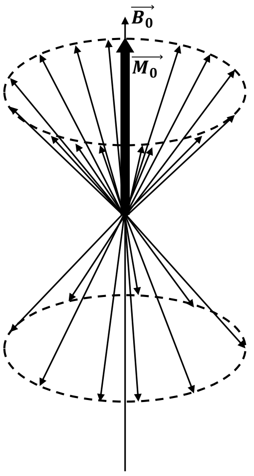

Figure A.3: Macroscopic magnetization of a collection of electrons or nuclei with a spin quantum number s or I = 1/2 in the presence of an external magnetic field with strength B_0.

A.1.5 The resonance condition

In magnetic resonance experiments (such as EPR and NMR), transitions are induced between two energy levels (in accordance to the selection rule $\Delta m = \pm 1$) by irradiation of the system with electromagnetic waves. A transition from the lower to the higher energy states corresponds to the absorbance of energy and a transition from the higher to the lower energy state correspond to the emission of energy. Both transitions are possible and result in a change of the spin orientation. Due to the population excess in the lower energy state, the absorbance of energy is the dominating process. This is observed as a signal whose intensity is proportional to (i) the population difference (i.e. $\mathrm{N}_{\text{low energy state}}-\mathrm{N}_{\text{high energy state}}$), (ii) the total number of spins in the system and (iii) to the concentration of magnetic resonance active species. If the populations are equal (i.e. $\mathrm{N}_{\text{low energy state}} = \mathrm{N}_{\text{high energy state}}$), the absorption and emission process cancel each other and no signal is observed. This is called *saturation*.

Such a transition can only be achieved if the energy of the electromagnetic radiation matches the energy difference between both energy states: see Equations A.26 and A.27 for the energy difference in case of electron spin states or nuclear spin states, respectively. The frequency of this electromagnetic radiation is called the *resonance frequency* or the *Larmor frequency*, ν_L. The Larmor frequency for an electron spin transition $\nu_{L,s}$ and a nuclear spin transition $\nu_{L,I}$ is expressed in Equations A.30 and A.31, respectively.

$$\textit{Free electron spin}: \quad \nu_{L,s} = \frac{g_e \mu_B B_0}{h} \tag{A.30}$$

$$\textit{Free nuclear spin}: \quad \nu_{L,I} = \frac{\gamma \hbar B_0}{h} = \frac{\gamma B_0}{2\pi} \tag{A.31}$$

A.2 Modulation of the macroscopic magnetization

Despite their similar resonance condition, NMR and EPR methods have developed separately. Therefore, it is not obvious or possible to transfer NMR methods or ideas to EPR and vice versa. Thus, the specific methods in NMR or in EPR and their parameters will be discussed separately. Nevertheless, the basic idea behind pulsed NMR and pulsed EPR is the modulation of the macroscopic magnetization. This modulation will be introduced in this section.

The equilibrium state of the macroscopic magnetization is shown in Figure A.3. This macroscopic magnetization is due to the small population difference between the energy states and corresponds to a stable, thermal equilibrium. In pulsed magnetic resonance techniques, the aim is to modulate this macroscopic magnetization and to analyze its return to its thermal equilibrium.

A.2.1 Pulse

The magnetization can be modulated by inducing transitions from the low energy state to the high energy state to such an extent that both spin states are equally populated. This can be realized by exciting all the spin states simultaneously by a radio frequent pulse, operating at the appropriate frequency and originating from an additional, oscillating magnetic field $\overrightarrow{B_1}$ along the laboratory x-axis. This radiation is only switched on for a very short time, the pulse time τ_p. This pulse time is typically in the order of μs and ns for a pulsed NMR and a pulsed EPR experiment, respectively. In this context a 90° ($\pi/2$) and 180° (π) pulse are defined if the pulse is turned off exactly as $\overrightarrow{M_0}$ reaches the xy-plane and if the pulse is turned off exactly as $\overrightarrow{M_0}$ reaches its opposite direction, respectively. Figure A.4 shows the displacement of $\overrightarrow{M_0}$ after a $\pi/2$ and π pulse. Thus, immediately after a $\pi/2$ pulse the initial macroscopic magnetization along the z-axis is transferred to a macroscopic magnetization along the y-axis. At this point, the spins are *phase coherent* in the xy-plane. The π pulse on the other hand inverts the population of spin states.

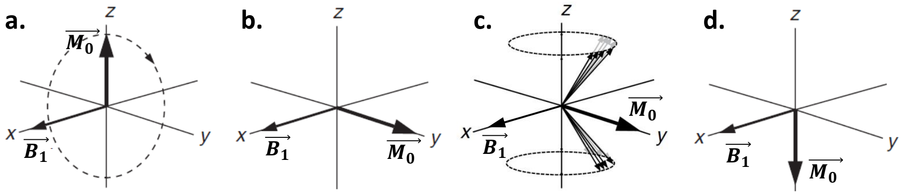

Figure A.4: Displacement of $\overrightarrow{M_0}$ after a $\pi/2$ pulse, macroscopic view (b), a $\pi/2$ pulse, microscopic view (c) and a π pulse, macroscopic view (d).[185]

A.2.2 Relaxation

After the $\pi/2$ pulse, (i) a transverse magnetization exists along the y-axis and (ii) no magnetization remains along the z-axis. Since this situation does not correspond to the equilibrium condition defined by the Boltzmann distribution, the system will try to restore its equilibrium. Two processes are responsible for the disappearance of the transverse magnetization: spin-lattice (longitudinal) relaxation and spin-spin (transverse) relaxation. Figure A.5 shows the origin of T_2 relaxation and the return of the magnetization to its equilibrium position[2].

In the **longitudinal relaxation** process, the excited spins transfer energy to their surrounding molecular framework to re-establish their equilibrium condition. This process leads to the re-gain of longitudinal magnetization and is described, exponentially with time, by Equation A.32. The associated time constant is called the spin-lattice relaxation time T_1 and is typically in the order of seconds (NMR) or microseconds (EPR). Typically, after a period of $5\,T_1$, the longitudinal magnetization is recovered by 99 %. Temperature, solution viscosity, structure and molecular size strongly influence this relaxation process and its time scale. In the **transverse relaxation** process, energy is transferred to neighboring nuclei. As a consequence, the individual magnetization vectors will fan-out which ultimately leads to the loss of net magnetization in the transverse plane. This process can be described by an exponential decay with time (Equation A.33) and is associated with a spin-spin relaxation

---

[2] Note that the x and y axis in Figure A.5 correspond to the coordinates of the rotating frame which rotates with the Larmor frequency with respect to the static, laboratory frame.

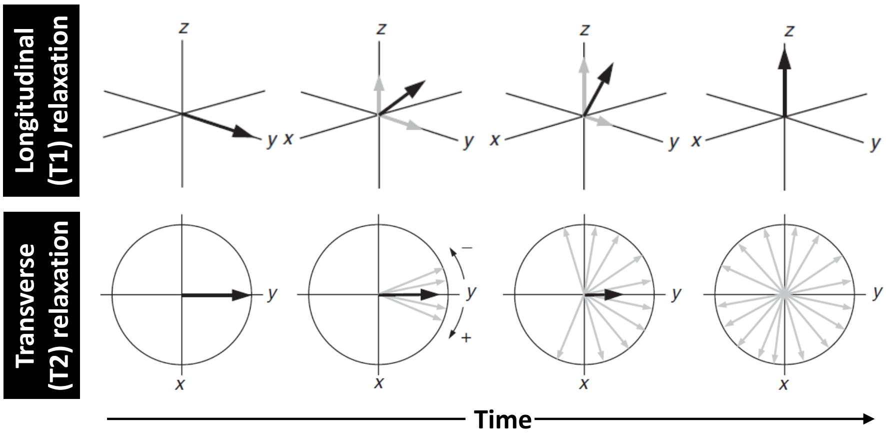

Figure A.5: Longitudinal and transverse relaxation after a $\pi/2$ pulse in function of relaxation time.[185]

time T_2. In general, it holds that $T_2 \leq T_1$ and that T_2 varies between microseconds and seconds (NMR) or between nano- and microseconds. Due to the significant smaller relaxation times, EPR analysis must be performed at very low temperatures (i.e. < 10 K). Inhomogeneity of the magnetic field and the presence of paramagnetic species contribute largely to this spin-spin relaxation.

$$I = I_0(1-e^{-t/T_1}) \tag{A.32}$$

$$I = I_0 e^{-t/T_2} \tag{A.33}$$

The most important mechanism for relaxation for nuclei with a nuclear spin of $1/2$ arises from the **dipole interaction** between spins. As two dipoles approach, their associated magnetic fields interact (i.e. attraction or repulsion depending on their relative orientation). Fluctuations in this interaction induce relaxation. For nuclei that possess an electrical quadrupole moment, which occurs for nuclei with a spin quantum number > $1/2$ as is the case for ^{51}V, **quadrupole relaxation** is the dominating relaxation pathway. An electrical quadrupole can be viewed as two back-to-back electrical dipoles and arise from the ellipsoidal charge distribution of the nucleus. This quadrupole moment is influenced by the local electrical field. As the molecule tumbles at an appropriate frequency, this local field changes and causes spin relaxation. An important factor influencing this quadrupole relaxation is the magnitude of the quadrupole itself (i.e. $-4.8 fm^2$ for the ^{51}V nucleus[36]). Large values result in a more efficient spin relaxation leading to a broader linewidth. Thus, nuclei with small quadrupole moments are favored for NMR experiments.

A.2.3 Time and Frequency Domain

The decay of the transverse magnetization is detected as a *Free Induction Decay*, FID. If the sample contains a collection of electrons or nuclei in a specific chemical environment (each with its characteristic resonance frequency), the different transverse magnetization components are superimposed resulting in a complex FID. A few examples of such complex FID are given in Figure A.6. The direct interpretation of the FID is very difficult and therefore the FID is converted from the time domain to the frequency domain by a *Fourier Transformation*.

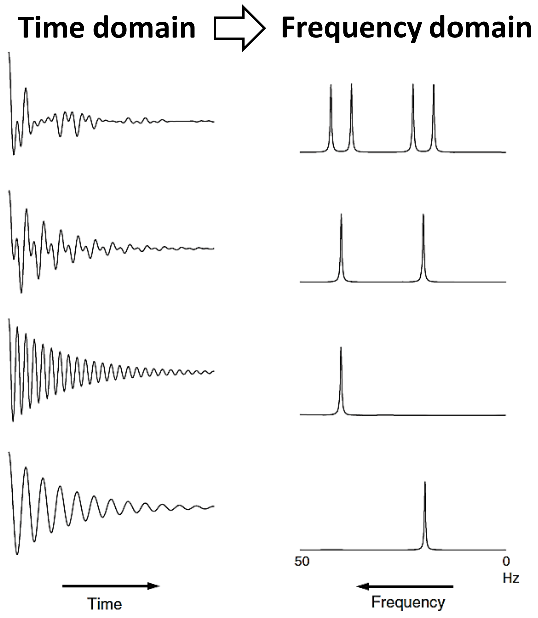

Figure A.6: The detected NMR time response during the spin relaxation: a FID in the time domain and its Fourier transformation to the frequency domain.[185]

A.3 Nuclear Magnetic Resonance

A.3.1 NMR Parameters

Chemical Shift

So far, only a collection of isolated nuclei have been considered which all resonate at the same resonance frequency. However, the resonances are strongly influenced by the chemical environment of the observed nuclei. This chemical environment shields the nucleus from the external magnetic field $\overrightarrow{B_0}$. Thus the effective magnetic field

$\overrightarrow{B}_{effective,i}$ observed by a nucleus i in a real system is always less than the external magnetic field. This effect is observable and is expressed in Equation A.34

$$\mathrm{B}_{\mathrm{effective,i}} = \mathrm{B}_0 - \sigma_i \mathrm{B}_0 = (1 - \sigma_i)\mathrm{B}_0 \tag{A.34}$$

The dimensionless shielding constant σ_i depends on the electron density around the nucleus and differs for each nucleus in a different chemical environment. Due to the variation in the effective magnetic field, the resonance frequency varies as well. Thus each nucleus in a specific chemical environment has a specific resonance frequency, $\nu_{L,i}$ (Equation A.35). In conclusion, nuclei that are chemically non-equivalent are shielded to a different extent and give separate resonance signals in the spectrum.

$$\nu_{L,i} = \frac{\gamma}{2\pi}(1 - \sigma_i)B_0 \tag{A.35}$$

The measured resonance frequencies depend on the magnitude of the external magnetic field and this would impede comparison between NMR analysis. Fortunately, in NMR Spectroscopy a relative scale is employed: the chemical shift δ_i Equation A.36). In this chemical shift, the frequency differences are given with respect to the resonance frequency of an arbitrary reference compound (e.g. tetramethylsilane for ^{1}H NMR and $VOCl_3$ for ^{51}V NMR). This relative chemical shift does not longer depend on the magnitude of the external magnetic filed, but only on the chemical environment (i.e. shielding constant) of the observed nucleus.

$$\delta_i = \frac{\nu_i - \nu_{reference}}{\nu_{reference}} 10^{\,6} = \frac{\sigma_{reference} - \sigma_i}{\sigma_{reference}} 10^{\,6} \quad (ppm) \tag{A.36}$$

Spin-Spin Scalar Coupling (J-couping)

Up to now the interaction of the magnetic moments of nuclear spins between neighboring nuclei is neglected. In reality, these magnetic moments will interact through the bonds and cause a change in the effective magnetic field $B_{effective}$. This spin-spin coupling affects the resonance frequency associated with both nuclei. In solution - where the direct dipole-dipole coupling is canceled - only the through bond, indirect spin-spin coupling remains. The result of such a spin-spin or J-coupling is the splitting of the signal in the NMR spectrum into multiple signals. The splitting distance (expressed in Hz) is referred to as the *Coupling constant*, J. More details on the spin-spin coupling can be found in the textbook of Friebolin: *Basic One- and Two-Dimensional NMR Spectroscopy*.[183]

Integration

The peak area of a signal in the NMR spectrum is proportional to the amount of chemical equivalent nuclei in the sample and proportional to the concentration of the species containing these chemical equivalent nuclei. This peak area is typically visualized as an *Integration line* in which the height difference corresponds to the peak area of the considered peak.

A.3.2 ^{51}V-NMR

General

Vanadium(V) compounds are often analyzed using ^{51}V−NMR due to the appropriate properties of the vanadium nucleus, given in Table A.4. With a spin I = $^7/_2$, the ^{51}V nucleus belongs to the quadrupolar nuclei with a relatively small nuclear quadrupole moment (Q = −4.8 fm^2), resulting in reasonably narrow resonance lines. The standard commonly used in ^{51}V NMR is $VOCl_3$. Since this compound easily hydrolyzes, it has to be handled under an inert and anhydrous atmosphere. Therefore, an aqueous solution of 0.1 M sodium orthovanadate (Na_3VO_4) at a pH of 12 is suggested as the alternative standard. This solution contains two characteristic species: $[VO_4]^{3-}$ and $[V_2O_7]^{4-}$, with a chemical shift of -535.7 and - 559.0 ppm, respectively, relative to $VOCl_3$. The chemical shift range covers roughly 4600 ppm: from +2600 ppm at the low shielding boundary to -2100 ppm at the high shielding boundary.[36, 58, 186]

Nucleus	Natural abundance (%)	Magnetogyric ratio γ(x 10^7 $\frac{rad}{s.T}$)	Nuclear spin I	Nuclear quadrupole moment Q(fm^2)
^{50}V	0.25	+2.6721	6	+21
^{51}V	99.75	+7.0492	$^7/_2$	-4.8

Table A.4: NMR parameters of naturally occurring vanadium nuclei.[58]

The basic requirement for a vanadium compound to be accessible for ^{51}V-NMR is their diamagnetic nature. This is the case for e.g. V(V) and V(III) with the [Ar] 3d^0 and the [Ar] 3d^2 electron configuration, respectively. Mononuclear V(IV) species or complexes with the [Ar] 3d^1 electron configuration are paramagnetic and thus result in very strong line-broadening making the signals undetectable (Equation A.37). However, dinuclear V(IV) centers with a strong anti-ferromagnetic coupling[3] are yet detectable by NMR. Naturally, this anti-ferromagnetic coupling is only feasible if both V(IV) nuclei are in their direct spatial environment.[36, 58, 186]

$$\nu_{1/2} = \frac{1}{\pi T_2} \tag{A.37}$$

---

[3] Such an anti-ferromagnetic coupling occurs if the magnetic moment of the unpaired, solitary electron of the first V(IV) nucleus is opposite to the magnetic moment of the unpaired, solitary electron of the second V(IV) nucleus.

Shielding in an isotropic medium

In this section, shielding in an isotropic medium (e.g. an aqueous solution) will be briefly discussed. In this isotropic medium, the species present continuously and freely move from one position to another. On a very short timescale each species occupies a certain position with a certain preferential orientation. However, on the NMR timescale each position and orientation is averaged out. Thus, the NMR signal is the signal of the average position or orientation of the considered species.

The chemical shift, δ_i, and the shielding constant, σ_i are directly related as given in Equation A.38. In a compound with a negative δ_i value, i.e. which resonates at a lower frequency (or at higher field) with respect to $VOCl_3$, the vanadium nucleus is thus more shielded than $VOCl_3$ and vice versa. The shielding constant, σ_i, itself can be expressed by the sum of three terms in Equation A.39.[36, 58, 186]

$$\delta_i = \frac{\sigma_{VOCl_3} - \sigma_i}{\sigma_{VOCl_3}} \tag{A.38}$$

$$\sigma_i = \sigma_{dia,i} + \sigma_{para,i} + \sigma_{nl,i} \tag{A.39}$$

The term $\sigma_{nl,i}$ stands for non-local contributions, i.e. contributions which do not arise from the immediate coordination sphere of the vanadium nucleus. This term reflects the influence of counter-ions and other matrix effects and is usually negligible in ^{51}V-NMR. The local term $\sigma_{dia,i}$ governs the shielding caused by electron movement around the nucleus. In the case of ^{1}H-NMR, this term is the largest contribution to the final shielding constant. However, for a ^{51}V nucleus this $\sigma_{dia,i}$ is dominated by the core electrons and is essentially a constant term which does not account for variations in the final shielding constant. Thus, the only term left is the local paramagnetic term, $\sigma_{para,i}$. In this context, shielding originates from electronically excited, paramagnetic states. These states arise from an electronic situation where an electron from a paired, occupied, diamagnetic ground state is promoted to an unpaired unoccupied state.[36, 58, 186]

Chemical shift in vanadates

In a series of vanadates, the chemical shift (and thus the shielding) varies with coordination number and the coordination geometry. Table A.5 lists the chemical shift of the main vanadate species present in an aqueous solution with $c_V \sim 1$ mM. The vanadium nuclei in tetrahedral sites all resonate in the range of -530 to -590 ppm. The actual shift depends on its chemical environment (i.e. the nuclearity and protonation state). The vanadium nuclei in octahedral sites on the other hand resonate at much lower field as is observed for the nuclei in the decavanadate species. The chemical shift of the vanadium nuclei in the central, octahedral site (V_C) at ~ -425 ppm is insensitive to the protonation site while the chemical shift of the vanadium nuclei in the peripheral sites clearly change with the protonation state.[36, 58, 186]

Notation	Species	Structure	Site	$\delta_{^{51}V-NMR}$ (ppm)
V^+	VO_2^+	Monovanadate(V)	Td	-542
V^{2-}	HVO_4^{2-}	Monovanadate(V)	Td	-534
V^-	$H_2VO_4^-$	Monovanadate(V)	Td	-560
V_2^{3-}	$HV_2O_7^{3-}$	Divanadate(V)	Td	-564
V_2^{2-}	$H_2V_2O_7^{2-}$	Divanadate(V)	Td	-573
V_4^{5-}	$HV_4O_{13}^{5-}$	Linear tetravanadate(V)	Td	-559
V_4^{4-}	$V_4O_{12}^{4-}$	Cyclic tetravanadate(V)	Td	-577
V_5^{5-}	$V_5O_{15}^{5-}$	Cyclic pentavanadate	Td	-585
V_{10}^{5-}	$HV_{10}O_{28}^{5-}$	Complex decavanadate(V)	Oh	-424 (V_C), -499 (V_B) and -515 (V_A)
V_{10}^{4-}	$H_2V_{10}O_{28}^{4-}$	Complex decavanadate(V)	Oh	-422 (V_C), -502 (V_B) and -519 (V_A)
V_{10}^{3-}	$H_3V_{10}O_{28}^{3-}$	Complex decavanadate(V)	Oh	-427 (V_C), -515 (V_B) and -538 (V_A)

Table A.5: Polynuclear vanadium(V) species present in an aqueous solution and their chemical shift in ^{51}V−NMR for $c_V \sim 1$ mM.[36, 58, 186] The different vanadium sites in the decavanadate species are shown in Figure 1.7.

A.4 Electron Paramagnetic Resonance

Electron Paramagnetic Resonance (EPR)[4] applies to paramagnetic systems and is, hence, complementary to NMR. An additional difference between EPR and NMR is the energy scale: GHz in EPR and MHz in NMR. Note that in NMR the external magnetic field is kept constant and the frequency is modulated to induce a transition while in the classic EPR experiment the frequency is kept constant and the magnetic field is swept. In this section, EPR will be briefly clarified, a thorough study is given by Weil et al. in the *Electron Paramagnetic Resonance: Elementary Theory and Practical Applications* textbook.[184]

A.4.1 The g-value

The electron spin resonance condition, stated in Equation A.30, assumes a free electron and its free electron g-value. In a real system, this unpaired electron is part of a molecular or ionic system with a specific chemical environment. Just as in NMR, the external magnetic field $\overrightarrow{B_0}$ is shielded by this environment. Thus, the effective field, $\overrightarrow{B}_{effective}$, observed by the electron differs from the external magnetic field (Equation A.34). In EPR, the shielding of the external magnetic field by the chemical environment of the unpaired electron is included in the effective g value (Equation A.40). The resonance condition is then expressed as a function of the effective g value in Equation A.41

---

[4] Also the less popular names *Electron Spin Resonance* and *Electron Magnetic Resonance* are used.

$$\mathrm{g} = \mathrm{g_e}(1-\sigma) \tag{A.40}$$

$$\nu_{L,s} = \frac{g\mu_B B_0}{h} \tag{A.41}$$

A.4.2 Interaction types

The situation described by Equation A.41 only applies for a system with one unpaired electron (S = ½), which is surrounded by non-magnetic nuclei.[187] However, most systems – including transition metal ion complexes – the unpaired electron(s) is surrounded by many magnetic nuclei with a nuclear spin I. Such system is characterized by the following interactions[5].[184, 187]

The first interaction type and basic condition to perform EPR is the **Electron Zeeman interaction** (EZ), discussed earlier and given in Equation A.42. This electron Zeeman interaction is very large and will dominate all other interactions.

$$\mathrm{E_{EZ}} = \mathrm{m_s}\mu_\mathrm{B}\mathrm{g}\mathrm{B_0} \tag{A.42}$$

A second interaction, i.e. the **Zero Field Splitting**, is only present for high-spin systems (S > ½) and reflects the dipole-dipole coupling between the electron spins and the spin-orbit contributions. This latter contribution is usually significant for transition metal ion complexes.

Another possible interaction is the coupling between the unpaired electron and the nuclei with a non-zero nuclear spin quantum number: the **hyperfine interaction** (HF). The hyperfine interaction of an unpaired electron with a nucleus with a spin quantum number I = ½ is given in Equation A.43. The term A corresponds to the hyperfine coupling constant and is, similar to the g-value, dependent on the chemical environment and the orientation of the species in the external magnetic field. In an isotropic medium, an average hyperfine coupling constant is obtained.

$$\mathrm{E_{HF}} = \mathrm{m_I}\mathrm{m_s}\mathrm{A} \tag{A.43}$$

If a nucleus with a non-zero nuclear spin quantum number is in the vicinity of the EPR active unpaired electron, also the **Nuclear Zeeman effect** (NZ) will play a role which results in an additional splitting of the energy levels (Equation A.44). As stated earlier, the energy splitting caused by the Nuclear Zeeman effect is in the order of MHz, while the energy splitting due to the Electron Zeeman effect is in the order of GHz. The contribution of the Nuclear Zeeman effect is small and is usually only detected in an pulsed EPR analysis.

---

[5] A detailed and extensive description of the possible spin interactions can be found in the textbook of Weil et al.

$$E_{NZ} = -m_I \hbar \gamma B_0 \tag{A.44}$$

Figure A.7 shows the energy level diagram of an unpaired electron with spin quantum number S = ½ in the presence of a nucleus with a spin quantum number I = ½. The first splitting is due to the Electron Zeeman effect, the second splitting is due to the Nuclear Zeeman effect. Finally, the last derivation of the energy level originates from the Hyperfine interaction. The energy of such a final magnetic state is given in Equation A.45. The blue arrows in Figure A.7 indicate the allowed CW-EPR transitions ($\Delta m_s = \pm 1$ and $\Delta m_I = 0$). The green arrows indicate the allowed, nuclear transitions ($\Delta m_I = \pm 1$).

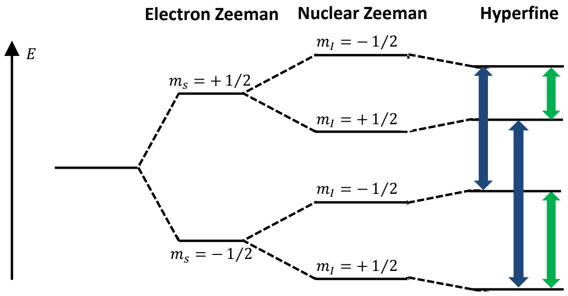

Figure A.7: Energy level diagram for an unpaired electron (S = ½) in the presence of a nucleus (I = ½). Adapted from reference [184]

$$E = m_s \mu_B g B_0 - m_I \hbar \gamma B_0 + m_I m_s A \tag{A.45}$$

In conclusion, the Electron Zeeman effect and the hyperfine interaction are the main interactions during an EPR experiment. The Electron Zeeman effect probes the local symmetry, the chemical environment and the electronic state (e.g. the oxidation state of a transition metal cation) around the unpaired electron. The hyperfine interaction measures the electronic structure of the nearby nucleus and the distance between the unpaired electron and the nearby nucleus.

A.4.3 EPR methods

Continuous Wave EPR (CW-EPR)

In the continuous wave (CW) experiment, microwaves[6] with a constant frequency are continuously irradiated on the sample, while the external magnetic field, B_0, is swept. If the frequency matches the resonance condition, the electron spin state can

---

[6] Microwaves are a part of the electromagnetic spectrum with a wavelength between 1 mm and 1 m, or alternatively a frequency between 300 GHz and 300 MHz.

change (Figure A.8). Due to the instrumentation and detection method used in EPR, the signal is not given in the expected absorption mode. The first derivative of this absorption line is rather represented. A few examples of typical spectra are given in Figure A.9.

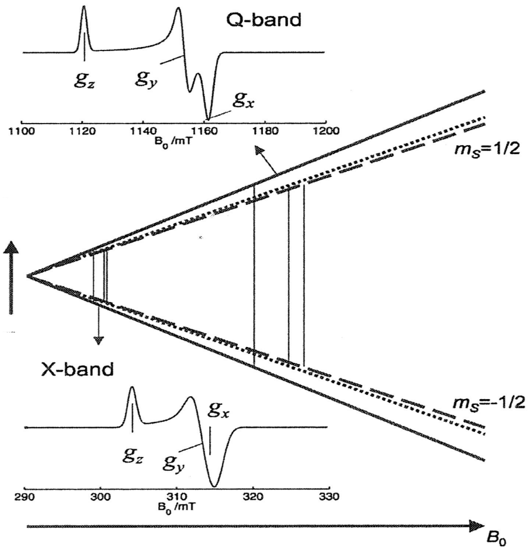

Figure A.8: Schematic illustration showing the lifting of the degeneracy fo the electronic spin states by an increasing external magnetic field B_0. The three pair of lines correspond to the situations found for $\overrightarrow{B_0}$ parallel to the g_z axis (solid lines), g_y axis (dotted lines) and g_x axis (dashed lines) of an $s = 1/2$ system. The corresponding powder CW-EPR spectra for this system are simulated at Q-band (35 GHz) and X-band (9.5 GHz) microwave frequencies.[187]

As stated earlier, the Electron Zeeman interaction is characterized by the g-value. This g-value depends on the chemical environment and the local symmetry. In general, three cases can be distinguished. (i) In a system with a cubic symmetry, all direction are identical which results in one g value: $g = g_x = g_y = g_z$. This is typically observed for liquid samples (e.g. an aqueous solution analyzed at room temperature) because the tumble time of the molecules present is much shorter than the EPR time scale. (ii) A system with an axial symmetry has two different g values: $g_{||}$ and $g_{\perp}$. An example of such a system is discussed in chapter 1. Both $g_{||}$ and $g_{\perp}$ are expressed as a function of the energy difference between two electronic states, the orbital coefficients and the spin-orbit coupling constant (see equations 1.16 and 1.17). (iii) A system with rhombic symmetry is characterized by three different g values: $g_x \neq g_y \neq g_z$. An example of an EPR spectrum of each symmetry type is given in Figure A.9.

Different types of EPR spectrometers exist. Each type is usually indicated by its

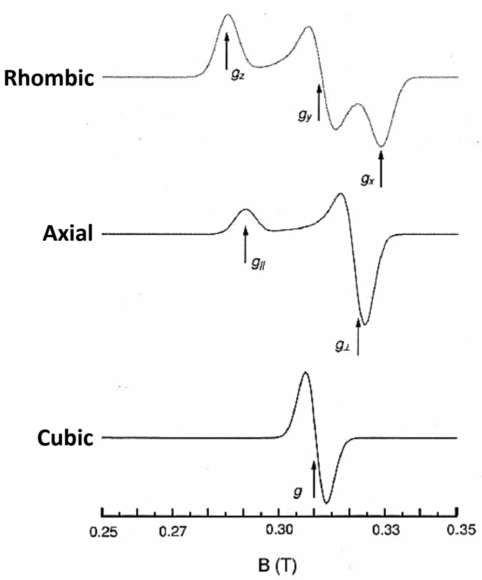

Figure A.9: Typical polycrystaline powder spectra of a s = ½ spin system: a cubic or isotropic spectrum with g = 2.13; a axial spectrum with $g_{||}$ = 2.28 and $g_\perp$ = 2.05 and a rhombic spectrum with g_x = 2.01, g_y = 2.12 and g_z = 2.32.[188]

operating microwave frequency (i.e. L-band: ~ 1 GHz, S-band: ~ 2-4 GHz, X-band: ~ 9.5 GHz, Q-band: ~ 35 GHz, W-band: ~ 95 GHz, ...). The standard EPR spectrometers operate at X-band with a magnetic field sweep between 0 and 1.4 T. The advantage of EPR analysis with higher microwave frequency is the gain in spectral resolution. In Figure A.8 Van Doorslaer et al compare the EPR spectrum obtained at X-band with those obtained at Q-band.[187] In this example it is clear that the resolution between the g_y and g_x signals is lost in the spectrum obtained at X-band and retained in the spectrum obtained at Q-band.

Pulsed EPR

CW-EPR can only resolve sufficiently large hyperfine interactions and hyperfine interactions of simple systems (with a limited number of hyperfine couplings). In transition metal complexes, this is feasible for hyperfine interactions with the central metal ion. The ligand hyperfine interaction on the other hand, can seldom be resolved in CW-EPR. Each EPR line of an electron (with s = ½) interacting with n nuclear spins splits into numerous lines (see Equation A.46), which leads to broad lines lacking all substructure.[187].

$$\textit{EPR line splitting}: \prod_n (2I+1) \tag{A.46}$$

In order to observe these different ligand hyperfine interactions, more advanced methods must be applied. The following discussion will be limited to the pulsed methods used in this work (i.e. pulsed methods based on the electron spin echo). An extensive list of pulsed and double resonance EPR methods and a more detailed description of the discussed EPR methods can be found in the textbook of Weil et al.[184]

Electron Spin Echo detected EPR (ESE-detected EPR)

The first pulsed EPR experiment is formed by the $^{\pi}/_{2}$$-\tau-\pi-\tau-$ echo sequence (Figure A.10).

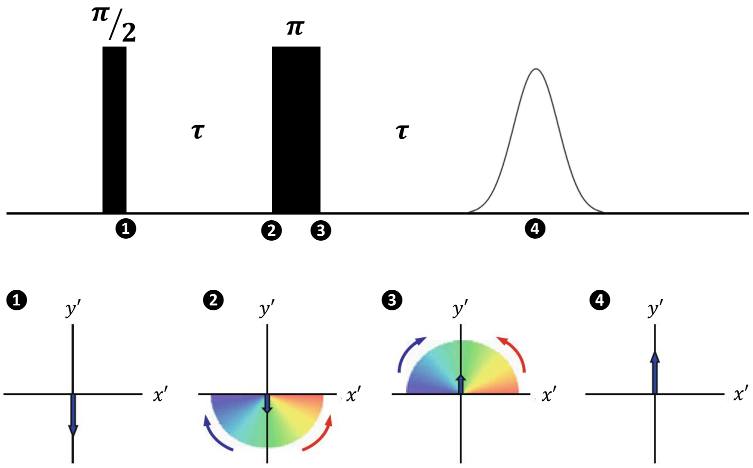

Figure A.10: Top: Pulse sequence for the ESE-detected EPR. Bottom: Graphical illustration of the magnetization vector at characteristic time positions in the pulse sequence. Note that x′ and y′ correspond to the rotating frame rotating at the Larmor frequency with respect to the laboratory frame.[189]

At thermal equilibrium, the magnetization vector $\overrightarrow{M}_0$ is oriented along the z-axis. The $^{\pi}/_{2}$ pulse along the x-axis displaces the magnetization into the xy-plane along the -y-axis (time point 1 in Figure A.10). After this pulse, the different magnetic moments start to precess in the xy-plane at their Larmor frequency. This Larmor frequency depends on the chemical environment of the associated unpaired electron. As a consequence, each magnetic moment will precess at a different Larmor frequency and macroscopic magnetization vector shrinks. This process is called *dephasing of the transverse magnetization*. After a certain time τ (time point 2 in Figure A.10), a π pulse along the x-axis is given which flips each magnetic moment around the xz-plane. After this π pulse (time point 3 in Figure A.10), each magnetic moment continues its precession. Since the precession direction of each individual magnetic moments is not changed by the refocusing pulse, all the vectors are re-aligned along the y-axis after another time τ (time point 4 in Figure A.10). This results in a refocused macroscopic magnetization along the y-axis. This is called the *Electron Spin Echo*. (time point 4).

The main goal of spin echo experiments is the elimination of undesired inhomogeneities of the magnetic field. In the first τ period, the magnetic moments diverge by T_2 relaxation and by undesired inhomogeneities of the magnetic field. During the rephasing after the π pulse, the magnetic moments converge and are corrected for the magnetic field inhomogeneities. In conclusion, the decrease of the macroscopic magnetization after a relaxation period 2τ is only due to the T_2 and longitudinal T_1 relaxation.

The spin echo intensity is measured as function of the magnetic field strength and results in a field dependent absorption spectrum (Figure A.11). In this absorption spectrum, each field value (or *observer position*) corresponds to a certain orientation. These observer positions are essential in more advanced experiments such as HYSCORE.

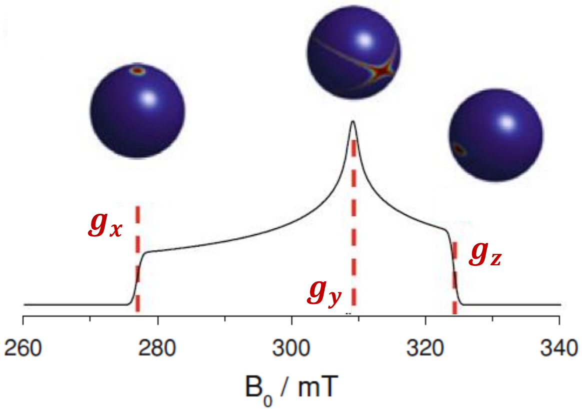

Figure A.11: Example of an ESE-detected EPR spectrum with $g_x = 2.05$, $g_y = 2.15$ and $g_z = 2.40$ at 9.3 GHz. The dotted lines mark the observer positions at the principal g-values. The spheres represent the orientation selection.[189]

Electron Spin Echo Envelope Modulation (ESEEM)

An ESEEM experiment consists of the same pulse frequency as in the ESE-detected EPR (i.e. the $^{\pi}/_{2} - \tau - \pi - \tau -$ echo sequence). The echo intensity is monitored with a variation in the time of the pulse intervals (i.e. τ). This leads to an one- or a multi-dimensional time-domain signal. Subsequent Fourier transformation allows the determination of the nuclear spin frequencies.[189]

Hyperfine Sublevel Correlation (HYSCORE)

A HYSCORE experiment is essentially a 2D ESEEM technique with a pulse sequence as given in Figure A.12.

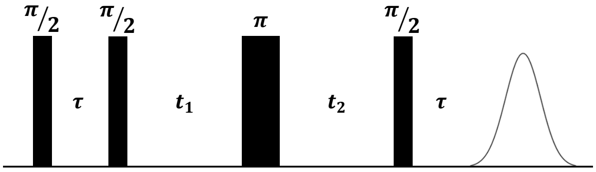

Figure A.12: Pulse sequence for the hyperfine sublevel correlation (HYSCORE) experiment.[187]

During the HYSCORE experiment, the times t_1 and t_2 are, independently, varied. After Fourier Transformation, a 2D spectrum in the frequency domain is obtained (Figure A.13). As illustrated in Figure A.13, the cross peaks relate to nuclear spin frequencies. A HYSCORE spectrum is recorded at a fixed external magnetic field, which corresponds to a certain observer position (see Figure A.11). Thus, the spectrum only reflects the nuclear spin frequencies corresponding to this specific orientation. For a s = $1/2$ and I = $1/2$ spin system, doublet peaks appear for nuclei for which the hyperfine coupling is less than twice the Zeeman interaction (i.e. weak coupling case). These peaks are centered at the Larmor frequency and are separated by the hyperfine coupling constant, A.[187, 189]

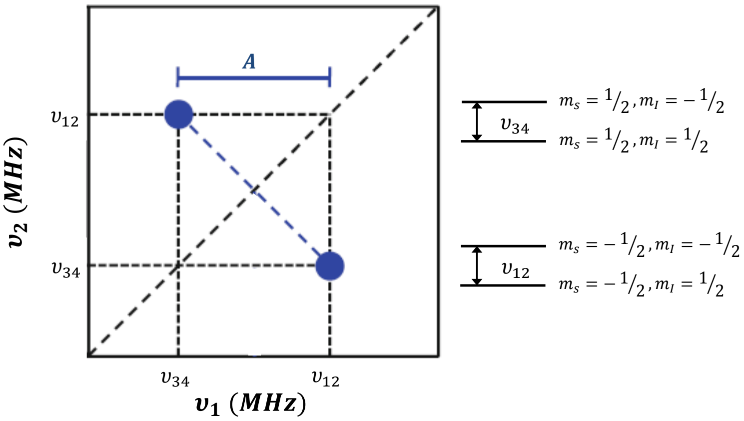

Figure A.13: Left: Schematic representation of a HYSCORE spectrum based on a s = $1/2$ and I = $1/2$ spin system in a weak coupling case (hyperfine coupling < twice the Zeeman interaction). Right: Energy level scheme corresponding to this s = $1/2$ and I = $1/2$ spin system. ν_{12} and ν_{34} are the nuclear frequencies corresponding to the $\Delta m_s = 0$ and $\Delta m_I = \pm 1$ transitions.[187, 189]

A.4.4 Applications for V(IV) species

Most vanadium(IV) complexes have a s = $^1/_2$ and I = $^7/_2$ spin system, which results in $2I+1 = 8$ EPR lines (if resolved). Its electronic ground state (s = $^1/_2$) splits in two electronic states under the influence of an external magnetic field, characterized by $m_s=-^1/_2$ and $m_s=^1/_2$.[58]

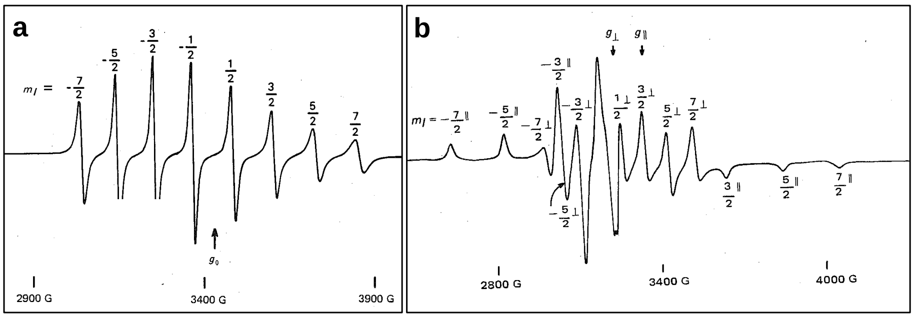

Figure A.14: X-band EPR of an aqueous solution containing the penta-aqua vanadyl(IV) ion: spectrum recorded at room temperature and at 9.521 GHz (a) or at 77 K and at 9.180 GHz (b). The spectrum at room temperature is a spectrum of an isotropic (cubic) system with an isotropic, g-value. The spectrum at 77 K correspond to a system with an axial symmetry (here C_{4V}) and shows two orientation depended g-values: $g_\perp$ and $g_\parallel$.[46]

Figure A.14 shows a X-band EPR spectrum, reported by Chasteen, of an aqueous solution containing the penta-aqua vanadyl(IV) ion either at room temperature or at 77K.[46] Under isotropic conditions, an eight-line pattern can thus be observed. In a condition where the isotropic tumbling of the molecules is prevented (as is the case for frozen solutions e.g. at 77 K), an anisotropic spectrum is obtained. This results in an additional splitting of the eight EPR lines. In the case of a vanadyl species, a system with an axial symmetry is observed in which the V=O unit defines the z-direction. For such a system, two sets of eight lines are observed with two g and two A values: $g_\perp$, $g_\parallel$, $A_\perp$ and $A_\parallel$ (Equations A.47 and A.48).[46, 58]

$$g_\perp = g_x = g_y \tag{A.47}$$

$$g_\parallel = g_z \tag{A.48}$$

The parallel component coincides with the z-axis and the direction of the external magnetic field. Equations A.49 and A.50 indicate the relation between (i) $g_\perp$ and $g_\parallel$ and (ii) $A_\perp$ and $A_\parallel$ for a vanadium(IV) species or complex with a C_{4V} symmetry.

$$g_\parallel < g_\perp < 2 \tag{A.49}$$

$$\mathrm{A}_{\parallel} \gg A_{\perp} \tag{A.50}$$

The anisotropic hyperfine coupling constant $A_{\parallel}$ for a system with axial symmetry reflects the equatorial ligands around the VO^{2+} ion. This hyperfine coupling constant can be estimated by the *additivity relationship*, given in Equation A.51 established by Chasteen.[46].

$$\mathrm{A}_{\parallel} = \frac{\sum_{i=1}^{4} A_{\parallel,i}}{4} \tag{A.51}$$

Equation A.51 assumes a square bipyramidal complex with the four ligands, each with its own partial parallel hyperfine coupling constant ($A_{\parallel,i}$), in the equatorial position with respect to the V=O unit. The fifth ligand, in the axial position, is assumed to be a H_2O ligand. For most complexes, an agreement between the calculated and experimental value is within $1.5 \cdot 10^{-4}\mathrm{cm}^{-1}$.[46] Table A.6 summarizes $A_{\parallel,i}$ values for different ligand types.

Ligand type	Partial hyperfine coupling constant $A_{\parallel,i}$ ($10^{-4}\mathrm{cm}^{-1}$)
H_2O	45.7
$R{-}CO_2^-$	42.7
$R{-}NH_2$	40.1
$R{-}OH^-$	38.7
$R{-}O^-$	35.3
$R{-}S^-$	31.9

Table A.6: Partial parallel hyperfine coupling constant $A_{\parallel,i}$ for various ligand types.[46, 58]

Appendix B

Overview of the Continuous Wave and Pulsed - Electron Paramagnetic Resonance experiments

In this Appendix, all data concerning CW- and Pulsed-EPR are given. All the experiments are performed by members the BIMEF (Laboratory of BioMedical Physics) research group of the University of Antwerp, under the supervision of Prof., Dr. Sabine Van Doorslaer.

Name	Synthesis of the solution				Removal of		Final	
	NH_4VO_3	Oxalic acid	Citric acid	NH_3	$(NH_4)_2C_2O_4$	Solvent	[V] (mM)	pH
A	xxx	3:1	-	-	-	H_2O	6.5	2.4
B	xxx	3:1	2:1	-	-	H_2O	5.0	1.4
D	xxx	3:1	2:1	xxx	-	H_2O	4.5	3.0
F	xxx	3:1	2:1	xxx	-	H_2O	4.9	5.0
I	xxx	3:1	2:1	xxx	-	H_2O	4.6	7.0
J	xxx	3:1	2:1	xxx	-	H_2O	4.3	8.2
K	xxx	3:1	2:1	xxx	xxx	H_2O	3.3	5.7
L	xxx	3:1	0.75:1	xxx	xxx	H_2O	4.9	7
M	xxx	3:1	1.50:1	xxx	xxx	H_2O	5.1	7
N	xxx	3:1	4.50:1	xxx	xxx	H_2O	4.6	7

Table B.1: Identification of the samples anaylzed by CW- or Pulsed-EPRP. All ratios are molar ratios to VO^{2+} unless otherwise specified.

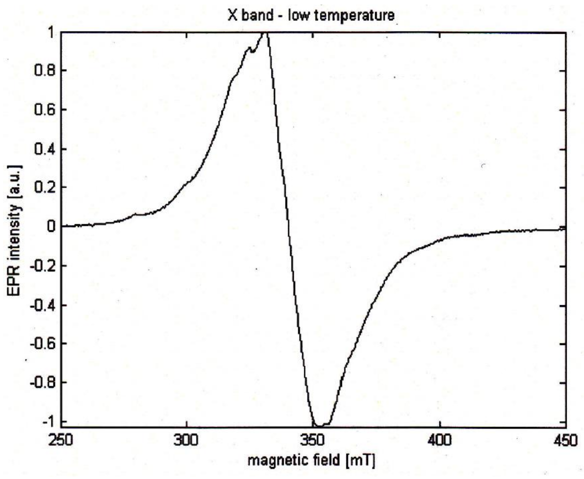

Figure B.1: Experimental CW-EPR spectrum of sample A. The CW-EPR spectrum is measured at 100 K using a modulation amplitude of 0.5 mT, a microwave power of 1 mW and a modulation frequency of 100 kHz.

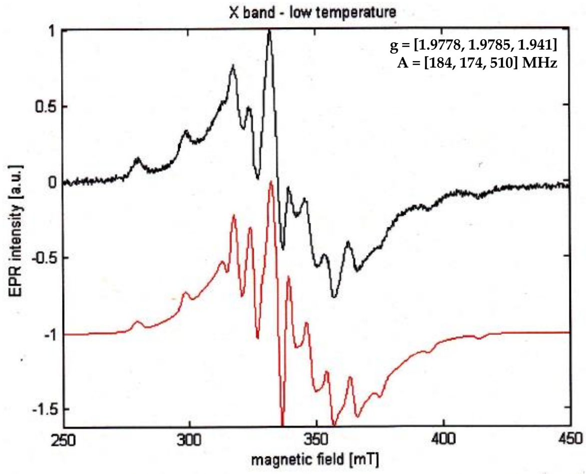

Figure B.2: Experimental (black, top) and simulated (red, bottom) CW-EPR spectrum of sample B. The CW-EPR spectrum is measured at 10 K using a modulation amplitude of 0.5 mT, a microwave power of 1 mW and a modulation frequency of 100 kHz.

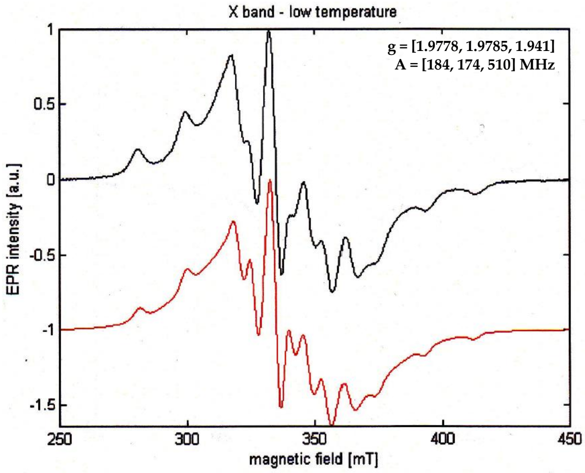

Figure B.3: Experimental (black, top) and simulated (red, bottom) CW-EPR spectrum of sample D. The CW-EPR spectrum is measured at 10 K using a modulation amplitude of 0.5 mT, a microwave power of 1 mW and a modulation frequency of 100 kHz.

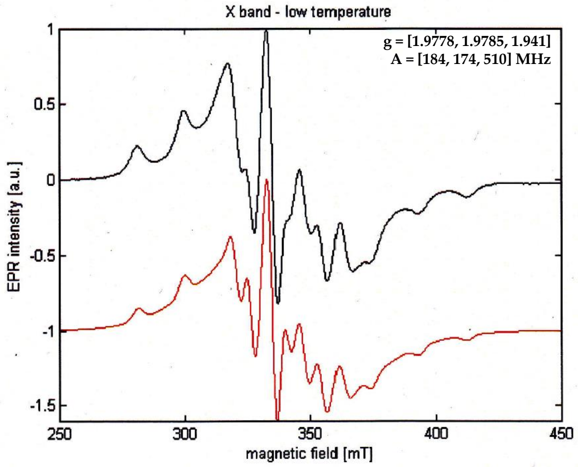

Figure B.4: Experimental (black, top) and simulated (red, bottom) CW-EPR spectrum of sample F. The CW-EPR spectrum is measured at 10 K using a modulation amplitude of 0.5 mT, a microwave power of 1 mW and a modulation frequency of 100 kHz.

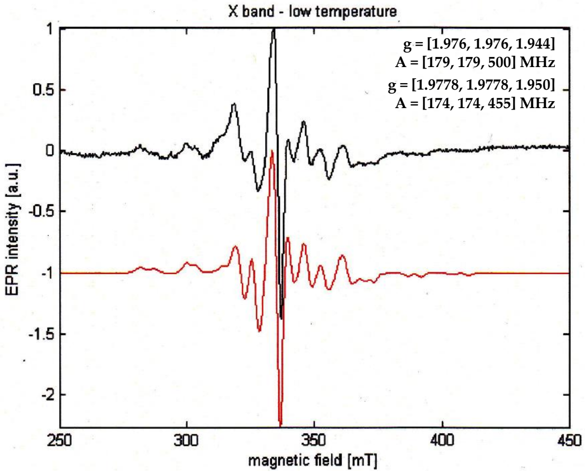

Figure B.5: Experimental (black, top) and simulated (red, bottom) CW-EPR spectrum of sample I. The CW-EPR spectrum is measured at 10 K using a modulation amplitude of 0.5 mT, a microwave power of 1 mW and a modulation frequency of 100 kHz.

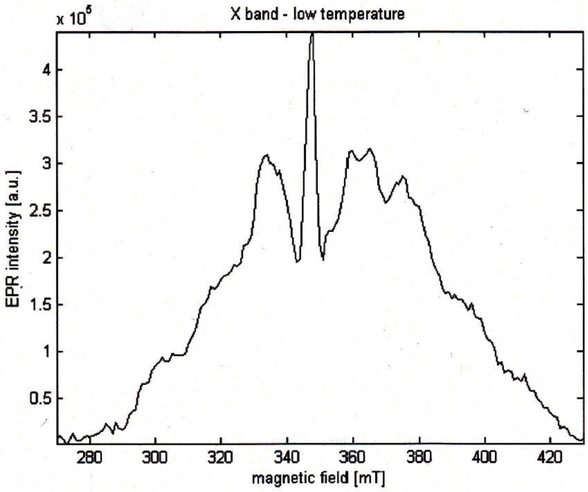

Figure B.6: ESE detected EPR of sample I, recorded at 10 K using a delay time of τ = 88 ns.

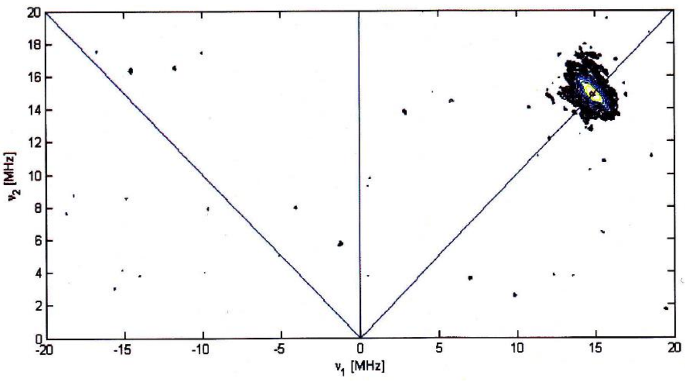

Figure B.7: HYSCORE spectrum of sample I, recorded at 10 K and taken at observer position $B_0 = 348\,\mathrm{mT}$. The HYSCORE spectrum is measured using the pulse sequence: $\pi/2 - \tau - \pi/2 - t_1 - \pi - t_2 - \pi/2 - \tau$ – echo, with $t_{\pi/2} = 16\,\mathrm{ns}$ and $t_\pi = 32\,\mathrm{ns}$; t_1 and t_2 were varied in steps of 16 ns. The spectrum is recorded for $\tau = 96$ and 172 ns.

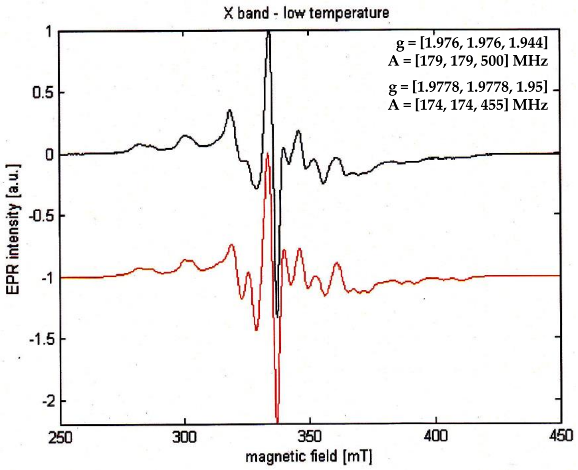

Figure B.8: Experimental (black, top) and simulated (red, bottom) CW-EPR spectrum of sample J. The CW-EPR spectrum is measured at 10 K using a modulation amplitude of 0.5 mT, a microwave power of 1 mW and a modulation frequency of 100 kHz.

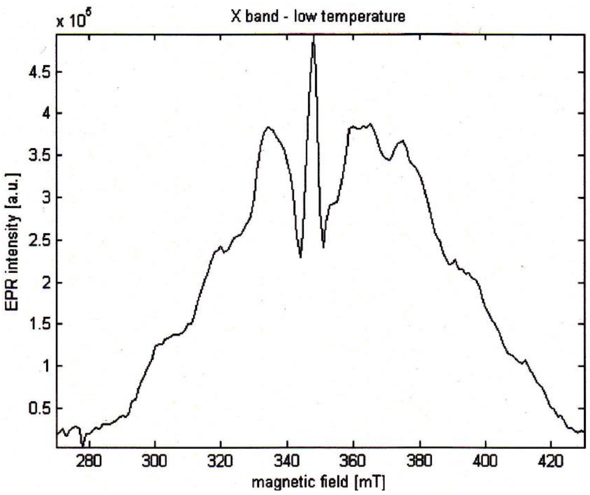

Figure B.9: ESE detected EPR of sample J, recorded at 10 K using a delay time of τ = 88 ns.

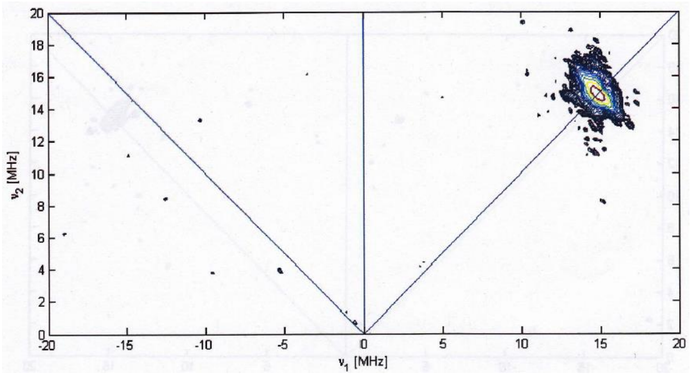

Figure B.10: HYSCORE spectrum of sample J, recorded at 10 K and taken at observer position B_0 = 348 mT. The HYSCORE spectrum is measured using the pulse sequence: $\pi/2$–τ – $\pi/2$–t_1–π – t_2–$\pi/2$–τ – echo, with $t_{\pi/2}$ = 16 ns and t_π = 32 ns; t_1 and t_2 were varied in steps of 16 ns. The spectrum is recorded for τ = 96 and 172 ns.

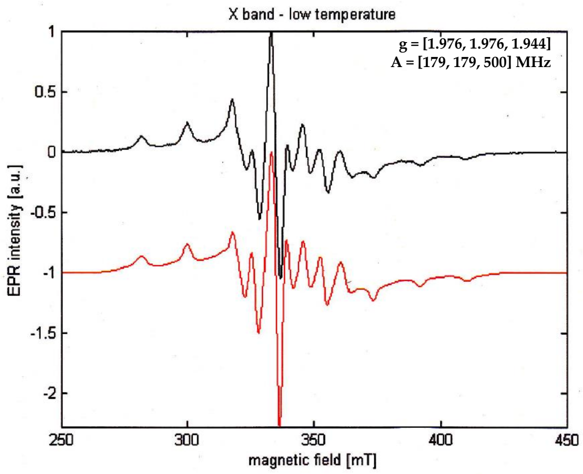

Figure B.11: Experimental (black, top) and simulated (red, bottom) CW-EPR spectrum of sample K. The CW-EPR spectrum is measured at 10 K using a modulation amplitude of 0.5 mT, a microwave power of 1 mW and a modulation frequency of 100 kHz.

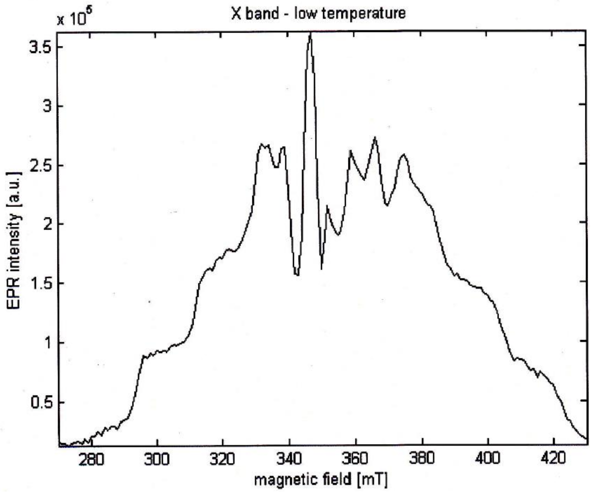

Figure B.12: ESE detected EPR of sample K, recorded at 10 K using a delay time of τ = 88 ns.

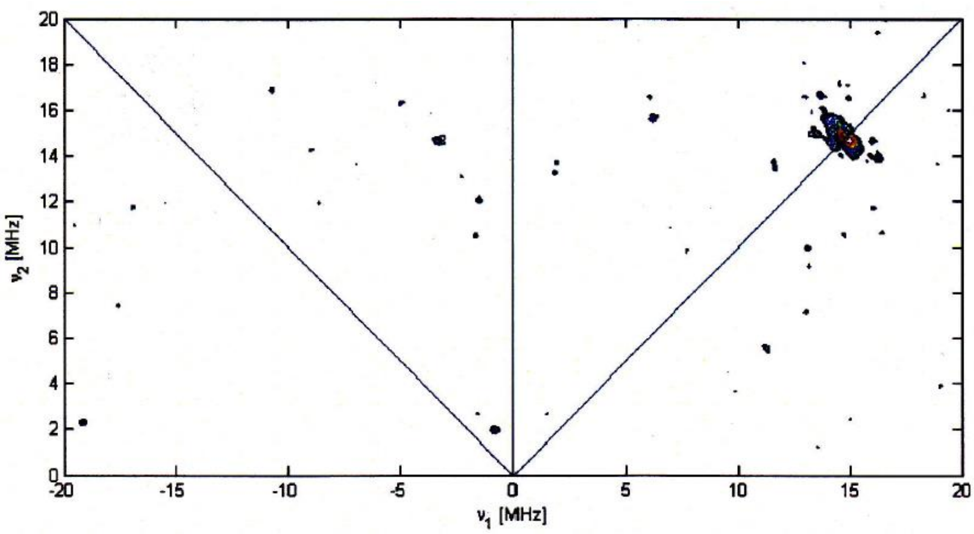

Figure B.13: HYSCORE spectrum of sample K, recorded at 10 K and taken at observer position B_0 = 348 mT. The HYSCORE spectrum is measured using the pulse sequence: $^{\pi}/_{2}-\tau-{}^{\pi}/_{2}-t_1-\pi-t_2-{}^{\pi}/_{2}-\tau-$ echo, with $t_{\pi/2}$ = 16 ns and t_{π} = 32 ns; t_1 and t_2 were varied in steps of 16 ns. The spectrum is recorded for τ = 96 and 172 ns.

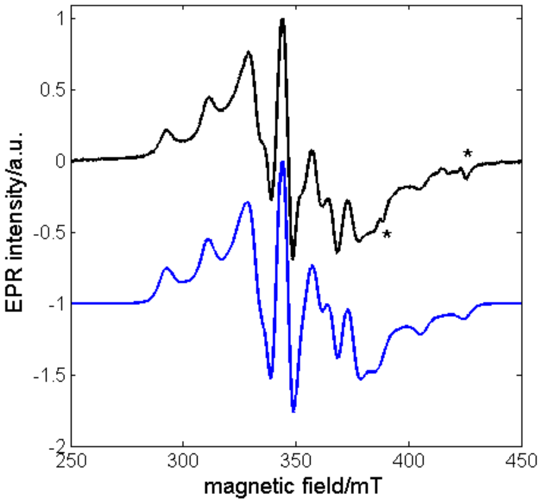

Figure B.14: Experimental (black, top) and simulated (blue, bottom) EPR spectrum of sample L. The spectrum is the sum of a mononuclear VO^{2+} complex (complex 1 in Table 3.1 of Chapter 3) and a broad background signal simulated by assuming the parameters of complex 1 with linewidths of 400 MHz (FWHM).

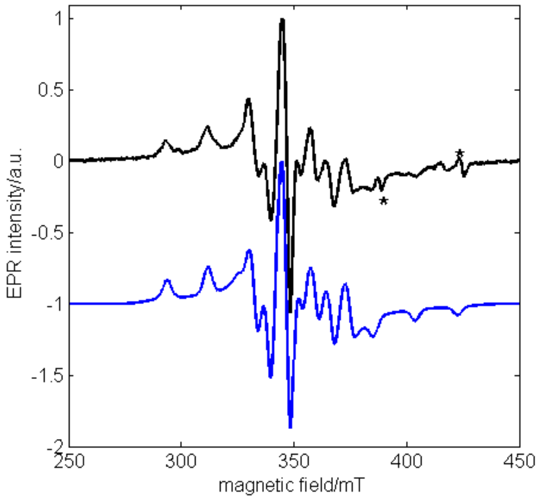

Figure B.15: Experimental (black, top) and simulated (blue, bottom) EPR spectrum of sample M. The spectrum is the sum of a mononuclear VO^{2+} complex (complex 2 in Table 3.1 of Chapter 3) and a small contribution of a broad background signal simulated by assuming the parameters of complex 1 with linewidths of 400 MHz (FWHM).

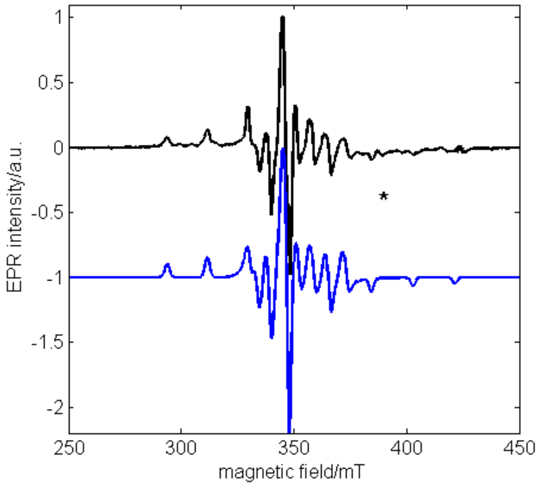

Figure B.16: Experimental (black, top) and simulated (blue, bottom) EPR spectrum of sample N. Only the contribution of the mononuclear VO^{2+} complex (complex 3 in Table 3.1 of Chapter 3) is simulated.

Appendix C

Experimental

In this chapter, all the experimental steps and analysis techniques will be clarified. The focus is on the experimental parameters used in this work, rather than a detailed theoretical description of each method or technique. (i) The experimental procedures for the synthesis of the VO^{2+} solutions studied in this work is given. (ii) The sequence of steps in the chemical solution deposition and subsequent film procession is discussed in chronological order. (iii) The solution analysis techniques used in this work are introduced. (iv) The powder characterization techniques and their thermal analyses are handled. (v) The characterization techniques applied on the obtained vanadium oxide structures will be described.

C.1 Solution synthesis

C.1.1 Oxalate rich citrato-VO^{2+} solution (citrate:VO^{2+} = 2:1)

In the first step of the synthesis of the aqueous VO^{2+} solution, ammonium metavanadate (1.17 g, NH_4VO_3, ≥ 99 %, Merck) was dissolved in water under reflux conditions (90 °C, 10 minutes). In a next step, oxalic acid dihydrate ($C_2O_4H_2 \cdot 2\,H_2O$, ≥ 99 %, Merck) was added, under reflux conditions (90 °C, 10 minutes), in a molar ratio to VO_2^+ ranging from 0.25:1 to 5:1. An optimal oxalic acid excess (3:1 against VO_2^+) was determined and maintained in the following steps. In the third step, citric acid ($C_6H_8O_7$, 99 %, Sigma-Aldrich) was added to the cooled VO^{2+} solution in a molar ratio of 2:1 to VO^{2+}. Ammonia (NH_3, 32 % aqueous solution, extra pure, Merck) was then added dropwise to set the pH at 7. The synthesis conditions were set such that a nominal vanadium concentration of 0.1 M was reached and experimentally confirmed by Inductively Coupled Plasma-Atomic Emission spectrometry.

C.1.2 Oxalate poor citrato-VO^{2+} solution (citrate:VO^{2+} = 2:1)

Initially, an aqueous VO^{2+} solution was synthesized as described above. In this synthesis, ammonium metavanadate (NH_4VO_3, ≥ 99 %, Merck) and oxalic acid dihydrate ($C_2O_4H_2 \cdot 2\,H_2O$, ≥ 99 %, Merck) were, consecutively, dissolved in water under reflux conditions (90 °C, 10 minutes) in a molar ratio of 3:1 ($C_2O_4H_2 \cdot 2\,H_2O$:NH_4VO_3). For the synthesis of the oxalate poor citrato-VO^{2+} solution, a separate solution of ammonium citrate was prepared first by dissolving di-ammonium hydrogen citrate ($C_6H_6O_7 \cdot 2\,NH_4$, ≥ 99 %, Merck) in water and by adding ammonia to this solution. A nominal citrate concentration of 3 M and a pH value of 7 were experimentally set. Before mixing the oxalato-VO^{2+} solution with the citrate solution, the pH of the VO^{2+} solution was increased to a value of 7 by adding ammonia and the volume was adjusted by H_2O to achieve a nominal VO^{2+} concentration of 1.5 M. Next, both solutions (1.5 M VO^{2+} solution with a pH value of 7 and 3 M citrate solution with a pH value of 7) were mixed in a volume ratio of 1:1. This mixed solution was aged for 7 days at 4 °C to induce precipitation, which was subsequently removed by filtration (Pall Life Sciences Supor 100 filters with 0.1 μm pore sizes). The precipitate was further washed with H_2O and dried at 60 °C in an air flow furnace to allow further analysis. Finally, the pH and volume of the filtrate were adjusted by adding NH_3 and H_2O, respectively, to obtain an aqueous citrato-VO^{2+} solution with a pH value of 7 and a vanadium concentration of 0.1 M.

C.1.3 Oxalato- and citrato-VO^{2+} solutions (various citrate:VO^{2+} ratios)

Firstly, an aqueous VO^{2+} solution was synthesized by the consecutive dissolution of ammonium metavanadate (NH_4VO_3, ≥ 99 %, Merck) and oxalic acid dihydrate ($C_2O_4H_2 \cdot 2\,H_2O$, ≥ 99 %, Merck) in water under reflux conditions (90 °C, 10 min.) in a molar ratio of 3:1 ($C_2O_4H_2 \cdot 2\,H_2O$:NH_4VO_3). Secondly, a separate solution of ammonium citrate was prepared by dissolving di-ammonium hydrogen citrate ($C_6H_6O_7 \cdot 2\,NH_4$, ≥ 99 %, Merck) in water and by adding ammonia to this solution. A nominal citrate concentration of 3 M and a pH value of 7 were experimentally set. Before mixing the VO^{2+} solution with the ammonium citrate solution, the pH of the VO^{2+} solution was increased to a value of 7 by adding ammonia and the volume was adjusted by adding H_2O to achieve a nominal VO^{2+} concentration of 1.5 M. Next, both solutions (1.5 M VO^{2+} solution with a pH value of 7 and 3 M citrate solution with a pH value of 7) were mixed in a volume ratio ranging between 2.67:1 and 0.44:1. All solutions were aged for 7 days at 4 °C to induce $(NH_4)_2C_2O_4$ precipitation, which was subsequently removed by filtration (Pall Life Sciences Supor 100 filters with 0.1 μm pore sizes). Finally, the pH and volume of each filtrate was adjusted by NH_3 and H_2O to obtain aqueous citrato-VO^{2+} solutions with a pH value of 7 and a vanadium concentration of 0.1 M. The molar ratio of citrate to VO^{2+} is varied between 0.75:1 and 4.5:1 by varying the aforementioned volume. All nominal vanadium concentration were experimentally confirmed by ICP-AES.

C.1.4 Vanadium free reference solutions

Vanadium free solutions of ammonium oxalate and ammonium citrate were prepared by the dissolution of ammonium oxalate monohydrate ($(COONH_4)_2 \cdot H_2O$, 99.0 – 101.0 %, Alfa Aesar) or di-ammonium hydrogen citrate ($C_6H_6O_7 \cdot 2\,NH_4$, ≥ 99 %, Merck) in water, respectively. For both vanadium free solution solutions, ammonia and water were added to obtain a solution with a pH value of 7 and a nominal oxalate or citrate concentration of 0.3 M.

C.2 Chemical solution deposition and film processing

The solutions were spin coated (3000 rpm, 30 s, 1000 $^{rpm}/_{s}$) onto small pieces (± 6 cm^2) of p-type Si with (i) 1.2 nm SiO_2, 200 nm SiO_2, 10 nm γ-Al_2O_3 or Pt, cleaned in a sulfuric acid peroxide mixture and ammonia peroxide mixture or (ii) 70 nm TiN or 7.5 nm TiO_2 treated in an in-situ generated O_3 atmosphere (UV-O_3, 50 °C, 30 minutes). A hot plate treatment was carried out on each deposited layer at 90 °C for 2 minutes. An intermediate anneal was carried out in a rapid thermal anneal system (Accutherm AW-610), systematically with a chamber N_2 flush of 2 minutes, a heating rate of 10 $°C{\cdot}s^{-1}$, an isothermal period and a slow cooling (≥ 5 minutes) in a N_2 environment (10 SLPM). During the isothermal period the following parameters are varied: time (10 – 30 minutes), temperature (400 °C – 900 °C) and ambient (0 % – 1 % O_2) by a controlled co-flow (5 SLPM) of high purity N_2 and 1 % O_2 (in Ar). The deposition cycle (spin coating - hot plate - intermediate anneal) was repeated multiple times to ensure sufficient substrate coverage. A post deposition anneal was performed in the same rapid thermal anneal system under identical conditions with identical parameters.

The low pO_2 anneals are carried out in a rapid thermal anneal system (Accutherm AW-610). Prior to the anneal experiment, the chamber is flushed for 2 minutes with N_2 (10 SLPM). Each anneal experiment is performed with a heating from T_{Room} to the desired temperature at a heating rate of 10 °C s^{-1} in N_2 (10 SLPM). During the isothermal period, 0.1 % O_2 ambient condition is obtained by a controlled co-flow (5 SLPM) of high purity N_2 (4.5 SLPM) and 1 % O_2 in Ar (0.5 SLPM). After the isothermal period, natural cooling is allowed in N_2 (10 SLPM). Though, these experimental conditions seem very solid, the following experimental deviations could have appeared:

- The 1 % O_2 originates from fixed gas bottle (not from a central gas line, as is the case for N_2) which is manually operated. Small deviations in the output pressure (regulated by a manual gas pressure reductor) could influence the final 0.1 % O_2 atmosphere.

- The 1 % O_2 gas flows through the gas line which is used in other experiments as the 100 % O_2 gas line. A gas valve allows the choice between both gasses. Thus prior to each set of experiments, this gas line is flushed with the 1 % O_2 gas. As a consequence, the total volume of 1 % O_2 passed through the line is the lowest for the first experiment(s) which might result in a slightly higher oxygen content in comparison to the last experiment.
- The entire system is annually calibrated which might cause deviations in the experimental parameters (such as temperature and co-gas flow) depending on the time after the last calibration.
- The temperature is controlled by either a thermocouple or a pyrometer if the temperature is below or above 600 °C which could cause deviations between experiments performed below or above 600 °C.
- Additionally, the pyrometer is not able to control the temperature below 100 °C which is problematic during the natural cooling because you don't know at which temperature the furnace is opened and air is allowed to the sample.

Since, the 0.1 % O_2 condition is really on the lower limit of tool, the smallest variation in one (or more) of the above mentioned parameters could undesirably influence the experimental outcome.

C.3 Solution characterization

Electron Paramagnetic Resonance (EPR) spectroscopy

X-band CW-EPR

X-band continuous-wave EPR spectra are recorded on a Bruker ESP300E spectrometer (microwave frequency of 9.43 GHz) equipped with a liquid helium cryostat (Oxford Inc.), allowing for operation from room temperature down to 2.5 K. The temperature, modulation amplitude, microwave power and modulation frequency vary for every measurement. Simulations of all CW-EPR spectra were performed with the EasySpin program, a MATLAB toolbox developed for EPR simulations.[190, 191]

Electron Spin Echo (ESE) detected EPR spectroscopy

ESE-detected EPR spectra were carried out with the pulse sequence: $\pi/2$ - π - τ - echo with $t_{\pi/2}$ = 16 ns, t_{π} = 32 ns and τ = 88 ns.

Hyperfine Sublevel Correlation (HYSCORE) spectroscopy

The HYSCORE (hyperfine sublevel correlation) spectra[192] were recorded on a Bruker Elexsys E500 spectrometer (microwave frequency 9.76 GHz) equipped with a liquid-helium cryostat (Oxford Inc.). The HYSCORE spectra were measured using the pulse sequence: $\pi/2$ - τ - $\pi/2$ - t_1 - π - t_2 - $\pi/2$ - τ - echo. A four-step phase cycle was performed in all cases to remove the unwanted echoes. The HYSCORE traces were baseline corrected using a third-order polynomial, apodized with a Hamming window and zero-filled. After Fourier transformation the absolute-value spectra were computed and the spectra recorded at different τ values were added together to reduce the blind-spot effect.

Inductively Coupled Plasma - Atomic Emission Spectroscopy (ICP-AES)

The V^{x+} concentration is determined via ICP-AES (PerkinElmer Optima 3300V). Each ICP-AES analysis, used in this work, consist of three steps. In the first step, a calibration curve is set using reference solutions with a metal ion concentration of 0, 1, 2, 5 and 10 ppm. In the second step, the concentration of the metal ion in the sample is determined using these calibration curves. In the last step, the reference sample of 5 ppm is remeasured (*Quality Check*) to identify a possible drift. All references and samples are diluted in 5 % HNO_3 (J.T. Baker, 69–70 %, Baker Instra-analyzed Reagent^{TM}) to obtain either a concentration within the 0 to 10 ppm calibration curve. Table C.1 shows the characteristic emission lines used in this work.

Element	Emission lines (nm)			
Vanadium	270.093	292.402	309.310	310.230

Table C.1: Overview of characteristic emission lines used in this work to determine the metal ion concentration via ICP-AES.

pH measurement

The pH of the aqueous solutions is measured by a Sentix 60 (3 M KCl) pH electrode. This pH electrode is daily calibrated using buffer solutions at pH 4 an 7.

Ultraviolet-Visible (UV-Vis) spectroscopy

Solution UV-Vis spectra are recorded on a UV-Vis, Ultrospec^{TM} 100 pro spectrophotometer with a wavelength range of 330–830 nm, a spectral bandwidth of 8 nm, a wavelength accuracy of ± 2 nm and a wavelength reproducibility of ± 1 nm. Disposable macro-UV-cuvettes with a light path of 10 mm are used as container during the UV-Vis measurement.

^{51}Vanadium - Nuclear Magnetic Resonance (^{51}V-NMR) spectroscopy

All ^{51}V liquid-state NMR spectra are acquired at 78.9 MHz on a Varian Inova 300 spectrometer at room temperature in a 5 mm four-nucleus PFG probe. The chemical shift scale is calibrated at - 559.0 ppm with a 0.1 M sodium orthovanadate (Na_3VO_4, 99.9 %, Alfa Aesar) solution at pH 12.[36] Free induction decays are collected with a 90 °pulse of 5.0 μs, a spectral width of 292 kHz, an acquisition time of 0.1 s, a preparation delay of 1 s and 300 accumulations. A line-broadening factor of 2 Hz is applied before Fourier transformation to the frequency domain. All solution are diluted, in a 1:2 volume ratio, by D_2O (99 %, Cambridge Isotope Laboratories) to guarantee a significant lock signal.

C.4 Powder characterization

Fourier Transform Infra-Red (FTIR) Spectroscopy

FTIR spectra are recorded at T_{Room} between 4000 and 400 cm^{-1} on a Bruker Vertex 70 spectrometer (128 scans, 4 cm^{-1} resolution). The sample is systematically dispersed in KBr pellets (1 wt. %) and analyzed in transmission mode.

Thermogravimetrical Analysis (TGA)

The thermal decomposition pathway of the powders is examined by means of thermogravimetrical (TG) analysis. All TG analyses are carried out on the as-received commercial product or on a dried powder (60 °C), heated from room temperature to a desired end temperature (typically between 600 °C and 800 °C) at a heating rate of 10 °C · min^{-1}. After sufficient flushing with the analysis gas, the decomposition is studied in dry air or in N_2 (100 mL · min^{-1}). TG analyses are performed on (i) a TA Instruments SDT Q600 (± 5 mg of sample) for simultaneous TG-DSC[1] analysis and (ii) a TA Instruments TGA Q5000 (± 2 mg of sample) coupled with a Pfeiffer Vacuum ThermoStar^{TM} MS for simultaneous TG-MS[2] analysis.

Raman spectroscopy

Raman spectra were recorded on a Horiba Jobin Yvon micro-Raman (T64000) using a 488 nm laser as excitation source (LEXEL 95 SHG) operating at 200 mW.

X-Ray Diffraction (XRD)

The obtained powders were analyzed by XRD on a Siemens D5000 Diffractometer, operating in a Bragg-Brentano configuration (coupled θ-2θ scan)

---

[1] The abbreviation *DSC* corresponds to *Differential Scanning Calorimetry* and measures, in addition to a standard TG analysis, the heat flow developed during the thermal decomposition pathway as function of the temperature.

[2] The abbreviation MS corresponds to *Mass Spectrometry* and measures, in addition to a standard TG analysis, the amount of ionized mass fragments (differentiated by their m/z ratio) developed during the thermal decomposition pathway as function of the temperature.

C.5 Vanadium oxide characterization

Atomic Force Microscopy (AFM)

The topography of the films was visualized by tapping mode AFM on a Veeco Dimension microscope with Digital Instruments Nanoscope III controller and an etched Si probe NANOSENSORSTM.

Contact angle

The films' wetting properties were analyzed using contact angle measurements (DataPhysics OCA 230L Contact Angle System).

Energy Dispersive X-ray (EDX) spectroscopy

Chemical analysis is carried out by EDX with a Si(Li) detector and Bruker software, performed in a scanning electron microscope (FEI Quanta 200FEG).

Grazing angle Attenuated Total Reflectance-Fourier Transform Infrared (GATR-FTIR) spectroscopy

The obtained films were characterized by means of GATR-FTIR spectroscopy, using a 65° single reflection Ge-ATR (Harrick) crystal, placed inside the sample compartment of a FTIR spectrometer (Bruker, Vertex 70, 32 scans, 4 cm^{-1} resolution).

In-situ High-Temperature X-Ray Diffraction (HT-XRD)

HT-XRD analyzes are performed on a Bruker, Vantec Diffractometer, spanning 20 $°2\theta$ with a step size of 0.014 $°2\theta$. Heating occurred in a home-built heating chamber using a dynamic dry air ambient (Vantec setup) with a heating rate of 0.2 $°\mathrm{C} \cdot \mathrm{s}^{-1}$.

Scanning Electron Microscopy (SEM)

The deposited structures were visualized with Scanning Electron Microscopy (SEM, FEI, NOVA 200) in secondary electrons imaging mode. Both 45°-tilted and cross-sectional (X-SEM) view were used.

Single-wavelength ellipsometry

Film thicknesses were obtained from single wavelength ellipsometry (Plasmos, 632.8 nm) using a single layer model with a refractive index of 3.1.

X-Ray Diffraction (XRD)

The crystal phase of the vanadium oxide nanostructures was determined by means of XRD (PANalytical X'pert Pro, Cu Kα) in a Bragg-Brentano configuration (coupled θ-2θ scan) with a PIXcel detector in scanning mode (step size 0.0098 °).

Bibliography

[1] H. A. Wriedt. The O-V (Oxygen-Vanadium) System. *Bulletin of Alloy Phase Diagrams*, 10(3):1989, 1989.

[2] H. Katzke, P. Tolédano, and W. Depmeier. Theory of morphotropic transformations in vanadium oxides. *Physical Review B*, 68(2):024109, 2003.

[3] A. L. Pergament. Metal-Insulator Transition Temperatures and Excitonic Phases in Vanadium Oxides. *ISRN Condensed Matter Physics*, 2011(1):1–5, 2011.

[4] U. Schwingenschlögl and V. Eyert. The vanadium Magnéli phases V_nO_{2n-1}. *Annals of Physics*, 510(9):475–510, 2004.

[5] F. J. Morin. Oxides which show a metal-to-insulator transition at the Neel temperature. *Physical review letters*, 3(1):34–36, 1959.

[6] C. G. Granqvist. Transparent conductors as solar energy materials: A panoramic review. *Solar Energy Materials and Solar Cells*, 91(17):1529–1598, 2007.

[7] J. Nag and R. F. Haglund. Synthesis of vanadium dioxide thin films and nanoparticles. *Journal of Physics: Condensed Mater*, 20:264016, 2008.

[8] J. Y. Suh, R. Lopez, L. C. Feldman, and R. F. Haglund. Semiconductor to metal phase transition in the nucleation and growth of VO_2 nanoparticles and thin films. *Journal of Applied Physcis*, 96(2):1209–1214, 2004.

[9] S. A. Pauli, R. Herger, P. R. Willmott, E. U. Donev, J. Y. Suh, and R. F. Haglund. X-ray diffraction studies of the growth of vanadium dioxide nanoparticles. *Journal of Applied Physics*, 102:073527, 2007.

[10] M. S. Whittingham, Y. Song, S. Lutta, P. Y. Zavalij, and N. A. Chernova. Some transition metal (oxy) phosphates and vanadium oxides for lithium batteries. *Journal of Materials Chemistry*, 15:3362–3379, 2005.

[11] H. Li, P. He, Y. Wang, E. Hosono, and H. Zhou. High-surface vanadium oxides with large capacities for lithium-ion batteries: from hydrated aerogel to nanocrystalline VO_2(B), V_6O_{13} and V_2O_5. *Journal of Materials Chemistry*, 21(29):10999, 2011.

[12] D. W. Murphy and P. A. Christian. Solid State Electrode for High Energy Batteries. *Science*, 205(4407):651–656, 1979.

[13] C. Delmas, H. Cognac-Auradou, J. M. Cocciantelli, and J. P. Doumerc. The $Li_xV_2O_5$ system : An overview of the structure modifications induced by the lithium intercalation. *Solid State Ionics*, 69:257–264, 1994.

[14] C. Piccirillo, R. Binions, and I. P. Parkin. Synthesis and Functional Properties of Vanadium Oxides: V_2O_3, VO_2, and V_2O_5 Deposited on Glass by Aerosol-Assisted CVD. *Chemical Vapor Deposition*, 13:145–151, 2007.

[15] G. Rampelberg, M. Schaekers, K. Martens, Q. Xie, and D. Deduytsche. Semiconductor-metal transition in thin VO_2 films grown by ozone based atomic layer deposition. *Applied Physics Letters*, 98:162902, 2011.

[16] P. A. Premkumar, M. Toeller, I. P. Radu, C. Adelmann, M. Schaekers, J. Meersschaut, T. Conard, and S. Van Elshocht. Process Study and Characterization of VO_2 Thin Films Synthesized by ALD Using TEMAV and O_3 Precursors. *ECS Journal of Solid State Science and Technology*, 1(4):169–174, 2012.

[17] R. Lopez, R. F. Haglund, L. C. Feldman, L. A. Boatner, and T. E. Haynes. Optical nonlinearities in VO_2 nanoparticles and thin films. *Applied Physics Letters*, 85(22):5191–5194, 2004.

[18] R. Lopez, L. A. Boatner, and T. E. Haynes. Switchable reflectivity on silicon from a composite VO_2-SiO_2 protecting layer. *Applied Physics Letters*, 85(8):1410–1413, 2004.

[19] Z. Luo, Z. Wu, T. Wang, X. Xu, W. Li, W. Li, and Y. Jiang. Comparison of the optical responses of O-poor and O-rich thermochromic VO_X films during semiconductor-to-metal transition. *Journal of Physical and Chemistry of Solids*, 73(9):1122–1126, 2012.

[20] Y. Cui and S. Ramanathan. Substrate effects on metal-insulator transition characteristics of RF-sputtered epitaxial VO_2 thin films. *Journal of Vacuum Science & Technology A: Vacuum, Surfaces, and Films*, 29(4):041502, 2011.

[21] H. Van den Rul, M. K. Van Bael, A. Hardy, K. Van Werde, and J. Mullens. Aqueous Solution-Based Synthesis of Nanostructured Metal Oxides. In T.-Y. Tseng and H. S. Nalwa, editors, *Handbook of Nanoceramics and Their Based Nanodevices: Synthesis and Processing*, pages 267–300. American Scientific Publishers, 1st edition, 2009.

[22] D. P. Partlow, S. R. Gurkovich, K. C. Radford, and L. J. Denes. Switchable vanadium oxide films by a sol-gel process. *Journal of Applied Physics*, 70(1):443–452, 1991.

[23] B. G. Chae, H. T. Kim, S. J. Yun, B. J. Kim, Y. W. Lee, and K. Y. Kang. Comparative Analysis of VO_2 Thin Films Prepared on Sapphire and SiO_2/Si Substrates by the Sol-Gel Process. *Japanese Journal of Applied Physics*, 46(2):738–743, 2007.

[24] J. Livage. Vanadium Pentoxide Gels. *Chemistry of Materials*, 3:578–593, 1991.

[25] Y. Dachuan, X. Niankan, Z. Jingyu, and Z. Xiulin. Vanadium dioxide films with good electrical switching property. *Journal of Physics D: Applied Physics*, 29(4):1051–1057, 1996.

[26] S. Burojevic, I. Shweky, A. Bino, D. A. Summers, and R. C. Thompson. Synthesis, structure and magnetic properties of an assymmetric dinuclear oxocitratovanadate(IV) complex. *Inorganic Chimica Acta*, 251:75–79, 1996.

[27] M. Velayutham, B. Varghese, and S. Subramanian. Magneto-Structural Correlation Studies of A Ferromagnetically Coupled Dinuclear Vanadium(IV) Complex. Single-Crystal EPR Study. *Inorganic chemistry*, 37(6):1336–1340, 1998.

[28] Z.-H. Zhou, H.-L. Wan, S.-Z. Hu, and K.-R. Tsai. Syntheses and structures of the potassium-ammonium dioxocitratovanadate(V) and sodium oxocitratovanadate(IV) dimers. *Inorganic Chimica Acta*, 237:193–197, 1995.

[29] M. Tsaramyrsi, M. Kaliva, and A. Salifoglou. Vanadium(IV) - Citrate Complex Interconversions in Aqueous Solutions. A pH-Dependent Synthetic, Structural, Spectroscopic, and Magnetic Study. *Inorganic chemistry*, 40:5772–5779, 2001.

[30] T. Kiss, P. Buglyó, D. Sanna, G. Micera, P. Decock, and D. Dewaele. Oxovanadium (IV) complexes of citric and tartaric acids in aqueous solution. *Inorganica Chimica Acta*, 239:145–153, 1995.

[31] S. Berto, P. G. Daniele, E. Prenesti, and E. Laurenti. Interaction of oxovanadium(IV) with tricarboxylic ligands in aqueous solution: A thermodynamic and spectroscopic study. *Inorganica Chimica Acta*, 363(13):3469–3476, 2010.

[32] E. Lodyga-Chruscinska, D. Sanna, and G. Micera. Potentiometric, spectroscopic, electrochemical and DFT characterization of oxovanadium(IV) complexes formed by citrate and tartrates in aqueous solution at high ligand to metal molar ratios: the effects of the trigonal bipyramidal distortion in bis-. *Dalton Transactions*, 28(36):4903–4916, 2008.

[33] R. W. Schwartz, T. Schneller, and R. Waser. Chemical solution deposition of electronic oxide films. *Compte Rendus Chimie*, 7:433–461, 2004.

[34] M. E. Weeks. Discovery of the elements. *Journal of Chemical Education*, 1960.

[35] O. Wallach. *Briefwechsel zwischen J. Berzelius und F. Wohler*. Verlag von Wilhelm Engelmann, 1901.

[36] D. Rehder. *Bioinorganic Vanadium Chemistry*. John Wiley & Sons, 2008.

[37] J. C. Bailar, H. J. Emeléus, R. Nyholm, and A. F. Trotman-Dickenson. *Comprehensive Inorganic Chemistry.* Pergamon Press, 1973.

[38] European Commission. Report of the ad-hoc working group on defining critical raw materials. Technical report, European Union, 2010.

[39] J. Livage, M. Henry, and C. Sanchez. Sol-gel chemistry of transition metal oxides. *Progress in Solid State Chemistry*, 17(4), 1988.

[40] J.-P. Jolivet, M. Henry, and J. Livage. *Metal Oxide Chemistry and Synthesis*. John Wiley & Sons, 2000.

[41] A. F. Holleman and E. Wiberg. *Lehrbuch der Anorganischen Chemie.* Walter de Gruyter, 1955.

[42] J. Haber. Fifty years of my romance with vanadium oxide catalysts. *Catalysis Today*, 142(3-4):100–113, 2009.

[43] M. Pourbaix. *Atlas of Electrochemical Equilibria in Aqueous Solutions*. National Association of Corrosion Engineers, Houston, 1974.

[44] R. Meier, M. Boddin, S. Mitzenheim, and K. Kanamori. *Vanadium and Its Role in Life.* Marcel Dekker, 1995.

[45] K. Kanamori. Structures and properties of multinuclear vanadium(III) complexes: seeking a clue to understand the role of vanadium(III) in ascidians. *Coordination Chemistry Reviews*, 237:147–161, 2003.

[46] N. D. Chasteen. Vanadyl(IV) EPR Spin Probes: Inorganic and Biochemical Aspects. In *Biological Magnetic Resonance*, pages 53–119. Springer, 1981.

[47] E. J. Baran. Review: Spectroscopic studies of oxovanadium coordination compounds. *Journal of Coordination Chemistry*, 54(3–4):215–238, 2001.

[48] R. H. Petrucci, F. G. Herring, J. D. Madura, and Bissonnette C. *General Chemistry: Principles and Modern Applications.* Prentice Hall, 8th edition, 2002.

[49] C. J. Ballhausen and H. B. Gray. The Electronic Structure of the Vanadyl Ion. *Inorganic chemistry*, 1(1):111–122, 1962.

[50] P. Atkins and J. De Paula. *Atkins' Physical Chemistry.* Oxford University Press, 8th edition, 2006.

[51] J. Selbin. the Chemistry of oxovanadium(IV). *Chemical reviews*, 65(2):153–175, 1965.

[52] M. M. Iannuzzi and P. H. Rieger. Nature of vanadium(IV) in basic aqueous solution. *Inorganic Chemistry*, 14(12):2895–2899, 1975.

[53] T. M. Dunn. Spin-orbit coupling in the first and second transition series. *Transactions Faraday Society*, 57:1441–1444, 1961.

[54] E. I. Solomon and A. B. P. Lever. *Inorganic Electronic Structure and Spectroscopy. Volume 1: Methodology.* John Wiley & Sons, 1th edition, 1999.

[55] C. F. Baes and R. E. Mesmer. *The Hydrolysis of Cations.* John Wiley & Sons, 1976.

[56] D. C. Crans, J. J. Smee, E. Gaidamauskas, and L. Yang. The chemistry and biochemistry of vanadium and the biological activities exerted by vanadium compounds. *Chemical reviews*, 104(2):849–902, 2004.

[57] D. T. Richens. *The Chemistry of Aqua Ions*. John Wiley & Sons, 1976.

[58] D. Rehder. Vanadium NMR of organovanadium complexes. *Coordination Chemistry Reviews*, 252:2209–2223, 2008.

[59] A. Gorzsás, I. Andersson, and L. Pettersson. Speciation in aqueous vanadate-ligand and peroxovanadate-ligand systems. *Journal of inorganic biochemistry*, 103(4):517–26, 2009.

[60] A. Hardy, S. Van Elshocht, W. Knaepen, J. D'Haen, T. Conard, B. Brijs, W. Vandervorst, G. Pourtois, J. Kittl, C. Detavernier, M. K. Heyns, M. Van Bael, H. Van den Rul, and J. Mullens. Crystallization resistance of barium titanate zirconate ultrathin films from aqueous CSD: a study of cause and effect. *Journal of Materials Chemistry*, 19(8):1115, 2009.

[61] A. Hardy, S. Van Elshocht, D. Dewulf, S. Clima, N. Peys, C. Adelmann, K. Opsomer, P. Favia, H. Bender, I. Hoflijk, T. Conard, A. Franquet, H. Van den Rul, J. A. Kittl, S. De Gendt, M. K. Van Bael, and J. Mullens. Properties of Ultrathin High Permittivity $(Nb_{1-x}Ta_x)_2O_5$ Films Prepared by Aqueous Chemical Solution Deposition. *Journal of The Electrochemical Society*, 157(1):G13, 2010.

[62] D. Dewulf, N. Peys, S. Van Elshocht, G. Rampelberg, C. Detavernier, S. De Gendt, A. Hardy, and M.K. Van Bael. Interfacial reactions of Gd- and Nb-oxide based high-k layers deposited by aqueous chemical solution deposition. *Microelectronic Engineering*, 88(7):1338–1341, 2011.

[63] A. E. Martell and R. M. Smith. *Critical stability constants.* Plenium Press, 3th edition, 1977.

[64] M. Tsaramyrsi, D. Kavousanaki, C. P. Raptopoulou, A. Terzis, and A. Salifoglou. Systematic synthesis, structural characterization, and reactivity studies of vanadium(V)-citrate anions $[VO_2(C_6H_6O_7)]^{2-}$, isolated from aqueous solutions in the presence of different cations. *Inorganica Chimica Acta*, 320:47–59, 2001.

[65] M. Kaliva, C. P. Raptopoulou, A. Terzis, and A. Salifoglou. Systematic studies on pH-dependent transformations of dinuclear vanadium(V)-citrate complexes in aqueous solutions. A perspective relevance to aqueous vanadium(V)-citrate speciation. *Journal of inorganic biochemistry*, 93(3-4):161–73, 2003.

[66] M. Kaliva, E. Kyriakakis, C. Gabriel, C.P. Raptopoulou, A. Terzis, J.-P. Tuchagues, and A. Salifoglou. Synthesis, isolation, spectroscopic and structural characterization of a new pH complex structural variant from the aqueous vanadium(V)-peroxo-citrate ternary system. *Inorganica Chimica Acta*, 359(14):4535–4548, 2006.

[67] M. Kaliva, C. Gabriel, C. P. Raptopoulou, A. Terzis, and A. Salifoglou. pH-specific synthesis, isolation, spectroscopic and structural characterization of a new dimeric assembly of dinuclear vanadium(V)-citrate-peroxo species from aqueous solutions. *Inorganica Chimica Acta*, 361(9-10):2631–2640, 2008.

[68] C. Gabriel, J. Venetis, M. Kaliva, C. P. Raptopoulou, A. Terzis, C. Drouza, B. Meier, G. Voyiatzis, C. Potamitis, and A. Salifoglou. Probing for missing links in the binary and ternary V(V)-citrate-(H_2O_2) systems: synthetic efforts and in vitro insulin mimetic activity studies. *Journal of inorganic biochemistry*, 103(4):503–16, 2009.

[69] M. Kaliva, C. Gabriel, C. P. Raptopoulou, A. Terzis, G. Voyiatzis, M. Zervou, C. Mateescu, and A. Salifoglou. A unique dinuclear mixed V(V) oxo-peroxo complex in the structural speciation of the ternary V(V)-peroxo-citrate system. potential mechanistic and structural insight into the aqueous synthetic chemistry of dinuclear V(V)-citrate species with H_2O_2. *Inorganic chemistry*, 50(22):11423–36, 2011.

[70] A. Gorzsás, K. Getty, I. Andersson, and L. Pettersson. Speciation in the aqueous $H^+/H_2VO_4^-/H_2O_2$/citrate system of biomedical interest. *Dalton transactions*, 20(18):2873–82, 2004.

[71] P. M. Ehde, I. Andersson, and L. Petterson. Multicomponent Polyanions 43. A study of Aqueous Equilibria in the Vanadocitrate System. *Acta Chemica Scandinavica*, 43:136–143, 1989.

[72] D. R. Lide. *Handbook of Chemistry and Physics*. Press, CRC, 83 edition, 2002.

[73] J. Tatiersky, S. Pacigová, M. Sivák, and P. Schwendt. Monoperoxidovanadium(V) complexes: synthesis, structure and solution properties. *The Journal of the Argentine Chemical Society*, 97:181–198, 2009.

[74] N. Peys, P. Adriaensens, S. Van Doorslaer, S. Gielis, E. Peeters, C. De Dobbelaere, S. De Gendt, A. Hardy, and M. K. Van Bael. Aqueous citrato-oxovanadate(IV) precursor solutions for VO_2: synthesis, spectroscopic investigation and thermal analysis. *Submitted for publication*, 2014.

[75] K. Nakamoto. *Infrared and Raman Spectra of Inorganic and Coordination Compounds - Part B: Applications in Coordination, Organometallic, and Bioinorganic Chemistry*. John Wiley & Sons Inc., New York, 5th edition, 1997.

[76] S. Petit, D. Righi, J. Madejova, and A. Decarreau. Interpretation of the infrared spectrum of the NH_4^+-clays: application to the evaluation of the layer charge. *Clay Minerals*, 34(4):543–549, 1999.

[77] M. E. Brown, L. Glasser, and B. V. Stewart. The thermal decomposition of ammonium metavanadate. *Journal of Thermal Analysis*, 6:529 – 541, 1974.

[78] A. Legrouri, T. Baird, and J. R. Fryer. Electron optical studies of the thermal decomposition of ammonium metavanadate (NH_4VO_3). *Reactivity of Solids*, 5:53–68, 1988.

[79] N. McCann, M. Wagner, and H. Hasse. A thermodynamic model for vanadate in aqueous solution - equilibria and reaction enthalpies. *Dalton Transactions*, 42:2622–2628, 2013.

[80] D. Rehder. The Future of/for Vanadium. *Dalton Transactions*, 42:11749–11761, 2013.

[81] A. S. Tracey, M. J. Gresser, and Parkinson; K. M. Vanadium(V) oxyanions: interactions of vanadate with oxalate, lactate and glycerate. *Inorganic Chemistry*, 26(5):629–638, 1987.

[82] E. M. Voronova and A. A. Ivakin. Spectrophotometric study of oxalato-complexes of vanadium(V) in aqueous solution. *Russian Journal of Inorganic Chemisty*, 14:818, 1969.

[83] V. I. E. Bruyère, L. A. García Rodenas, P. J. Morando, and M. A. Blesa. Reduction of vanadium(V) by oxalic acid in aqueous acid solutions. *Journal of the Chemical Society, Dalton Transactions*, 1(24):3593–3597, 2001.

[84] R. W. Schwartz and Narayanan M. Chemical solution deposition: basic principles. In D. B. Mitzi, editor, *Solution Processing of Inorganic Materials*, volume 1, chapter 2, pages 33–76. Wiley & sons, 2009.

[85] D. Nelis, D. Mondelaers, G. Vanhoyland, A. Hardy, K. Van Werde, H. Van Den Rul, M. K. Van Van Bael, J. Mullens, L. C. Van Van Poucke, and J. D'Haen. Synthesis of strontium bismuth niobate ($SrBi_2Nb_2O_9$) using an aqueous acetate-citrate precursor gel: thermal decomposition and phase formation. *Thermochimica Acta*, 426(1-2):39–48, 2005.

[86] K. Van Werde, D. Mondelaers, G. Vanhoyland, D. Nelis, and M. K. Van Bael. Thermal decomposition of the ammonium zinc acetate citrate precursor for aqueous chemical solution deposition of ZnO. *Journal of Materials Science*, 37:81–88, 2002.

[87] A. Hardy, K. Van Van Werde, G. Vanhoyland, M. K. Van Bael, J. Mullens, and L. C. Van Poucke. Study of the decomposition of an aqueous metal-chelate gel precursor for $(BiLa)_4Ti_3O_{12}$ by means of TGA-FTIR , TGA-MS and HT-DRIFT. *Thermochimica Acta*, 397:143–153, 2003.

[88] T. S. Smith, R. Lobrutto, and V. L. Pecoraro. Paramagnetic spectroscopy of vanadyl complexes and its applications to biological systems. *Coordination Chemistry Reviews*, 228:1–18, 2002.

[89] N. M. Atherton and J. F. Shackleton. Proton ENDOR of $VO(H_2O)_5^{2+}$ in $Mg(NH_4)_2(SO_4)_2 \cdot 6\,H_2O$. *Molecular Physics*, 39:1471–1485, 1980.

[90] S. C. Larsen. DFT Calculations of Proton Hyperfine Coupling Constants for $[VO(H_2O)_5]^{2+}$: Comparison with Proton ENDOR Data. *Journal of Physical Chemistry A*, 105(319):8333–8338, 2001.

[91] K. Fukui, H. Ohya-nishiguchi, and H. Kamada. ^{14}N Coupling Parameters in Oxovanadium(IV)-Amine, -Imine, and -Isothiocyanate Complexes Studied by Electron Spin Echo Envelope Modulation Spectroscopy. *Inorganic chemistry*, 36:5518–5529, 1997.

[92] R.L. Frost. Raman spectroscopy of natural oxalates. *Analytica Chimica Acta*, 517(1-2):207–214, 2004.

[93] M. Cadene and A. Fournel. Phonons optiques de l'oxalate d'ammonium hydraté à 295 K et 10 K. *Journal of Molecular Structure*, 37:35–57, 1977.

[94] E. Pretsch, P. Bühlmann, and M. Badertscher. *Structure Determination of Organic Compounds: Tables of Spectral Data*. Springer-Verlag Berlin Heidelberg, 4th edition, 2009.

[95] C. Djordjevic, M. Lee, and E. Sinn. Oxoperoxo(citrato-) and Dioxo(citrato)vanadates(V): Synthesis, Spectra, and Structure of a Hydroxyl Oxygen Bridged Dimer, $K_2[VO(O_2)(C_6H_6O_7)]_2 \cdot 2\,H_2O$. *Inorganic Chemistry*, 28(4):719–723, 1989.

[96] JCPDS. *Powder diffraction file of inorganic phases*. The International Centre for Diffraction Data, Swarthmore, 1997.

[97] N. Peys, Y. Ling, D. Dewulf, S. Gielis, C. De Dobbelaere, D. Cuypers, P. Adriaensens, S. Van Doorslaer, S. De Gendt, A. Hardy, and M. K. Van Bael. V_6O_{13} films by control of the oxidation state from aqueous precursor to crystalline phase. *Dalton Transactions*, 42(4):959–968, 2013.

[98] A. Hardy, J. D'Haen, L. Goux, D. Wouters, M. K. Van Bael, H. Van Den Rul, and J. Mullens. Aqueous Chemical Solution Deposition of Ferroelectric Ti^{4+} Cosubstituted $(BiLa)_4Ti_3O_{12}$ Thin Films. *Chemistry of Materials*, 19:2994–3001, 2007.

[99] P. Buglyó, E. Kiss, I. Fábián, T. Kiss, D. Sanna, E. Garribba, and G. Micera. Speciation and NMR relaxation studies of VO(IV) complexes with several O-donor containing ligands: oxalate, malonate, maltolate and kojate. *Inorganica Chimica Acta*, 306(2):174–183, 2000.

[100] E. Garribba, G. Micera, A. Panzanelli, and D. Sanna. Electronic structure of oxovanadium(IV) complexes of alpha-hydroxycarboxylic acids. *Inorganic chemistry*, 42(13):3981–7, 2003.

[101] A. Pöppl, P. Manikandan, K. Köhler, P. Maas, P. Strauch, R. Böttcher, and D. Goldfarb. Elucidation of structure and location of V(IV) ions in heteropoly-acid catalysts $H_4PVMo_{11}O_{40}$ as studied by hyperfine sublevel correlation spectroscopy and pulsed electron nuclear double resonance at W- and X-band frequencies. *Journal of the American Chemical Society*, 123(19):4577–4584, 2001.

[102] A. Schweiger and G. Jeschke. *Principles of Pulse Electron Paramagnetic Resonance*. Oxford university press, 2001.

[103] H. Van Willigen. Proton ENDOR on $VO(H_2O)_5^{2+}$ in solid solution. *Journal of Magnetic Resonance*, 39(1):37–46, 1980.

[104] B. Baruah, V. Golub, C. J. O'Connor, and A. Chakravorty. Synthesis of Oxalato-Bridged (Oxo)vanadium(IV) Dimers Using L-Ascorbic Acid as Oxalate Precursor: Structure and Magnetism of Two Systems. *European Journal of Inorganic Chemistry*, 2003(12):2299–2303, 2003.

[105] M. A. Mohamed, A. K. Galwey, and S. A. Halawy. A comparative study of the thermal reactivities of some transition metal oxalates in selected atmospheres. *Thermochimica Acta*, 429:57–72, 2005.

[106] P. M. Ehde, L. Petterson, and J. Glaser. Multicomponent Polyanions. 45. A Multinuclear NMR Study of Vanadate(V)-Oxalate Complexes in Aqueous Solution. *Acta Chemica Scandinavica*, 45:998–1005, 1991.

[107] M. Rajendran and M. S. Rao. Formation of $BaTiO_3$ from citrate precursor. *Journal of Solid State Chemistry*, 113(2):239–247, 1994.

[108] K. Van Werde. *Realisatie en optimalisering van de waterige oplossing-gel methode voor de bereiding van perovskiet PZN en gedopeerde PZN-verbindingen.* PhD thesis, Limburgs Universitair Centrum, 2003.

[109] M. M. Barbooti and D. A. Al-Sammerrai. Thermal decomposition of citric acid. *Thermochimica Acta*, 98(0):119–126, 1986.

[110] T. N. Sorrell. *Interpreting Spectra of Organic Molecules.* University Science Books, 1988.

[111] K. Muraishi and Y. Suzuki. The thermal behaviour atmospheres of dicarboxylic acids in various. *Thermochimica Acta*, 232:195–203, 1994.

[112] Van Genechten D. *Watergebasseerde bereiding van ferro-elektrische nanogestructureerde* $Pb(Zr_{0.3}Ti_{0.7})O_3$ *films.* PhD thesis, Limburgs Universitair Centrum, 2005.

[113] L. Abello, E. Husson, Y. Repelin, and G. Lucazeau. Vibrational spectra and valence force field of crystalline V_2O_5. *Spectrochimica Acta*, 39A(7):641–651, 1983.

[114] J. McMurry. *Organic Chemistry.* Thomson Brooks/Cole, 2004.

[115] H. T. Kim, T. Mun, C. Park, S. W. Jin, and H. Y. Park. Characteristics of lithium phosphorous oxynitride thin films deposited by metal-organic chemical vapor deposition technique. *Journal of Power Sources*, 244:641–645, 2013.

[116] N. F. Mott. Metal-Insulator Transition. *Reviews of Modern Physics, Session I - Introduction*, 40(4):677–683, 1968.

[117] F. Beteille, L. Mazerolles, and J. Livage. Microstructure and metal-insulating transition of VO_2 thin films. *Materials Research Bulletin*, 34(99):2177–2184, 2000.

[118] B. G. Chae, H. T. Kim, and S. J. Yun. Characteristics of W- and Ti-Doped VO_2 Thin Films Prepared by Sol-Gel Method. *Electrochemical and Solid-State Letters*, 11(6):2008–2010, 2008.

[119] B. G. Chae and H. T. Kim. Effects of W doping on the metal-insulator transition in vanadium dioxide film. *Physica B: Condensed Matter*, 405(2):663–667, 2010.

[120] H.-K. Chen, H.-C. Hung, T. C.-K. Yang, and S.-F. Wang. The preparation and characterization of transparent nano-sized thermochromic VO_2-SiO_2 films from the sol-gel process. *Journal of Non-Crystalline Solids*, 347(1-3):138–143, 2004.

[121] W. Chen, J. Peng, L. Mai, H. Yu, and Y. Qi. Synthesis and characterization of novel vanadium dioxide nanorods. *Solid State Communications*, 132(8):513–516, 2004.

[122] T. J. Hanlon, J. A. Coath, and M. A. Richardson. Molybdenum-doped vanadium dioxide coatings on glass produced by the aqueous sol-gel method. *Thin Solid Films*, 436(2):269–272, 2003.

[123] T. J Hanlon, R. E Walker, J. A. Coath, and M. A. Richardson. Comparison between vanadium dioxide coatings on glass produced by sputtering, alkoxide and aqueous sol-gel methods. *Thin Solid Films*, 405(1-2):234–237, 2002.

[124] R. Lopez, L. A. Boatner, T. E. Haynes, R. F. Haglund, and L. C. Feldman. Enhanced hysteresis in the semiconductor-to-metal phase transition of VO_2 precipitates formed in SiO_2 by ion implantation. *Applied Physics Letters*, 79(19):3161–3163, 2001.

[125] R. Lopez, L. A. Boatner, and T. E. Haynes. Synthesis and characterization of size-controlled vanadium dioxide nanocrystals in a fused silica matrix. *Journal of Applied Physics*, 92(7):4031–4037, 2002.

[126] J. Qi, G. Ning, and Y. Lin. Synthesis, characterization, and thermodynamic parameters of vanadium dioxide. *Materials Research Bulletin*, 43:2300–2307, 2008.

[127] C. G. Granqvist. Electrochromic oxides - a undefined view. *Solid State Ionics*, 70:678–685, 1994.

[128] C.G. Granqvist, P.C. Lansåaker, N.R. Mlyuka, G.a. Niklasson, and E. Avendaño. Progress in chromogenics: New results for electrochromic and thermochromic materials and devices. *Solar Energy Materials and Solar Cells*, 93(12):2032–2039, 2009.

[129] H.-T. Kim, B.-G. Chae, D.-H. Youn, S.-L. Maeng, G. Kim, K.-Y. Kang, and Y.-S. Lim. Mechanism and observation of Mott transition in VO_2-based two- and three-terminal devices. *New Journal of Physics*, 6:52–52, 2004.

[130] H. T. Kim, B.-G. Chae, D.-H. Youn, G. Kim, K.-Y. Kang, S.-J. Lee, K. Kim, and Y.-S. Lim. Raman study of electric-field-induced first-order metal-insulator transition in VO_2-based devices. *Applied Physics Letters*, 86(24):242101, 2005.

[131] M.-J. Lee, Y. Park, D.-S. Suh, E.-H. Lee, S. Seo, D.-C. Kim, R. Jung, B.-S. Kang, S.-E. Ahn, C.-B. Lee, D.-H. Seo, Y.-K. Cha, I.-K. Yoo, J.-S. Kim, and B.-H. Park. Two Series Oxide Resistors Applicable to High Speed and High Density Nonvolatile Memory. *Advanced Materials*, 19(22):3919–3923, 2007.

[132] G. Stefanovich, A. Pergament, and D. Stefanovich. Electrical switching and Mott transition in VO_2. *Journal of Physics: Condensed Matter*, 12:8837–8845, 2000.

[133] C. Chen, R. Wang, L. Shang, and C. Guo. Gate-field-induced phase transitions in VO_2: Monoclinic metal phase separation and switchable infrared reflections. *Applied Physics Letters*, 93(17):171101, 2008.

[134] K. M. Martens, I. P. Radu, G. Rampelberg, J. Verbruggen, S. Mertens, X. Shi, M. Schaekers, C. Huyghebaert, C. Detavernier, M. Heyns, and J. A Kittl. VO_2, a Metal-Insulator Transition Material for Nanoelectronic Applications. *ECS Transactions*, 45(4):151–158, 2012.

[135] P. Baum, D.-S. Yang, and A. H. Zewail. 4D visualization of transitional structures in phase transformations by electron diffraction. *Science*, 318(5851):788–92, 2007.

[136] A. Cavalleri, T. Dekorsy, H. H. W. Chong, J. C. Kieffer, and R. W. Schoenlein. Evidence for a structurally-driven insulator-to-metal transition in VO_2: a view from the ultrafast timescale. *Physics Review B*, 70:161102, 2004.

[137] Z. Yang, C. Ko, and S. Ramanathan. Oxide Electronics Utilizing Ultrafast Metal-Insulator Transitions. *Annual Review of Materials Research*, 41:337–367, 2011.

[138] J. H. Park, J. M. Coy, T. S. Kasirga, C. Huang, Z. Fei, S. Hunter, and D. H. Cobden. Measurement of a solid-state triple point at the metal-insulator transition in VO_2. *Nature*, 500:431–434, 2013.

[139] Y. Gao, H. Luo, Z. Zhang, L. Kang, Z. Chen, J. Du, M. Kanehira, and C. Cao. Nanoceramic VO_2 thermochromic smart glass: A review on progress in solution processing. *Nano Energy*, 1(2):221–246, 2012.

[140] V. Eyert. The metal-insulator transition of VO_2: a band theoretical approach. *Annalen der Physik*, 11(9):650–702, 2002.

[141] B.-J. Kim, Y. W. Lee, B.-G. Chae, S. J. Yun, S.-Y. Oh, H.-T. Kim, and Y.-S. Lim. Temperature dependence of the first-order metal-insulator transition in VO_2 and programmable critical temperature sensor. *Applied Physics Letters*, 90(2):023515, 2007.

[142] R. M. Wentzcovitch, W. W. Schulz, and P. B. Allen. VO_2: Peierls or Mott-Hubbard? A view from Band Theory. *Physical Review Letters*, 72(21):3389–3391, 1994.

[143] Q. Shi, W. Huang, J. Wu, Y. Zhang, and Y. Xu. Terahertz transmission characteristics across the phase transition in VO_2 films deposited on Si, sapphire, and SiO_2 substrates. *Journal of Applied Physics*, 112:033523, 2012.

[144] Z. Zhang, Y. Gao, Z. Chen, J. Du, C. Cao, L. Kang, and H. Luo. Thermochromic VO_2 Thin Films: Solution-Based Processing, Improved Optical Properties, and Lowered Phase Transformation Temperature. *Langmuir*, 26(13):10738–10744, 2010.

[145] V. Keppens, D. Mandrus, and L. A. Boatner. Chemical and sonochemical approaches to the formation of VO_2 films and VO_2-impregnated materials. *Chemical Aspects of Electronic Ceramics Processing*, 495:439–444, 1998.

[146] N. Y. Yuan, J. H. Li, and C. L. Lin. Valence reduction process from sol-gel V_2O_5 to VO_2 thin films. *Applied Surface Science*, 191(1–4):176–180, 2002.

[147] B. G. Chae, H. T. Kim, S. J. Yun, B. J. Kim, Y. W. Lee, D. H. Youn, and K. Y. Kang. Highly Oriented VO_2 Thin Films Prepared by Sol-Gel Deposition. *Electrochemical and Solid-State Letters*, 9(1):C12, 2006.

[148] C. Batista, R. M. Ribeiro, and V. Teixeira. Synthesis and characterization of VO_2-based thermochromic thin films for energy-efficient windows. *Nanoscale research letters*, 6(1):301, 2011.

[149] F. Beteille and J. Livage. Optical switching in VO_2 thin films. *Journal of Sol-Gel Science and Technology*, 13:915–921, 1998.

[150] L. Kang, Y. Gao, Z. Zhang, J. Du, C. Cao, Z. Chen, and H. Luo. Efffects of Annealing Parameters on Optical Properties of Thermochromic VO_2 Films Prepared in Aqueous Solution. *Journal of Physical Chemistry*, 114:1901–1911, 2010.

[151] B. Y. Wang, K. Takahashi, K. Lee, and G. Cao. Nanostructured Vanadium Oxide Electrodes for Enhanced Lithium-Ion Intercalation. *Advanced Functional Materials*, 16:1133–1144, 2006.

[152] C. M. Julien. Lithium intercalated compounds Charge transfer and related properties. *Materials Science and Engineering: R: Reports*, 40:47–102, 2003.

[153] D. W. Murphy, P. A. Christian, F. J. DiSalvo, J. N. Carides, and J. V. Waszczak. Lithium Incorporation by and Related Vanadium (+4, +5) Oxide Cathode Materials. *Journal of The Electrochemical Society*, pages 2053–2060, 1981.

[154] K. West, B. Zachau-Christiansen, and T. Jacobson. Electrochemical properties of non-stoichiometric V_6O_{13}. *Electrochemica Acta*, 17:2526–2552, 1983.

[155] N. A. Chernova, M. Roppolo, A. C. Dillon, and M. S. Whittingham. Layered vanadium and molybdenum oxides: batteries and electrochromics. *Journal of Materials Chemistry*, 19(17):2526, 2009.

[156] B. Zachau-Christiansen, K. West, T. Jacobsen, and S. Skaarup. Lithium insertion in isomorphous MO_2 (B) structures. *Solid State Ionics*, 53-56:364–369, 1992.

[157] M. Pan, H. Zhong, S. Wang, J. Liu, Z. Li, X. Chen, and W. Lu. Properties of VO_2 thin film prepared with precursor $VO(acac)_2$. *Journal of Crystal Growth*, 265:121–126, 2004.

[158] M. B. Sahana, C. Sudakar, C. Thapa, G. Lawes, V. M. Naik, R. J. Baird, G. W. Auner, R. Naik, and K. R. Padmanabhan. Electrochemical properties of V_2O_5 thin films deposited by spin coating. *Materials Science and Engineering B*, 143:42–50, 2007.

[159] L. Kang, Y. Gao, and H. Luo. A novel solution process for the synthesis of VO_2 thin films with excellent thermochromic properties. *ACS applied materials & interfaces*, 1(10):2211–8, 2009.

[160] S. Deki, Y. Aoi, and A. Kajinami. A novel wet process for the preparation of vanadium dioxide thin films. *Journal of Materials Science*, 32:4269–4273, 1997.

[161] Y. Jiazhen, Z. Yue, H. Wanxia, and T. Mingjin. Effect of Mo-W Co-doping on semiconductor-metal phase transition temperature of vanadium dioxide film. *Thin Solid Films*, 516(23):8554–8558, 2008.

[162] IMEC academy. Open course program: Advanced cleaning, 2011.

[163] S. L. Hellstrom. Basic models of spin coating., 2007.

[164] S. Saitzek, F. Guinneton, G. Guirleo, L. Sauques, K. Aguir, and J.-R. Gavarri. VO_2 thin films deposited on silicon substrates from V_2O_5 target: Limits in optical switching properties and modeling. *Thin Solid Films*, 516:891–897, 2008.

[165] J. W. Mullin. *Crystallization.* Butterworth Heinemann, 4th edition, 2001.

[166] C. V. Thompson. Solid-State Dewetting of Thin Films. *Annual Review of Materials Research*, 2012.

[167] D. J. Srolovitz and S. A. Safran. Cappillary instabilities in thin films. I. Energetics. *Journal of Applied Physics*, 60:247–245, 1986.

[168] I. L. Botto, M. B. Vassallo, E. J. Baran, and G. Minelli. IR spectra of VO_2 and V_2O_3. *Materials Chemistry and Physics*, 50:267–270, 1997.

[169] K. Ishikawa, Y. Uchiyama, H. Ogawa, and S. Fujimura. Dependence of TO and LO mode frequency of thermally grown silicon dioxide films on annealing temperature. *Applied Surface Science*, 117–118:212–215, 1997.

[170] S. Surnev, M. G. Ramsey, and F. P. Netzer. Vanadium oxide surface studies. *Progress in Surface Science*, 73:117–165, 2003.

[171] B. Lefez, J. Lopitaux, B. Hannoyer, M.-P. Bacos, and E. Beucher. Fourier transform infrared reflection absorption spectroscopy and microspectroscopy, a tool to investigate thermally grown oxide scales. *Thin Solid Films*, 516(2-4):349–354, December 2007.

[172] R. N. Wenzel. Resistance of solid surfaces to wetting by water. *Industrials and Engineering Chemistry*, 28(8):988–994, 1936.

[173] G. Wolansky and A. Marmur. Apparent contact angles on rough surfaces : the Wenzel equation revisited. *Colloids and Surfaces*, 156:381–388, 1999.

[174] M. K. Van Bael, D. Nelis, A. Hardy, D. Mondelaers, K. Van Werde, J. D'Haen, G. Vanhoyland, H. Van den Rul, J. Mullens, L. C. Van Poucke, F. Frederix, and D. J. Wouters. Aqueous chemical solution deposition of ferroelectric thin films. *Integrated Ferroelectrics*, 45:113–122, 2002.

[175] C. Leroux and G. Nihoul. From $VO_2(B)$ to $VO_2(R)$: Theoretical structures of VO_2 polymorphs and in situ electron microscopy. *Physical Review B*, 57(9):5111–5121, 1998.

[176] N. C. Saha and H. G. Tompkins. Titanium nitride oxidation spectroscopy study chemistry: An x-ray photoelectron of bulk TiN. *Journal of Applied Physics*, 7(72), 1992.

[177] H. G. Tompkins. Oxidation of titanium nitride in room air and in dry 02 . *Journal of Applied Physics*, 70:3876–3880, 1991.

[178] X. Hou, K.-C. Chou, and M. Zhang. The Model for Oxidation Kinetics of Titanium Nitride Coatings. *International Journal of Applied Ceramic Technology*, 7(2):248–255, 2010.

[179] P. C. McIntyre and S. R. Summerfelt. Kinetics and mechanisms of TiN oxidation beneath Pt thin films. *Journal of Applied Physics*, 82(9):4577–4585, 2001.

[180] S. Deng, S. W. Verbruggen, S. Lenearts, J. A. Martens, S. Van den Berghe, K. Devloo-Casier, W. Devulder, J. Dendooven, D. Deduytsche, and C. Detavernier. Controllable nitrogen doping in as deposited TiO_2 film and its effect on post deposition annealing. *Journal of Vacuum Science and Technology*, 2014.

[181] Muraoka Y. and Z. Hiroi. Metal-insulator transition of VO_2 thin films grown on TiO_2 (001) and (110) substrates. *Applied Physics Letters*, 80(4):583–585, 2002.

[182] E. Abreu, M. Liu, J. Lu, K. G. West, S. Kittiwatanakul, W. Yin, S. A. Wolf, and R. D. Averitt. Thz spectroscopy of VO_2 epitaxial films: controlling the anisotropic properties through strain engineering. *New Journal of Physics*, 14:083026, 2012.

[183] H. Friebolin. *Basic One- and Two-Dimensional NMR Spectroscopy.* Wiley-VCH Verlag GmbH & Co., 4th edition, 2005.

[184] J. A. Weil and J. R. Bolton. *Electron Paramagnetic Resonance: Elementary Theory and Practical Applications.* John Wiley & Sons, 2nd edition, 2007.

[185] T. D. W. Claridge. *High-Resolution NMR Techniques in Organic Chemistry.* Elsevier, 2nd edition, 2009.

[186] D. Rehder, T. Polenova, and M. Bu. Vanadium-51 NMR. *Annual Reports in NMR Spectroscopy*, 62:50–114, 2007.

[187] S. Van Doorslaer, I. Caretti, I. A. Fallis, and D. M. Murphy. The power of electron paramagnetic resonance to study asymmetric homogeneous catalysts based on transition-metal complexes. *Coordination Chemistry Reviews*, 253:2116–2130, 2009.

[188] A. Bencini and G. Gatteschi. *Inorganic Electronic Structure and Spectroscopy. Volume 1: Methodology, chapter 2: Electron Paramagnetic Resonance Spectroscopy.* John Wiley & Sons, 1995.

[189] M. J. N. Junk. *Assessing the Functional Structure of Molecular Transporters by EPR Spectroscopy.* Springer Theses, 2012.

[190] http://www.easyspin.org., 2013.

[191] S. Stoll and A. Schweiger. EasySpin, a comprehensive software package for spectral simulation and analysis in EPR. *Journal of Magnetic Resonance*, 178:42–55, 2006.

[192] P. Höfer, A. Grupp, H. Nebenführ, and M. Mehring. Hyperfine Sublevel Correlation (HYSCORE) Spectroscopy: A 2D ESR Investigation of the Squaric Radical. *Chemical Physics Letters*, 132(3):279–282, 1986.